磁性を示す遷移金属水酸塩化物の分光学的研究

2013 年 9 月

劉 暁東

Dissertation for the Doctoral Degree in Science

Study on Optical Spectra of Magnetic Hydroxyl Halides

Candidate：	Xiao-Dong Liu
Supervisor：	Prof. Xu-Guang Zheng
Academic Degree Applied For :	Doctor of Science
Speciality：	Physics
Date of Submission：	28 June 2013
Date of Oral Examination：	12 Aug. 2013
University：	Saga University

Abstract

In recent years, geometrically frustrated magnets receive intense attention because they are playgrounds for unconventional quantum states such as spin liquid and other novel properties. Many exotic quantum magnetic phenomena related to the **magnetic geometrical frustration** (MGF) have been found and studied in several kinds of uniformly crystallized materials, including the **hydroxyl chlorides** $M_2(OH)_3X$ series. Because there is the existing **spin-phonon coupling** effect in the MGF system, it should be possible to probe the magnetic properties through measuring the lattice vibration (phonon) features accompanied with dynamic coupling to spin interactions by using infrared (IR) and Raman spectroscopic technologies. Till now, although there have been a lot of research on the relationship of crystal lattice and magnetism, few have been conducted on their dynamic coupling. In this work, evaluation of the dynamic coupling, as is exemplified in the γ-$Cu_2(OH)_3Cl$, is the final research aim.

To reach the aim, the author of this dissertation has performed a standard **factor group analysis** (FGA) on all four kinds of space groups to which the all geometrically frustrated transition-metal hydroxyl halides $M_2(OH)_3X$ (M=Co, Ni, Cu; X=Cl, Br) belong, measured the **IR** and **Raman spectra** at room temperature (RT) and assigned almost all the normal modes as complete as possible, and conducted the low-temperature Raman scattering experiments on several samples to investigate their Raman spectroscopic response to the MGF properties. The structure of this dissertation is as the following:

In Chapter **1**, some elementary physical topics related to the dissertation and research situation of spectral studies on hydroxyl halides are introduced, and then research aims and methods of the doctoral dissertation are given in detail.

In Chapter **2**, the author has performed, for the first time to the best of our knowledge, a standard FGA on the space groups of No. 166, No. 62, No. 14 and No. 11, through working out corresponding point group character and correlation tables by considering carefully all cite symmetric species. These have built up the foundation for the complete normal mode assignment.

In Chapter **3**, the author has performed spectral analysis of IR and Raman spectra of most of hydroxyl halides $M_2(OH)_3X$ at RT. The following results have been obtained:

(1) Using five spectral analyzing methods, it is found that the whole IR or Raman spectrum of each sample can be divided into four well-separated regions: [OH/D] function group, [OH/D] correlation peak, M-O and M-X fingerprint regions, respectively. In addition, wrong assignments of some bands in previous publications are pointed out.

(2) In each spectral region, most experimental spectral bands have been assigned definitely and are considered to correspond well to their normal modes predicted by the standard FGA method. From those sharp band profiles in each spectrum, it is concluded that each sample is well crystallized and suitable for the further spectral study.

(3) After checking the [OH] stretching frequency of each sample and its crystal structure, three kinds of $(OH)_3\cdots X$ hydrogen-bond are found to exist in these materials according to the structural symmetry, and they have been nominated **trimeric hydrogen-bond** by our research team. The trimeric H-bonds in this series are found to have four subtypes and two more subtypes are predicted to exist in nature.

(4) Furthermore it is found that the trimeric H-bond concept and the approximate linearity between the [OH] stretching frequency and [OH] distance can be applied to estimate and evaluate the rightness of the OH distances given by other authors, and determine the difference between different OH groups, *etc*.

In Chapter **4**, through the temperature-dependent Raman spectroscopic investigation on the clinoatacamite γ-$Cu_2(OH)_3Cl$, the following results are obtained and given:

(1) Among eight representative normal modes, the trend as a whole of five frequency variations and all eight width variations in the wide-temperature range presents a normal thermal expansion behavior of a normal non-magnetic and isolating material. Yet each of the other three frequency variations shows an abnormal behavior, and it has been elucidated by the dominating effect of the trimeric hydrogen-bond.

(2) It is found that the commonly used fitting formula of both frequency and width variations resulting from the sum of lattice and phonon-phonon anharmonic terms at the high-temperature are not suitable for fitting the high frequency modes.

(3) Obvious Raman spectroscopic evidences of successive magnetic transition are found at the Curie temperatures T_{c1}=18 K and T_{c2}=6 K: it comes from the apparently anomalous temperature-dependent Raman band frequencies and linewidths of 8 modes below about 18 K because of spin-phonon coupling effect.

(4) Based on the quantitative analysis on the pronounced background at high-temperature and the broad continuum at the intermediate and low-temperatures, it is verified that the coexistence of partial **magnetic order** and **spin fluctuations** of a picosecond time scale at the intermediate phase in the temperature range of T_{c1}=18 K and T_{c2}=6 K comes from quasi-two-dimensional antiferromagnet lattice structure.

In Chapter **5**, the above-mentioned works are concluded, and an outlook is given.

In summary, the author has obtained several achievements in respect of the dynamic coupling of lattice vibration and the magnetism in the geometrically frustrated $M_2(OH)_3X$ series. In particular, the low-temperature investigation of γ-$Cu_2(OH)_3Cl$ of Raman spectra has given the spectral evidence of the successive magnetic transitions and revealed the nature of coexistence of magnetic order and spin fluctuations in the intermediate phase between T_{c1} and T_{c2}. Unpolarized Raman scattering can only provide limited information about the dynamic coupling, therefore, it is hoped that further experiments of polarized Raman scattering experiments on single crystals be performed to completely uncover the exotic nature of the frustrated magnetism in the hydroxyl chlorides $M_2(OH)_3X$ series.

Keywords:

(1) Hydroxyl Halide

(2) Spin-phonon Coupling

(3) Magnetic Order

(4) Spin Fluctuation

(5) Geometric Frustration

(6) IR Spectrum

(7) Raman Spectrum

(8) Factor Group Analysis

(9) Trimeric Hydrogen Bond

Table of physical quantities, symbols and abbreviations

Crystallography

M	− Transition metal (Co, Ni, Cu)
α, β, γ	− Degree among the unit cell's axes
θ	− Degree among three atoms or ions
d	− Distance
XRD	− X-ray diffraction
X	− Halogen (Cl, Br, I)
TE	−Thermal expansion
NTE	− Negative thermal expansion

Magnetism and Thermodynamics

AFM	− Antiferromegnetic
FM	− Ferromegnetic
M	− Magnetization
H	− Magnetic field (A/m)
J	− AFM change constant (K, mev)
T_c	− Critical transition temperature (K)
T_C	− Curie temperature (K)
T_N	− Neel temperature (K)
θ_{CW}	− Curie-Weiss temperature (K)
C_P	− Heat capacity (special heat)
C	− Curie constant (emu K mol^{-1})
μ_B	− Bohr magnon
NN	− Nearest neighbor
NNN	− Next nearest neighbor
	−

Spectroscopy

SG	− Space group
FG	− Functional group
FP	− Fingerprint
CP	− Correlation peak
FGA	− Factor group analysis
k	− Force constant (mdyn/Å)
ω	− Frequency (cm^{-1})
P_L	− Laser power (mW)
v_s	− Symmetry stretching vibration
v_{as}	− Asymmetry stretching vibration
SLC	− Spin-lattice coupling
SPC	− Spin-phonon coupling
FWHM	− Full Width of Half Maximum
LLH	− Local laser heating
Γ	− Phonon linewidth (cm^{-1})
γ_α	− SPC linewidth coefficient
λ_α	− SPC frequency coefficient
τ	− Response time
c	− Light speed in vacuum
h	− Plank constant
μSR	− Muon spin rotation
MGF	− Magnetic geometric frustration
T	− Temperature (K)
RT	− Room temperature (~295 K)
	−

Contents

Chapter 1

Introduction

Physics of solid state matters is very interesting. In this chapter I will first introduce general physical, especially magnetic properties of solid state matters in Sects. 1.1 and 1.2, magnetic geometric frustration in magnetic matters in Sect. 1.3, and infrared (IR) and Raman spectral properties of solid state matters in Sect. 1.4. In consideration of the possible significance of hydrogen bonds in our samples, century's achievements are chiefly reviewed in Sect. 1.5 to lay the groundwork for our research. In order to master the important achievement mainly obtained by our group in recent years, I also collect the structural, thermal and magnetic properties of $M_2(OH)_3X$ in Sect. 1.6, to give the basic to realize my research aims of this doctoral dissertation described in Sect. 1.7.

1.1 General physical properties of solid state matters

General physical properties of solid state matters are investigated in the so-called solid-state physics, which is the study of rigid matter, or solids, through methods such as quantum mechanics, crystallography, electromagnetism, and metallurgy.[1] It is the largest branch of condensed matter physics. Solid-state physics studies how the large-scale properties of solid materials result from their atomic-scale properties, and forms the theoretical basis of material science. It also has direct applications, for example in the technology of transistors, semiconductors and superconductors.[1]

Solid state matters are formed from densely-packed atoms, which interact intensely. These interactions produce the mechanical, thermal, electrical, magnetic and optical properties of solids. Depending on the material involved and the conditions in which it is formed, the atoms may be arranged in a regular, geometric pattern or irregularly (an amorphous solid).

The bulk of the solid-state physics theory is focused on crystals. Primarily, this is because the periodicity of atoms in a crystal — its defining characteristic — facilitates mathematical modeling. Likewise, crystalline materials often have electrical, magnetic, optical, or mechanical properties that can be exploited for engineering purposes.

The forces between the atoms in a crystal can take a variety of forms. For example, in a

crystal of sodium chloride (NaCl, common salt), the crystal is made up of Na^+ and Cl^-, and held together with ionic bonds. In others, the atoms share electrons and form covalent bonds. In metals, electrons are shared amongst the whole crystal in metallic bonding. Finally, the noble gases do not undergo any of these types of bonding. The differences between the types of solid result from the differences between their bonding.

Many properties of materials are affected by their crystal structure. The sizes of the individual crystals in a crystalline solid material vary depending on the material involved and the conditions when it was formed. Most crystalline materials encountered in everyday life are polycrystalline, with the individual crystals being microscopic in scale, but macroscopic single crystals can be produced either naturally (e.g. diamonds) or artificially.

The crystal lattice can vibrate. These vibrations are found to be quantized, the quantized vibrational modes being known as phonons. Phonons play a major role in many of the physical properties of solids, such as the transmission of sound. In insulating solids, phonons are also the primary mechanism by which heat conduction takes place, and are necessary for understanding the lattice heat capacity, as in the Einstein model and the later Debye model.

The material's properties, such as electrical conduction and heat capacity, are investigated by solid-state physics, while magnetism is a property of materials that respond at an atomic or subatomic level to an applied magnetic field *H*. [1, 2] Ferromagnetism is the strongest and most familiar type of magnetism. It is responsible for the behavior of permanent magnets, which produce their own persistent *H*s, as well as the materials that are attracted to them. However, all materials are influenced to a greater or lesser degree by the presence of an *H*. Some are attracted to an *H* (paramagnetism, PM); others are repulsed by an *H* (diamagnetism); others have a much more complex relationship with an applied *H*. Substances that are negligibly affected by *H*s are known as non-magnetic substances. The hierarchy of types of magnetism given by Myers is shown in Fig. 1.1.1. [2]

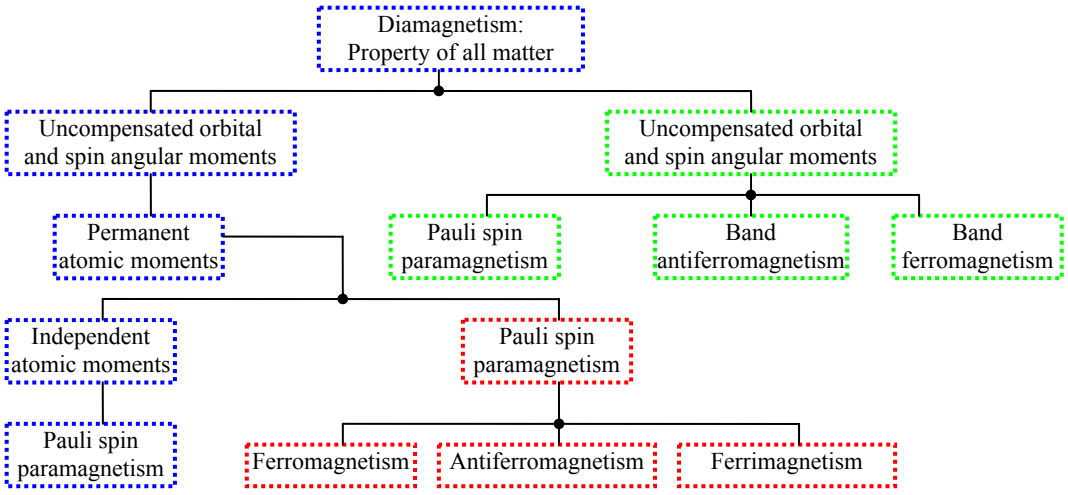

Fig. 1.1.1. The structure of types of magnetism.

Diamagnetism is a very general phenomenon, because all electrons, including the electrons of an atom, will always make a weak contribution to the material's response. In most materials, diamagnetism is a weak effect, and completely overpowered for materials that show some other form of magnetism (such as ferromagnetism or paramagnetism).

Paramagnetism occurs only in the presence of an externally applied *H*. [2] The magnetic moment induced by the applied field is linear in the field strength and rather weak. Constituent atoms or molecules of paramagnetic materials have permanent magnetic moments, even in the absence of an applied field. This generally occurs due to the spin of unpaired electrons in the atomic/molecular electron orbitals. In pure paramagnetism, the dipoles do not interact with one another and are randomly oriented in the absence of an external field due to thermal agitation, resulting in zero net magnetic moment. Even in the presence of the field there is only a small induced magnetization because only a small fraction of the spins will be oriented by the field. This fraction is proportional to the field strength and this explains the linear dependency. In general paramagnetic effects are also small. Fig. 1.1.2 (a) gives a simple illustration of a paramagnetic probe made up from miniature magnets.

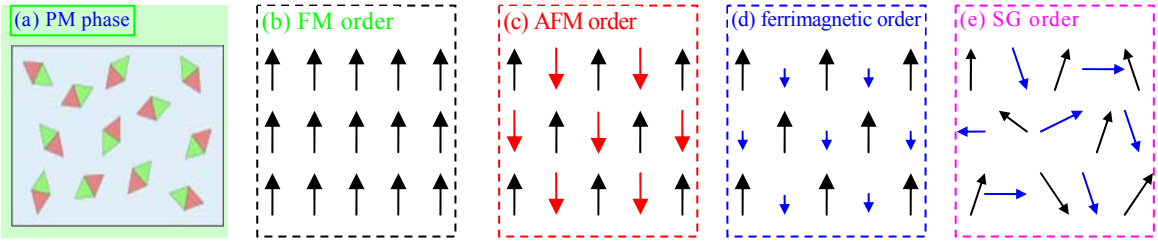

Fig. 1.1.2. (a) PM phase, (b) FM, (c) AFM, (d) ferrimegnetic and (e) random spin-glassy (SG) orders.

Ferromagnetism is the basic mechanism by which certain materials (such as iron) form permanent magnets. Ferromagnetism (including ferrimagnetism) is the strongest type; it is the only type strong enough to be felt, and is usually responsible for the common phenomena of magnetism encountered in everyday life, apparent to the ancient world. In the microscopic viewpoint, a material is "ferromagnetic (FM)" in a stricter sense only if all of its magnetic ions add a positive contribution to the net magnetization, see Fig. 1.1.2 (b).

Antiferromagnetism is exhibited in materials if the magnetic moments of atoms or molecules, usually related to the spins of electrons, align in a regular pattern with neighboring spins (on different sublattices) pointing in opposite directions, see Fig. 1.1.2 (c). In other words, if the moments of the aligned and anti-aligned ions balance completely so as to have zero net magnetization, despite the magnetic ordering, then it is antiferromagnetic (AFM).

Ferrimagnetism is exhibited in materials if some of the magnetic ions subtract from the net magnetization (if they are partially anti-aligned as in antiferromagnetism), see Fig. 1.1.2

(d). However, in ferrimagnetic materials, the opposing moments are unequal and a spontaneous magnetization remains like ferromagnetism. Generally ferrimagnetic materials have high resistivity and have anisotropic properties.

The phenomenon of magnetism is mediated by the magnetic field (H). In a normal material, when an $\boldsymbol{H}$ exits at some temperature T, the response of the magnetization $\boldsymbol{M}(T, \boldsymbol{H})$

$$\boldsymbol{M}(T,\boldsymbol{H}) \equiv \chi(T)\boldsymbol{H}, \text{ or } \chi(T) \equiv \frac{M(T,H)}{H} \tag{1.1.1}$$

where the magnetic susceptibility $\chi(T)$ is a dimensionless proportionality constant that indicates the degree of magnetization $\boldsymbol{M}(T, \boldsymbol{H})$ (the magnetic dipole moment per unit volume, measured in A/m) of a material in response to an applied $\boldsymbol{H}$ (A/m). Surely in a hard magnet such as a ferromagnet, $\boldsymbol{M}(T, \boldsymbol{H})$ is not proportional to the field and is generally nonzero even when $\boldsymbol{H}$ is zero.

In a ferromagnet (including ferrimagnet), as the temperature increases, thermal motion, or entropy, competes with the FM tendency for dipoles to align. When the temperature rises beyond a certain point, called the Curie or Curie-Weiss temperature T_C (or T_{CW}), there is a second-order phase transition and the system can no longer maintain a spontaneous magnetization, although it still responds paramagnetically to an external field. Below that T, there is a spontaneous symmetry breaking and random domains form (in the absence of an external field). The T_C itself is a critical point, where the magnetic susceptibility is theoretically infinite and, although there is no net magnetization, domain-like spin correlations fluctuate at all length scales. A simple theory predicts that, above the T_C, the magnetic susceptibility χ is given by the Curie-Weiss law:

$$\chi(T) = \frac{C}{T - T_C}, \quad \chi^{-1}(T) = \frac{T - T_C}{C} \tag{1.1.2}$$

where C is a material-specific Curie constant, temperature is measured in kelvins. Thus, the magnetic susceptibility χ approaches infinity as the temperature approaches T_c.

An antiferromagnet becomes typically paramagnetic when the temperature above the Néel or magnetic ordering temperature T_N,—that is, the thermal energy becomes large enough to destroy the macroscopic magnetic ordering within the material.[2] Generally, AFM order may exist at sufficiently low temperatures. χ of an AFM material typically shows a maximum at T_N, and is given by:

$$\chi(T) = \frac{C}{T + T_N}, \quad \chi^{-1}(T) = \frac{T + T_N}{C} \tag{1.1.3}$$

In some cases, Eqs. 1.1.2 and 1.1.3 are unified to an idealized Curie–Weiss form:

$$\chi(T)=\frac{C}{T-\theta_{CW}},\quad \chi^{-1}(T)=\frac{T-\theta_{CW}}{C} \tag{1.1.4}$$

Here, when $\theta_{CW}>0$, FM $T_C \equiv \theta_{CW}$; $\theta_{CW}<0$, AFM $T_N \equiv -\theta_{CW}$. In real nonideal FM or AFM case, the T point (usually close to or even far from $|\theta_{CW}|$) deviating from ideal behavior is called T_C or T_N. [3]

When the temperature is low enough, if there is sufficient energy exchange between neighbouring dipoles they will interact, and may spontaneously align or anti-align and form magnetic domains, resulting in ferromagnetism (permanent magnets) or antiferromagnetism, respectively. Paramagnetic behavior can also and must be observed both in ferromagnets that are above their T_C, and in antiferromagnets above their T_N. [2]

The study of these magnetic phase transitions, especially via the simplified Ising spin model, had an important impact on the development of statistical physics.

The specific heat capacity, often simply called specific heat (usually denoted by a capital C_p)**,** characterizes the amount of heat required to change a substance's temperature per unit mass of a material by a given amount (in unit of $J\cdot mol^{-1}\cdot K^{-1}$). Translation, rotation, and the two types of energy in vibration (kinetic and potential) represent the degrees of freedom of motion which classically contribute to C_p of a thermodynamic system. For quantum mechanical reasons, some of these degrees of freedom may not be available, or only partially available to store thermal energy, at a given temperature. As the temperature approaches absolute zero, the specific heat capacity of a system also approaches zero, due to loss of available degrees of freedom due to the quantum mechanical effect. For a more modern and precise analysis of the heat capacities of solids, especially at low temperatures, it is useful to use the idea of phonons, whose contribution to C_p in a solid is estimated by the Debye model that correctly predicts the low T dependence of $C_p(T)$, which is proportional to T^3 – the Debye T^3 law just like the Einstein model.

For other bosonic quasi-particles, e.g. for magnons (quantized spin waves) in ferromagnets instead of the phonons (quantized sound waves), at low frequencies one has different dispersion relations, e.g. $E(v)\sim k^2$ in the case of magnons, instead of $E(v)\sim k$ for phonons and different sum rules. [4] As a consequence, in ferromagnets one gets a magnon contribution to the heat capacity (magnetic specific heat C_m), $C_m\sim T^{3/2}$, which dominates at sufficiently low temperatures the phonon contribution $C_{phonon}\sim T^3$. Therefore abnormal T-dependence of the C_p of a magnetic material at low frequencies must include the magnetic contribution to the total specific heat, provide a lot of information on its low- temperature magnetic structure, and become an important aspect in its experimental study, especially for a magnetic geometric frustration (MGF) material. [4]

In general, the related physical properties can be experimentally investigated by the following means: (1) magnetic susceptibility $\chi(T, \boldsymbol{H})$ and the magnetization $\boldsymbol{M}(T, \boldsymbol{H})$ by the superconducting quantum interference device (SQUID); (2) heat capacity (specific heat) C_p by the adiabatic heat pulse method; (3) the phonon spectrum by the IR spectroscopy and Raman spectroscopy; (4) the crystal structure by a range of crystallographic techniques, including general X-ray diffraction (XRD) crystallography, and elastic neutron diffraction; (5) the magnetic structure by the NMR, neutron diffraction and muon spin resonance (μSR), *etc*.

1.2 Magnetic geometric frustration in magnetic matters

MGF may appear in many kinds of matter system and society, such as the hard-disk fluid system, the strong electric (Coulomb) mutual repulsion system and the opposite sex dinner seating system.

Most of the geometrically frustrated systems studied in physics these years may be concerned with magnetic ones, such as the lattice systems with two-dimensional spin ladder, triangle, and Kagome configurations. All kinds of such systems can, to some extent, lead to many kinds of exotic quantum states, e.g. unconventional spin glass, spin ice, spin liquid, monopole states/phases and therefore has received a large amount of attention in the magnetism community. [5-20]

Till now many exotic quantum magnetic phenomena related to the MGF principle have been found and studied in several kinds of uniformly crystallized materials, such as the pyrochlore series $A_2^{3+}B_2^{4+}O_7$ (space group No. 227), [21-30] perovskite series ABO_3 (mainly space group No. 62), [31-40] spinel series AB_2C_4 (mainly space group No. 227), [41-50] hydroxyl chlorides $M_2(OH)_3X$, [51-100] Herbertsmithite, [101-150] *etc*.

Interestingly, a few real MGF materials may exhibit spin glass state, spin ice state, spin liquid state, "monopole flux" state, or even negative thermal expansion.

In the field of MGF physics theoretical methods have included the Debye model, Hubbard model, Heisenberg model, Ising model, *t-J* model, *etc*.

One simple and highly convenient measure of the level of frustration in magnetic systems is the so-called frustration parameter/index *f*, defined as [4]

$$f \equiv \frac{|\theta_{CW}|}{T^*} \tag{1.2.1}$$

Here θ_{CW} is the Curie-Weiss temperature, the temperature T^* is the critical temperature T_c (or Néel temperature T_N) at which the system ultimately develops long-range spin order. In the case of freezing into a glassy state, which may correspond to a genuine thermodynamic

spin-glass transition, T^* would be the freezing temperature T_f. The more frustrated a system is, the lower T^* is compared to θ_{CW}.

A **spin glass** is a magnet with frustrated interactions, augmented by stochastic disorder, where usually FM and AFM bonds are randomly distributed as shown in Fig. 1.2.1 (a). In other words, the spin-glass state is one where the combination of randomness and frustration prevents the development of conventional long-range magnetic order characterized by delta-function magnetic Bragg peaks. Its magnetic ordering resembles the positional ordering of a conventional, chemical glass. Spin glasses display many metastable structures leading to plenitude of time scales which are difficult to explore experimentally or in simulations.

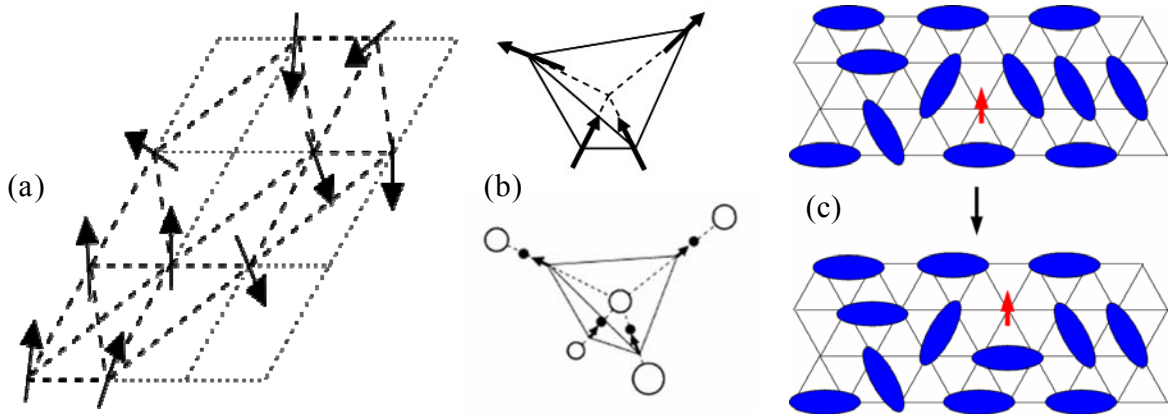

Fig. 1.2.1 (a) spin-glass state, (b) spin ice and water ice, (c) Spinon moving in spin liquids

A **spin ice** is a substance that is similar to water ice in that it can never be completely frozen. This is because it does not have a single minimal-energy state. A spin ice has "spin" degrees of freedom (i.e. it is a magnet), with frustrated interactions which prevent it freezing. It shows low-temperature properties – in particular residual entropy – closely related to those of crystalline water ice. The magnetic ordering of a spin ice resembles the positional ordering of hydrogen atoms in conventional water ice as shown in Fig. 1.2.1 (b).

Spin liquid state denotes a state of matter, where local permanent magnetic moments are present in the material, but do not show any sign of ordering down to the lowest Ts despite comparable strong AFM interactions with spinon "moving" in the magnet as shown in Fig. 1.2.1 (c). [5] Since there is no single experimental feature that identifies a material as a spin liquid, several experiments have to be conducted to gain information on different properties which characterize a spin liquid. An indication is given by a large value of the **frustration parameter** $f > 100$. In most real materials there are, however, perturbative interactions, H', that ultimately intervene at low-T and lead to the development of order out of the spin-liquid state. Even though many theories study spin liquids, no definite spin-liquid material has been found yet, although there are a few possible spin liquid candidates under investigation.

Till now, $Y_2Mo_2O_7$ and $Tb_2Mo_2O_7$ are found to exhibit spin-glass like behavior with T_f =22 K and 25 K, respectively, and the most prominent compounds with spin-ice properties are $Dy_2Ti_2O_7$, $Ho_2Ti_2O_7$ and $A_2Sn_2O_7$ (A=Pr, Dy, and Ho), while only a few candidate pyrochlore materials have been identified, namely, $Tb_2Ti_2O_7$, $Yb_2Ti_2O_7$, $Er_2Sn_2O_7$, and $Pr_2Ir_2O_7$ to exhibit the least ordered and most dynamic spin liquid phases. [4] We hope more and more materials developing these exotic quantum magnetic features can appear to provide us more opportunities to understand the MGF.

1.3 Structural, thermal and magnetic properties of $M_2(OH)_3X$

Good luck to the GMF community, following the discovery of MGF magnetism in deformed pyrochlore lattice γ-$Cu_2(OH)_3Cl$, Prof. X.G. Zheng and his colleagues at *Saga University* have extensively studied the material series in the chemical formula of $M_2(OH)_3X$ (transition metal hydroxyl halide series), with M = Mn, Fe, Co, Ni, Cu, and X = Cl, Br, I, [51-100] from the material preparing to the property measuring. In these years, most of the samples with these 15 chemical formulas are successfully prepared and their structural, thermal and magnetic properties are studied to some extent. Table 1.3.1 summarizes the space groups of obtained crystal structures of our successfully prepared samples.

Table 1.3.1 Known crystal structure (space group: order number, Hermann-Mauguin notation and Schonflies notation) of synthesized polycrystalline $M_2(OH)_3X$ series obtained from Refs. [51~100].

$M_2(OH)_3X$	**Cl^-**, I=3/2. ^{35}Cl : 75.5% ^{37}Cl : 24.5%	**Br^-**, I=3/2 ^{79}Br: 50.5% ^{81}Br: 49.5%	I^-, I=5/2. ^{127}I: ~100%
Cu^{2+} ($3d^9$), S=1/2 I=3/2, μ_T=1.7-3.5 ^{63}Cu: 69%, ^{65}Cu: 31%	**$Cu_2(OH)_3Cl$** α-: No.11, C_{2h}^2, $P2_1/m$ β-: No.62, D_{2h}^{16}, *Pnma* γ-: No.14, C_{2h}^5, $P2_1/n$	**$Cu_2(OH)_3Br$** α-: No.11, C_{2h}^2, $P2_1/m$	$Cu_2(OH)_3I$ α-: No.11, C_{2h}^2, $P2_1/m$
Ni^{2+} ($3d^8$), S=1 I=3/2, μ_T=2.8-5.6 ^{59}Ni: 98%, ^{61}Ni: 1.2%	**$Ni_2(OH)_3Cl$** β-: No.62, D_{2h}^{16}, *Pnma*	**$Ni_2(OH)_3Br$** α-: No.11, C_{2h}^2, $P2_1/m$	$Ni_2(OH)_3I$
Co^{2+} ($3d^7$), S=3/2, I=7/2, μ_T=3.9-6.6 ^{59}Co: ~100%	**$Co_2(OH)_3Cl$** β-: No.166, D_{3d}^5, $R\bar{3}m$	**$Co_2(OH)_3Br$** β-: No.166, D_{3d}^5, $R\bar{3}m$	$Co_2(OH)_3I$ β-: No.166, D_{3d}^5, $R\bar{3}m$
Fe^{2+} ($3d^6$), S=2 I=1/2, μ_T=5.9-2.8 ^{55}Fe: 98%, ^{57}Fe: 2%	$Fe_2(OH)_3Cl$ β-: No.166, D_{3d}^5, $R\bar{3}m$	$Fe_2(OH)_3Br$ β-: No.166, D_{3d}^5, $R\bar{3}m$	$Fe_2(OH)_3I$ β-: No.166, D_{3d}^5, $R\bar{3}m$
Mn^{2+} ($3d^5$), S=5/2 I=5/2, μ_T=5.9 ^{55}Mn: ~100%	$Mn_2(OH)_3Cl$ β-: No.62, D_{2h}^{16}, *Pnma*	$Mn_2(OH)_3Br$ β-: No.62, D_{2h}^{16}, *Pnma*	$Mn_2(OH)_3I$

The polymorphs of $Cu_2(OH)_3Cl$ are not only the corrosion products of copper, brass and bronze, but also the painting coloring agents. Historically the mineral $Cu_2(OH)_3Cl$ with the crystal structure of space group No. 11 was first found and called Botallackite, so it is denoted as α-$Cu_2(OH)_3Cl$ after the well-known mineral "atacamite" $Cu_2(OH)_3Cl$ with the crystal structure of space group No. 62 was determined, and the latter is denoted as β-$Cu_2(OH)_3Cl$**.** So generally $Cu_2(OH)_3X$ or $Ni_2(OH)_3X$ with the crystal structure of space group No. 11 is written as *α*-$Cu(OH)_3X$ or *α*-$Ni(OH)_3X$, respectively, and $Cu_2(OH)_3X$ or $Ni_2(OH)_3X$ with the crystal structure of space group No. 62 is written as β-$Cu(OH)_3X$ or β-$Ni(OH)_3X$, respectively. This notation "β-" is different from that of β-$Co_2(OH)_3X$ and β-$Fe_2(OH)_3X$ whose space groups are all No. 166.

From Table 1.3.1, one can see that we have prepared four kinds of samples according to the space group classification of crystal structures, see Figs. 1.5.1 (a)~(d).

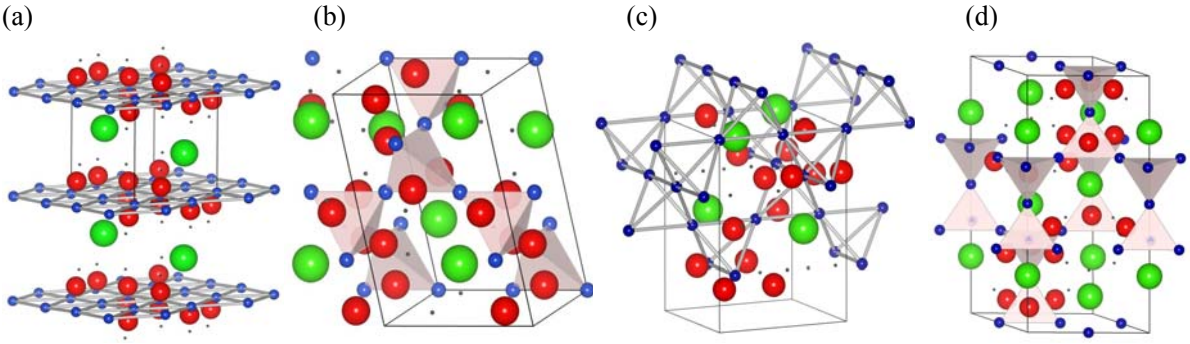

Fig. 1.3.1 $M(OH)_3X$ Crystal structures of (a) No.11, (b) No.14, (c) No.62, (d) No.166. Here the blue, red, black and green balls presents *M*, O, H and *X* ions respectively.

As above-mentioned, the thermal properties of materials, especially specific heat $C_p(T)$ of a magnetic material at low frequencies provide a lot of information on its low-T magnetic structure. As examples, Fig. 1.3.2 gives published $C_p(T)$ data of our prepared γ-$Cu_2(OH)_3Cl$, and β-$Ni_2(OH)_3Cl$ and β-$Co_2(OH)_3Br$, and detailed demonstrations of these data can be found in corresponding papers.

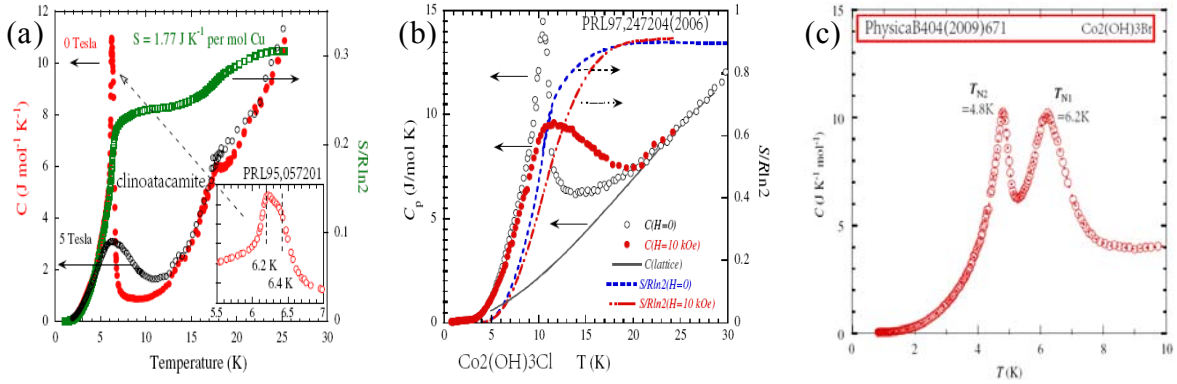

Fig. 1.3.2. Published $C_p(T)$ of (a) γ-$Cu_2(OH)_3Cl$, [69] (b) β-$Ni_2(OH)_3Cl$, [85] (c) β-$Co_2(OH)_3Br$.[88, 95]

Two of the most common magnetic properties are magnetic susceptibility $\chi(T)$ (χ^{-1} at direct current magnetic field conditions is usually present) and magnetization $\boldsymbol{M}(T, \boldsymbol{H})$, which can give the value information of θ_{CW}, T_C and/or T_N. As examples, Fig. 1. 3. 3 gives published

$\chi(T)$ (or χ^{-1}) and $\boldsymbol{M}(T, \boldsymbol{H})$ of our three $M_2(OH)_3X$ samples.[72, 85, 90, 91]

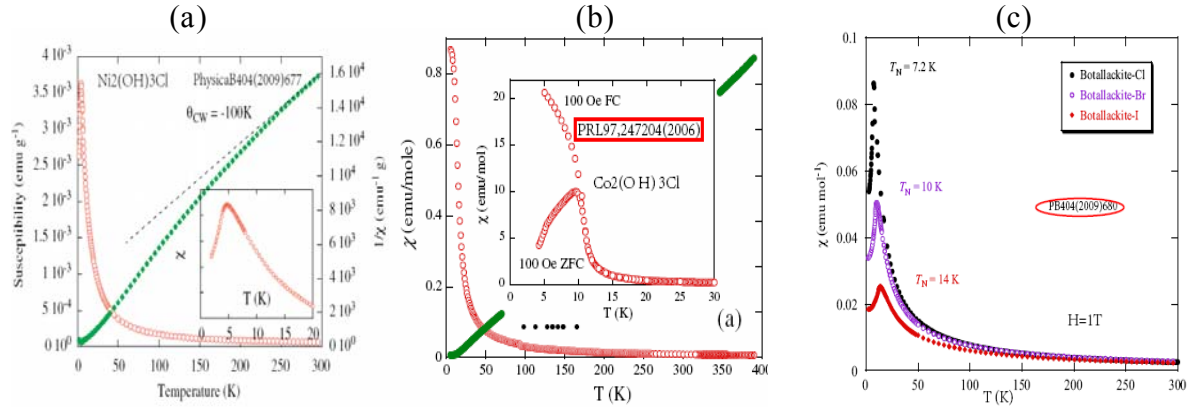

Fig. 1.3.3. susceptibility χ of (a) β-$Ni_2(OH)_3Cl$, [90, 85] (b) $Co_2(OH)_3Cl$, [72] and (c) α-$Cu_2(OH)_3Cl/Br/I$. [91]

From the experimental crystal structure, magnetic susceptibility $\chi(T)$, magnetization $M(T, H)$, specific heat $C_p(T)$ or $C_p(T, H)$, neutron scattering/diffraction, μSR, and NMR data, our group has also done some works on the magnetic ordering modeling to explain the observed phenomena. For example, through suggesting the magnetic structure—the spins on the triangular lattice plane are FM ordered and those on the kagome lattice plane are disordered, with "1-in 2-out" and "2-in 1-out" spin degrees of freedom (see Fig. 1.3.4(a)), Zheng *et al* has successfully demonstrated the "coexisting ferromagnetic order and disorder in a uniform system of β-$Co_2(OH)_3Cl$". [72] Recently, magnetic structures and spin configurations (Fig. 1.3.4(b,c)) for the antimagnetic phase below T_{N1}=6.2 K and high field phase of β-$Co_2(OH)_3Br$ were proposed to explain their AFM transitions satisfactorily. [96]

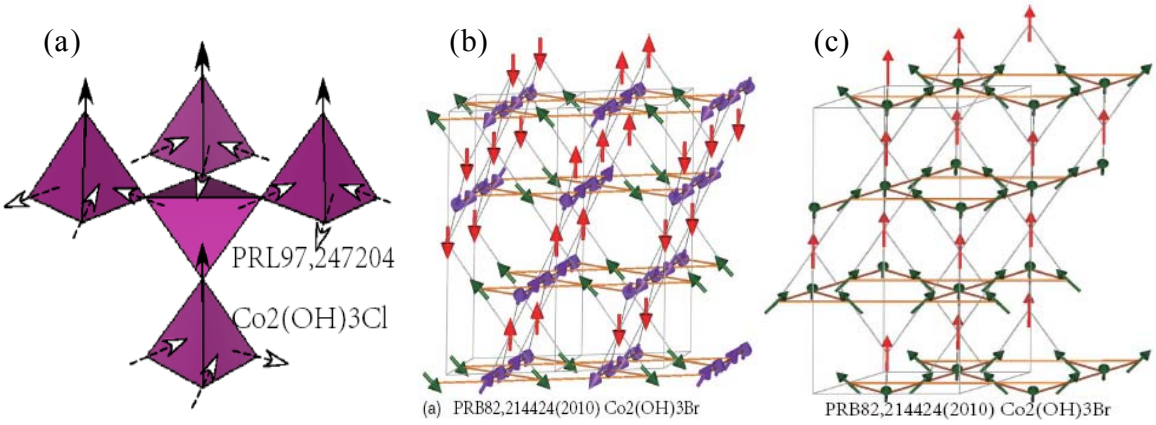

Fig. 1.3.4. (a) Suggested magnetic structures of β-$Co_2(OH)_3Cl$, [72] and proposed spin configurations for (b) the antimagnetic phase below T_{N1}=6.2 K and (c) high field phase of β-$Co_2(OH)_3Br$. [96]

Activated by our research results, many other researchers began the similar investigation on this material series, among them some have performed fruitful experimental studies using samples prepared by our group. For examples, Wills *et al* [86] and Maegawa *et al* have suggested spin configurations for the low-T phases of γ-$Cu_2(OH)_3Cl$, [93] respectively.

In the meanwhile, so-called structurally perfect quantum kagome system $ZnCu_3(OH)_6Cl_2$ (and $Zn_xCu_{4-x}(OH)_6Cl_2$, or $Zn_xCu_{2-x}(OH)_3Cl$) began to be mentioned with, [101-150] and the

results are helping to understand the basic MGF physics.

It can be safely said that our work on $M_2(OH)_3X$ outlines a new magnetic system to study geometric frustration for *d*-electrons.

1.4 IR and Raman spectral properties of solid state matters

Through quantum mechanical considerations, the vibration energy eigenvalues of diatomic *XY* system as a harmonic oscillator (mass: m_X and m_Y, force constant: k) is presented by [151, 152]

$$E_n = h\nu(n+\frac{1}{2}) = \frac{hc}{\lambda}(n+\frac{1}{2}) \tag{1.4.1}$$

with vibration fundamental frequency ν (wavenumber λ^{-1}):

$$\nu = \frac{1}{2\pi}\sqrt{\frac{k}{\mu}} \quad (\lambda^{-1} = \frac{1}{2\pi c}\sqrt{\frac{k}{\mu}}), \quad \mu = \frac{m_X \cdot m_Y}{m_X + m_Y} \tag{1.4.2}$$

In the spectroscopy community, vibration frequency or energy is described by the wavenumber and usually denoted by ω (equal to λ^{-1}, not angular frequency) in unit of cm^{-1} (Kayser). Therefore

$$\omega = \frac{1}{2\pi c}\sqrt{\frac{k}{\mu}} = 1303\sqrt{\frac{k}{\mu}}\ (cm^{-1}) \tag{1.4.3}$$

with k is in unit of mdyn/Å (100 N/m, 1 mdyn=10^{-8} N) and μ atomic quantity without dimensions.

As to the stretching vibration of a linear triatomic XY_2 system, such as CO_2, vibration frequencies $\omega_{1,2}$ of two modes:

$$\omega_1 = 1303\sqrt{\frac{k}{m_Y}}\ (cm^{-1}) \text{ and } \omega_2 = 1303\sqrt{\frac{k}{\mu}}\ (cm^{-1}), \ \mu = \frac{m_X m_Y}{m_X + 2m_Y} \tag{1.4.4}$$

In addition to stretching vibrations, a tricatomic or multiatomic system has always one or more bend/bending (or say, deformation/deforming) modes, e.g. CO_2 and H_2O. For CO_2, ω_1=1340 cm^{-1}, ω_2=2350 cm^{-1}, and ω_3=667 cm^{-1}. In the case of H_2O, ω_1=3657 cm^{-1}, ω_2=1595 cm^{-1}, and ω_3=3756 cm^{-1}.

In general, the stretching vibration frequencies of a functional group (FG) including a light atom are high and its bending frequencies are moderate. They may appear simultaneously and well separately in the high and moderate frequency regions, respectively, so the corresponding spectral parts are called FG and correlation peak (CP) regions, respectively. Whereas the vibration frequencies of a group with heavy atoms are relatively much lower and numerous, they distribute in the low frequency spectral part, the so-called fingerprint (FP) region. For our samples, the obtained three kinds of FG, CP and FP spectral

regions are in the 4000-3000 cm^{-1} part for the [OH] group (3000-2000 cm^{-1} for the [OD] group), 1000-600 cm^{-1} part for the [OH] group (800-500 cm^{-1} for the [OD] group), and <600 cm^{-1} part for the [*M*-O] and [*M*-*X*] groups, respectively.

IR or Raman spectra, whose physical origins are markedly different, see Figs. 1.4.1 (a) and (b) respectively, can reflect the atomic vibrational transitions of a material. IR (absorption) spectra originate in photons in the IR region that are absorbed by transitions between two vibrational levels of the molecule in the electronic ground state. On the other hand, Raman spectra have their origin in the electronic polarization caused by ultraviolet, visible, and near-IR light. The former is the relationship between the transmittance (≤100%) and IR frequency (or wavenumber), while the latter is frequency shift signal sum of every ω_α whose intensity is much weaker than Rayleigh scattering (by a factor of 10^{-3}-10^{-5}) and still easy to observe by using a strong exciting source. Figs. 1.4.1 (c) gives the energy level diagram showing the states.

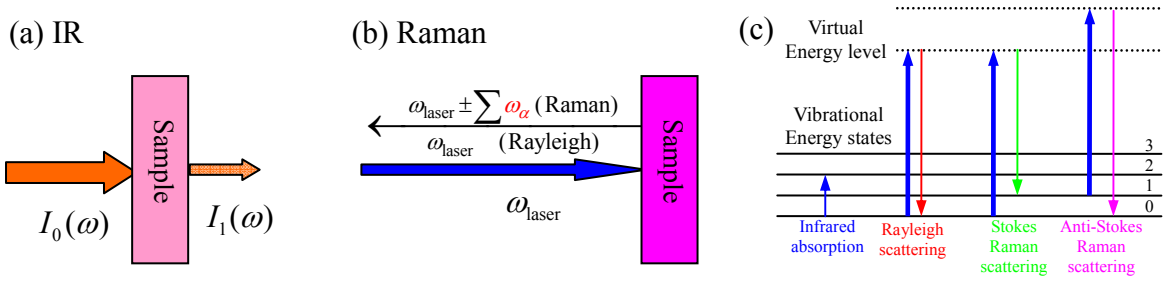

Fig. 1.4.1 Mechanics of (a) IR absorption, (b) Raman scattering and (c) Energy level diagram showing the states. The line thickness reflects roughly the signal strength from the different transitions.

For small molecules, the IR and Raman activities may be determined by simple inspection of their normal modes.

First, the vibration is IR-active if the dipole moment is changed during the vibration. It is obvious that the vibration of a homopolar diatomic molecule is not IR-active, whereas that of a heteropolar diatomic molecule is always IR-active.

Second, the vibration is Raman-active if one of these six components of the polarizability changes during the vibration. Thus, it is obvious that the vibration of a homopolar diatomic molecule is Raman-active but not IR-active, whereas the vibration of a heteropolar diatomic molecule is both IR- and Raman-active.

Polyatomic molecules have 3*N*−6 or, if linear, 3*N*−5 normal vibrations. For any given molecule, however, only vibrations that are permitted by the selection rule for that molecule appear in the IR and Raman spectra. The selection rule is determined by the symmetry of the molecule, while the spatial geometric arrangement of the nuclei constituting the molecule determines its symmetry.

For example, there are four normal modes for a pyramidal XY_3 molecule and all four

vibrations are both IR- and Raman-active.

For molecules and ions in crystals where the vibration modes are called phonons, however, it is necessary to consider some additional symmetry operations that characterize translational symmetries in the lattice. To analyze the spectra of crystals, it is necessary to carry out a site group or factor group analysis, as described in the following Chapter.

Almost all the real MGF materials are determined by measuring their T-dependent specific heat, magnetic susceptibility, and even directly crystal structure. To experimentally measure intrinsic MGF properties and crystal structures, the researchers in the field of magnetism usually employ the above-mentioned advanced measuring facilities. Fortunately from their invention days the IR spectroscopy and Raman scattering spectroscopy, which are the sensitive probes to the crystal symmetry, can help to determine the constitutions, crystal and even bio-system structures from the lattice vibration mode assignation.

Till now, IR and Raman studies on the MGF systems are fruitful.[153-200] Figure 1.4.2 shows two typical examples of T-dependences of the phonon wavenumber observed for samples $Tb_2Ti_2O_7$ (space group $Fd\bar{3}m$, O_h^7, No. 227), [161] and $HgCr_2S_4$ and $CdCr_2S_4$ (space group $Fd\bar{3}m$, O_h^7, No. 227), [171] who are the representatives of the pyrochlores, and spinels, respectively.

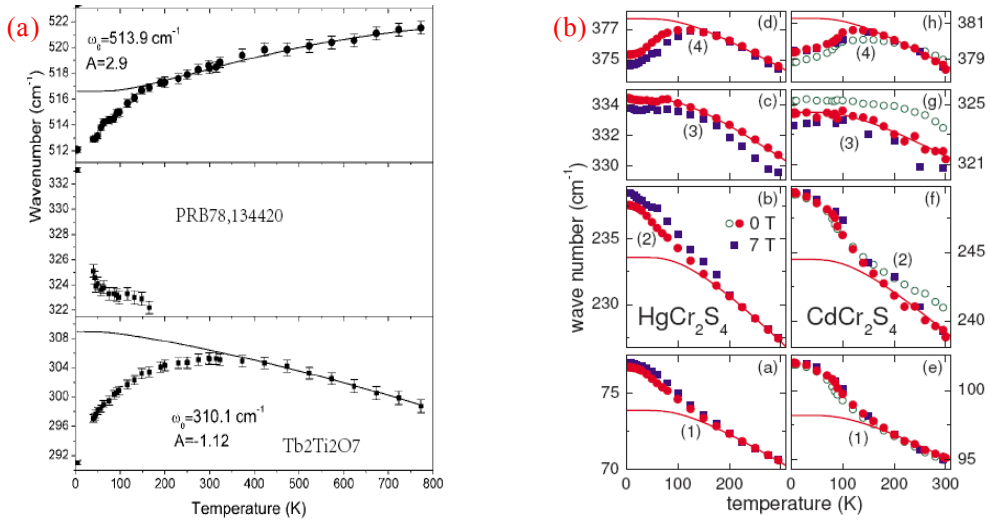

Fig. 1.4.2 Published examples of temperature dependences of the phonon wavenumber observed for samples (a) $Tb_2Ti_2O_7$ and (b) $HgCr_2S_4$ and $CdCr_2S_4$, respectively. [161, 171]

Theoretical and experimental demonstrations are naturally focused on the expectations resulting from the coupling between the lattice and spin degrees of freedom, namely spin-lattice coupling or spin-phonon coupling (SPC), see Section 4.1 in Chapter 4, when the MGF-related phenomena occur.

1.5 Hydrogen bond in solid state matters

In general, whatever symmetry a solid state material with *X*H groups is, the famous hydrogen bond/bonding (H-bond) *X*H···*Y* (*Y* is an anion and H-acceptor) exists in it, e.g. OH···O and OH···Cl. [201-240] The discovery of the H-bond cannot be attributed to a single author, and no genuine "first paper" can be quoted. Specialized articles developing relevant ideas began to appear at the beginning of the 20th century, but the far-reaching relevance of the H-bond was not yet recognized. More studies and clear general concepts were published from the 1920s on, with pioneering roles usually attributed to L. Pauling, *et al*. By the end of the 1930s, a "classical" view of the H-bond was established that dominated the field for half a century. Research into H-bonds experienced a peak in the 1950s and 1960s, followed by relative stagnation from the mid-1970s to the late 1980s. An intense revival occurred from about 1990 on, and theoretical concepts were later replaced by modern quantum chemical models. [227]

After 100 years' discovery of H-bond, it still is a topic of vital scientific research. The reason for this long-lasting interest lies in the eminent importance of hydrogen bonds for the structure, function, and dynamics of a vast number of chemical and physical systems.

Till now several types of H-bonds are found, see Fig. 1.5.1 for 4 most popular examples.

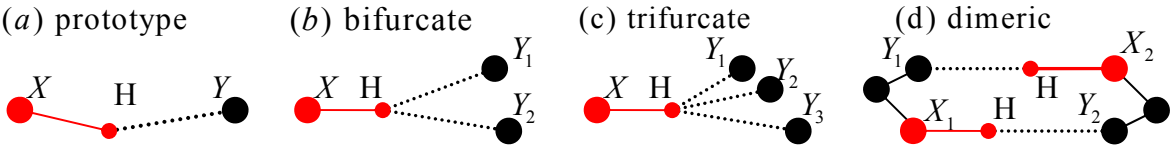

Fig. 1.5.1 Schemes of 4 most popular examples.

In fact, it is well known in the spectroscopic community, most of OH stretching frequencies less than the so-called "free" OH stretching frequency $\omega_v\{(OH)^{-1}\}$ 3600 cm^{-1} are caused by an H-bond (or say a red-shifted H-bond) which is seldom paid close attention to in the magnetism community. In general the forming of a typical H-bond like OH···*Y* should satisfy two conditions: (1) angle θ_{OHY}>120° (directionality) and (2) distance $d_{O\cdots Y}$ (bond-length) is near to the sum d^0_{OY} of the common mean O^{2+} radius R^0_O~1.40 Å and *Y* anion radius R^0_Y.

H-bonds can be classified into three strength categories in different ways, that is, with borders between the categories placed differently, and different names can be attached to the categories depending on the personal focus of interest. In a general view on H-bonds, it seems appropriate to attach the names "strong" (quasi-covalent nature) and "weak" (electrostatic/dispersion) to the extremes of the scale, and use a term such as "moderate"

(mainly electrostatic) for the intermediate range. According to the classification of Jeffrey, an H-bond is termed "strong", "moderate" or "weak" when O-H lengthening Δd_{OH} is 0.08~0.25 Å, 0.02~0.08 Å or <0.02 Å according to a specific "free" d_{OH} ~0.983 Å for $Cu_3{\equiv}OH$. In the language of IR/Raman OH stretching frequency red-shift, three classes of H-bonds appear when $\Delta\omega\{(OH)^{-1}\}$ is larger than 25% (>900 cm^{-1}), 10~25% (350~900 cm^{-1}), or <10% (<350 cm^{-1}) comparing to a specific "free" OH stretching frequency $\omega_{free}\{(OH)^{-1}\}$~3555.6 cm^{-1}.

Many authors have performed synthetic studies on published H-bond data just before their works, e.g. Novak's "OH stretching frequency as a function of *r*(OH)" (Fig. 1.5.2 (a)), [201] Steiner's "scatter plot of IR stretching frequencies against O···O distances in OH···O" (Fig. 1.5.2 (b)), [221] and Lutz's "bond valences of internal O-H bonds of OH^- ions versus the wave numbers of the respective uncoupled OD stretching modes" (Fig. 1.5.2 (c)) [229].

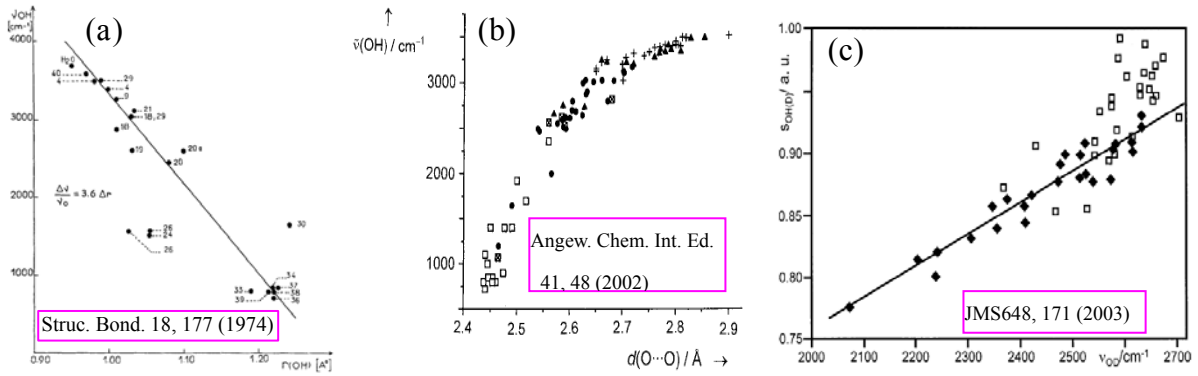

Fig.1.5.2 Published studies on (a) "OH stretching frequency as a function of *r*(OH)", [201] (b) "scatter plot of IR stretching frequencies against O···O distances in OH···O" , [221] (c) "bond valences of internal O-H bonds of OH^- ions versus the wave numbers of the respective uncoupled OD stretching modes" [223].

Because there are mainly two techniques for H/D atom location, X-ray diffraction (XRD, locating the electron-density maxima of the covalent H/D atoms) and neutron diffraction (locating the H/D nuclei), and the results often differ by about 0.1 Å. Neither of the two results is truer than the other, but they are complementary and both represent useful pieces of information. Nevertheless, neutron diffraction results are much more precise and reliable, and allow the proton positions to be located as accurately as other nuclei. It has become a practice in the analysis of XRD results to "normalize" the OH bonds by shifting the position found for the H atom (that is, the position of the electron center of gravity) to the average neutron-determined inter-nuclear distance, namely, to the approximate position of the proton, although many researchers may be unaware this and have led to some unpleasant complications for other studies.

So the Novak's relationship of $\Delta\omega\{(OH)^{-1}\}/\Delta d_{OH} \sim -11000\ cm^{-1}/Å = 11\ cm^{-1}/0.001Å$ is practical today, and the Lutz's bond valence relationship will come in handy.

1.6 Research Situation of Spectral Studies on hydroxyl halides

Till the starting (Oct. 2009) of this doctoral study, I have found that few groups had reported the IR and Raman spectral studies only on polymorphs of $Cu_2(OH)_3Cl$. The most recent works were reported by R. L. Frost group, Queensland University of Technology, in three papers from the viewpoint of chemistry and mineralogy before 2003, Because the polymorphs of $Cu_2(OH)_3Cl$ are not only the corrosion products of copper, brass and bronze, but also the painting coloring agents.[58-60]

R. L. Frost *et al*, also gave Raman experimental data of some natural atacamite and paratacamite at 77 K, [58] but they pointed out few explanations about the spectral difference between two temperatures.

I agreed with the most assignment by R. L. Frost group, [58-60] e.g.

(1) IR/Raman bands/peaks of OH stretching vibration modes are located in the region >3000 cm^{-1}, and the number of main bands is the number of different OH distances.

(2) IR/Raman bands/peaks of OH bending vibration modes are located in the region 1200~600 cm^{-1}, and the number of main bands is the number of different CuOH distances

(3) IR/Raman bands/peaks of CuO or CuCl vibration modes are less than 600 cm^{-1}, and the number of main bands can not be predicted because of band-overlapping or band-degeneration.

I have performed the band assignment following this method from the beginning of my study on the spectral analysis of our samples, except for the suggestion that the 367, 420 and 445 cm^{-1} bands are [CuCl] modes. Till now, more and more evidences agree with my suggestion that the frequencies of [CuCl] modes are less than 200 cm^{-1} in our material series, see the following Chapter.

When some Cu sites of $Cu_2(OH)_3Cl$ are occupied by Zn, Ni, or/and Co, etc, it is called are paratacamite, especially the so-called perfect kagome system $ZnCu_3(OH)_6Cl$ is the famous herberthsmithite. As can be seen in the next Chapter, since Zn cations in herbersmithite $ZnCu_3(OH)_3Cl_2$ occupy the same sites with inversion symmetry like those of Co^T in $Co_2(OH)_3Cl$, they can not induce any other type Raman-active modes compared with $Co_2(OH)_3Cl$. Regarding the similarity of Cu and Co, theoretically we predict the spectra of $Co_2(OH)_3Cl$ and $ZnCu_3(OH)_3Cl_2$ are completely similar at room temperature (RT).

Fortunately till now we have another experimental reference, even including not complete spectral information and some unconvincing assignment, to help our assignment, not like that of the famous pyrochlore, perovskite and spinel series. But the incomplete and therefore indefinitely assigned Raman spectra of herbertsmithite were only reported in recent two years (July 2010~July 2012) by the P. Lemmens group, Technical University of Braunschweig,

Germany, see Fig. 1.6.1. [133, 148] The authors present the study on the "interplay of thermal and quantum spin fluctuations" in their herbertsmithites, and gave simple band assignment, focusing on the low wavenumber region <700 cm^{-1}.

Although their spectra are similar to those of our recent theoretical and experimental results, unfortunately, three viewpoints don't win my agreement:

(1) "5 phonons at about 3500~700 cm^{-1} are $2A_{1g}+3E_g$" maybe wrong.

(2) "both phonons at 124 and 148 cm^{-1} are A_{1g} " maybe wrong.

(3) They had ignored the assignment of 943 cm^{-1} bands and the assignment about 697-702 cm^{-1} bands may be wrong.

(4) They gave an unsealed assertion that no interaction between the high energy [OH] phonon modes and low-energy magnetic excitations exists to support the practice of ignoring the high energy [OH] stretching and deformation modes.

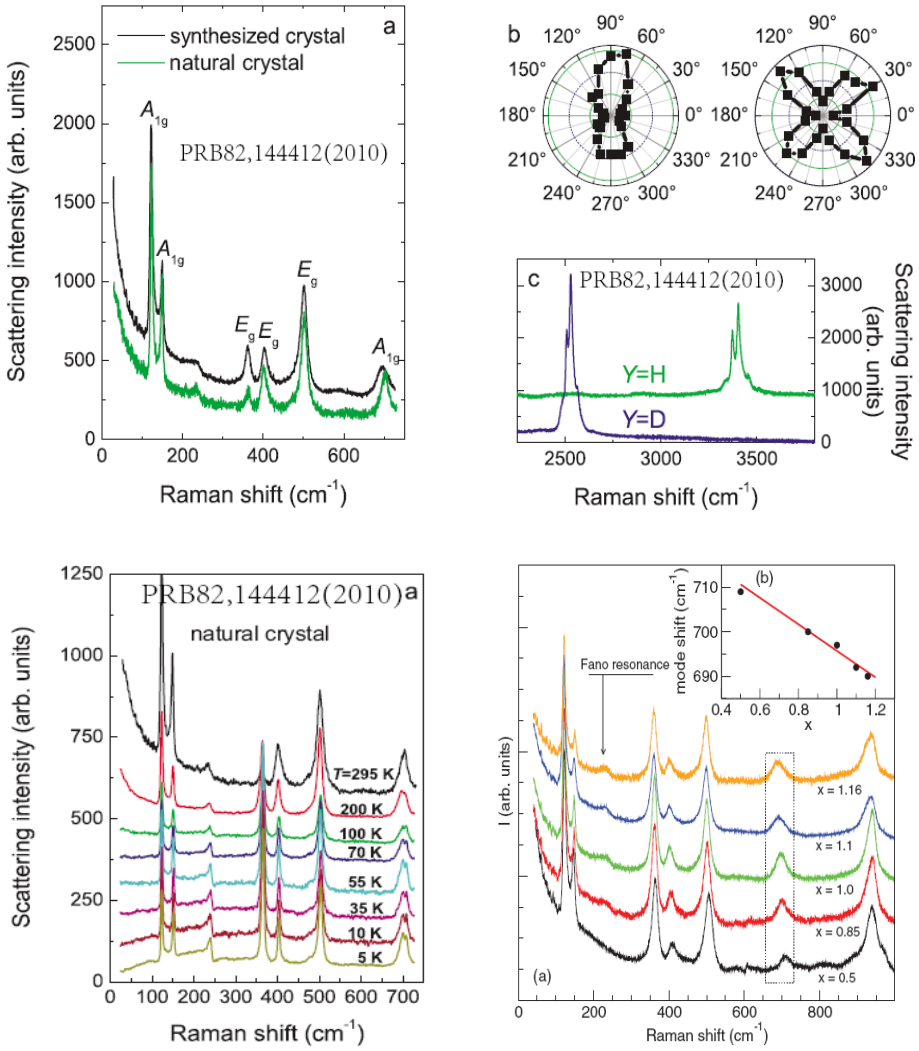

Fig. 1.6.1 Published Raman data of $ZnCu_3(OH/D)_6Cl$. [133, 148]

1.7 Research aims and methods of the doctoral dissertation

My research aims at

- Performing a standard factor group analysis, which will build the basic to the complete normal mode assignment at RT, on the space groups:
  (1) No. 166 (deformed pyrochlore $Co_2(OH)_3Cl$ and $Co_2(OH)_3Br$),
  (2) No. 62 (Atacamite β-$Cu_2(OH)_3Cl$ and Atacamite-type β-$Ni_2(OH)_3Cl$),
  (3) No. 14 (Clinoatacamite γ-$Cu_2(OH)_3Cl$),
  (4) No. 11 (Botallackite α-$Cu_2(OH)_3Cl$, Botallackite-type α-$Cu_2(OH)_3Br$ and α-$Ni_2(OH)_3Br$).
- Measuring the IR and Raman spectra at RT and assigning their normal modes as complete and correctly as possible.
- Obtaining an elementary knowledge on the H-bonds appearing possibly in our $\boldsymbol{M_2(OH)_3X}$ samples.
- Getting the change information of band frequencies, widths and spectral profiles of selected $\boldsymbol{M_2(OH)_3X}$ samples at low-temperature related to those at RT, in order to try to reveal the underlying physics of some magnetic/thermal properties around transition temperatures from the viewpoint of spin-lattice/phonon coupling in quantum magnetism field.

To reach these aims, I employ the following methods:

- Performing the **theoretical** factor group analysis on four space groups to which our materials belong to set the basis for IR and Raman spectral analysis at RT;
- Measuring the IR absorption and Raman scattering spectra of selected typical $\boldsymbol{M_2(OH)_3X}$ at RT, and assigning them by dividing every spectrum into four spectral regions, combining the results of the above-mentioned factor group analysis and checking one against another;
- Collecting the IR and Raman band data of [OH/D] group stretching frequencies and crystal structure data obtained previously;
- Measuring Raman spectra of selected typical $\boldsymbol{M_2(OH)_3X}$ at low-temperature (down to liquid Helium temperature) and checking the change information of band frequencies, widths and spectral profiles using the SPC model.

Chapter 2

IR and Raman selection rules for $M_2(OH)_3X$

Exact IR and Raman spectral analysis needs to know the selection rules for the specific material with the special space group symmetry. In this chapter I will introduce first the notations of group theory used in this thesis and the method of obtaining the IR and Raman selection rules from standard factor group analysis (FGA) in Sect. 2.1, and then using this method, derive out IR and Raman selection rules involved in our four kinds of space groups in Sects. 2.2~2.5.

2.1 General

First of all, for any given molecule, however, only vibrations that are permitted by the selection rule for that molecule appear in the infrared and Raman spectra. Since the selection rule is determined by the symmetry of the molecule, I here give the notations of symmetry elements used in my thesis: identity I, a plane of symmetry σ, a center of symmetry i, a p-fold axis of symmetry C_p^*, a p-fold rotation–reflection axis S_p^*. [151, 152]

A molecule may have more than one of these symmetry elements. A possible combination of symmetry operations whose axes intersect at a point is called a point group. I also give the notations of point groups used in my thesis:

(1) C_p. Molecules having only a C_p and no other elements of symmetry: C_1, C_2, C_3, and so on.

(2) C_{ph}. Molecules having a C_p and a σ_h perpendicular to it: $C_{1h}\equiv C_s$, C_{2h}, C_{3h}, and so on.

(3) C_{pv}. Molecules having a C_p and $p\sigma_v$ through it: $C_{1v}\equiv C_s$;C_{2v};C_{3v};C_{4v}; . . . ; $C_{\infty v}$:

(4) D_{ph}. Molecules having a C_p, $p\sigma_v$ through it at angles of $360°/2p$ to one another, and a σ_h perpendicular to the C_p: $D_{1h}\equiv C_{2v}$; $D_{2h}\equiv V_h$; D_{3h}; D_{4h}; D_{5h};D_{6h}; . . . ; $D_{\infty}h$.

(5) D_{pd}. Molecules having a C_p, pC_2 perpendicular to it, and $p\sigma_d$ which go through the C_p and bisect the angles between two successive C_2 axes: $D_{2d}\equiv V_d$, D_{3d}, D_{4d}, D_{5d}, and so on.

In this thesis, the species (or the irreducible representations) of the point group are labeled according to the following rules:

(1) *A* and *B* denote nondegenerate species (1D representation). *A* represents the symmetric species (character=+1) with respect to rotation about the principal axis (chosen as z axis), whereas *B* represents the antisymmetric species (character =−1) with respect to rotation

about the principal axis; *E* and *F* denote doubly degenerate (2D representation) and triply degenerate species (3D representation) respectively.

(2) If two species differ in the character of *i*, they are distinguished by subscripts *g* and *u*.

(3) If two species in the same point group differ in the character of *C* (other than the principal axis), they are distinguished by subscripts 1, 2, 3, ...

(4) If two species differ in the character to *s* (other than σ_v), they are distinguished by ′ and ″. If these rules allow several different labels, *g* and *u* take precedence over 1, 2, 3, . . . , which in turn take precedence over ′ and ″.

Here, the point groups in the bold type are those appearing in our samples. The combination of all these symmetry operations results in a total of 230 different space groups describing all possible crystal symmetries.

In order to perform an accurate assignment of lattice vibrational modes in the IR and Raman spectra of a sample, one must construct the relation table (Factor group analysis, FGA), or say, the IR and Raman selection rules for related lattice vibrations according to the site symmetry and the belonged space group, as the following routing process:

(1) Draw the nearest neighbor site surrounding for every inequivalent atom and give the site symmetry representation (point group), e.g., C_{3v} in No. 166;

(2) Find and copy the character table of every abovementioned site symmetry representation (point group) in Appendix I of the Tateley's Book or the Nakamoto's Book;

(3) Find and copy the character table of the point group corresponding to the same space group of the crystal (D_{3d}, D_{2h}, C_{2h}) in Appendix I of the Nakamoto's book;[152]

(4) Find and copy the correlation table of the space group including only the abovementioned point groups;

(5) Construct a correlation table, filling with the number of mode species, the number of acoustic modes, the activity (IR active, Raman active or inactive);

(6) Give every mode species the vibrational model related to its ionic group and estimate its wavenumber.

In this process, the important points are as followings:

(1) For a reliable FGA one should know the exact Wyckoff sites of each atom in the crystal lattice, the number *N* of atoms in the primitive unit cell (Bravais cell), and the number Z^B of primitive unit cells (formula units) present in the unit cell.

(2) The rule for determination of acoustic modes (having nearly zero frequency) is very easy. Acoustic modes are related to translations of the whole unit cell along three mutually orthogonal directions. By symmetry they coincide with the translational degrees of freedom. Check the distribution of translations (T_x, T_y and T_z) in character tables (pp. 181-200 in the

Tateley's Book) [151] and one will know where the three acoustic modes belong.

(3) For IR and Raman activity of vibrations belonging to a certain symmetry species one should look at the last two columns of the character tables. IR activity is related to *x, y,* or *z* component of the transition dipole moment vectors, but they belong to the same species as translations T_x, T_y, and T_z. (Therefore, there are at most 3 IR active symmetry species.)

(4) Raman active species are those that contain any components of the polarizability tensor, i.e., α_{xx}, α_{xy}, ..., α_{zz}. Thus, some species can be both IR and Raman active. On the contrary, vibrations belonging to those symmetry species where one cannot find any translation *T* or polarizability component α will be (spectrally) IR-inactive or Raman-inactive, respectively.

The related $M_2(OH)_3X$ polycrystalline samples totally belong to the following four space groups, respectively, as shown in Table 2.1.1 which also gives the related site symmetry:

Table 2.1.1 Selected samples, and corresponding space groups and their site symmetries

Space group	Site symmetry	Samples
No.11, $P2_1/m$, C_{2h}^2	4C_i(4); C_s(2); C_1(4)	α-$Cu_2(OH/D)_3Cl$; α-$Cu_2(OH/D)_3Br$
No.14, $P2_1/n$, C_{2h}^5	4C_i(2); C_1(4)	γ-$Cu_2(OH/D)_3Cl$
No.62, *Pnma*, D_{2h}^{16}	2C_i(4); C_s(4); C_1(8)	β-$Cu_2(OH)_3Cl$ (natural mineral); β-$Ni_2(OH/D)_3Cl$; β-$Ni_2(OH/D)_3Br$
No.166, $R\bar{3}m$, D_{3d}^5	2D_{3d}(1); C_{3v}(2); 2C_{2h}(3); 2C_2(6); C_s(6); C_1(12)	$Co_2(OH/D)_3Cl$; $Co_2(OH)_3Br$

For examples, both Y_2TiO_5 and $CaCO_3$ (Aragonite) also belongs to orthorhombic space group (*Pnma*, D_{2h}^{16}, No. 62) with Z^B=4. Because of different atomic site symmetries included in them, the normal modes predicted are largely different. [151]

In Y_2TiO_5, the site symmetry is C_s for all the atoms: Y^1, Y^2, Ti^1, O^1, O^2, O^3, O^4, O^5 according to measured crystal structure. Then the FGA result of Y_2TiO_5 predicts: [151]

$$\begin{cases} \Sigma_{\text{opt}} = (16A_g + 8B_{1g} + 16B_{2g} + 8B_{3g}) + (8A_u + 15B_{1u} + 7B_{2u} + 15B_{3u}) \\ \Sigma_{\text{acoust}} = B_{1u} + B_{2u} + B_{3u} \end{cases} . \quad (2.1.1)$$

Raman active vibrations per set of ion are Y^1: $2A_g + B_{1g} + 2B_{2g} + B_{3g}$ and the same for the rest of ions.

While in Aragonite $CaCO_3$, the site symmetry is C_s for the atoms Ca, C and O^1, C_1 for O^2 according to XRD data. Then the FGA result predicts: [151]

$$\begin{cases} \Sigma_{\text{opt}} = (9A_g + 6B_{1g} + 6B_{2g} + 6B_{3g}) + (8A_u + 5B_{1u} + 8B_{3u}) \\ \Sigma_{\text{inactive}} = 6A_u \\ \Sigma_{\text{acoust}} = B_{1u} + B_{2u} + B_{3u} \end{cases} . \quad (2.1.2)$$

2.2 IR and Raman selection rules with space group No. 166

Fig. 2.2.1 (a), (b) and (c) show crystal structure, kagome plane environment, triangle plane environment, respectively, of $Co_2(OH)_3Cl$ as an example of our crystals $M_2(OH)_3X$ with the crystal symmetry $R\bar{3}m \equiv D_{3d}^5$ of space group No. 166. The detail crystal structure parameters of $Co_2(OH/D)_3Cl$ and $Co_2(OH/D)_3Br$ are listed in Table A1 in Appendix A for reference.

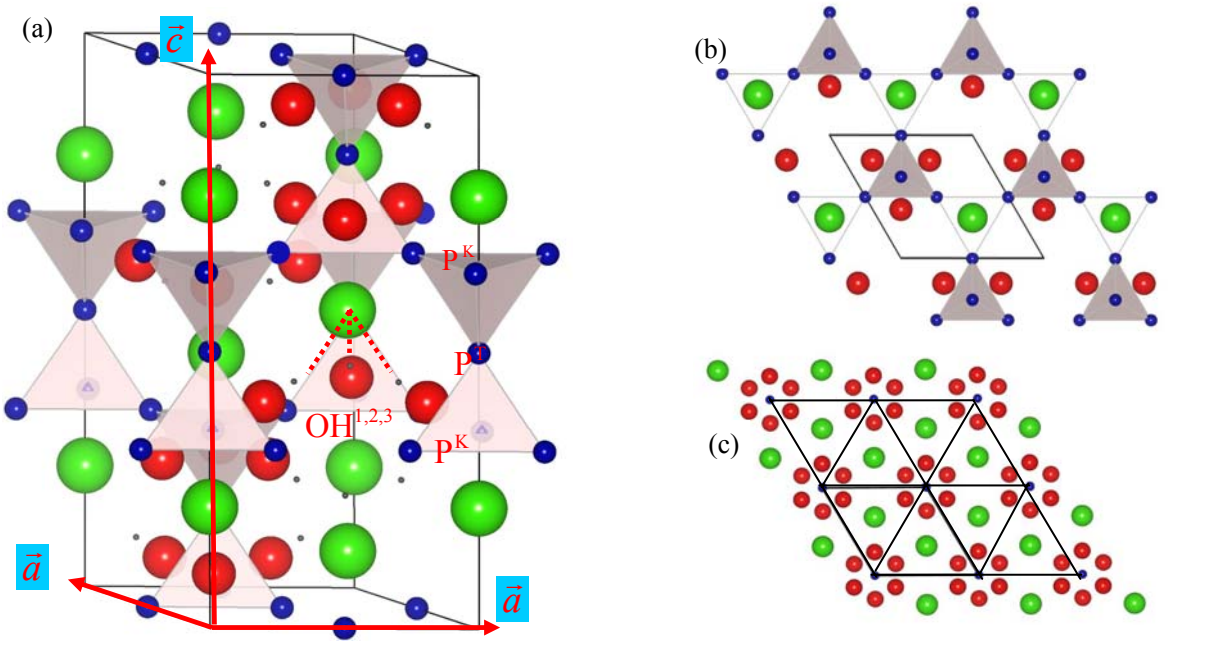

Fig. 2.2.1 (a) Crystal structure, (b) Kagome plane environment, (c) Triangle plane environment of $Co_2(OH)_3Cl$ as an example of our crystals with the crystal symmetry of space group No. 166.

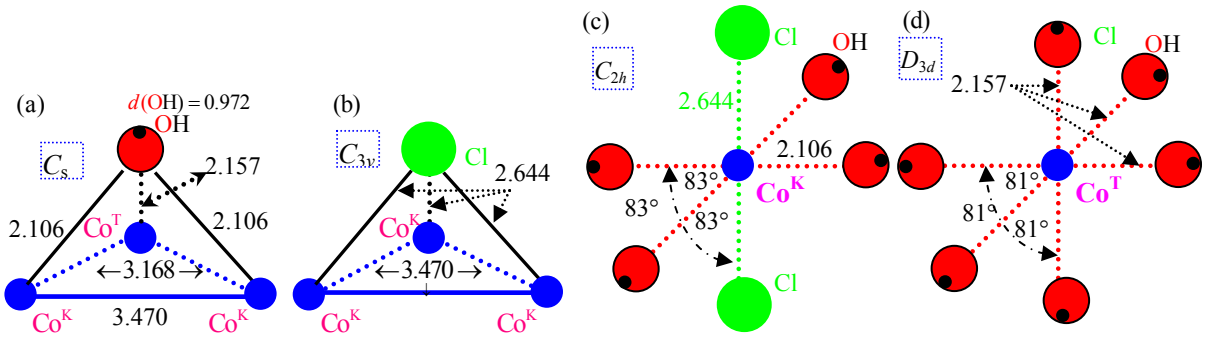

Fig. 2.2.2 (a) O-site, (b)Cl-site environment, (c) Co^K-site environment, (d) Co^T-site environment of $Co_2(OH)_3Cl$ as an example of our crystals with the crystal symmetry of space group No. 166. Here related distances are in units of Å

The magnetic ions of M^{2+} form a 3D network of linked tetrahedra that can be viewed as alternative stacking layers of kagome and triangular lattice planes in the (001) direction. A

prominent structural feature is a notable distortion in the tetrahedron, where the M^T-M^K distance is about 10% longer than M^K-M^K distance on the kagome lattice plane.

Fig. 2.2.2 (a) ~ (d) show Cl-site environment, (d) Co^K-site environment, and (e) Co^T-site environment of β-$Co_2(OH)_3Cl$ as an example of our crystals with the crystal symmetry of space group No. 166. Here related distances are in units of Å.

Follow the routing process of FGA, point group character tables of C_s , C_{2h} , C_{3v} and D_{3d} are given in Tables 2.2.1~4, respectively, and part of the correlation table for D_{3d} factor group species and selected site species is given in Tables 2.2.5. [151, 152]

Table 2.2.1. Character table of C_s point group.

C_s	I	σ_h		
A'	+1	+1	T_x, T_y, R_z	α_{xx}, α_{yy}, α_{zz}, α_{xy}
A''	+1	−1	T_z, R_x, R_y	α_{yz}, α_{xz}

Table 2.2.2. Character table of C_{2h} point group.

C_{2h}	I	C_2(z)	$\sigma_h(xy)$	i		
A_g	+1	+1	+1	+1	R_z	α_{xx}, α_{yy}, α_{zz}, α_{xy}
A_u	+1	+1	−1	−1	T_z	
B_g	+1	−1	−1	+1	R_x, R_y	α_{yz}, α_{xz}
B_u	+1	−1	+1	−1	T_x, T_y	

Table 2.2.3. Character table of C_{3v} point group.

C_{3v}	I	$2C_2$(z)	$3\sigma_v$		
A_1	+1	+1	+1	T_z	α_{xx}+α_{yy}, α_{zz}, α_{xy}
A_2	+1	+1	−1	R_z	
E	+2	−1	0	T_x, T_y; R_x, R_y	α_{xx}-α_{yy}, α_{xy}; α_{yz}, α_{xz}

Table 2.2.4. Character table of D_{3d} point group.

D_{3d}	I	$2C_3$	$3C_2$	i	$2S_6$	$3\sigma_6$	T, R	α
A_{1g}	1	1	1	1	1	1		α_{xx}+α_{yy}, α_{zz}
A_{2g}	1	1	−1	1	1	−1	R_z	
E_g	2	−1	0	2	−1	0	(R_x, R_y)	(α_{xx}-α_{yy}, α_{xy}); (α_{yz}, α_{xz})
A_{1u}	1	1	1	−1	−1	−1		
A_{2u}	1	1	−1	−1	−1	1	T_z	
E_u	2	−1	0	−2	1	0	(T_x, T_y)	

Table 2.2.5. Part of the correlation table for D_{3d} factor group species and selected site species.

D_{3d}	…	C_s	C_{2h}	C_{3v}
A_{1g}	…	A'	A_g	A_1
A_{2g}	…	A''	B_g	A_2
E_g	…	A'	A_g+B_g	E
A_{1u}	…	A''	A_u	A_2
A_{2u}	…	A'	B_u	A_1
E_u	…	A'	A_u+B_u	E

According to Tables 2.2.1~5, the correlation table for D_{3d} factor group species and selected site species can be constructed, see Table 2.2.6. As a result the collected distribution of vibration modes, or say, IR and Raman selection rule can be obtained in Tables 2.2.7.

Table 2.2.6. Correlation table for site and factor group species ($R\bar{3}m \equiv D_{3d}^5$, No. 166).

Site atoms /Site group	Site group species	Factor group D_{3d} species ($Z^B = 2$)
6H		$2A_{1g}(T_x, T_y)$
($HOM^K{}_2M^T$)	$2A'(T_x, T_y, R_z)$	$A_{2g}(T_z)$
6O		$3E_g(T_x, T_y, T_z)$
($OM^K{}_2M^T$)		$A_{1u}(T_z)$
C_s	$A''(T_z, R_x, R_y)$	$2A_{2u}(T_x, T_y)$
		$3E_u(T_x, T_y, T_z)$
M^K		$A_{1u}(T_z)$
($M^KO_4X_2$)	$A_u(T_z)$	$2A_{2u}(T_x, T_y)$
C_{2h}	$2B_u(T_x, T_y,)$	$3E_u(T_x, T_y, T_z)$
X ($XM^K{}_3$)		$A_{1g}(T_z)$
C_{3v}	$A_1(T_z)$	$E_g(R_x, R_y)$
	$E[(T_x, T_y), (R_x, R_y)]$	$A_{2u}(T_z)$
		$E_u(T_x, T_y)$
M^T (M^TO_6)	$A_{2u}(T_z)$	$A_{2u}(T_z)$
D_{3d}	$E_u(T_x, T_y)$	$E_u(T_x, T_y)$

Table 2.2.7. Collected distribution of vibrational modes ($R\bar{3}m \equiv D_{3d}^5$ (No. 166).

Factor group species	6H $HOM_2^KM^T$ C_s	6O $HOM_2^KM^T$ C_s	$3M^K$ $M^KO_4X_2$ C_{2h}	M^T M^TO_6 D_{3d}	$2X$ XM_3^K C_{3v}	Sum modes	Minus acoustic modes	Γ_{vib}	Spectral activity
A_{1g}	2	2			1	5		5	Raman
A_{2g}	1	1			0	2		2	Inactive
E_g	3	3			1	7		7	Raman
A_{1u}	1	1	1	0	0	3		3	Inactive
A_{2u}	2	2	2	1	1	8	−1	7	IR
E_u	3	3	3	1	1	11	−1	10	IR
Σ	12	12	6	2	4	36	−2	34	

We can check the relationship of the number of atoms in the unit cell N=9, the number of each mode and Z^B=2:

$$3N\cdot Z^B = n(A_{1g})+ n(A_{2g})+2n(E_g)+ n(A_{1u})+ n(A_{2u})+ 2n(E_u)=54 \quad (2.2.1)$$

Summarizing the above results, we obtain the 12 Raman active and 17 IR active modes.

At the disadvantage conditions that we have not prepared successfully a big single crystal and therefore can not perform the polarization Raman experiments, we should do our best to know the exact atomic displacement configurations of all the following modes:

$\Gamma_{166}^R = 2A_{1g}(\mathbf{H}OCo_3) + 3E_g(\mathbf{H}OCo_3) + 2A_{1g}(\mathbf{O}Co_3) + 3E_g(\mathbf{O}Co_3) + A_{1g}(\mathbf{Cl}Co_3) + E_g(\mathrm{Cl}Co_3)$.

The atomic displacement patterns of all the 12 Raman modes are shown in Figs. 3 (a) ~ (l). According to numerous physical and chemical data, both wavenumbers $\omega[A_{1g}^{ss}(\mathbf{H}OCo_3)]$/ $\omega[E_g^{as}(\mathbf{H}OCo_3)]$ of the OH symmetric/antisymetric stretching modes $A_{1g}^{ss}(\mathbf{H}OCo_3)$/ $E_g^{as}(\mathbf{H}OCo_3)$ (Figs. 3 (a) and (b)) will be located in the OH FG region, all wavenumbers $\omega[A_{1g}^{sipb}(\mathbf{H}OCo_3)]/\omega[E_g^{aipb}(\mathbf{H}OCo_3)]$ and $\omega[E_g^{aopb}(\mathbf{H}OCo_3)]$ of the $OHCo_3$ symmetric/ antisymmetric in-plane bending modes $A_{1g}^{sipb}(\mathbf{H}OCo_3)/E_g^{aipb}(\mathbf{H}OCo_3)$ (Figs. 3 (c) and (d), the OH group is located on C_s symmetry plane, so in the former vibration H and O move perpendicular to the O-O bond but within the C_s plane) and antisymmetric out-of-plane bending mode $E_g^{aopb}(\mathbf{H}OCo_3)$ (Figs. 3 (e)) fall in the OH CP region.

Meanwhile, all wavenumbers $\omega[A_{1g}^{sb}(OCo_3)]/\omega[A_{1g}^{ss}(OCo_3)]$, $\omega[E_g^{aipb}(OCo_3)]/$ $\omega[E_g^{aips}(OCo_3)]$, and $\omega[E_g^{opb}(OCo_3)]$ of the OCo_3 symmetric stretching/bending modes $A_{1g}^{sb}(OCo_3)/A_{1g}^{ss}(OCo_3)$ (Figs. 3 (f) and (g)), antisymmetric in-plane bending/streching modes $E_g^{aipb}(OCo_3)/E_g^{aips}(OCo_3)$ (Fig. 3 (h) and(i)), out-of-plane bending mode $E_g^{opb}(OCo_3)$ (Figs. 3 (j), in the former O atoms move in the C_s plane, but in the latter perpendicularly to the C_s plane) will be located in the high frequency part of the so-called OCo_3 FP region of

about 600~200 cm^{-1}, and two wavenumbers $\omega[A_{1g}{}^{ss}(ClCo_3)]$ and $\omega[E_g{}^{sb}(ClCo_3)]$ of the $ClCo_3$ symmetric stretching/bending modes (Figs. 3 (k) and (l)) in the low frequency part of $ClCo_3$ FP region of less than 200 cm^{-1}.

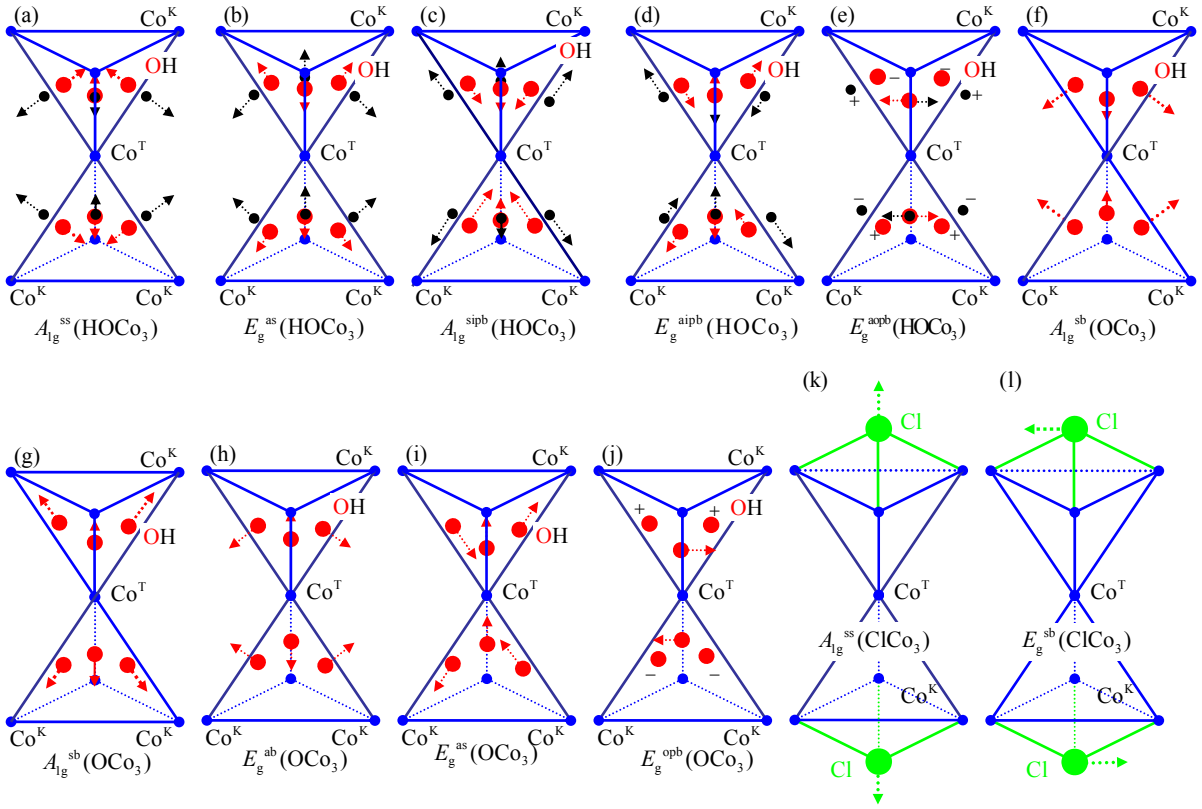

Fig. 2.2.3 The atomic displacement patterns of all the 12 Raman modes of $Co_2(OH)_3Cl$ with blue, red and black balls representing Co, O and H ions, respectively.

Due to the polycrystalline nature of our samples, our Raman spectra exhibit simultaneously all Raman-active modes. Further, according to the atomic displacement patterns in Fig.2.2.3, we can predict the relationship among these mode wavenumbers as followings:

(1). 3800 cm^{-1}>$\omega[A_{1g}{}^{ss}(\mathbf{H}OCo_3)]$>$\omega[E_g{}^{as}(\mathbf{H}OCo_3)]$>3200 cm^{-1} in the OH FG region;

(2). 1000 cm^{-1}>$\omega[A_{1g}{}^{ipb}(\mathbf{H}OCo_3)]$>$\omega[E_g{}^{aipb}(\mathbf{H}OCo_3)]$>$\omega[E_g{}^{aopb}(\mathbf{H}OCo_3)]$>600 cm^{-1} in the OH CP region;

(3). 600 cm^{-1}>$\omega[A_{1g}(OCo_3)]$>$\omega[A_{1g}(OCo_3)]$>$\omega[E_g(OCo_3)]$ >$\omega[E_g(OCo_3)]$> $\omega[E_g(OCo_3)]$>200 cm^{-1} in the OCo_3 FP region. We predict $\omega[E_g(\mathbf{H}OCo_3)]$ will exhibit maximum extra shift caused by the spin-lattice coupling effect than others.

(4). 200 cm^{-1}>$\omega[A_{1g}{}^{ss}(\mathbf{Cl}Co_3)]$>$\omega[E_g{}^{sb}(\mathbf{Cl}Co_3)]$ in the $ClCo_3$ FP region.

2.3 IR and Raman selection rules for space group No. 62

Figure 2.3.1 shows the crystal structure of β-$Ni_2(OH)_3Cl$ as an example of our crystals $M_2(OH)_3X$ with the crystal symmetry D_{3d}^5 of space group No. 62. The detail crystal structure parameters of Atacamite β-$Cu_2(OH)_3Cl$ and Atacamite-type β-Ni_2 $(OH/D)_3Cl$ are listed in Table A2 in Appendix A for reference.

The magnetic ions of M^{2+} form a 3D network of linked tetrahedra that can be viewed as alternative stacking layers of kagome and triangular lattice planes in the (001) direction. A prominent structural feature is a notable distortion in the tetrahedron, where the M^T-M^K distance is about 10% longer than M^K-M^K distance on the kagome lattice plane.

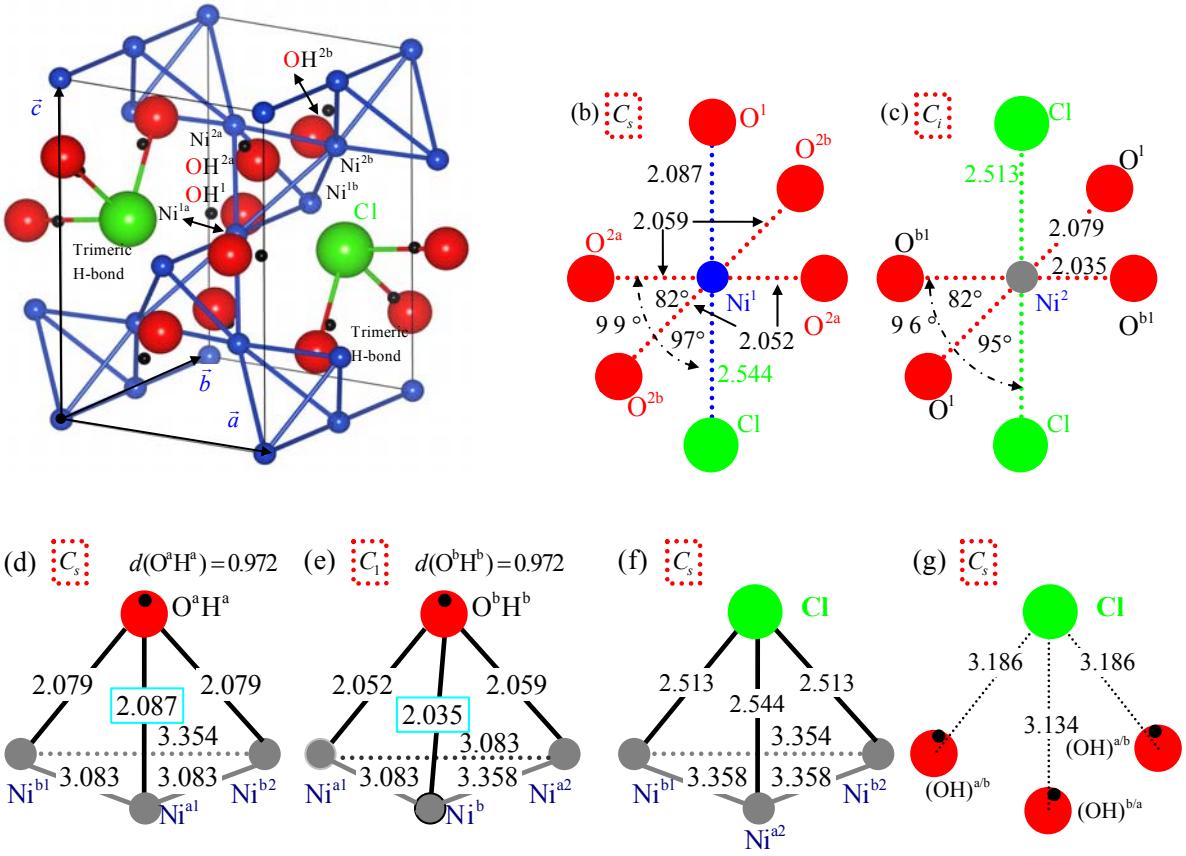

Fig. 2.3.1 (a) Crystal structure, and (b) Ni^1-site, (c) Ni^2-site, (d) O^1H^1-site, (e) O^2H^2-site, (f) Cl-site, (g) trimeric H-bond environments of β-$Ni_2(OH)_3Cl$ as an example of our crystals with the crystal symmetry of space group No. 62. Here related distances are in units of Å

Follow the routing process of FGA, point group character tables of C_s , C_i and C_1 are given in Tables 2.3.1~4, respectively, and part of the correlation table for D_{2h} factor group species and selected site species is given in Tables 2.3.5. [151, 152]

Table 2.3.1 Character table of point group C_1.

C_1	I
A	1

Table 2.3.2 Character table of point group C_s.

C_s	I	$\sigma(xy)$		
A'	+1	+1	T_x, T_y, R_z	α_{xx}, α_{yy}, α_{zz}, α_{xy}
B''	+1	−1	T_z,R_x, R_y	α_{yz}, α_{xz}

Table 2.3.3 Character table of point group C_i.

C_i	I	i		
A_g	+1	+1	R_x, R_y, R_z	All of α
A_u	+1	−1	T_x, T_y,T_z,	

Table 2.3.4. Character table of point group D_{2h}.

D_{2h}	I	$2C_3$	$3C_2$	i	$\sigma(xy)$	$3\sigma_6$		
A_g	1	1	1	1	1	1		α_{xx}, α_{yy}, α_{zz}
B_{1g}	1	1	−1	1	1	−1	R_z	α_{xy}
B_{2g}	1	−1	0	1	−1	0	R_y	α_{xz}
B_{3g}	1	1	1	1	−1	−1	R_x	α_{yz}
A_u	1	1	−1	−1	−1	1		
B_{1u}	1			−1			T_z	
B_{2u}	1			−1			T_y	
B_{3u}	1	−1	0	−1	1	0	T_x	

From this table, one can see all A_u modes which belong to the symmetry specie where one cannot find any translation T will be IR-inactive. Also B_{1u}, B_{2u} and B_{3u} are related to the translations T_z, T_y and T_x, respectively, therefore acoustic modes are a B_{1u}, a B_{2u} and a B_{3u}.

Table 2.3.5. Part of the correlation table for D_{2h} (No. 47~74) factor group and selected site species.

D_{2h}	…	$\sigma(xy)$ C_s	$\sigma(zx)$ C_s	$\sigma(yz)$ C_s	C_i	C_1
A_g	…	A'	A'	A'	A_g	A
B_{1g}	…	A'	A''	A''	A_g	A
B_{2g}	…	A''	A'	A''	A_g	A
B_{3g}	…	A''	A''	A'	A_g	A
A_u	…	A''	A''	A''	A_u	A
B_{1u}	…	A''	A'	A'	A_u	A
B_{2u}	…	A'	A''	A'	A_u	A
B_{3u}	…	A'	A'	A''	A_u	A

According to Tables 2.2.1~5, the correlation and mode distribution tables as the selection rule for D_{3d} factor group species and selected site species can be constructed, see Tables 2.3.6. and 2.3.7, respectively.

Table 2.3.6. Correlation table for site and factor group species (*Pnma*≡ D_{2h}^{16}, No. 62).

Site Atoms /Site group	Site group species	Factor group D_{2h} ($Z^B = 4$) species
$H^1(H^1O^1Ni_3)$ $O^1(H^1O^1Ni_3)$ C_1	$3A[(T_x,\ T_y,\ T_z),$ $(R_x,\ R_y,\ R_z)]$	$3A_g$ $3B_{1g}(R_z)$ $3B_{2g}(R_y)$ $3B_{3g}(R_x)$ $3A_u$ $3B_{1u}(T_z)$ $3B_{2u}(T_y)$ $3B_{3u}(T_x)$
$Ni^1(Ni^1O_4Cl_2)$ C_i	$3A_u(T_x, T_y, T_z)$	$3A_u$ $3B_{1u}(T_z)$ $3B_{2u}(T_y)$ $3B_{3u}(T_x)$
$H^2(H^2O^2Ni_3)$ $O^2(H^2O^2Ni_3)$ $Cl(ClNi_3)$ $Ni^2(Ni^2O_5Cl)$ $C_s^{xy}(\sigma_{xy})$	$2A'(T_x, T_y, R_z)$ $A''(T_z, R_x, R_y)$	$2A_g$ $2B_{1g}(R_z)$ $B_{2g}(R_y)$ $B_{3g}(R_x)$ A_u $B_{1u}(T_z)$ $2B_{2u}(T_y)$ $2B_{3u}(T_x)$

Table 2.3.7. Collected distribution of vibrational modes (*Pnma*≡ D_{2h}^{16}, No. 62).

Factor group species	$8H^1$ $H^1O^1Ni_3$ C_1	$4H^b$ $H^2O^2Ni_3$ C_s	$8O^1$ O^1Ni_3 C_1	$4O^2$ O^2Ni_3 C_s	$4Ni^1$ $Ni^1O_4Cl_2$ C_i	$4Ni^2$ Ni^2O_5Cl C_s	4Cl $ClNi_3$ C_s	Minus acoustic modes	Γ_{vib}	Spectral activity
A_g	3	2	3	2		2	2		14	Raman
$B_{1g}(R_z)$	3	2	3	2		2	2		14	Raman
$B_{2g}(R_y)$	3	1	3	1		1	1		10	Raman
$B_{3g}(R_x)$	3	1	3	1		1	1		10	Raman
A_u	3	1	3	1	3	1	1	−13	0	inactive
$B_{1u}(T_z)$	3	1	3	1	3	1	1	−1	12	IR
$B_{2u}(T_y)$	3	2	3	2	3	2	2	−1	16	IR
$B_{3u}(T_x)$	3	2	3	2	3	2	2	−1	16	IR
Σ	24	12	24	12	12	12	12	−16	92	

We can check the relationship of the number of atoms in the unit cell N=9, the number of each mode and Z^B=4:

$$3N\cdot Z^B = n(A_g)+ n(B_{1g})+n(B_{2g})+n(B_{3g}) + n(A_u)+ n(B_{1u})+ n(B_{2u})+ n(B_{3u})=108 \quad (2.3.1)$$

Summarizing the above results, we obtain 44 IR active modes and 48 Raman active modes. But it is too difficult to draw the atomic displacement patterns of all the 48 Raman modes because of large Z^B=4.

2.4 IR and Raman selection rules for the C_{2h}^5 (No. 14) $M_2(OH)_3X$

Among the materials belonging to our $M_2(OH)_3X$ series, only γ-$Cu_2(OH)_3Cl$ (clinoatacamite) has been designated to belong to SG No. **14**. Fig. 2.4.1 (a) shows its crystal structure, whose unit cell has four formula units and is featured by a layered structure with the magnetic ions of Cu^{2+} forming a 2D triangular lattice planes (110). Fig. 2.4.1 (b) shows a typical layer (the middle layer) of Fig. 2.4.1 (a). The detail crystal structure parameters of Clinotacamite γ-$Cu_2(OH)_3Cl$ are listed in Table A3 in Appendix A for reference.

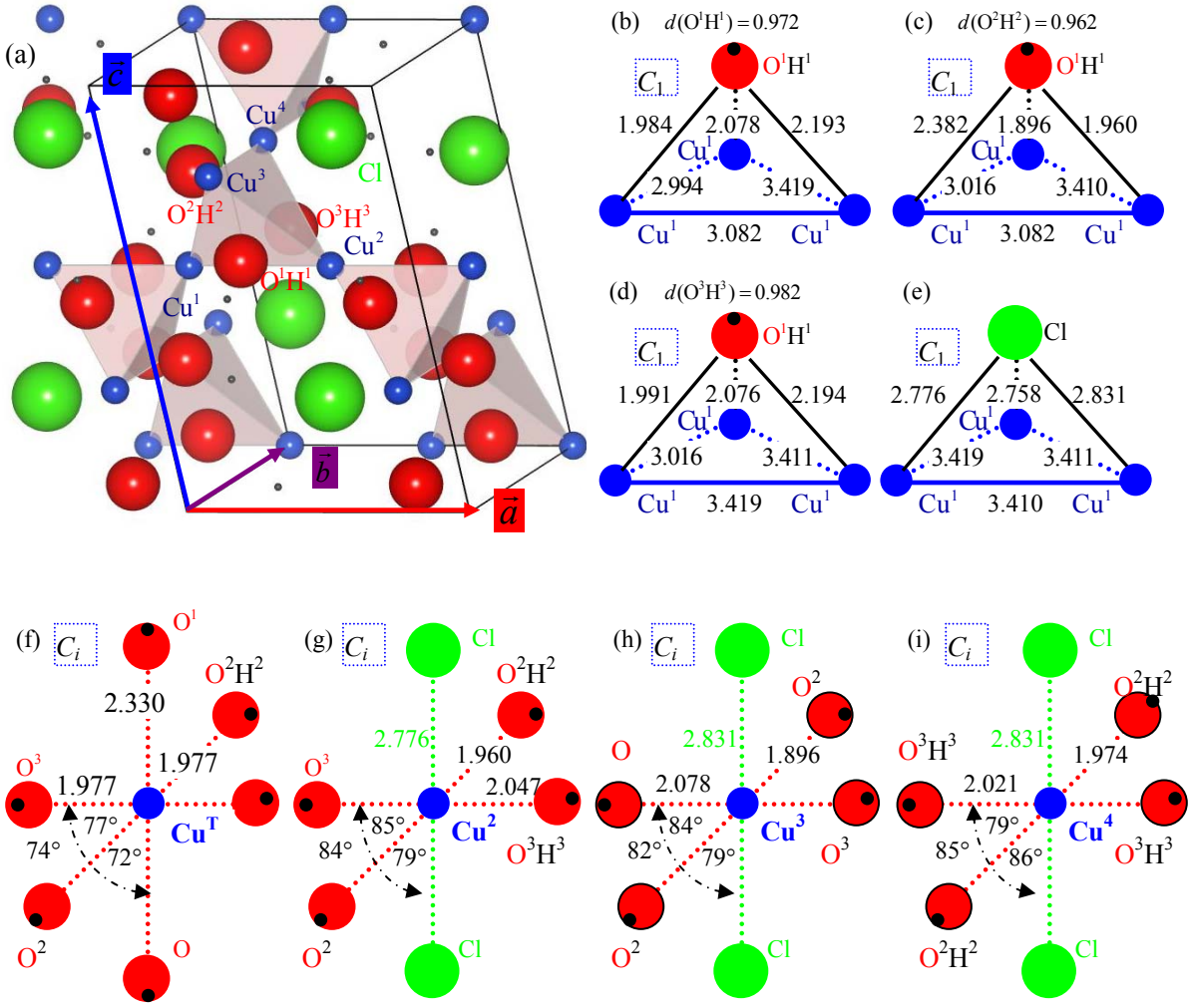

Fig. 2.4.1 (a) Crystal structure, and (b)~(i) all crystallographically in-equivalent site units of γ-$Cu_2(OH)_3Cl$.

Follow the routing process of FGA, character tables of point groups C_i and C_{2h} are given in Tables 2.4.1~5, respectively, and part of the correlation table for C_{2h} factor group species and selected site species is given in Tables 2.4.6. [151, 152]

Table 2.4.1 Character table of point group C_i.

C_i	I	i		
A_g	+1	+1	R_x, R_y, R_z	All of α
A_u	+1	−1	T_x, T_y, T_z,	

Table 2.4.2 Character table of point group C_{2h}.

C_{2h}	I	C_2(z)	$\sigma_h(xy)$	i		
A_g	+1	+1	+1	+1	R_z	α_{xx}, α_{yy}, α_{zz}, α_{xy}
B_g	+1	−1	−1	+1	R_x, R_y	α_{yz}, α_{xz}
A_u	+1	+1	−1	−1	T_z	
B_u	+1	−1	+1	−1	T_x, T_y	

From Table 2.4.2, one can see all A_g and B_g modes are Raman active and all A_u and B_u modes are IR active. Also A_u is related to the translation T_z, and B_u is related to the translations T_y and T_x, therefore acoustic modes are one A_u and two B_u.

Table 2.4.3. Correlation table of point group C_{2h}

C_{2h}	C_2	C_s	C_i	C_1
A_g	A	A'	A_g	A
B_g	B	A''	A_g	A
A_u	A	A''	A_u	A
B_u	B	A'	A_u	A

Table 2.4.4. Correlation table of SG C_{2h} (Z^B =4)

Site Atoms	Site group species	Factor group species
$H^{1\sim3}$	$\boldsymbol{C_1}$	3 A_g
$O^{1\sim3}$	$3A(T_x, T_y, T_z)$	3 B_g
Cl		3 A_u
		3 B_u
Cu^1	$\boldsymbol{C_i}$	3 A_u
$Cu^{2\sim4}$	$3A_u(T_x, T_y, T_z)$	3 B_u

According to Tables 2.4.1~4, the correlation and mode distribution tables for C_{2h}^2 factor group species and selected site species can be constructed, see Tables 2.4.4 and 2.4.5, respectively.

Table 2.4.5. Collected distribution of vibrational modes of γ-$Cu_2(OH)_3Cl$.

Factor group species	$4H^{1\sim3}$ [OH] C_1	$4O^{1\sim3}$ [Cu_3O] C_1	4Cl [Cu_3Cl] C_1	$2Cu^1$ [CuO_6] C_i	$2Cu^{2\sim4}$ [CuO_4Cl_2] C_i	Sum modes	Γ_{acoust}	Γ_{vib}	Spectral activity
A_g	3×3	3×3	3	0	0	21	0	21	Raman
B_g	3×3	3×3	3	0	0	21	0	21	Raman
A_u	3×3	3×3	3	3	3×3	33	−1	32	IR
B_u	3×3	3×3	3	3	3×3	33	−2	31	IR
Σ	12×3	12×3	12	6	6×3	108	−3	105	

We can check the relationship of the number of atoms in the unit cell N=9, the number of each mode and Z^B=4:

$$3N\cdot Z^B=3N\cdot Z^B= n(A_g)+ n(B_g)+ n(A_u)+ n(B_u) =108 \quad (2.4.1)$$

Summarizing the above results, we obtain the 42 Raman active and 63 IR active modes. But it is too difficult to draw the atomic displacement patterns of the IR and Raman modes because of large Z^B=4.

2.5 Selection rules for $M_2(OH)_3X$ with space group No. 11

Among the materials belonging to our $M_2(OH)_3X$ series, the space group of α-$Cu_2(OH/D)_3Cl$, α-$Cu_2(OH/D)_3Br$ and α-$Ni_2(OH/D)_3Br$ has been designated C_{2h}^2 (), or the $P2_1/m$ (Patterson Symmetry), which is given No. **11** in the table of 230 crystallographic space groups. In general, α-$Cu_2(OH)_3Cl$ is called Botallackite. Fig. 2.5.1 (a) shows this kind of crystal structure, whose unit cell has two formula units and is featured by a layered structure with the magnetic ions of M^{2+} forming a 2D triangular lattice planes (110). Fig. 2.5.1 (b) shows a typical layer (the middle layer). Fig. 2.5.2 show all crystallographically in-equivalent site units of α-$Cu_2(OH)_3Cl$ as an example of our crystals $M_2(OH)_3X$ with the space group No. 11. The detail crystal structure parameters of botallackite α-$Cu_2(OH)_3Cl$, botallackite–type α-Cu_2 $(OH/D)_3Br$ and α-Ni_2 $(OH/D)_3Br$ are listed in Table A4 in Appendix A for reference.

Follow the routing process of FGA, character tables of point groups C_s, C_i and C_{2h} are given in Tables 2.5.2~5, respectively, and part of the correlation table for C_{2h} factor group species and selected site species is given in Tables 2.5.6. [151, 152]

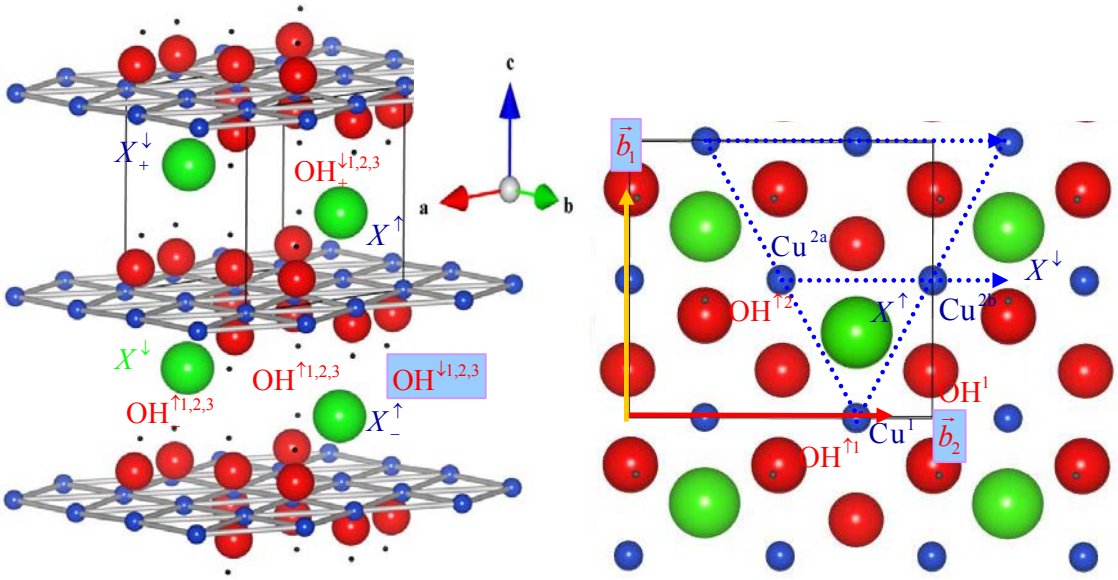

Fig. 2.5.1 (a) The crystal structure and (b) of the middle layer of $M_2(OH)_3X$ with No. **11**

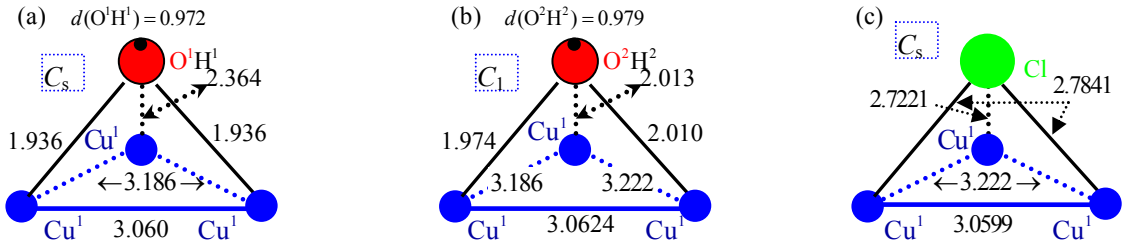

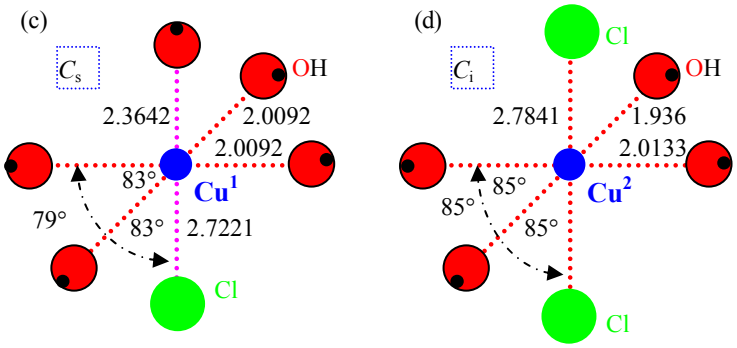

Fig. 2.5.2 (a) O^1H^1-site, (b) O^1H^1-site, (c) Cl-site, (d) Cu^1-site, (d) Cu^2-site units of α-$Cu_2(OH)_3Cl$ as an example with space group No. 11. Here related distances are in units of Å.

Table 2.5.1 Character table of point group C_s.

C_s	I	σ(*xy*)		
A'	+1	+1	T_x, T_y, R_z	α_{xx}, α_{yy}, α_{zz}, α_{xy}
B''	+1	−1	T_z,R_x, R_y	α_{yz}, α_{xz}

Table 2.5.2 Character table of point group C_i.

C_i	I	*i*		
A_g	+1	+1	R_x, R_y, R_z	All of α
A_u	+1	−1	T_x, T_y,T_z,	

Table 2.5.3. Character table of point group C_{2h}.

C_{2h}	I	C_2(z)	$\sigma_h(xy)$	i		
A_g	+1	+1	+1	+1	R_z	α_{xx}, α_{yy}, α_{zz}, α_{xy}
B_g	+1	−1	−1	+1	R_x, R_y	α_{yz}, α_{xz}
A_u	+1	+1	−1	−1	T_z	
B_u	+1	−1	+1	−1	T_x, T_y	

Table 2.5.4. Correlation table of space group C_{2h}.

C_{2h}	C_2	C_s	C_i	C_1
A_g	A	A'	A_g	A
B_g	B	A''	A_g	A
A_u	A	A''	A_u	A
B_u	B	A'	A_u	A

According to Tables 2.5.1~4, the correlation and mode distribution tables for C_{2h}^2 factor group species and selected site species can be constructed, see Tables 2.2.5 and 2.2.6.

Table 2.2.5. Correlation table of space group C_{2h} (No. 10~15)

Atoms	Site group / species	Factor group / species $\boldsymbol{C_{2h}}$ (Z^B =2)
M^2	$\boldsymbol{C_i}$	3 A_u
	3 $A_u(T_x, T_y, T_z)$	3 B_u
M^1	$\boldsymbol{C_s}$	2 A_g
O^1	2 $A'(T_x, T_y)$	1 B_g
H^1		1 A_u
X	1 $A''(T_z)$	2 B_u
O^2	$\boldsymbol{C_1}$	3 A_g
H^2		3 B_g
	3 $A(T_x, T_y, T_z)$	3 A_u
		3 B_u

Table 2.5.6. Collected distribution of vibrational modes of α-$Cu_2(OH)_3Cl$/Br.

Factor group species	$2O^1$ $M_3O^1H^1$ C_s	$2H^1$ $M_3O^1H^1$ C_s	$4O^2$ $M_3O^2H^2$ C_1	$4H^2$ $M_3O^2H^2$ C_1	$2M^1$ $O_5\boldsymbol{M^1}X$ C_s	$2M^2$ $M^2O_4X_2$ C_i	$2X$ M_3X C_s	Sum modes	Γ^{acoust}	Γ_{vib}	Spectral activity
A_g	2	2	3	3	2	0	2	14	0	14	Raman
B_g	1	1	3	3	1	0	1	10	0	10	Raman
A_u	1	1	3	3	1	3	1	13	−1	12	IR
B_u	2	2	3	3	2	3	2	17	−2	15	IR
Σ	6	6	12	12	6	6	6	54	−3	51	

Here one A_u and two B_u modes are acoustic modes from Table 2.5.6. We can check the relationship of the number of atoms in the unit cell N=9, the number of each mode and Z^B=2:

$$3N\cdot Z^B = n(A_g)+ n(B_g)+n(A_u)+ n(B_u) =54 \quad (2.5.1)$$

Summarizing the above results, we obtain the 24 Raman active and 17 IR active modes. But it is too difficult to draw the atomic displacement patterns of the IR and Raman modes because of the low symmetry.

2.6 Summary

From the FGA of the Sections 2.2~3.5, one obtains the following optical active Raman and IR modes of the $M_2(OH)_3X$ with space groups No.166, No.62, No.14 and No.11, respectively:

$$\begin{cases} \sum_{166}^{R} = 5A_{1g} + 7E_g \\ \sum_{166}^{IR} = 7A_{2u} + 10E_u \end{cases}, \quad (2.6.1)$$

$$\begin{cases} \sum_{62}^{R} = 14A_g + 14B_{1g} + 10B_{2g} + 10B_{3g} \\ \sum_{62}^{IR} = 12B_{1u} + 16B_{2u} + 16B_{3u} \end{cases}, \quad (2.6.2)$$

$$\begin{cases} \sum_{14}^{R} = 21A_g + 21B_g \\ \sum_{14}^{IR} = 32A_u + 31B_u \end{cases}, \quad (2.6.3)$$

$$\begin{cases} \sum_{11}^{R} = 14A_g + 10B_g \\ \sum_{11}^{IR} = 12A_u + 15B_u \end{cases}. \quad (2.6.4)$$

I also collect the predicted numbers of IR and Raman modes in the FG, CP, *M*O (*MO*X) FP and *MX* regions of the $M_2(OH)_3X$ spectra, respectively, see Table 2.6.1.

Table 2.6.1 Predicted numbers of IR and Raman modes in the FG, CP, *M*O (*MO*X) FP and *MX* regions of the $M_2(OH)_3X$ spectra, respectively.

	No. 166		No. 62		No. 14		No. 11	
	IR	Raman	IR	Raman	IR	Raman	IR	Raman
Total	**17**	**12**	**44**	**48**	**63**	**42**	**27**	**24**
FG	2	2	14	18	18	18	9	9
CP	3	3						
FP 1	12-2	5	28-2	24	42-3	18	18-3	12
FP 2	2	2	5-1	6	6	6	3	3

Chapter 3

RT spectral analysis of $M_2(OH/D)_3X$

As the first step to study the MGF properties at low T using the spectroscopic method, it is very important and necessary to obtain experimentally the related RT IR and Raman spectra and perform the spectral analysis as more exact as possible. In this chapter I first introduce the RT IR and Raman experimental methods, and give several spectral analysis methods in Sect. 3.1, and then assign the normal modes of four classes of samples with four space group symmetries using the spectral analysis methods in Sects. 3.2~3.5, respectively.

3.1 General methods

RT IR and Raman experimental methods are simple relative to the low *T* ones, but several methods must be adopted simultaneously when performing the spectral analysis. Most pictures of the related experimental devices are presented in Appendix B. Here the sample preparation, structure determination and magnetic property measurement methods are not given, because they have been described in the previously published papers.

3.1.1. RT IR and Raman experimental methods

IR spectra were obtained using Bruker Vector 22 and Bruker Sensor 37 FTIR spectrometers (see Fig.1.1.1) whose measurement regions are all over the 4000-400 cm^{-1}, and the used spectral resolution are 2 cm^{-1}. The measurement method belongs to the normal KBr disc technology using the agate crucible-grinding rod, mould of KBr-tablet preparation, hydraulic machinery (see Fig.1.1.2), and all the spectra from two spectrometers agree well with each other, so we analyze the spectra from the former only.

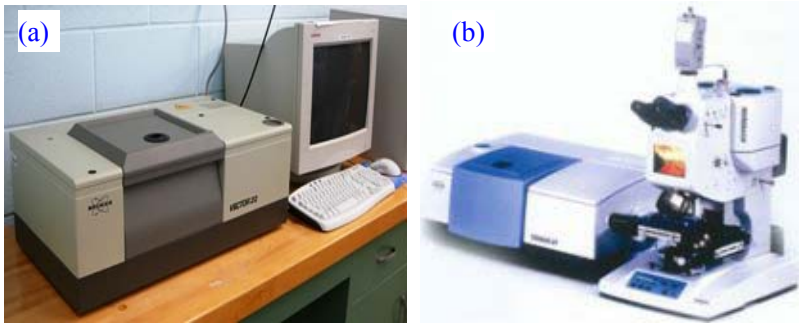

Fig. 1.1.1 Pictures of
(a) Brucker Vector 22 and
(b) Brucker Tensor 37

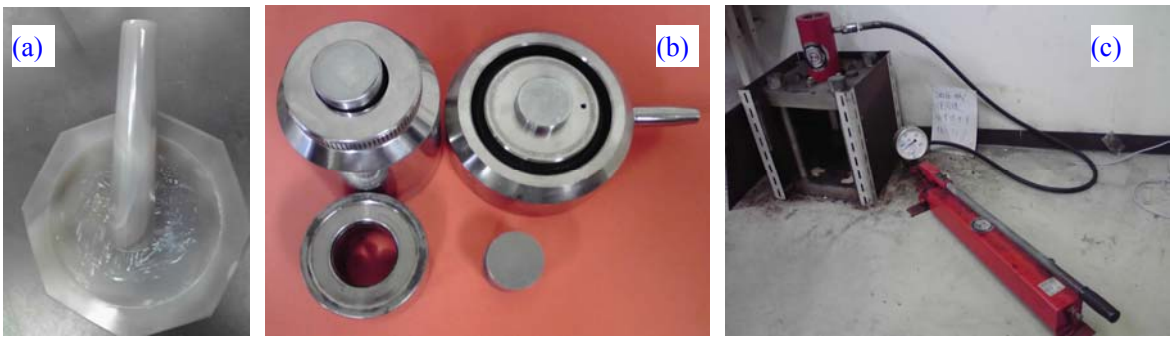

Fig. 3.1.2. Pictures of the (a) agate crucible-grinding rod, (b) mould of KBr-tablet preparation, and (c) hydraulic machinery.

Raman spectra were obtained using HR800 HORIBA Jobin Yvon Laser micro-Raman microscopy, and the software was Ramspec 5.0, see Fig. 3.1.3.

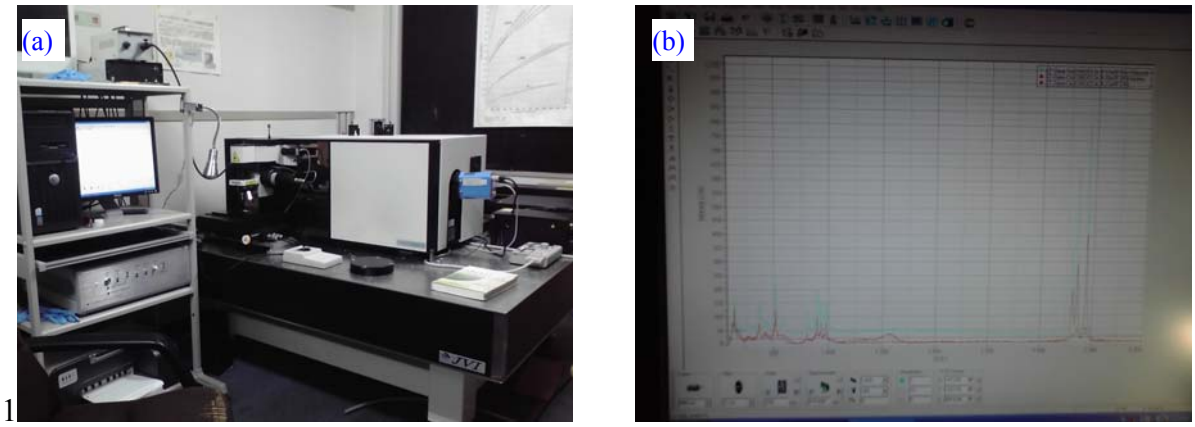

Fig. 3.1.3. HR800 HORIBA Jobin Yvon Laser Raman microscopy (a) and software interface (b).

The related experimental conditions are as follows:

(1) Exciting laser: Spectra-Physics model 127 Ar^{+} laser (488.0 nm, 15-100 mW, available power attenuation: 2^{-1}/D0.3 ($-\lg 2^{-1} \approx 0.3$), 4^{-1}(D0.6), 10^{-1}(D1), …); (2) resolution ratio: 0.5 cm^{-1} (1800 g/mm); (3) long work-distance (10.6 mm) objectives on the objective holder (see Fig. 3.1.4 (a)): 10X (PLAN 10X,), 50X (LMPLan 50X); (4) Hole: 200 μm; (5) notch filter: <92 cm^{-1}; (6) acquisition setup: 5 times acquisition average and 5s accumulation per time per spectral part (total 7 parts between 95 and 4000 cm^{-1}); (7) laser power: 10~30 mW (controlled by a laser power controller, see Fig. 3.1.4 (b)) using 10X objective or 1~3 mW using L50X objective (LMPlanFLN50X, WD=10.6 mm, see Fig. 3.1.4 (c)), and dark background photon counts 5-10 photons per 5s with a liquid-nitrogen cooled CCD (see Fig. 3.1.4 (d)); (8) samples: little tablets pressed from powder samples(see Fig. 3.1.3); (9) data processing: 5-10 times spectrum smoothing, 5~10 order automatically baseline correcting and subtracting, normalization (100%) according to the largest counting peak value.

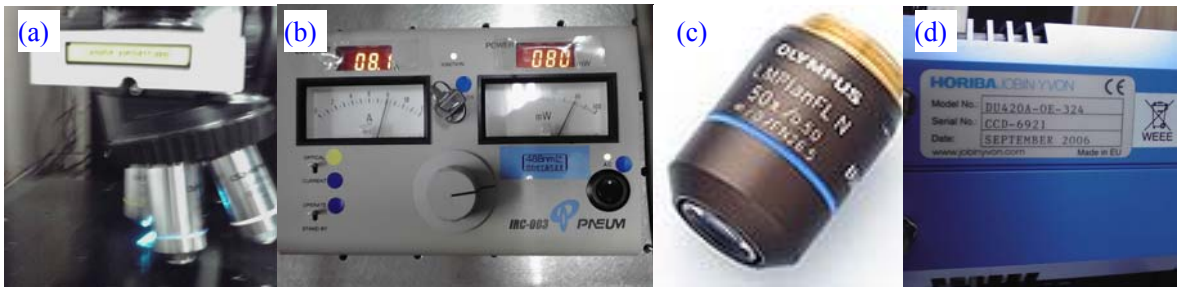

Fig. 3.1.4. Pictures of, (a) objective holder, (b) the laser power controller, (c) LNPlanFL 50X objective, and (d) CCD (a single photon counter, model DU420A-OE-324).

Raman data in the range of 95~4000 cm^{-1} are collected through recording the photon intensities of the following 9 sections in the period of about 5 minutes: 95~(**415**)~722 ~(**963**)~251 ~(**1477**)~1748 ~(**1961**)~2215 ~(**2415**)~2655 ~(2844)~3071 ~(3249)~3463 ~(3631)~3834 ~(3993)~4000 cm^{-1}. Here the numbers in the brackets are the approximate grating-center positions of the corresponding sections displayed on the software interface.

The grating is calibrated with standard single crystal silicon at 520.0 cm^{-1}, and the stability degree of the Raman system is estimated to be ±1.0 cm^{-1}/day. At RT Raman experiments in air aiming at a complete mode assigning and a local laser heating (LLH) effect checking, the laser power P_L=5, 20 and 40 mW are used to obtain Raman signals strong enough, while the irradiated surface of the sample pellet on the focus plane breaks down to other chemicals at an intensive P_L≈60 mW. At low T Raman experiments in vacuum, P_L=5 mW is used to mainly avoid the LLH effect despite relatively bad signals.

The powder sample is poured into a 5×5 mm^2 soft paper stall in the mould of tablet preparation (Fig. 3.1.2 (b)), and then pressed into a tablet by the hydraulic machinery (Fig. 3.1.2 (c)) under the pressure of 100 kg (intensity of pressure is 100kg/0.25cm^{-2}=400 kg/cm^{-2}=40Mpa). The resulted tablets (see Fig. 3.1.5) can tolerate several times higher breaking power density than the naturally placed powder sample because their thermal conductance property has been improved greatly.

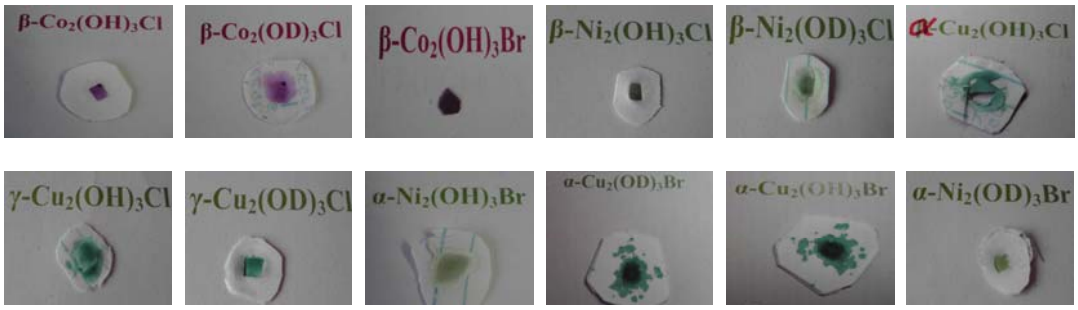

Fig. 3.1.5. Sample pellets pressed from the responding polycrystalline powders for Raman experiments.

RT Raman experiments aim at obtaining the Raman modes as many as possible through using relatively high laser power density and increasing the signal-to-noise ratio to facilitate

the perfect mode assignment, not pursue the exact values of Raman modes because the LLH effect is not avoidable and there exist the contradiction between the local heating and signal clarity. After a relatively perfect mode assignment has been done at RT, one can study several signal-strong, important and representative/exemplary Raman modes at low-T using the laser power density weak enough to avoid the LLH effect as well as possible, although at the expense of the spectral clarity and possible loss of signal-weak modes.

3.1.2. RT spectral analysis methods

It is usually a first and difficult task to assign completely the bands and set up definitely the relationship between the bands and the crystal structure of a new material, even with a high symmetry and especially with a low symmetry.

The FGA method in the previous Chapter is necessary and basic although it is still a well approximate one. Besides this, I also use successfully the following five methods to make the assignment at RT as more complete and definite as possible:

(1) IR and Raman complementation method

Raman and mid-IR spectroscopy are actually complementary techniques and usually both are required to completely measure the vibrational modes of a molecule. Although some vibrations may be active in both Raman and IR, these two forms of spectroscopy arise from different processes and different selection rules. In general, Raman spectroscopy is best at symmetric vibrations of non-polar groups while IR spectroscopy is best at the asymmetric vibrations of polar groups.

As to our work, the IR absorption spectrum has mainly embodied the important complementation role to the Raman spectrum in the aspect of helping the assignment of [OH/D] related modes, although it can show only few bands (>400 cm^{-1}) in the FP_1 region.

(2) FGA and non-FGA language alternative description method

In general, two different approaches are used for the interpretation of vibrational spectroscopy and elucidation of molecular structure: (a) Use of group theory with mathematical calculations of the forms and frequencies of the molecular vibrations. (b) Use of empirical characteristic frequencies for chemical FGs.

The first **description method** is called by the Factor Group Analysis (FGA) language, the second is called **non-FGA language.** Many empirical group frequencies have been explained and refined using this FGA approach (which also increases reliability). In fact, many identification problems are solved using the empirical approach even without the FGA. Certain FGs show characteristic vibrations in which only the atoms in that particular group are displaced. Since these vibrations are mechanically independent from the rest of the molecule, these group vibrations will have a characteristic frequency, which remains relatively unchanged regardless of what molecule the group is in. Typically, group frequency

analysis is used to reveal the presence and absence of various FGs in the molecule, thereby helping to elucidate the molecular structure with the **FGA language**, especially for the low symmetry case.

For the low symmetry case, as a good approximation, the empirical non-FGA language has provided us several useful reference relations from the large amount of spectral practice, which can be used in the investigation on our material series $M_2(OH)_3X$:

1) The band number from the FGA prediction is very large for the material with a low symmetry only caused by a slightly asymmetric atomic arrangement, such as for the γ-$Cu_2(OH)_3Cl$ because of the Jahn-Teller effect. The obtained experimental spectrum maybe still relative simple, originated from the apparent and massive band overlappings. At that time the intuitive non-FGA language will be suitable for describe the vibration modes of the main bands which can reflect sufficiently the key vibration properties of this material.

2) The number of main bands in the FG region equals that of crystallographically apparently different [OH], and the number of main bands in the CP region is approximatively same as that of crystallographically apparently different [*M*-O].

3) In the FP region, the mode with the highest frequency can be assigned to the "purest" stretching vibration, the mode with the lowest frequency can be considered to be the "purest" bending vibration one and the former can be used to estimate the metal-anion bond strength *k*.

4) For the asymmetric chemical group, the appearance of an IR band usually indicates the existing of a Raman band with the nearly equal frequency, and vice versa.

5) Normally for the inorganic insulated oxide materials, the metal-O^{2-} stretching mode can seldom approach 700 cm^{-1}, although it is usually masked by the [OH/D] bending modes. As to our $M_2(OH)_3X$, the reason that the highest and lowest [M_3O] mode frequencies are <600 and >200 cm^{-1} comes from the fact that the each $[OH]^-$ are bonded to three *M* ions as a whole and the lowest [M_3O] mode frequency is usually larger than one-third of the highest one, i.e., *k*(MO) or *k*(M_3-OH) of this series is commonly less than 3.6 mdyn/Å according to Eqn. 1.4.4. Therefore we can not pluck up our courage to believe the validity of the assignment of the Raman 700 cm^{-1} phonon band to a [Cu_3O] Raman vibrational mode, like the related discussion in Herbersmithite $ZnCu_3(OH)_6Cl_2$.

6) Similarly, because *k*(M_3-Cl/Br) is usually <1 mdyn/Å (the ionic radius is much larger than $[OH]^-$), the highest [M_3-Cl/Br] mode frequency may be < 218/145 cm^{-1} according to Eqn. 1.4.4 with $m_{Cl/Br}$=35.45/79.9. Considering further the existing of the trimeric H-bond, a well separated spectral window around 200 cm^{-1} between [*M*O] FP_1 and [*M*X] FP_2 regions also exists, just like that between FG and CP regions, and that CP and FP_1 regions.

(3) H/D isotopic substitution method

The most convincing assertion that these bands belong to the Raman [OH/D] stretching modes is based on the unique advantage of the famous H-isotope dilute or complete

substitution technology in the spectroscopic community.

According to the biatomic vibration frequency's formula Eqn. 1.4.4, the redshift rate (renormalization factor) of the [OD] stretching modes relative to the [OH] one is estimated to be $[(16+1)/(16+2)]^{1/2}$=**72.8%**, or more approximate $[m_H/m_D]^{1/2}$=71%. Then if, for example, an [OH] stretching/bending frequency $\omega_{\alpha/\beta}$[OH]=3500/800 cm^{-1} in some $M_2(OH)_3X$, the corresponding $\omega_{\alpha/\beta}$[OD] in the $M_2(OD)_3X$ will be about 2550/600 cm^{-1}.

In addition, most ω[*M*-O] in the 600~200 cm^{-1} FP_1 region (the <200 cm^{-1} FP_2 one usually includes the [*M*-*X*] modes with more lower frequency because of the much more heavy halogen atom than the O atom) of some $M_2(OH)_3X$ maybe slightly larger than those of some $M_2(OD)_3X$ because the [*M*-O] vibration is in fact [*M*-OH/D] one where OH or OD vibrates a whole group and the redshift rate of the [*M*-OD] band maybe about $\{[16\times1/(16+1)]/[16\times2/(16+2)]\}^{1/2}$=**97.2%**. Then if, for example, an [*M*-O] mode frequency ω_α[*M*-O]=300 cm^{-1} in some $M_2(OH)_3X$, the corresponding apparent redshifting $\Delta\omega_\alpha$[*M*-O] of the $M_2(OD)_3X$ relative to that of $M_2(OH)_3X$ will be about 8 cm^{-1}.

This relationships have played very important roles in our work, with help of the fully deuterized sample prepared originally for the aim of the neutron scattering research. It not only helps us select correctly the [OH] bands, but also determine the boundaries between the FG and CP regions, CP and FP_1 regions and even FP_1 and FP_2 region.

(4) Cl/Br halogen anion substitution method

Because the [*M*-O] FP_1 and [*M*-*X*] FP_2 regions are very near, it is not so easy to assign the [*M*-*X*] stretching modes with the highest frequency among the [*M*-*X*] related normal modes. Also according to Eqn. 1.4.4, the redshift rate of the [*M*-Br] stretching modes relative to the [*M*-Cl] one is estimated to be $(35.5/79.9)^{1/2}$=66.7%. Then if, for example, the [*M*-Cl] stretching frequency ω[*M*-Cl]=180 cm^{-1} in some $M_2(OH)_3Cl$, the corresponding ω[*M*-Br] in the $M_2(OH)_3Br$ will be about 120 cm^{-1}.

On the other hand, the [*M*-O] FP_1 and [*M*-*X*] FP_2 regions overlap to some extent in some cases, the halogen anion substitution method becomes also important. For example, $[CuO_4Cl_2]$ related Raman normal modes of α-$Cu_2(OH)_3Cl$ may have frequencies in the FP_2 region but are almost the same as those of α-$Cu_2(OH)_3Br$, then one can select out determinedly the [*M*-*X*] related normal modes in the FP_2 region with the aid of this method.

(5) low-*T* assistance method

At RT, the signals of some modes are broad, or weak, or not well separated from others, or overlap with the neighbors' to become the shoulder. At low *T*, they may become sharper, or stronger, or well distinguished from the neighbors to show the band splittings although the crystal symmetry does not changed at all. Consulting the low *T* spectrum, one can determine more real normal modes which maybe ignored at the first glance to accord with the theoretical prediction, even only in the number aspect as well as possible.

3.2 RT spectral analysis of the D_{3d}^5 (No. 166) $M_2(OH/D)_3X$

According to the result of the standard FGA method in Sect. 2.2, the IR and Raman normal modes are presented by:

$$\begin{cases} \Sigma_{166}^{R} = 5A_{1g} + 7E_g \\ \Sigma_{166}^{IR} = 7A_{2u} + 10E_u \end{cases}$$

Two kinds of samples $Co_2(OH/D)_3Cl$ and $Co_2(OH/D)_3Br$ with space group D_{3d}^5 ($R\bar{3}m$, No.166) are successfully prepared in our group, and their IR and Raman spectra are measured at RT and analyzed by the standard FGA method in this section, accompanied by the description of the simpler and more intuitive non-group theory language. The RT crystal structure parameters of $Co_2(OH/D)_3Cl$ and $Co_2(OH/D)_3Br$ are collected in Appendix A1for helping the spectral analysis.

3.2.1 RT spectral analysis of $Co_2(OH/D)_3Cl$

Figs. 3.2.1 (a) and (b) show the whole normalized IR (4000-400 cm^{-1}) and Raman spectra (4000-95 cm^{-1}, P_L=20 mW using L50X objective) of $Co_2(OH/D)_3Cl$ in air at RT, respectively.

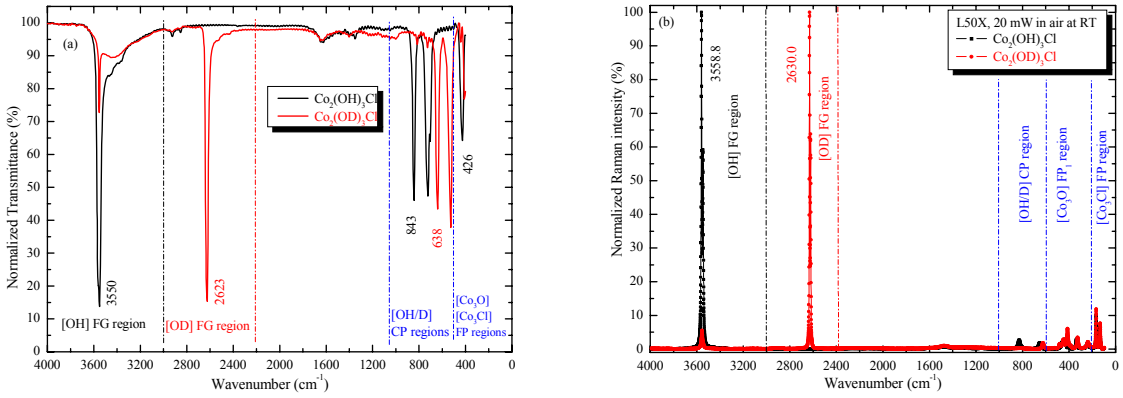

Fig. 3.2.1 The whole normalized IR (a) and Raman (b) spectra of $Co_2(OH/D)_3Cl$.

From Fig. 3.2.1(a) and (b), one can see that the three kinds of spectral regions are really well separated to make the assignment convenient. The bands appeared in the 3000~1000 cm^{-1} IR/Raman parts for $Co_2(OH)_3Cl$ and the 2000~800 cm^{-1} IR/Raman parts for $Co_2(OD)_3Cl$ are apparently the water, CO_2 and overtone related ones, which will not be discussed anymore in this dissertation.

Because useful spectral bands in the all regions are still located in a too narrow range, and the maximum intensities of the Raman bands in the CP and FP regions are only about 10 % of those in the respective FG regions, I enlarge them in Fig. 3.2.2 (a) ~ (d), respectively.

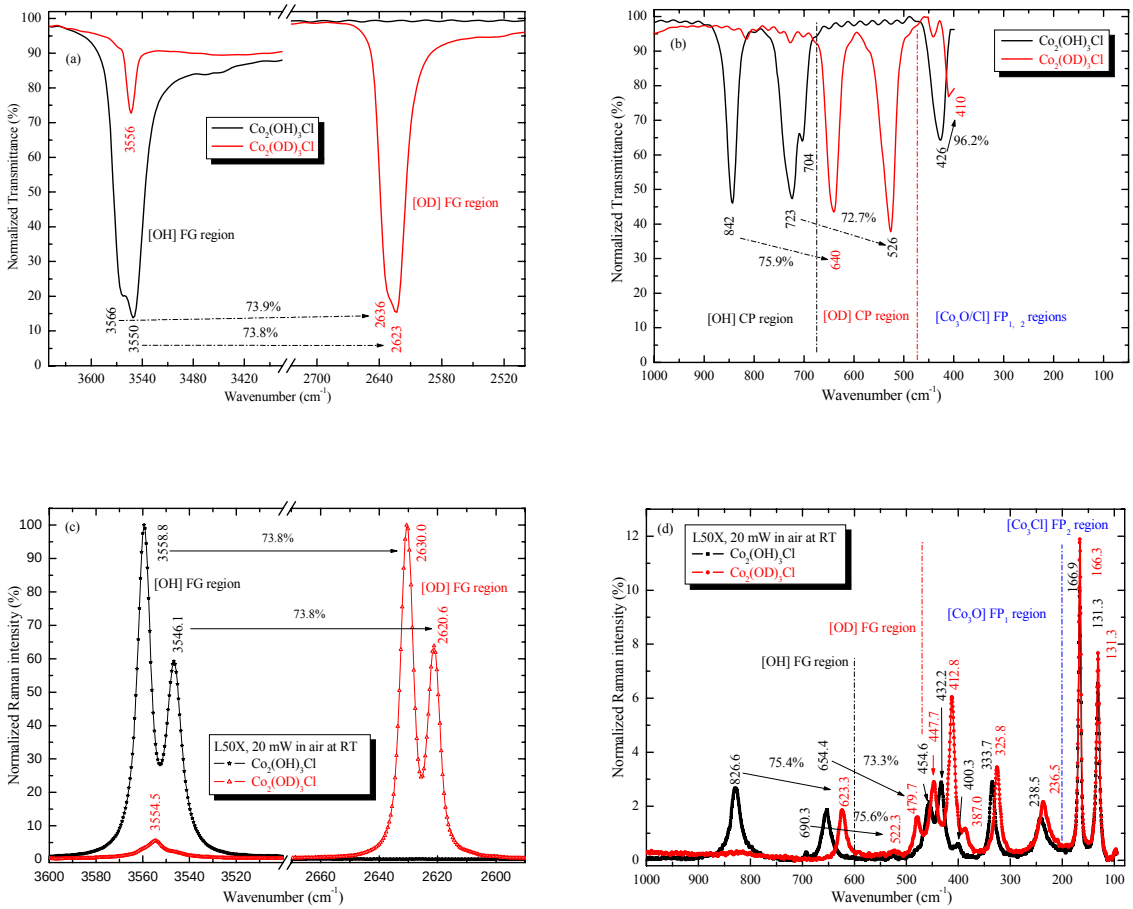

Fig. 3.2.2 The enlarged IR (a) and (b) spectral regions, and Raman (c) and (d) spectral regions of $Co_2(OH/D)_3Cl$.

(1) **[OH/D] stretching modes in the FG region**

In this region, two bands are expected to appear according to the FGA in IR and Raman, respectively. From Fig.3.2.2 (a) and (c) one can see clearly two IR bands (3566/2636 and 3550/2623 cm^{-1}) and two Raman bands (3558.8/2630.0 and 3546.1/2620.6 cm^{-1}) with peak separations of about 10 cm^{-1} in these FG regions. From the fact that all redshift ratios are close to the theoretical prediction 72.8%, these modes can be safely assigned to corresponding IR A_{2u}[**OH/D**], IR E_u[**OH/D**], Raman A_{1g}^{ss}[**OH/D**] and Raman E_g^{as}[**OH**] (the latter two are shown in Figs. 2.2 (a) and (b)), and this two-band phenomenon is called as the factor group splitting or the Davydov splitting (crystal splitting, or transversal and longitudinal optic phonon TO/LO splitting) [251-253] of the [OH/D] stretching mode in the non-FGA language because only one d(OH/D) exists in $Co_2(OH/D)_3Cl$.

In addition, $k_{OH/D}$ can be derived to be about 7.0 mdyn/Å for both $Co_2(OH)_3Cl$ and $Co_2(OD)_3Cl$ according to Eqn. (1.4.4).

(2) [OH/D] bending modes in the CP regions

In this region, three bands are expected to appear according to the FGA in IR and Raman spectra, respectively. From Fig. 3.2.2 (b) and (d), as expected, three IR bands (842/640, 723/526 and 704/--- cm^{-1}) and three Raman bands (826.6/623.3, 690.3/522.3 and 654.4/479.7 cm^{-1}) appear in the [OH/D] CP regions. From the fact that all redshift ratios are close to the theoretical prediction 72.8%, these bands are reasonably assigned to IR (A_{2u}[O**H/D**]+ $2E_u$[O**H/D**]) and Raman A_{1g}^{ipb}[O**H**], E_g^{aipb}[O**H**] and E_g^{aopb}[O**H**] as shown in Figs. 3.2.2 (c)~(e), respectively, although the band corresponding to the weak IR 704 cm^{-1} band does not appear in the IR spectrum of $Co_2(OD)_3Cl$. This identification of the lowest frequency [OH/D] bending modes and the 650-500 cm^{-1} wide window between [OH/D] CP and [Co_3O] FP_1 regions is very important for the assignment of [Co_3O] FP_1 regions.

In the non-FGA language, the four sets of strong bending modes may attribute to the fact that there exist two kinds of crystallographic un-equivalent $d(Co^KO)$ and $d(Co^TO)$ where an O connects two equivalent $Co^{K1, 2}$ and a Co^T.

(3) [Co_3O] vibrational modes in the FP_1 region

In this region, ten IR and five Raman bands are expected to appear according to the FGA in IR and Raman spectra, respectively. Limited by the IR measurement range (>400 cm^{-1}), IR 426/410 cm^{-1} band can be assigned to the [Co_3O] mode, and may designate five Raman bands 454.6/447.7, 432.2/412.8, 400.3/387.0, 337.8/325.8 and 238.5/236.5 cm^{-1} in the [Co_3O] FP_1 region to the theoretical A_{1g}[Co_3O], A_{1g}[Co_3O], E_g[Co_3O], E_g[Co_3O] and E_g[Co_3O] modes caused by the six [Co_3O] groups as shown in Figs. 3.2.2 (f)~(j), respectively. Here the slight redshift phenomenon of all five [Co_3O] bands for $Co_2(OD)_3Cl$ just demonstrates that in [Co_3O] vibration modes, as abovementioned, O is in fact moving along with H/D as a whole group [OH/D], and the effective atomic weight of O is in fact 17/18 for [Co_3O] vibrations. Here most of the redshift ratios in this region agree well with the theoretical value 97.2%.

Furthermore, according to the highest IR and Raman band frequencies 426/416 and 454.6/447.7 cm^{-1}, one can deduced the effective k[Co_3O] to be about 2.1 mdyn/Å for both $Co_2(OH)_3Cl$ and $Co_2(OD)_3Cl$, with the effective m_O=17/18, respectively.

As to the small 524.6 cm^{-1} band, we can not give out its true origin till now, and hope someone can build a connection between it and some magnetic features in future. While for the lowest frequency 238.5/236.5 cm^{-1} band with a Fano line shape, which is almost same as the 230 cm^{-1} one in Herbersmithite $ZnCu_3(OH)_6Cl_2$,[133, 148] we also agree the idea given by D. Wulferding *et al* that the Fano line shape may originate from the coupling of the corresponding phonon E_g^{opb}[Co_3O] to a continuum of magnetic excitation states. As its energy range is within the energy range of spin fluctuations, and the compound is an insulator while the corresponding continuum is attributed to magnetic fluctuations.

(4) [Co_3Cl] vibrational modes in the FP_2 region

In order to determine the remaining low frequency parts of Raman spectra, as an application of the Cl/Br halogen anion substitution method, I provide the enlarged IR and Raman spectra of $Co_2(OH)_3Cl$ and $Co_2(OH)_3Br$ in Fig. 3.2.3. From Fig. 3.2.3, one can find the extreme similarity between the IR and Raman spectra of $Co_2(OH)_3Cl$ and $Co_2(OH)_3Br$ in the FG, CP and FP_1 regions, and the redshift ratio of Raman 118.7/166.9=71.1% is close to the theoretical value 66.7%, which indicates that the 166.9/118.7 cm^{-1} can be definitely assigned to the [Co_3Cl/Br] stretching mode with the highest frequency in this region.

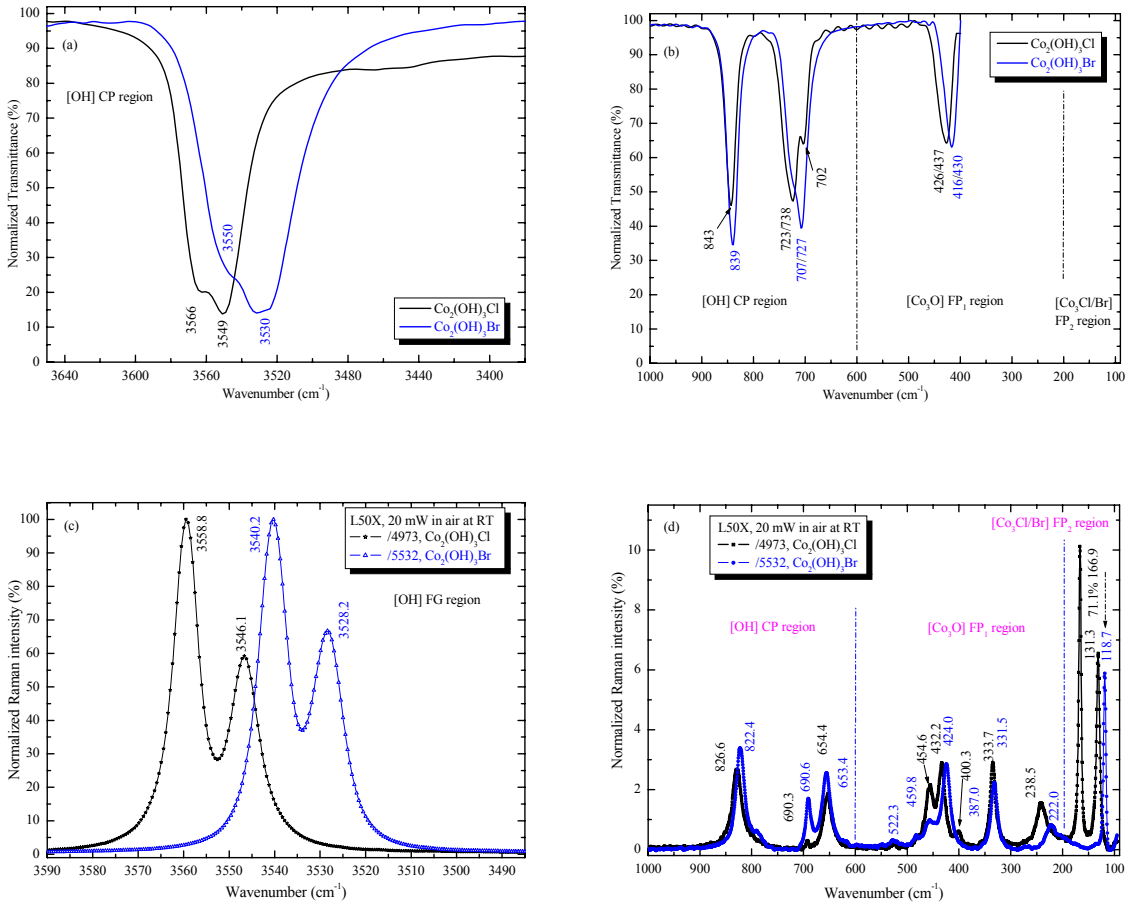

Fig. 3.2.3 The enlarged IR (a) and (b) spectral regions, and Raman (c) and (d) spectral regions of $Co_2(OH)_3Cl$ and $Co_2(OH)_3Br$.

Thanks to the spectral line clarity in the [Co_3Cl] Raman FP_2 region for $Co_2(OH)_3Cl$, we have observed both predicted modes within the detection range, and can determinately assign $\omega(A_{1g}{}^{ss}[Co_3\mathbf{Cl}])$=166.9/166.3 cm^{-1} and $\omega(E_g{}^{sb}[Co_3Cl])$=131.3/131.3 cm^{-1}. Compared with the 148/123 cm^{-1} bands in Herbersmithite $ZnCu_3(OH)_6Cl_2$, [133, 148] our assignment of 131.3 cm^{-1} is to E_g, not A_{1g}. Our larger values originate from the stronger interaction between Cl and $Co^K{}_3$ (weaker interaction between O and $Co^K{}_2Co^T$) than that between Cl and $Cu^K{}_3$ in

$ZnCu_3(OH)_6Cl_2$. From Refs. 133 and 148, one can safely validate that no lower frequency normal modes will exist below 100 cm^{-1}. Here one can deduced the effective k[Co_3Cl] to be about **0.58** mdyn/Å, with the mass m_{Cl}=35.45, for both $Co_2(OH/D)_3Cl$ which is very consistent with that of other chloride materials.[212]

IR data of $Co_2(OH)_3Cl$ are collected in TABLE B1 in Appendix B, where Raman data are those measured using P_L=5 mW in vacuum at 295 K for the sake of future comparison with the low-T data. It should be noted that those Raman data must slightly differentiate data presented here, radically because of the LLH effect. Fig. 3.2.4 shows four $Co_2(OH)_3Cl$ pellet Raman spectra at the RT experimental conditions with P_L=5, 20 and 40 mW in air.

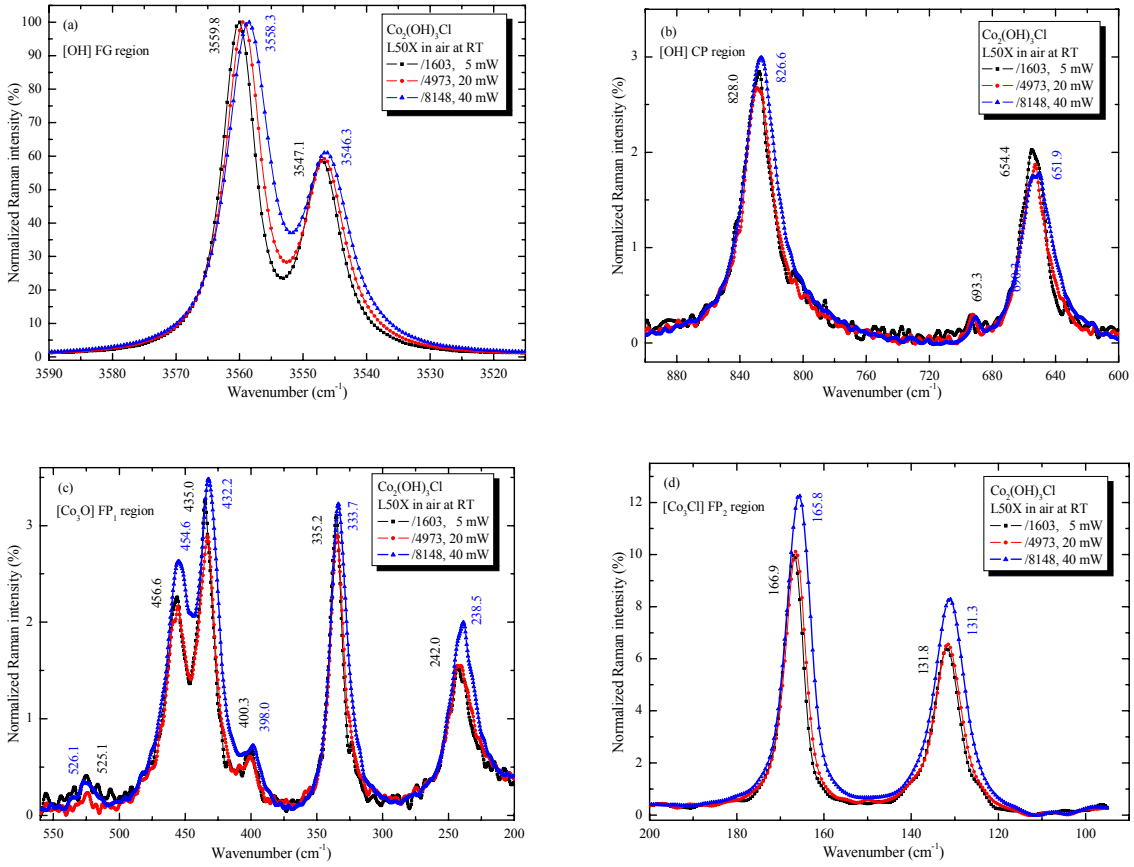

Fig. 3.2.4 Enlarged (a) [OH] FG, (b) the [OH] CP, and (c) [Co_3O] FP_1 and [Co_3Cl] FP_2 regions of Raman spectra of $Co_2(OH)_3Cl$ at P_L=5, 20 and 40 mW respectively.

From Fig. 3.2.4, one can see that the LLH effect on the Raman spectroscopy is apparent. Further more, from this P_L–dependent LLH effect at RT Raman experiment, one can share in the profits of predicting the low T (possibly down to the liquid nitrogen temperature) behavior when the sample is cooled down whatever the constant P_L is. Here we can obtain that the temperature coefficients $d\omega/dT$ are normally negative (redshifting when T or P_L increases) for most of the Raman normal modes at least around RT, which accords with the lattice thermal expansion rule for the normal materials.

3.2.2 RT spectral analysis of $Co_2(OH/D)_3Br$

Figs. 3.2.5 (a) and (b) show the normalized $Co_2(OH)_3Br$ IR (4000-400 cm^{-1}) and whole $Co_2(OH/D)_3Br$ Raman spectra (4000-95 cm^{-1}, P_L=20 mW using L50X objecrive) in air at RT, respectively, while Figs. 3.2.5 (c) and (d) present the their enlarged Raman [OH/D] FG regions and [OH/D] CP, [Co_3O] FP and [Co_3Br] FP regions, respectively.

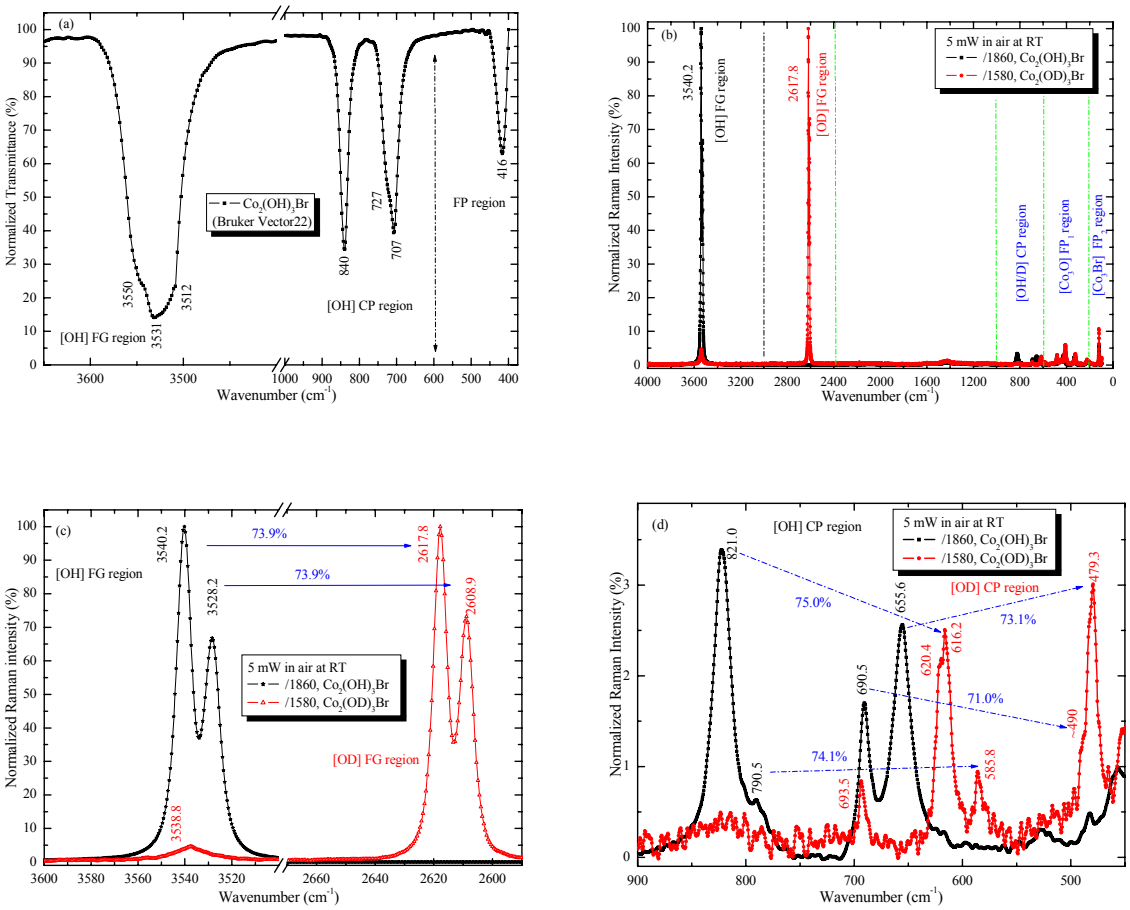

Fig. 3.2.5 The IR (a) and Raman (b) spectral profiles, and the enlarged Raman (c) and (d) spectral regions of $Co_2(OH/D)_3Br$.

(1) **[OH/D] stretching modes in the FG region**

In this region, two bands are expected to appear according to the FGA in IR and Raman, respectively. From Fig.3.2.5 (a) and (c) one can see clearly two IR bands (3550 and 3530 cm^{-1}) and two Raman bands (3540.2/2617.8 and 3528.2/2608.9 cm^{-1}) with peak separations of about 10 cm^{-1} in these FG regions. From the fact that all redshift ratios are close to the theoretical prediction 72.8%, these modes can be safely assigned to corresponding IR A_{2u}[**OH/D**], IR E_u[**OH/D**], Raman A_{1g}^{ss}[**OH/D**] and Raman E_g^{as}[**OH**], and this two-band phenomenon is the same as that in $Co_2(OH/D)_3Cl$.

In addition, $k_{OH/D}$ can be derived to be about 6.9 mdyn/Å for both $Co_2(OH)_3Br$ and $Co_2(OD)_3Br$ according to Eqn. 1.4.4. As to the Raman 3538.8 cm^{-1} band, it originates obviously from the incompletely deuterized effect with the 5 % "impurity" H, which was not previously detected by other experiments.

(2) [OH/D] bending modes in the CP regions

In this region, three bands are expected to appear according to the FGA in IR and Raman spectra, respectively. From Fig. 3.2.5 (b) and (d), as expected, three IR bands (840, 727 and 707 cm^{-1}) and three Raman bands (821.0/623.3, 690.3/522.3 and 654.4/479.7 cm^{-1}) appear in the [OH/D] CP regions. From the fact that all redshift ratios are close to the theoretical prediction 72.8%, these bands are reasonably assigned to IR (A_{2u}[**OH/D**]+ $2E_u$[**OH/D**]) and Raman A_{1g}^{ipb}[**OH**], E_g^{aipb}[**OH**] and E_g^{aopb}[**OH**] as shown in Figs. 3.2.2 (c)~(e), respectively. This identification of the lowest frequency [OH/D] bending modes and the 650-500 cm^{-1} wide window between [OH/D] CP and [Co_3O] FP_1 regions is very important for the assignment of [Co_3O] FP_1 regions.

In the non-FGA language, the four sets of strong bending modes may attribute to the fact that there exist two kinds of crystallographic un-equivalent $d(Co^KO)$ and $d(Co^TO)$ where an O connects two equivalent $Co^{K1,2}$ and a Co^T.

(3) [Co_3O] vibrational modes in the FP_1 region

In this region, ten IR and five Raman bands are expected to appear according to the FGA in IR and Raman spectra, respectively. Limited by the IR measurement range (>400 cm^{-1}), IR 426 cm^{-1} band can be assigned to the [Co_3O] mode, and five Raman bands 454.6/447.7, 432.2/412.8, 400.3/387.0, 337.8/325.8 and 238.5/236.5 cm^{-1} in the [Co_3O] FP_1 region may be designated to the theoretical A_{1g}[Co_3O], A_{1g}[Co_3O], E_g[Co_3O], E_g[Co_3O] and E_g[Co_3O] modes caused by the six [Co_3O] groups as shown in Figs. 3.2.2 (f)~(j), respectively. Here the slight redshift phenomenon of all five [Co_3O] bands for $Co_2(OD)_3Br$ just demonstrates that in [Co_3O] vibration modes, as abovementioned, O is in fact moving along with H/D as a whole group [OH/D], and the effective atomic weight of O is in fact 17/18 for [Co_3O] vibrations.

Furthermore, according to the highest IR and Raman band frequencies 426/416 and 454.6/447.7 cm^{-1}, one can deduced the effective k[Co_3O] to be about 2.1 mdyn/Å for both $Co_2(OH)_3Cl$ and $Co_2(OD)_3Cl$, with the effective m_O=17/18, respectively. While most of the redshift ratios in this region agree well with the theoretical value 97.2 %.

As to the small 524.6 cm^{-1} band, we can not give out its true origin till now, and hope someone can build a connection between it and some magnetic features in future.

(4) [Co_3Br] vibrational modes in the FP_2 region

By use of the Cl/Br halogen anion substitution method**,** from Fig. 3.2.3, we have already found that the 118.8 cm^{-1} can be definitely assigned to the [Co_3Br] stretching mode with the

highest frequency in this region, the $\omega(E_g^{sb}[Co_3Br])$ will exist near 95 cm^{-1}. Here one can deduced the effective $k[Co_3Br]$ to be about 0.66 mdyn/Å, with the mass m_{Br}=79.9, for both $Co_2(OH/D)_3Br$.

IR data of $Co_2(OH)_3Br$ are collected in TABLE B1 in Appendix B, where Raman data are those measured using P_L=5 mW in vacuum at 295 K for the sake of future comparison with the low-T data. It should be noted that those Raman data must slightly differentiate data presented here, radically because of the LLH effect. Fig. 3.2.6 shows four $Co_2(OH)_3Br$ pellet Raman spectra at the RT experimental conditions with P_L=5, 15 and 25 mW in air.

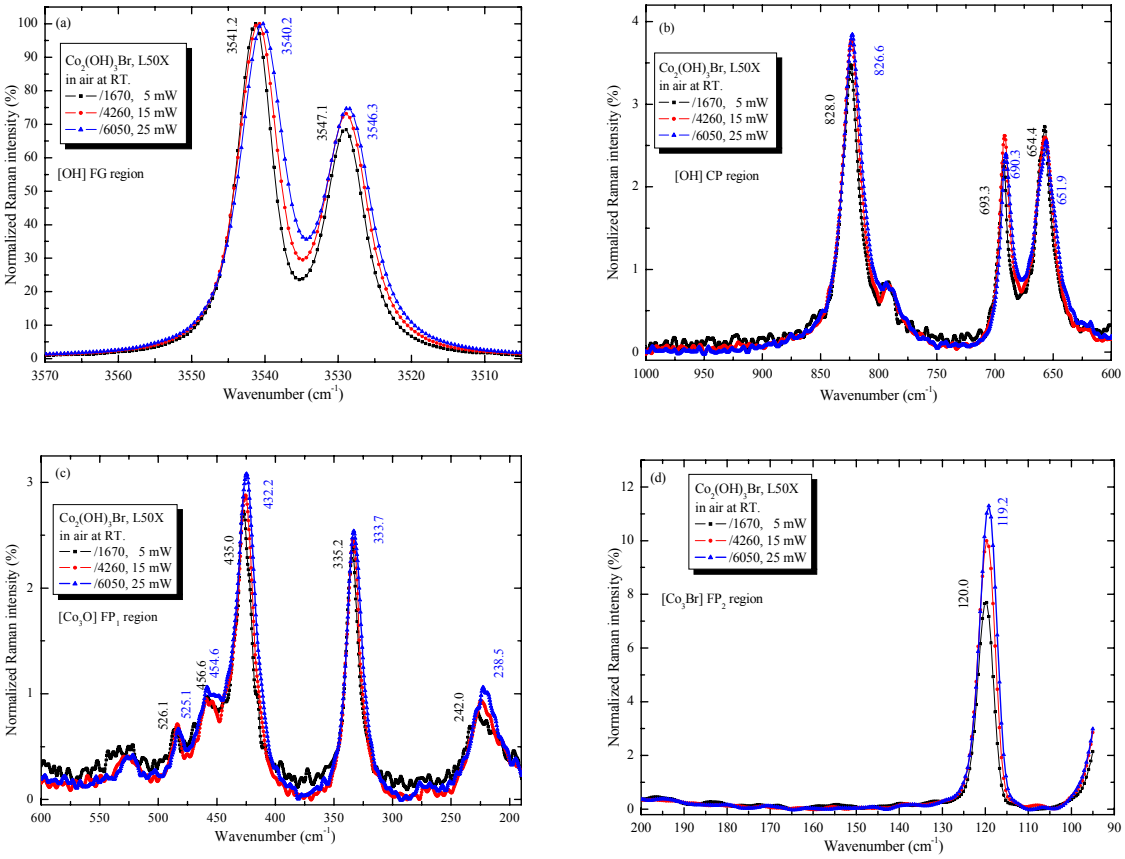

Fig. 3.2.6 Enlarged (a) [OH] FG, (b) [OH] CP, and (c) $[Co_3O]$ FP_1 and $[Co_3Cl]$ FP_2 regions of Raman spectra of $Co_2(OH)_3Br$ at P_L=5, 15 and 25 mW respectively.

From Fig. 3.2.6, one can see that the LLH effect on the Raman spectroscopy is apparent. Further more, from this P_L–dependent LLH effect at RT Raman experiment, one can predict the low T (possibly down to the liquid nitrogen temperature) behavior. Here we can obtain that the temperature coefficients $\Omega=d\omega/dT$ are normally negative for most of the Raman normal modes at least around RT, which accords with the TE rule for the normal materials.

3.3 RT Spectral analysis of the D_{2h}^{16} (No. 62) $M_2(OH)_3X$

According to the result of the standard FGA method in Sect. 2.3, the IR and Raman normal modes are presented by:

$$\begin{cases} \Gamma_{62}^{R} = 14A_g + 14B_{1g} + 10B_{2g} + 10B_{3g} \\ \Gamma_{62}^{IR} = \quad 12B_{1u} + 16B_{2u} + 16B_{3u} \end{cases}$$

Our samples with space group D_{2h}^{16} (*Pnma*, No.62) are natural atacamite β-$Cu_2(OH)_3Cl$ from Arizona, USA and β-$Ni_2(OH)_3Cl$ are prepared by the normal hydrothermal reaction.[68, 85] The RT crystal structure parameters of β-$Cu_2(OH)_3Cl$ and β-$Ni_2(OH)_3Cl$ are collected in Appendix A2 for helping the spectral analysis.

3.3.1 Spectral analysis of β-$Cu_2(OH)_3Cl$

Figs. 3.3.1 (a) and (b) show two whole normalized IR (4000-400 cm^{-1}, obtained by Brucker Vector 22 and Sensor 37) and two Raman spectra (4000-95 cm^{-1}, P_L=22 and 20 mW using 100X and L50X objectives at different positions) of β-$Cu_2(OH)_3Cl$ in air at RT, respectively.

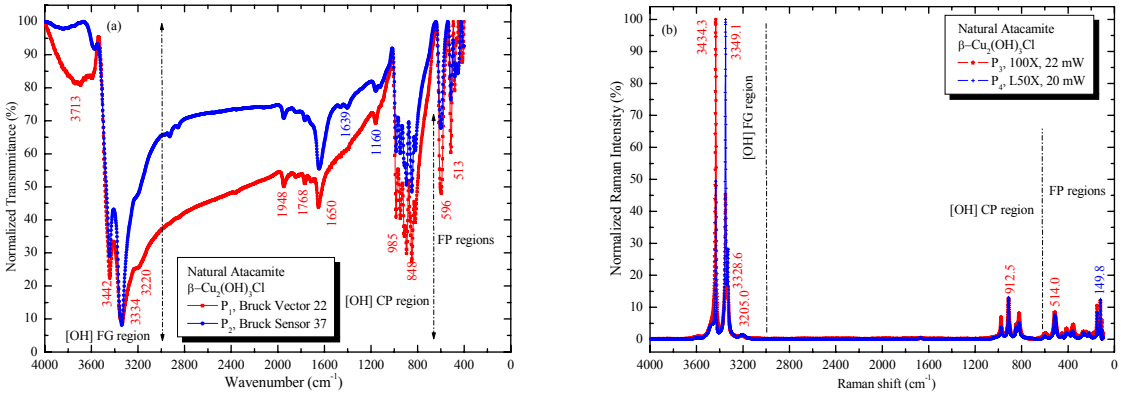

Fig. 3.3.1 The whole normalized IR (a) and Raman (b) spectra of Natural atacamite β-$Cu_2(OH)_3Cl$ from Arizona, USA. The samples used for two IR spectra are peeled off (剥げる, はげる) from the bulk at two different surface positions P_1 and P_2, while two Raman spectra were obtained through irradiating the laser on P_3 and P_4 using different P_L (22 and 20 mW) and objectives (100X and L50X), respectively.

From comparison of two IR and two Raman spectra, one can see that the samples on the surface of the bulk are uniformly crystallized and their main bands agree well with those of the Atacamite reported by other researchers.

Because useful spectral bands in the all regions are still located in a too narrow range, and the maximum intensities of the Raman bands in the CP and FP regions are only about 20 % of those in the respective FG regions, I enlarge them in Fig. 3.3.2 (a) ~ (d), respectively.

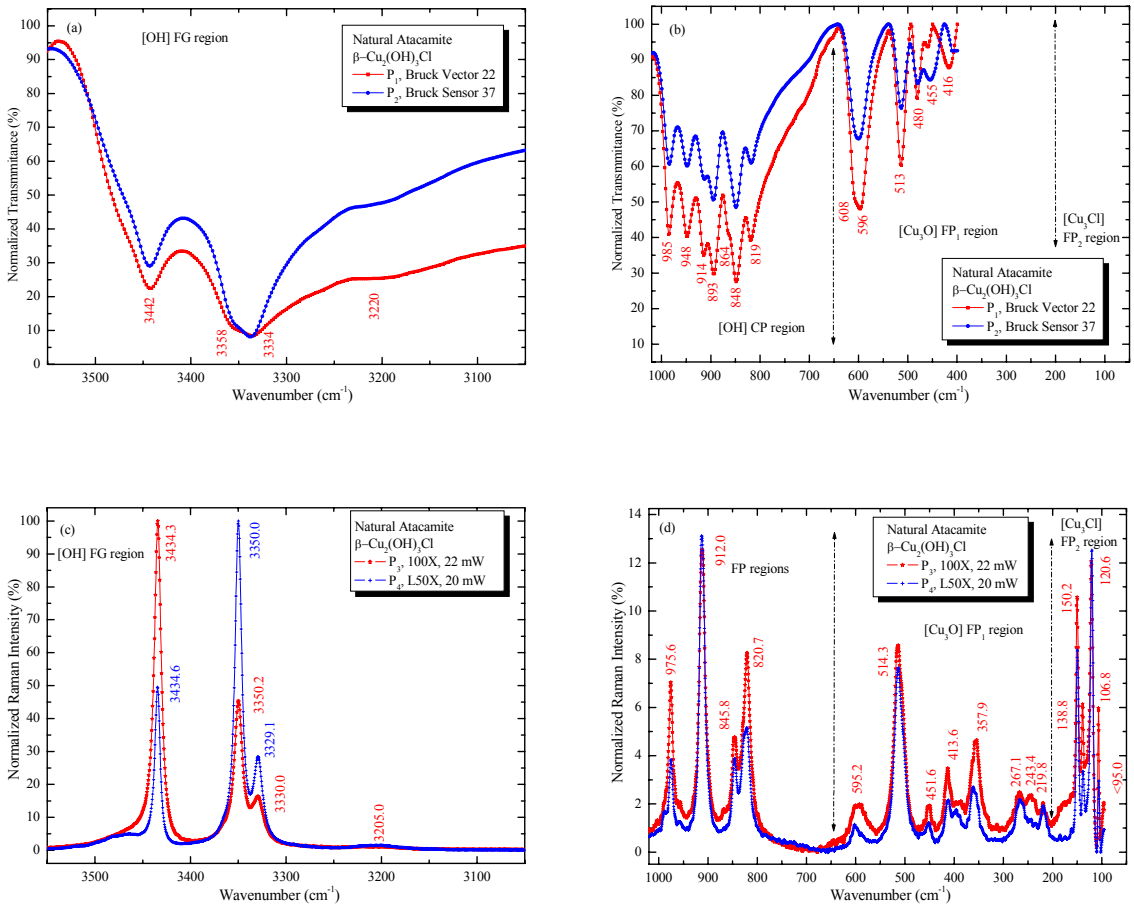

Fig. 3.3.2 Enlarged IR [OH] FG (a), [OH] CP and $[Cu_3O]/[Cu^2O_5Cl]/[Cu_3Cl]$ FP (b) regions, and Raman [OH] FG (c) and $[Cu_3O]/[Cu^2O_5Cl]/[Cu_3Cl]$ FP (d) regions of β-$Cu_2(OH)_3Cl$, respectively.

(1) **[OH] stretching modes in the FG region**

In these FG regions, two main bands are expected to appear in IR and Raman spectra, respectively, according to the fact that there are two crystallographic non-equivalent [OH] FPs although till now I can not predict exactly how many bands of predicted IR ($4B_{1u}+5B_{2u}+5B_{3u}$ including CP modes) and Raman ($5A_g+5B_{1g}+4B_{2g}+4B_{3g}$ including CP modes) [OH] related bands of β-$Cu_2(OH)_3Cl$ will appear here because of its relatively low symmetry.

From Fig.3.3.2 (a) and (c) one can really see two clear IR main bands (3442 and 3334 cm^{-1}) and two Raman bands (3434.6 and 3350.2 cm^{-1}) with peak separations of 108 cm^{-1} (IR) and 84 cm^{-1} (Raman) in these FG regions. Although there are no β-$Cu_2(OH)_3Cl$ data, we can still safely assign them to [O**H**] stretching modes. From the differences of 108 cm^{-1} (IR) and 84 cm^{-1} (Raman), it can be estimated that the difference of two [OH] distances is between 0.008~0.011 **Å**, which does not agree with the experimental difference (0.08 Å).

From the Raman main band data, the force constants can be derived to be $k(O^1H^1)\approx 7.38$ mdyn/Å, $k_1(O^2H^2)\approx 7.02$ mdyn/Å for β-$Cu_2(OH)_3Cl$ according to Eqn. (1.4.4).

(2) [OH] bending modes in the CP regions

In this region, at least four to five main bands (bending vibration modes) may be expected to appear in IR and Raman spectra, respectively, according to the fact that there are four to five apparently different *d*(CuO), see TABLE A2 in the Appendix A. Also till now I can not predict exactly how many bands of predicted IR ($4B_{1u}+5B_{2u}+5B_{3u}$ including FG modes) and Raman ($5A_g+5B_{1g}+4B_{2g}+4B_{3g}$ including FG modes) [OH] related bands of β-$Cu_2(OH)_3Cl$ will appear in this FG region because of its low symmetry.

From Fig. 3.3.2 (c) and (e), as expected, six IR bands (985, 948, 914, 893, 848 and 819 cm^{-1}) and four Raman main bands (975.6, 912.0, 845.8 and 820.7 cm^{-1}) appear in the [OH] CP regions. Although there are no β-$Cu_2(OH)_3Cl$ data, we can still safely assign them to [O**H**] bending vibration modes. This identification of the lowest frequency [OH] bending modes and the 800-650 cm^{-1} wide window between [OH] CP and [Cu_3O] FP_1 regions is very important for the assignment of [Cu_3O] FP_1 regions.

(3) [Cu_3O] and [Cu^2O_5Cl] vibrational modes in the FP_1 region

In this region, 19 IR ($5B_{1u}+7B_{2u}+5B_{3u}$) and 24 Raman ($7A_g+7B_{1g}+5B_{2g}+5B_{3g}$) bands caused by [$Cu_3O^{1,2}$] and [$Cu^2O_5Cl$] are expected to appear according to the FGA in IR and Raman, respectively. Limited by the IR measurement range (>400 cm^{-1}) and large accidental degeneracy, only five IR 596, 513, 480, 455 and 416 cm^{-1} main bands and seven Raman 595.2, 514.3, 451.6, 413.6, 357.9, 267.1, 243.4 and 219.8 cm^{-1} main bands are observed, and may be designated to their stretching and deformation modes. Here the first three bands can be attributed to the stretching modes of [Cu^2O_5Cl], [Cu_3O^2] and [Cu_3O^1], respectively, but I can not distinguish other [Cu^2O_5Cl] modes from other [Cu_3O] modes.

Furthermore, according to the Raman [Cu_3O^2] and [Cu_3O^1] band frequencies 514.3 and 451.6 cm^{-1}, one can deduce the effective *k*[Cu_3O^2] and *k*[Cu_3O^1] to be about 2.65 and 2.05 mdyn/Å, with the effective m_O=16+1 for β-$Cu_2(OH)_3Cl$ respectively.

(4) [Cu_3Cl] vibrational modes in the FP_2 region

In this region of the Raman spectrum, 6 Raman ($2A_g+2B_{1g}+B_{2g}+B_{3g}$) bands are expected to appear according to the FGA. Because till now nobody can prepare the β-$Cu_2(OH)_3Br$, the **Cl/Br halogen anion substitution method** can not be used here. Fortunately the remaining spectral part (<200 cm^{-1}) may include only [Cu_3Cl] vibrational modes because of relatively large distances *d*(Cu-Cl) (>2.75 Å, while for $Co_2(OH)_3Cl$, *d*(Co-Cl)≈2.60 **Å**).

From Fig. 3.3.2 (d), four clear Raman bands are observed and the fifth has begun to stand out conspicuously at the position of about 90 cm^{-1}. The highest frequency band 150.2 cm^{-1} band can be safely assigned to the [Cu_3Cl] stretching mode, there one can deduced a

reasonable effective k[Cu_3Cl] to be about **0.47 mdyn/Å**, with the mass m_{Cl}=35.45 for β-$Cu_2(OH)_3Cl$ which is very consistent with that of other chloride materials.[212]

IR data of β-$Cu_2(OH)_3Cl$ are collected in TABLE B3 in Appendix B, where Raman data are those measured using P_L=2 mW in vacuum at 295 K for the sake of future comparison with the low-T data. It should be also noted that those Raman data must slightly differentiate data presented here, radically because of the LLH effect, as seen from Fig. 3.4.2 showing the Raman spectra at the RT experimental conditions with P_L=5, 20 and 30 mW in air.

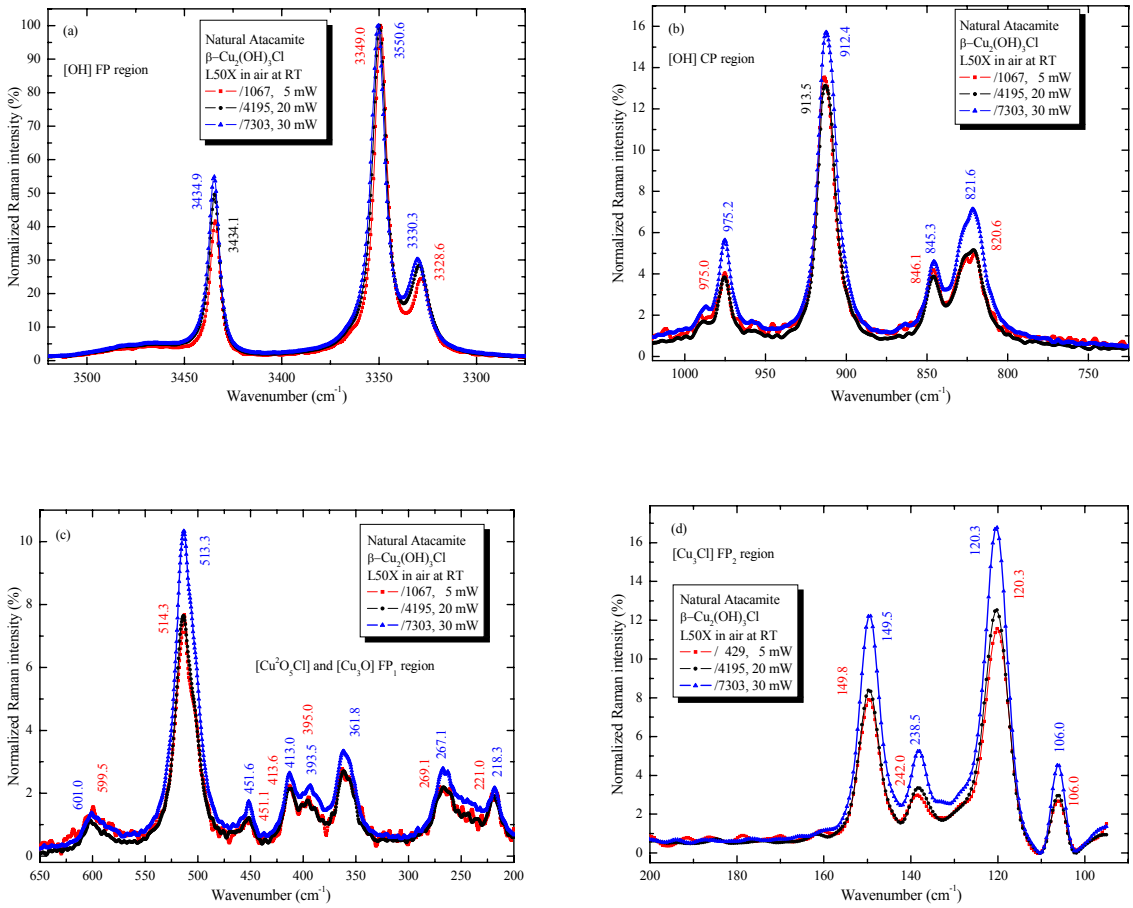

Fig. 3.3.3 Enlarged (a) [OH] FG, (b) [OH] CP, and (c) FP_1 and (d) FP_2 regions of Raman spectra of natural atacamite β-$Cu_2(OH)_3Cl$ at P_L=5, 20 and 30 mW, respectively.

From Fig.3.3.3, one can see that the LLH effect on the Raman spectroscopy is apparent. Further more, from this P_L–dependent LLH effect at RT Raman experiment, one can share in the profits of predicting the low T (possibly down to the liquid nitrogen temperature) behavior when the sample is cooled down whatever the constant P_L is. Here we can obtain that the temperature coefficients $\Omega \equiv d\omega/dT$ are abnormally positive (blueshifting when T or P_L increases) for most of the Raman normal modes at least around RT, which does not accord with the lattice NT rule for the normal materials.

3.3.2 Spectral analysis of β-$Ni_2(OH/D)_3Cl$

Fig. 3.3.4 (a) shows the normalized IR (4000-350 cm^{-1} measured by JASCO FT4100) and Figs. 3.3.4 (b)~(d) show the enlarged [OH/D] FG, [OH/D] CP and FP spectral regions of β-$Ni_2(OH/D)_3Cl$, respectively.

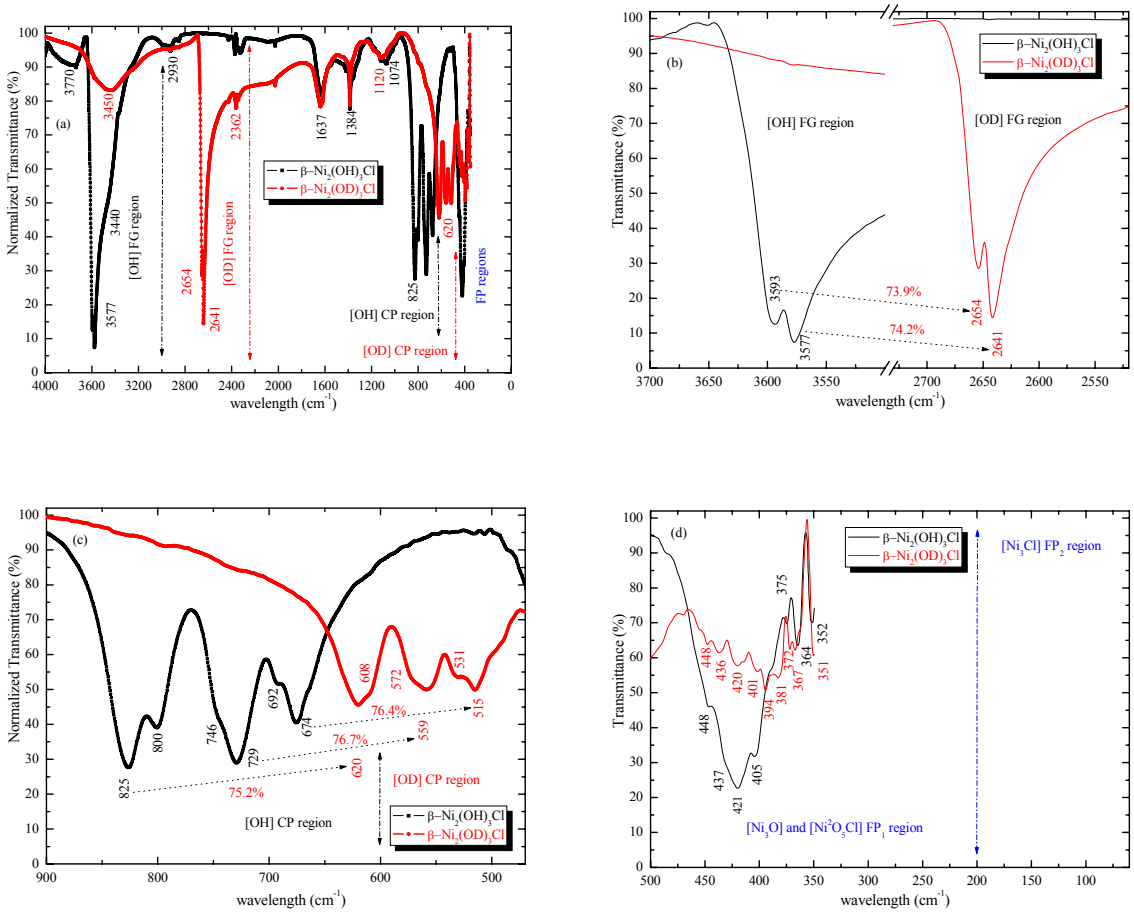

Fig. 3.3.4 The whole IR spectra (a) and the enlarged [OH/D] FG (b), [OH/D] CP (c) and FP (d) spectral regions of β-$Ni_2(OH/D)_3Cl$, respectively.

From Fig. 3.3.4 (a), one can see that several small bands (i.e., 2632, 1637, 1384 and 1120 cm^{-1}, and others) are situated between the [OH/D] FG and CP regions, which may be considered as bands caused by overtones, residual water in the KBr disk, water and CO_2 in air, or the intrinsic shortage of the background deduction technology. The spectral analysis on them will be done accompanying with the Raman spectra, shown in Fig. 3.3.5 whose (a)~(d) give the whole Raman spectra, the enlarged [OH/D] FG , [OH/D] CP and FP spectral regions of β-$Ni_2(OH/D)_3Cl$, respectively, because useful spectral bands in the all regions are still located in a too narrow range, and the maximum intensities of the Raman bands in the CP and FP regions are only about 10 % of those in the respective FG regions.

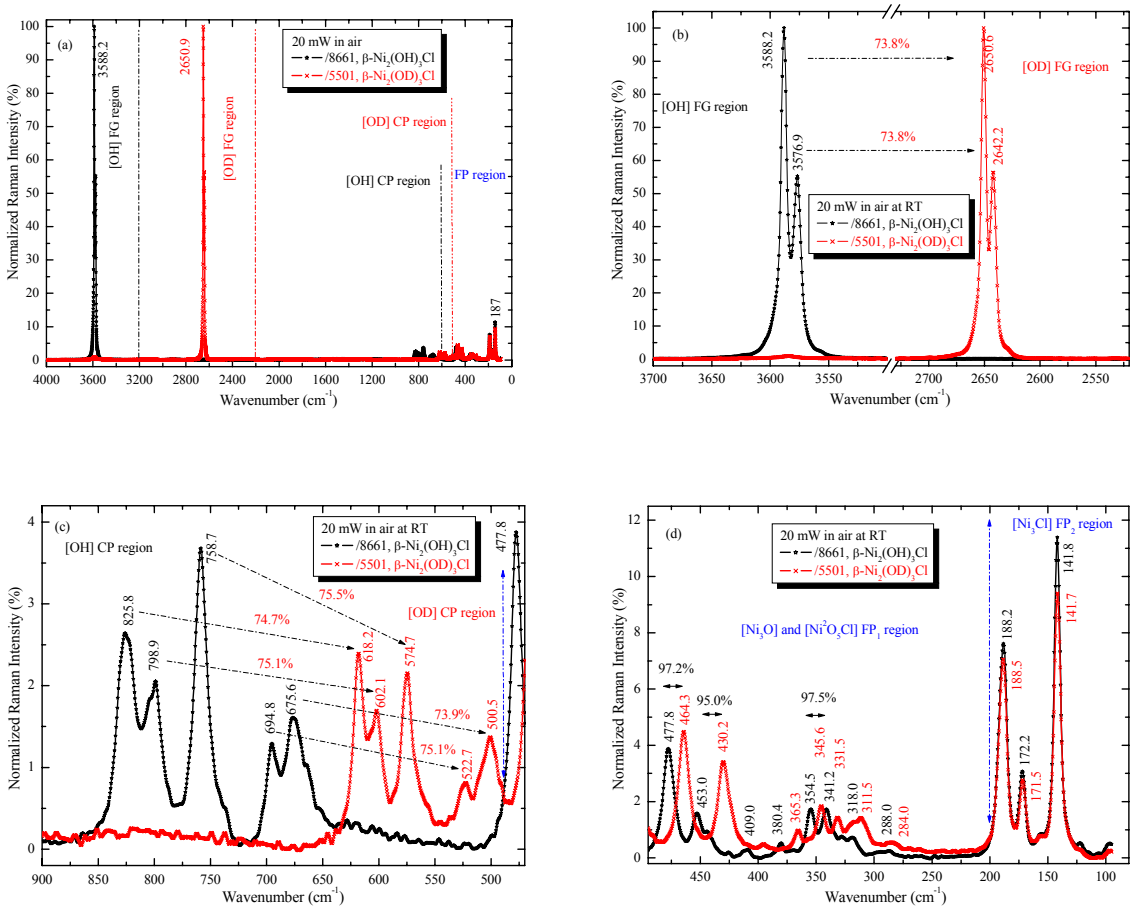

Fig. 3.3.5 The whole Raman spectra (a) and the enlarged [OH/D] FG (b), [OH/D] CP (c) and FP (d) spectral regions of β-$Ni_2(OH/D)_3Cl$ respectively.

(1) **[OH/D] stretching modes in the FG region**

In these FG regions, two main bands are expected to appear in IR and Raman spectra, respectively, according to the fact that there are two crystallographic non-equivalent [OH/D] FPs ($d(OH/D^1)$= 0.952 Å and $d(OH/D^2)$ = 0.997 Å) although till now I can not predict exactly how many bands of predicted IR ($4B_{1u}+5B_{2u}+5B_{3u}$ including CP modes) and Raman ($5A_g+5B_{1g}+4B_{2g}+4B_{3g}$ including CP modes) [OH/D] related bands of β-$Ni_2(OH/D)_3Cl$ will appear here because of the relatively low symmetry.

In the Figs. 3.3.4 (a) and 3.3.5 (a), from the fact that all redshift ratios are close to the theoretical prediction 72.8%, two IR (3593/2654 and 3577/2641 cm^{-1}) and two Raman (3588.2/2650.6 and 3576.9/2642.2 cm^{-1}) bands can be safely assigned to the corresponding [**OH/D**] asymmetric and symmetric stretching modes, but their small separation differences (16/13 and 11.3/8.4 cm^{-1}) throw me to be in a puzzle, because their band structures (the factor group splitting or the Davydov splitting, which can be considered as one main band

caused by only one [OH/D]) and high band frequencies (>3550 cm^{-1}) like very much those of $Co_2(OH/D)_3Cl$ and $Co_2(OH/D)_3Br$. Through comparing with the isostructural atacamite β-$Cu_2(OH/D)_3Cl$, as shown in Fig. 3.3.6, one has to suspect that the simulation of the crystal structure parameter data (the XRD, synchrotron radiation experiment or neutron diffraction experiments) need to be refined. The refined result may support a prediction that it belongs to another space group, supporting only one [OH/D], other than the Atacamite structure.

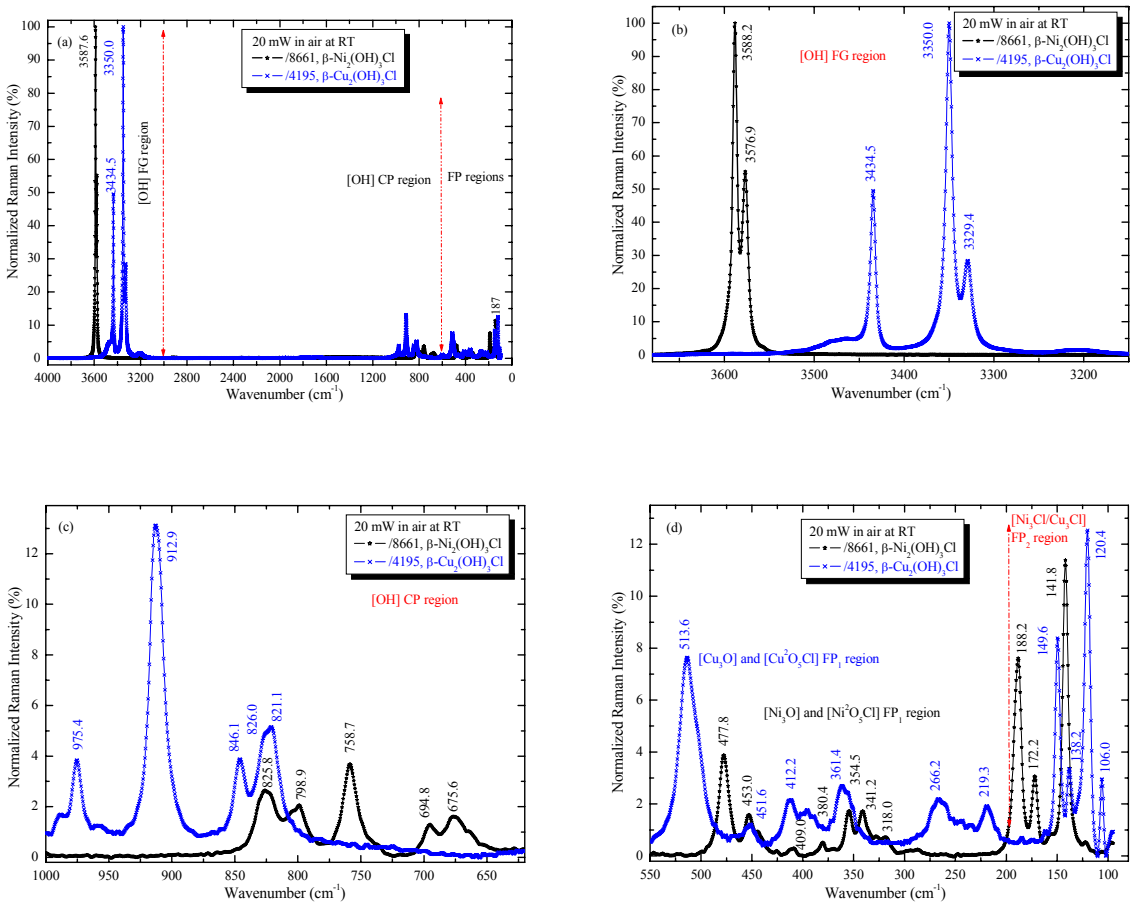

Fig. 3.3.6 The whole Raman spectra (a) and the enlarged [OH] FG (b), [OH] CP (c) and FP (d) spectral regions of β-$Ni_2(OH)_3Cl$ and β-$Cu_2(OH)_3Cl$, respectively.

Regardless of the true space group symmetry, one k(OH/D) can be derived to be about 7.14 mdyn/Å for β-$Ni_2(OH/D)_3Cl$ according to Eqn. (1.4.4).

(2) [OH] bending modes in the CP regions

In this region, at least four to five main bands (bending vibration modes) may be expected to appear in IR and Raman spectra, respectively, according to the prediction that there are four to five apparently different d(NiO), see TABLE A2 in the Appendix A. Also till now I can not predict exactly how many bands of predicted IR ($4B_{1u}$+$5B_{2u}$+$5B_{3u}$ including FG modes) and Raman ($5A_g$+$5B_{1g}$+$4B_{2g}$+$4B_{3g}$ including FG modes) [OH] related bands of

β-$Ni_2(OH/D)_3Cl$ will appear in this FG region because of its low symmetry.

From Figs. 3.3.4 (c) and 3.3.5 (c), six IR bands (825/620, 800/608, 746/572, 729/559, 692/531 and 674/515 cm^{-1}) and five Raman main bands (825.8/618.2, 798.9/602.1, 758.7/574.7, 694.8/522.7 and 675.6/500.5 cm^{-1}) appear in the [OH] CP regions, and their redshift ratios are also close to the theoretical prediction 72.8%. Therefore, we can still safely assign them to [O**H**] bending vibration modes. This identification of the lowest frequency [OH] bending modes and the wide window 650-500 cm^{-1} between [OH] CP and [Ni_3O] FP_1 regions is very important for the assignment of [Ni_3O] FP_1 regions.

It is very interesting that the band structure of β-$Ni_2(OH)_3Cl$ is similar to that of β-$Cu_2(OH)_3Cl$ as seen in Fig. 3.3.6 (c) although all the β-$Ni_2(OH)_3Cl$ bands have translated about 150 cm^{-1} to the low frequency direction relative to those of β-$Cu_2(OH)_3Cl$. This seems to throw me into be in the second puzzle. Therefore I have to perform a comparison among β-$Ni_2(OH)_3Cl$, α-$Cu_2(OH)_3Cl$, and γ-$Cu_2(OH)_3Cl$, as shown in Figs. 3.4.7 (a) and (b) with the FP regions for a further analysis.

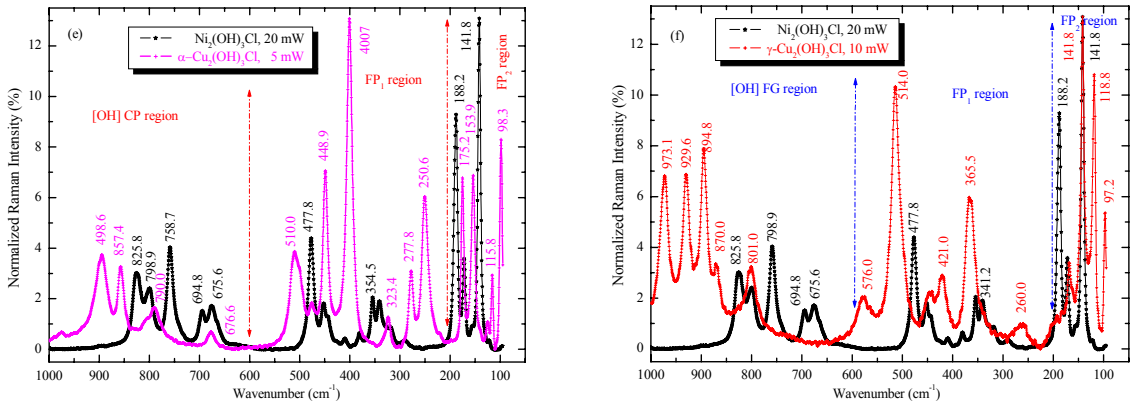

Fig. 3.3.7 Raman [OH] CP and FP spectral regions of β-$Ni_2(OH)_3Cl$ and α-$Cu_2(OH)_3Cl$ (a) and β-$Ni_2(OH)_3Cl$ and γ-$Cu_2(OH)_3Cl$ (b), respectively.

From Fig. 3.4.7 (a), one can see that the band structure of β-$Ni_2(OH)_3Cl$ is more similar to that of α-$Cu_2(OH)_3Cl$ than β-$Cu_2(OH)_3Cl$, while very different from γ-$Cu_2(OH)_3Cl$ according to Fig. 3.4.7 (b). Surely the detail spectral analysis on the latter two will be performed in the next sections, and no conclusive suggestion can be further made from this comparison of [OH] CP spectral regions here.

(3) [Ni_3O] and [Ni^2O_5Cl] vibrational modes in the FP_1 region

In this region, 19 IR ($5B_{1u}+7B_{2u}+5B_{3u}$) and 24 Raman ($7A_g+7B_{1g}+5B_{2g}+5B_{3g}$) bands caused by [$Ni_3O^{1,2}$] and [$Ni^2O_5Cl$] are expected to appear according to the FGA in IR and Raman, respectively. Limited by the IR measurement range (>350 cm^{-1}) and large accidental

degeneracy, less than ten small IR bands can be found out, as shown in Fig. 3.3.4 (d), and the redshifting ratio 97.3 % relationship between band frequencies of β-$Ni_2(OD)_3Cl$ and β-$Ni_2(OH)_3Cl$ is also not easy to correspond with each clearly. However, this relationship develops well enough in the Raman spectra, as shown in Fig. 3.3.5 (d), where two main bands at 477.8/464.3 and 453.0/430.2 cm^{-1} are tentatively assigned to be the [Ni_3O^2] and [Ni_3O^1] stretching modes, respectively, because I can not predict the highest frequency range of [Ni^2O_5Cl] related modes, and also can not distinguish other [Ni^2O_5Cl] modes from other [Ni_3O] modes.

According to the Raman [Ni_3O^1] and [Ni_3O^2] band frequencies 453.0/430.2 and 477.8/464.3 cm^{-1}, one can deduce the effective k[Ni_3O^1] and k[Ni_3O^2] to be about 2.05 and 2.28 mdyn/Å, with the effective m_O=17/18 for β-$Ni_2(OH/D)_3Cl$, respectively.

In consideration of my doubt on its iso-structuredness with the Atacamite β-$Cu_2(OH)_3Cl$, I find out that the difference lies mainly on the existence of 266.2 and 219.3 cm^{-1} in the β-$Cu_2(OH)_3Cl$ spectrum, as shown in Fig. 3.3.6 (d), although there exists a similarity to some extent between them.

Furthermore, let's compare the FP_1 region of β-$Ni_2(OH)_3Cl$ Raman spectrum with those of α-$Cu_2(OH)_3Cl$ and γ-$Cu_2(OH)_3Cl$ in Figs. 3.4.7 (a) and (b). From the qualitative comparison, one can conclude that the main framework of β-$Ni_2(OH)_3Cl$ is very different from either those of α-$Cu_2(OH)_3Cl$ and γ-$Cu_2(OH)_3Cl$, and may be really the same as that accepted at the beginning.

(4) [Ni_3Cl] vibrational modes in the FP_2 region

In this region of the Raman spectrum, 6 Raman ($2A_g$+$2B_{1g}$+B_{2g}+B_{3g}) bands are expected to appear according to the FGA. Because till now nobody can prepare the atacamite structural β-$Ni_2(OH)_3Br$, the **Cl/Br halogen anion substitution method** can not be used here. Fortunately the remaining spectral part (<200 cm^{-1}) may include only [Ni_3Cl] vibrational modes and have a clear band distribution.

From Fig. 3.3.5 (d), three strong (188.2/188.5, 172.2/171.5 and 141.8/141.7 cm^{-1}) and three weak bands are observed, nearly unaffected by the H/D, in accordance with the prediction in the aspect of the band number. After comparing the band structural property with β-$Cu_2(OH)_3Cl$ (Fig. 3.3.6 (d)), α-$Cu_2(OH)_3Cl$ (Fig. 3.3.7 (a)) and γ-$Cu_2(OH)_3Cl$ (Fig. 3.3.7 (b)), one can see that it still behaviors like β-$Cu_2(OH)_3Cl$, other than the latter two, although the highest frequency of the 188.2 cm^{-1} band is much higher than β-$Cu_2(OH)_3Cl$.

The highest frequency band 188.2/188.5 cm^{-1} band can be safely assigned to the [Ni_3Cl] stretching mode, therefore one can deduced a reasonable effective k[Ni_3Cl] to be about **0.74 mdyn/Å** with the mass m_{Cl}=35.45 for β-$Ni_2(OH)_3Cl$, which is relatively high, but still very

consistent with that of other chloride materials.[212]

From the above mentioned analysis, we can still adopt the atacamite structure for β-$Ni_2(OH)_3Cl$, and its IR data are collected in TABLE B3 together with β-$Cu_2(OH)_3Cl$ in Appendix B, where Raman data are those measured using P_L=3 mW in vacuum at 295 K for the sake of future comparison with the low-T data. It should be also noted that those Raman data must slightly differentiate data presented here, radically because of the LLH effect, as seen from Fig. 3.3.8 showing the Raman spectra at the RT experimental conditions with P_L=2, 20 and 35 mW in air.

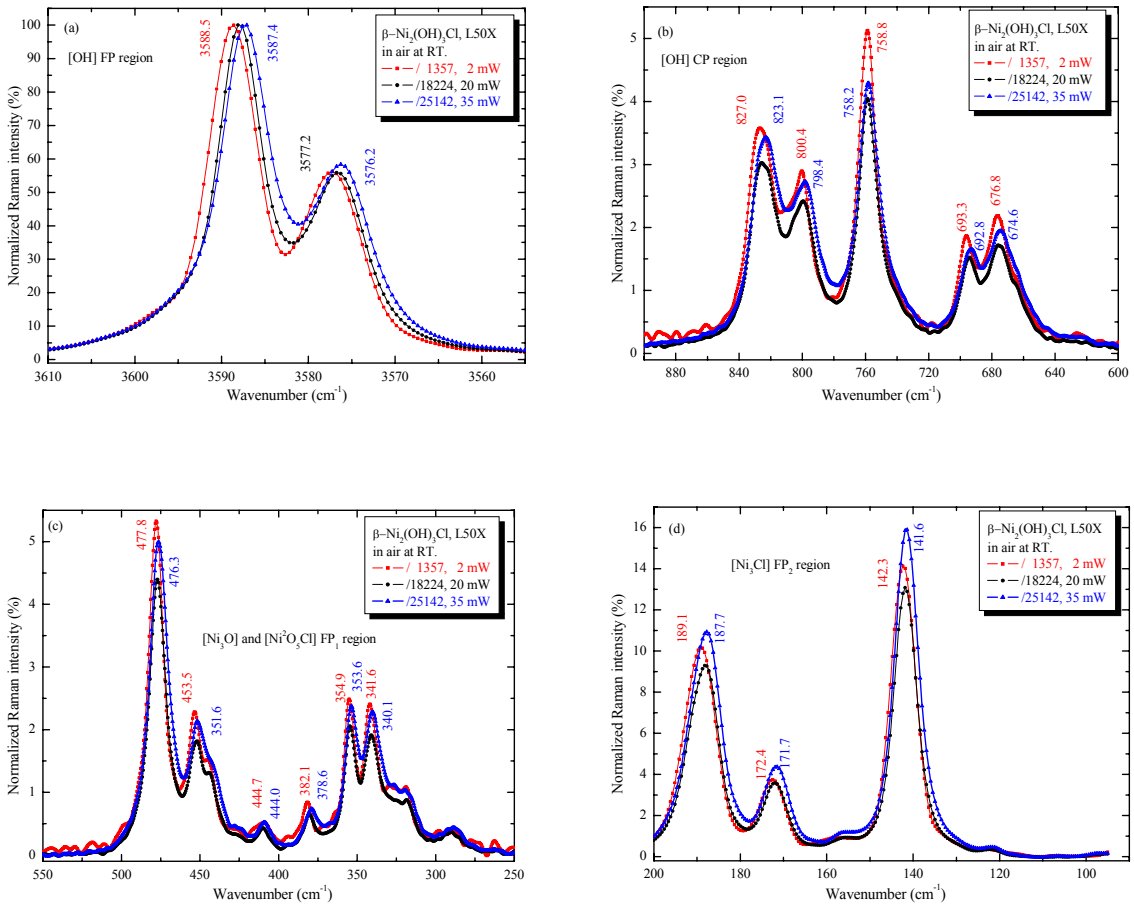

Fig. 3.3.8. Enlarged (a) [OH] FG, (b) [OH] CP, and (c) FP_1 and (d) FP_2 regions of Raman spectra of β-$Cu_2(OH)_3Cl$ at P_L=2, 20 and 35 mW in air at RT, respectively.

From Fig. 3.3.8, one can see that the LLH effect is apparent. Further more, from this P_L–dependent LLH effect at RT Raman experiment, one can predict the low T (near RT) behavior, e.g., the temperature coefficients $\Omega \equiv d\omega/dT$ are normally negative (redshifting when T or P_L increases) for most of the Raman normal modes, which accords with the lattice NT rule for the normal materials.

3.4 RT spectral analysis of the C_{2h}^5 (No. 14) γ-$Cu_2(OH/D)_3Cl$

Only one class of samples γ-$Cu_2(OH/D)_3Cl$ with space group C_{2h}^5 (No. 14) are successfully prepared, and their IR and Raman spectra are measured in air at RT and analyzed by the standard FGA method.

Figs. 3.4.1 (a) and (b) show the whole IR (4000~400 cm^{-1}) and Raman (4000~400 cm^{-1}, P_L=10 mW) spectra of γ-$Cu_2(OH/D)_3Cl$, and Figs. 3.4.1 (c)~(f) show the enlarged [OH/D] FG, [OH/D] CP, [Cu_3O] FP_1 and [Cu_3Cl] FP_2 regions, respectively.

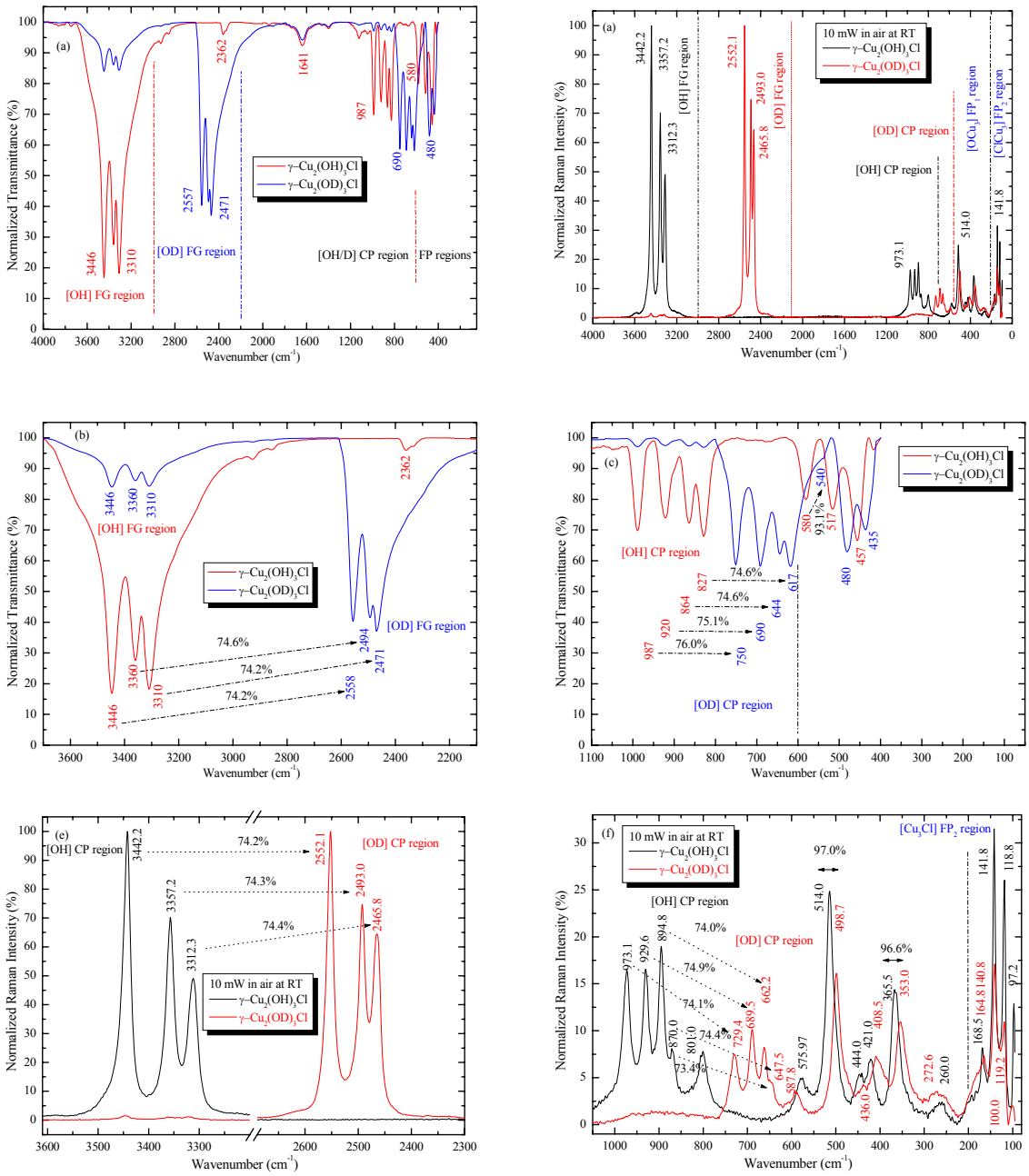

Fig. 3.4.1 the whole IR (a) spectra, Raman (P_L=10 mW) (b) spectra, the enlarged IR [OH/D] FG (c) and other (d) regions, Raman [OH/D] FG (e) and other (f) regions of γ-$Cu_2(OH/D)_3Cl$ respectively.

From Fig. 3.4.1(a) and (b), one can see that the four kinds of IR and Raman spectral regions are really well separated to make the assignment convenient. Because useful spectral bands in all regions are still located in a too narrow range, and the maximum intensities of the Raman bands in the CP and FP regions are only about 30 % of those in the respective FG regions, I enlarge them in Fig. 3.4.1 (c) ~ (f), respectively.

(1) **[OH/D] stretching modes in the FG region**

In this region, three main bands are expected to appear in IR and Raman spectra, respectively, according to the fact that there are three crystallographic non-equivalent [OH/D] FPs although till now I can not predict exactly how many bands of predicted IR ($9A_u$+$9B_u$) and Raman ($9A_g$+$9B_g$) [OH/D] related bands of γ-$Cu_2(OH/D)_3Cl$ will appear in these FG regions because of its low symmetry.

From Fig.3.4.1 (c) and (e) one can see clearly three IR main bands (3446/2557, 3360/2494 and 3310/2471 cm^{-1}) and three Raman bands (3442.2/2552.1, 3357.2/2493.0 and 3312.3/2465.8 cm^{-1}) with peak separations of several tens cm^{-1} in these FG regions. From the fact that all redshift ratios are close to the theoretical prediction 72.8%, these modes can be safely assigned to [O**H/D**] stretching modes in the non-FGA language corresponding to $d_3(O^3H^3/D^3)$≈0.871 **Å**, $d_2(O^2H^2/D^2)$ ≈1.035 **Å** and $d_1(O^1H^1/D^1)$ ≈1.047 **Å** respectively. The three Raman main band data agree with those of Ref. [59] very well.

From these main band data, the force constants can be derived to be $k_3(O^3H^3/D^3)$≈7.41 mdyn/Å, $k_2(O^2H^2/D^2)$ ≈7.05 mdyn/Å and $k_1(O^1H^1/D^1)$≈ 6.86 mdyn/Å for both γ-$Cu_2(OH)_3Cl$ and γ-$Cu_2(OD)_3Cl$ according to Eqn. (1.4.4).

(2) [OH/D] bending modes in the CP regions

In this region, about four to six main bands (bending vibration modes) may be expected to appear in IR and Raman spectra, respectively, according to the fact that there are four to six apparently different *d*(CuO), see TABLE A3 in the Appendix A. Also till now I can not predict exactly how many bands of predicted IR ($9A_u$+$9B_u$) and Raman ($9A_g$+$9B_g$) [OH/D] related bands of γ-$Cu_2(OH/D)_3Cl$ will appear in this FG region because of its low symmetry.

From Fig. 3.4.1 (d) and (f), as expected, four IR bands (987/750, 920/690, 864/644 and 827/617 cm^{-1}) and four Raman bands (973.1/729.4, 929.6/689.5, 894.8/662.2 and 801.0/587.8 cm^{-1}) appear in the [OH/D] CP regions. From the fact that all redshift ratios are close to the theoretical prediction 72.8%, these bands are reasonably assigned to IR and Raman [OH/D] bending vibration modes. This identification of the lowest frequency [OH/D] bending modes and the 600-500 cm^{-1} wide window between [OH] CP and [Cu_3O] FP_1 regions is very important for the assignment of [Cu_3O] FP_1 regions.

(3) [Cu_3O] vibrational modes in the FP_1 region

In this region, 18 IR ($9A_u$+$9B_u$) and 18 Raman ($9A_g$+$9B_g$) bands are expected to appear according to the FGA in IR and Raman, respectively. Limited by the IR measurement range (>400 cm^{-1}), IR 580/480, 517/435, 457/--- and 416/--- cm^{-1} bands can be assigned to the [Cu_3O] modes, and five Raman main bands 514.0/498.7, 444.0/436.0, 421.0/408.5, 365.5/353.0 and 260.0/272.6 cm^{-1} may be designated to the [Cu_3O] stretching and deformation modes. Here the slight redshift phenomenon of all [Cu_3O] bands for γ-$Cu_2(OD)_3Cl$ just demonstrates that in [Cu_3O] vibration modes, as abovementioned, O is in fact moving along with H/D as a whole group [OH/D], and the effective atomic weight of O is in fact 17/18 for [Cu_3O] vibrations.

Furthermore, according to the highest IR and Raman band frequencies 580/540 and 514.0/498.7 cm^{-1}, one can deduce the effective k[Cu_3O] to be about 2.65 mdyn/Å for both γ-$Cu_2(OH)_3Cl$ and γ-$Cu_2(OD)_3Cl$, with the effective m_O=16+1 for γ-$Cu_2(OH)_3Cl$ and 16+2 for γ-$Cu_2(OD)_3Cl$, respectively. While most of the redshift ratios in this region agree well with the theoretical value 97.2%.

As to the small Raman 577.0 cm^{-1} band, I can not give out its true origin till now, and hope someone can build a connection between it and some magnetic features in future.

As to the weak and wide 238.5/236.5 cm^{-1} Raman band, which is almost same as the 230 cm^{-1} one in Herbersmithite $ZnCu_3(OH)_6Cl_2$, [148] we also agree the idea given by D. Wulferding *et al* that the Fano line shape may originate from the coupling of the corresponding phonon to a continuum of magnetic excitation states. [133] As its energy range is within the energy range of spin fluctuations, and the compound is an insulator the corresponding continuum is attributed to magnetic fluctuations.

(4) [Cu_3Cl] vibrational modes in the FP_2 region

In this region, 6 Raman ($3A_g$+$3B_g$) bands are expected to appear according to the FGA in Raman spectra. Because till now nobody can prepare the γ-$Cu_2(OH/D)_3Br$, the **Cl/Br halogen anion substitution method** can not be used here. Fortunately the remaining spectral part (<200 cm^{-1}) may include only [Cu_3Cl] vibrational modes because of relatively large distances d(Cu-Cl) (>2.75 **Å, while for** $Co_2(OH)_3Cl/Br$, d(Co-Cl/Br)≈2.60/2.70 **Å**).

Although the highest band frequency is 168.5/164.8 cm^{-1}, considering that it has a weak intensity and an irregular lineshape accompanied with relatively large distances d(Cu-Cl) as just mentioned and stronger trimeric H-bonds, I strongly suggest the 141.8/140.8 cm^{-1} band to be the [Cu_3Cl] stretching mode. Here one can deduced the effective k[Cu_3Cl] to be about **0.42 mdyn/Å**, with the mass m_{Cl}=35.45, for both γ-$Cu_2(OH/D)_3Cl$ which is very consistent with that of other chloride materials.[42]

As to the above-mentioned 168.5/164.8 cm^{-1} band, I can not give the origin till now. For other bands besides the 141.8/140.8, 118.8/119.2 and 97.2/100.0 cm^{-1} bands, they may appear in the part below 95 cm^{-1}.

IR data of γ-$Cu_2(OH)_3Cl$ are collected in TABLE B3 in Appendix B, where Raman data are those measured using P_L=2 mW in vacuum at 295 K for the sake of future comparison with the low-T data. It should be also noted that those Raman data must slightly differentiate data presented here, radically because of the LLH effect, as seen from Fig. 3.4.2 showing the Raman spectra at the RT experimental conditions with P_L=2, 10 and 20 mW in air.

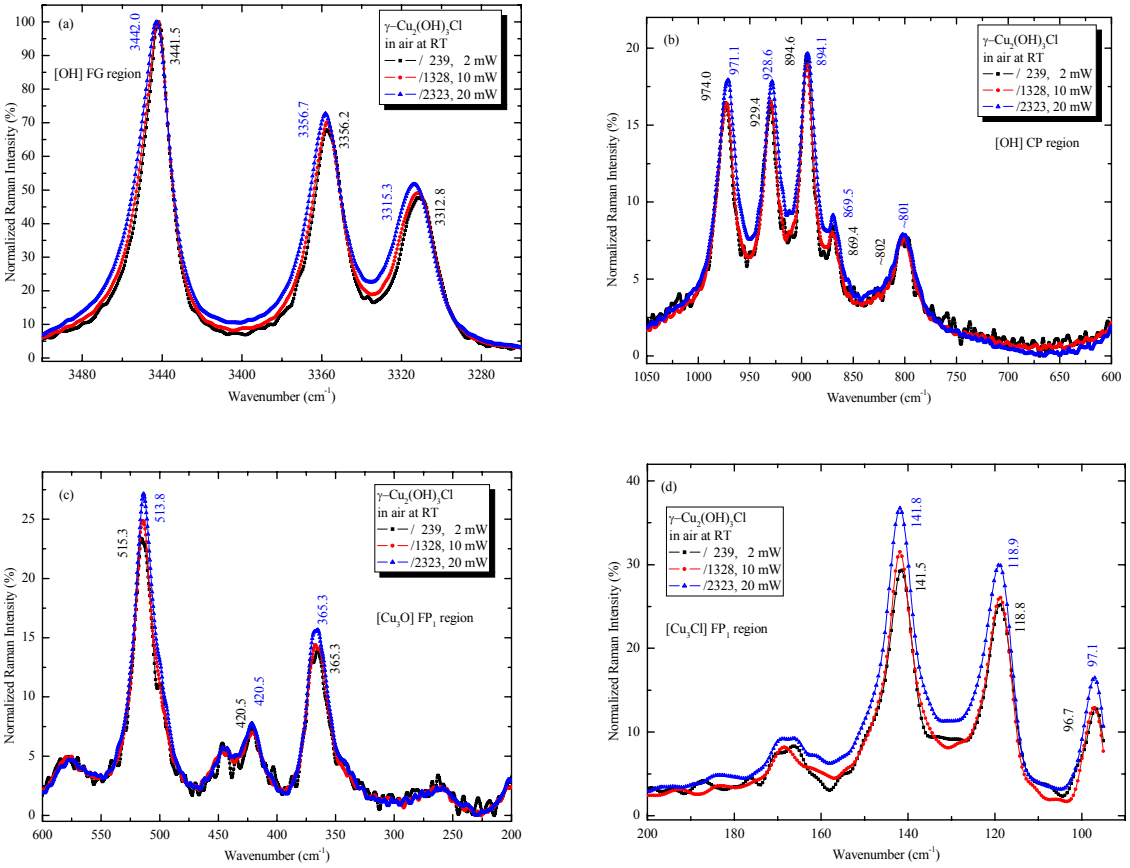

Fig. 3.4.2. Enlarged (a) [OH] FG, (b) the [OH] CP, and (c) [Cu_3O] FP_1 and [Cu_3Cl] FP_2 regions of Raman spectra of γ-$Cu_2(OH)_3Cl$ at P_L=5, 10 and 20 mW, respectively.

From Fig.3.4.2, one can see that the LLH effect on the Raman spectroscopy is apparent. Further more, from this P_L–dependent LLH effect at RT Raman experiment, one can share in the profits of predicting the low T behavior when the sample is cooled down whatever the constant P_L is. Here we can obtain that the temperature coefficients $d\omega/dT$ are abnormally positive (blueshifting when T or P_L increases) for most of the Raman normal modes at least around RT, which is in contrast with the lattice thermal expansion rule for the normal materials accords, but accords with the common phenomena occurred in the materials with relative strong H-bonds.

3.5 RT Spectral analysis of the C_{2h}^2 (No. 11) $M_2(OH/D)_3X$

According to the result of the standard FGA method in Sect. 2.5, the IR and Raman normal modes are presented by:

$$\Gamma_{11}^{IR} = 12A_u + 15B_u \text{ and } \Gamma_{11}^{R} = 14A_g + 10B_g$$

Our samples with space group C_{2h}^2 ($P2_1/m$, No.11) are α-$Cu_2(OH)_3Cl$, α-$Cu_2(OH/D)_3Br$ and α-$Ni_2(OH/D)_3Br$, which are prepared by the normal hydrothermal reaction.[109, 121] The their RT crystal structure parameters are collected in Appendix A2 for helping the spectral analysis. It is very pity that the IR and Raman spectra of α-$Cu_2(OD)_3Cl$ were not presented here because it was not so stable. Fortunately, according to the previous experience, the [OH] FG and CP regions of α-$Cu_2(OH)_3Cl$ can be still determined without help of α-$Cu_2(OD)_3Cl$.

3.5.1 RT Spectral analysis of α-$Cu_2(OH)_3Cl$

Without the IR and Raman spectra of α-$Cu_2(OD)_3Cl$, I show those of α-$Cu_2(OH)_3Cl$ in Figs. 3.5.1 and 3.5.2 respectively, together with those of α-$Cu_2(OH)_3Br$ to perform the comparative analysis. From them one can see that the four kinds of IR and Raman spectral regions are really well separated to make the assignment convenient. Here Raman data using the L50X objective are slightly different from those reported in [] using the 100X objective.

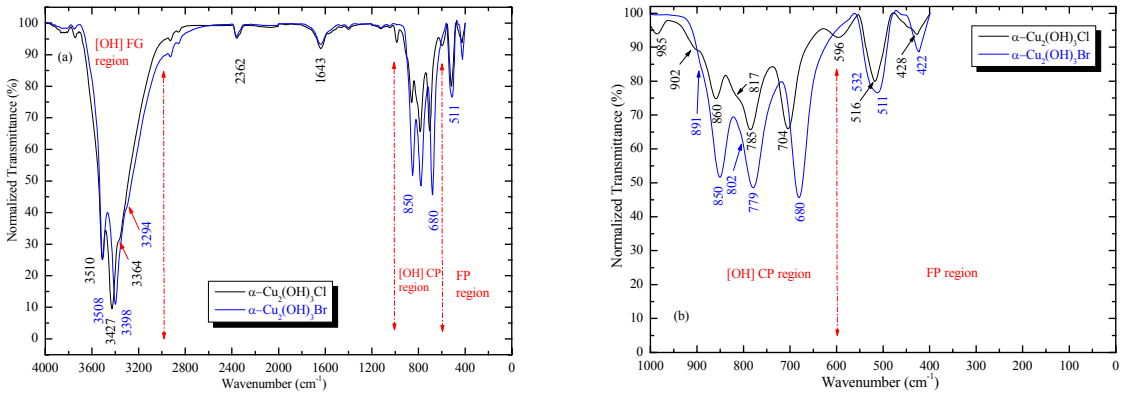

Fig. 3.5.1 (a) Whole IR spectra and (b) their enlarged [OH] CP and FP regions of α-$Cu_2(OH)_3Cl$ and α-$Cu_2(OH)_3Br$.

(1) **[OH] stretching modes in the FG region**

In this region, 2 main bands are expected to appear in IR and Raman spectra, respectively, according to the fact that there are 2 crystallographic non-equivalent [OH] FPs although till now I can not predict exactly how many bands of predicted IR ($4A_u$+$5B_u$) and Raman ($5A_g$+$4B_g$) [OH] related bands will appear in these FG regions because of the low symmetry.

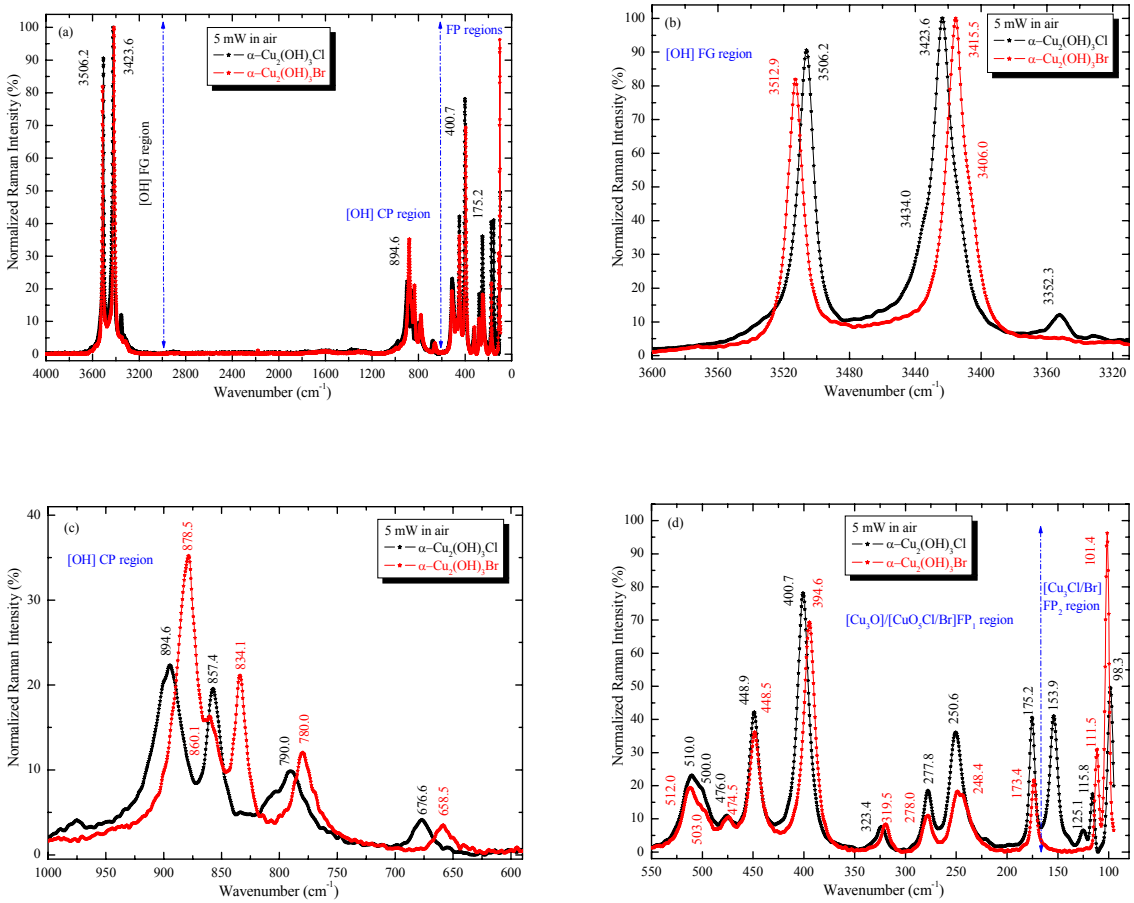

Fig. 3.5.2. (a) Whole Raman spectra and enlarged (b) [OH] FG, (c) [OH] CP, and (d) FP regions of α-$Cu_2(OH)_3Cl$ and α-$Cu_2(OH)_3Br$.

From Fig. 3.5.1 (a) and 3.5.2 (b) one can see clearly two IR main bands (3510 and 3427 cm^{-1}) and two Raman bands (3506.2 and 3423.6 cm^{-1} with a shoulder band 3434.0 cm^{-1}) with both peak separations of about 83 cm^{-1} in these FG regions. From the peak separation data, the higher bands can be safely assigned to [$O^1\mathbf{H}^1$] stretching modes in the non-FGA language and $d(O^1H^1)$ may be about 0.008 **Å** larger than $d(O^2H^2)$. The more complex spectral structure of lower bands agrees with the fact that the number of [$O^2\mathbf{H}^2$] groups is two times of that of [$O^1\mathbf{H}^1$] groups.

From these main band data, the force constants can be derived to be $k(O^1H^1)\approx 7.2$ mdyn/Å and $k(O^2H^2)\approx 6.9$ mdyn/Å for α-$Cu_2(OH)_3Cl$ according to Eqn. (1.4.4).

(2) [OH] bending modes in the CP regions

In this region, about three to six main bands (bending vibration modes) may be expected to appear in IR and Raman spectra, respectively, according to the fact that there are five different d(CuO), see TABLE A4 in the Appendix A. Also till now I can not predict exactly how many bands of α-$Cu_2(OH)_3Cl$ will appear in this FG region because of its low symmetry.

Through comparing the spectra of α-$Cu_2(OH)_3Cl$ with α-$Cu_2(OH)_3Br$, the IR 985/596 cm^{-1} and Raman 975.0 cm^{-1} bands can safely not be considered as normal modes because of the unstability of α-$Cu_2(OH)_3Cl$. Therefore from Figs. 3.5.1 (b) and 3.5.2 (c), as expected, five IR bands (902, 860, 817, 785 and 704 cm^{-1}) and five Raman main bands (894.6, 857.4, 790.0 and 676.6 cm^{-1}) appear in the [OH] CP regions. This identification of the lowest frequency [OH] bending modes (IR 704 cm^{-1} and Raman 676.6 cm^{-1}) and the 650-550 cm^{-1} wide window between [OH] CP and FP regions is very important for the assignment of FP_1 region.

(3) [Cu_3O]/[Cu^1O_5Cl]/[Cu^2O_4Cl] vibrational modes in the FP_1 region

In this region, 18 IR ($8A_u$+$10B_u$) bands caused by [$Cu_3O^{1,2}$]/[Cu^1O_5Cl]/[Cu^2O_4Cl] and 13 Raman ($7A_g$+$6B_g$) bands caused by [$Cu_3O^{1,2}$]/[Cu^1O_5Cl] are expected to appear according to the FGA in IR and Raman, respectively. Considering the long distances d($Cu^{1,2}$-Cl) and large mass m_{Cl}, one can neglect the effect of Cl (and therefore Br in α-$Cu_2(OH)_3Br$) on the mode frequencies, and the Cl/Br-independence suggests that the Raman FP_1 region of [Cu_3O] /[Cu^1O_5Cl] /[Cu^2O_4Cl] vibrational modes extends to 165 cm^{-1}, as shown in Fig. 3.5.2 (d).

Limited by the IR measurement range (>400 cm^{-1}) and large accidental degeneracy, only two IR (516 and 428 cm^{-1}) main bands and seven Raman (510.0, 448.9, 400.7, 323.4, 277.8, 250.6 and 175.2 cm^{-1}) main bands are observed, and may be designated to their stretching and deformation modes. In this Raman FP_1 region, the first three (510.0, 448.9 and 400.7 cm^{-1}) main bands can be attributed to the stretching modes of [Cu_3O^2], [Cu_3O^1] and [Cu^2O_5Cl], respectively, but I can not give further one-to-one mode assignment to distinguish other [Cu^2O_5Cl] modes from other [$Cu_3O^{1,2}$] modes.

Furthermore, according to the Raman [Cu_3O^2] and [Cu_3O^1] band frequencies 510.0 and 448.9 cm^{-1}, one can deduce the effective k[Cu_3O^2] and k[Cu_3O^1] to be about 2.64 and 2.04 mdyn/Å, respectively.

At first glance, the 175.2 cm^{-1} band may possibly assigned to some kind of lattice mode, for instance, caused by the relative translation of Cu atoms on two adjacent Kagome skeleton planes *a*-*b*, but this frequency must become apparently smaller in α-$Cu_2(OH)_3Br$ because the effective mass of Cu atom surrounded by Br atoms may increase and the relative distance c=6.064 Å between two planes is larger than c=5.718 Å in α-$Cu_2(OH)_3Cl$.

(4) [Cu_3Cl] vibrational modes in the FP_2 region

In this **FP_2** region, 3 Raman ($2A_g$+B_g) bands are expected to appear according to the FGA in Raman spectra. Thanks to the Cl/Br halogen anion substitution method (redshift ratio 66.6% provided with the same force constant k), as shown in Fig. 3.5.2 (d) (<165 cm^{-1}), the 153.9, 1115.8 and 98.3 cm^{-1} bands can be assigned to [Cu_3Cl] vibrational modes and the

highest one is the [Cu_3Cl] stretching mode (A_g). Without consideration of the effect of the trimeric H-bond, one can deduced the effective k[Cu_3Cl] to be about 0.50 mdyn/Å, with the mass m_{Cl}=35.45, which is very consistent with that of other chloride materials.[42]

IR data of α-$Cu_2(OH)_3Cl$ are collected in TABLE B4 in Appendix B, where Raman data are those measured using P_L=5 mW in vacuum at 295 K for the sake of future comparison with the low-T data. It should be also noted that those Raman data must slightly differentiate data presented here, radically because of the LLH effect, as seen from Fig. 3.5.2 showing the Raman spectra at the RT experimental conditions with P_L=2, 10 and 15 mW in air.

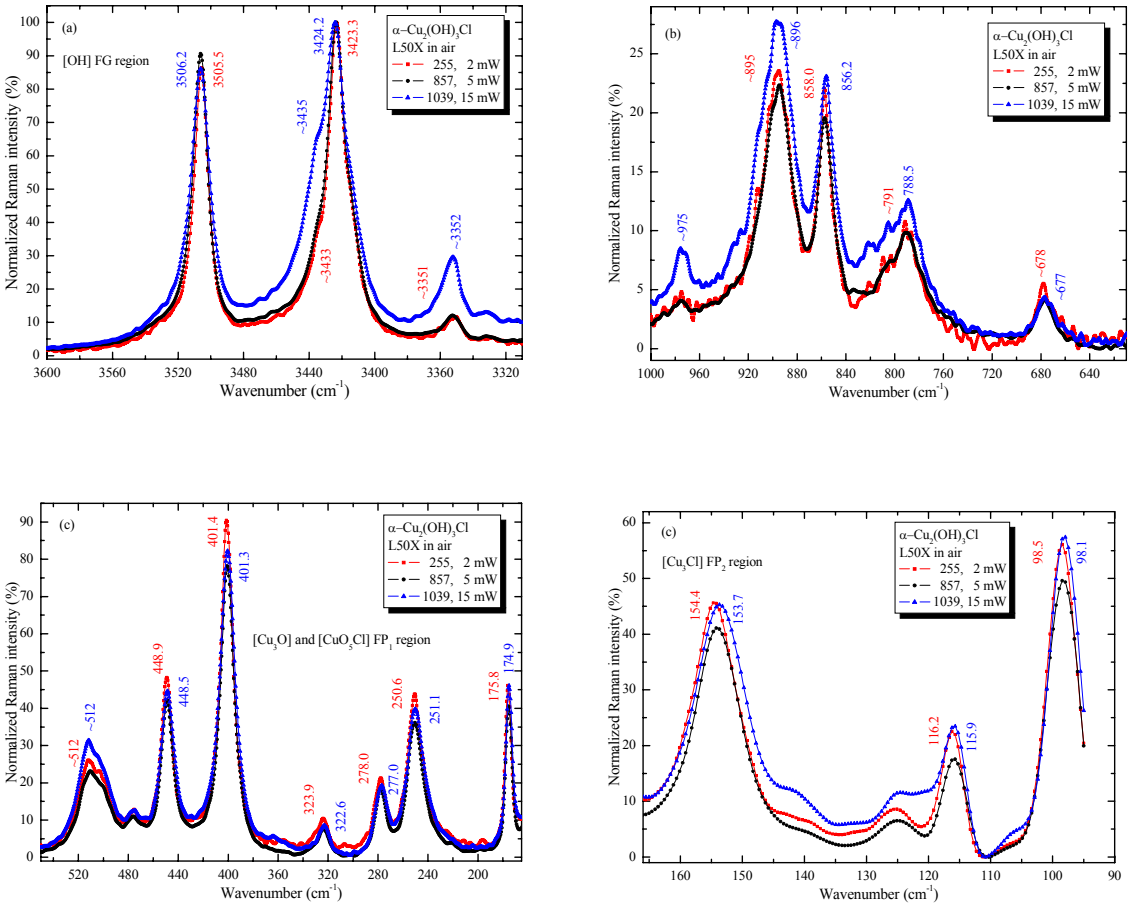

Fig. 3.5.3. Enlarged the (a) [OH] FG, (b) [OH] CP, (c) FP_1 and (d) [Cu_3Cl] FP_2 regions of Raman spectra of α-$Cu_2(OH)_3Cl$ at P_L=5, 10 and 15 mW in air, respectively.

From the P_L–dependent LLH effect as shown in Fig. 3.5.3, one can obtain that the temperature coefficients $d\omega/dT$ of the [OH] modes are abnormally positive (blueshifting when T or P_L increases) for most of the Raman normal modes at least around RT, which is in contrast with the lattice thermal expansion rule for the normal materials, but accords with the common phenomena occurred in the materials with relative strong H-bonds.

3.5.2 Spectral analysis of α-$Cu_2(OH/D)_3Br$

The IR and Raman spectra of α-$Cu_2(OH/D)_3Br$ are shown in Figs. 3.5.4 and 3.5.5.

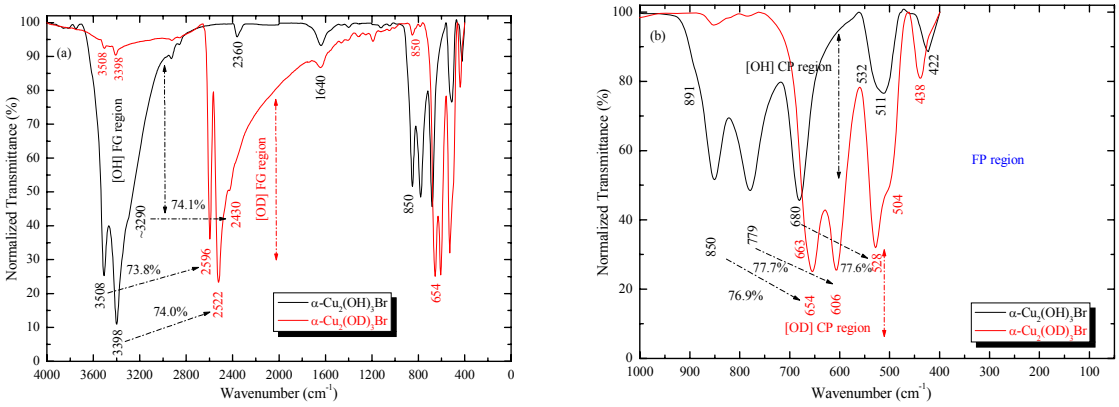

Fig. 3.5.4. The whole IR spectra (a) and the enlarged [OH/D] CP and FP (b) regions of α-$Cu_2(OH/D)_3Br$.

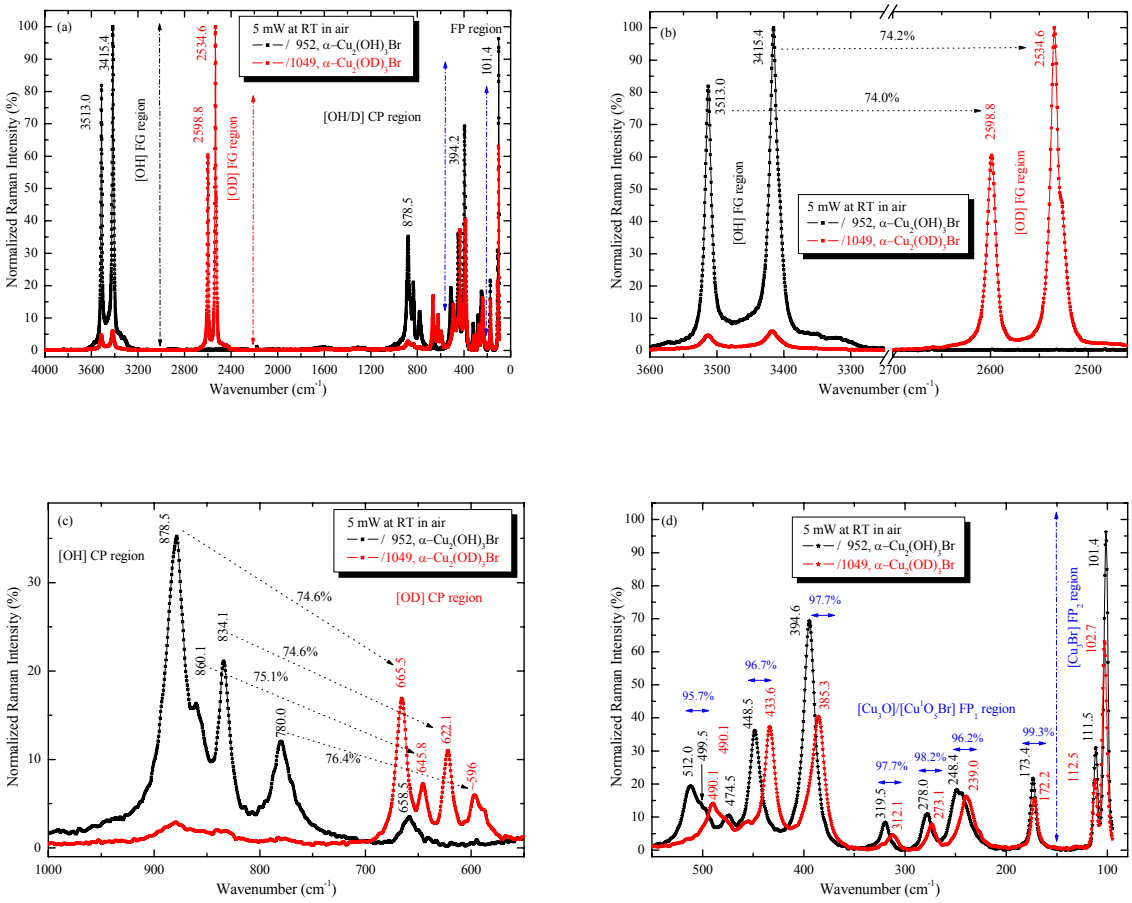

Fig. 3.5.5. The whole Raman spectra (a) and the enlarged [OH/D] FG (b), [OH/D] CP (c) and FP (d) regions of α-$Cu_2(OH/D)_3Br$.

From Fig. 3.5.4 (a), one can see that several small IR bands (i.e., 2360, 1640 cm^{-1}, and others) are situated between the [OH/D] FG and CP regions, which may be considered as bands caused by overtones, residual water in the KBr disk, water and CO_2 in air, or the intrinsic shortage of the background deduction technology, while in Fig. 3.5.5 the appearance of small Raman bands (3513.0, 3415.4 and 880 cm^{-1}) demonstrates that in the α-$Cu_2(OD)_3Br$ sample there are small amount (7~8%) of α-$Cu_2(OH)_3Br$, which was accidentally generated by the washing process of α-$Cu_2(OD)_3Br$ sediment with the H_2O water and never been detected by the neutron scattering experiments.

(1) **[OH/D] stretching modes in the FG region**

In these FG regions, two main bands are expected to appear in IR and Raman spectra, respectively, according to the fact that there are two crystallographic non-equivalent [OH/D] FPs ($d(OH/D^1)$= 0.971 Å and $d(OH/D^2)$ = 0.980 Å) although till now I can not predict exactly how many bands of predicted IR ($4A_u+5B_u$ including CP modes) and Raman ($5A_g+4B_g$ including CP modes) [OH/D] related bands of α-$Cu_2(OH/D)_3Br$ will appear here because of the relatively low symmetry.

In the Figs. 3.5.4 (a) and 3.5.5 (b), from the fact that all redshift ratios are close to the theoretical prediction 72.8%, two IR (3508/2596 and 3398/2522 cm^{-1}) and two Raman (3513.0/2598.8 and 3514.4/2534.6 cm^{-1}) main bands can be safely assigned to the corresponding [O**H/D**] asymmetric and symmetric stretching modes with the large separations (IR 110/74 and Raman 97.6/64.2 cm^{-1}). From the peak separation data, the higher bands can be safely assigned to [$O^1\mathbf{H}^1$] stretching modes in the non-FGA language and $d(O^1H^1)$ may be estimated to be about 0.010 **Å** larger than $d(O^2H^2)$, which is very close to the experimental value 0.009 **Å**. The more complex spectral structure of lower bands with shoulder bands agrees with the fact that the number of [$O^2\mathbf{H}^2$] groups is two times of that of [$O^1\mathbf{H}^1$] groups.

(2) [OH/D] bending modes in the CP regions

In this region, about three to six main bands (bending vibration modes) may be expected to appear in IR and Raman spectra, respectively, according to the fact that there are five different d(CuO), see TABLE A4 in the Appendix A. Also till now I can not predict exactly how many bands of α-$Cu_2(OH/D)_3Br$ will appear in this FG region because of its low symmetry.

From Figs. 3.5.4 (b) and 3.5.5 (c), three IR (850/654, 779/606, and 680/528 cm^{-1}) and five Raman (878.5/655.5, 860.1/645.8, 834.1/622.1, 780.0/596.0 and 658.5/- cm^{-1}) main bands appear in the [OH] CP regions, and their redshift ratios are also close to the theoretical

prediction 72.8%. Therefore, we can still safely assign them to [O**H**] bending vibration modes. Here the unobserved α-$Cu_2(OD)_3Br$ Raman band (about 490 cm^{-1}) corresponding to the 658.5 cm^{-1} band of α-$Cu_2(OH)_3Br$ may be immersed in the FP_1 region. This identification of the lowest frequency [OH] bending modes and the wide window 650-550 cm^{-1} between [OH] CP and FP_1 regions is very important for the assignment of FP_1 regions.

(3) [Cu_3O]/[Cu^1O_5Br]/[Cu^2O_4Br] vibrational modes in the FP_1 region

In this region, 18 IR ($8A_u$+$10B_u$) bands caused by [$Cu_3O^{1,2}$]/[Cu^1O_5Br]/[Cu^2O_4Br] and 13 Raman ($7A_g$+$6B_g$) bands caused by [$Cu_3O^{1,2}$]/[Cu^1O_5Br] are expected to appear according to the FGA in IR and Raman, respectively. Thanks to the Cl/Br halogen anion substitution method, from the Fig. 3.5.2 (d) in the previous section one can determine that the lower bound of this Raman FP_1 region is about 165 cm^{-1}, as shown in Fig. 3.5.5 (d). From Fig. 3.5.5 (d), the slight redshift phenomenon of all bands for α-$Cu_2(OD)_3Br$ just demonstrates that in these vibration modes, as abovementioned, O is in fact moving along with H/D as a whole group [OH/D], and the effective atomic weight of O is in fact 17/18. Here most of the redshift ratios in this region agree well with the theoretical value $(17/18)^{1/2}$=97.2%.

Limited by the IR measurement range (>400 cm^{-1}) and large accidental degeneracy, only two IR (511/504 and 422/438 cm^{-1}) main bands and seven Raman (512.0/490.1, 448.5/433.6, 394.6/385.3, 319.5/312.1, 278.0/273.1, 248.4/239.0 and 173.4/172.2 cm^{-1}) main bands are observed, and may be designated to their stretching and deformation modes. In this Raman FP_1 region, the first three (512.0/490.1, 448.5/433.6 and 394.6/385.3 cm^{-1}) main bands can be attributed to the stretching modes of [Cu_3O^2], [Cu_3O^1] and [Cu^2O_5Br], respectively, but I can not give further one-to-one mode assignment to distinguish other [Cu^2O_5Br] modes from other [$Cu_3O^{1,2}$] modes.

Furthermore, according to the Raman [Cu_3O^2] and [Cu_3O^1] band frequencies, one can deduce the effective k[Cu_3O^2] and k[Cu_3O^1] to be about 2.63 and 2.01 mdyn/Å, respectively.

(4) [Cu_3Br] vibrational modes in the FP_2 region

In this **FP_2** region, 3 Raman ($2A_g$+B_g) bands are expected to appear according to the FGA in Raman spectra. In Fig. 3.5.5 (d) (<165 cm^{-1}), the 111.5/112.5 and 101.1/102.7 cm^{-1} bands can be safely assigned to two [Cu_3Br] vibrational modes and the higher one is the [Cu_3Br] stretching mode (A_g). Here limited by the Raman experimental range, the third mode whose frequency must be less than 90 cm^{-1} is therefore not observed. Using the mass m_{Br}=79.9, one can deduced the effective k[Cu_3Br] to be about 0.58 mdyn/Å, which is slightly larger than k[Cu_3Cl] of α-$Cu_2(OH)_3Cl$.

IR data of α-$Cu_2(OH)_3Br$ are collected in TABLE B4 in Appendix B, where Raman data are those measured using P_L=5 mW in vacuum at 295 K for the sake of future comparison

with the low-T data. It should be also noted that those Raman data must slightly differentiate data presented here, radically because of the LLH effect, as seen from Fig. 3.5.6 showing the Raman spectra at the RT experimental conditions with P_L=2, 5 and 10 mW in air.

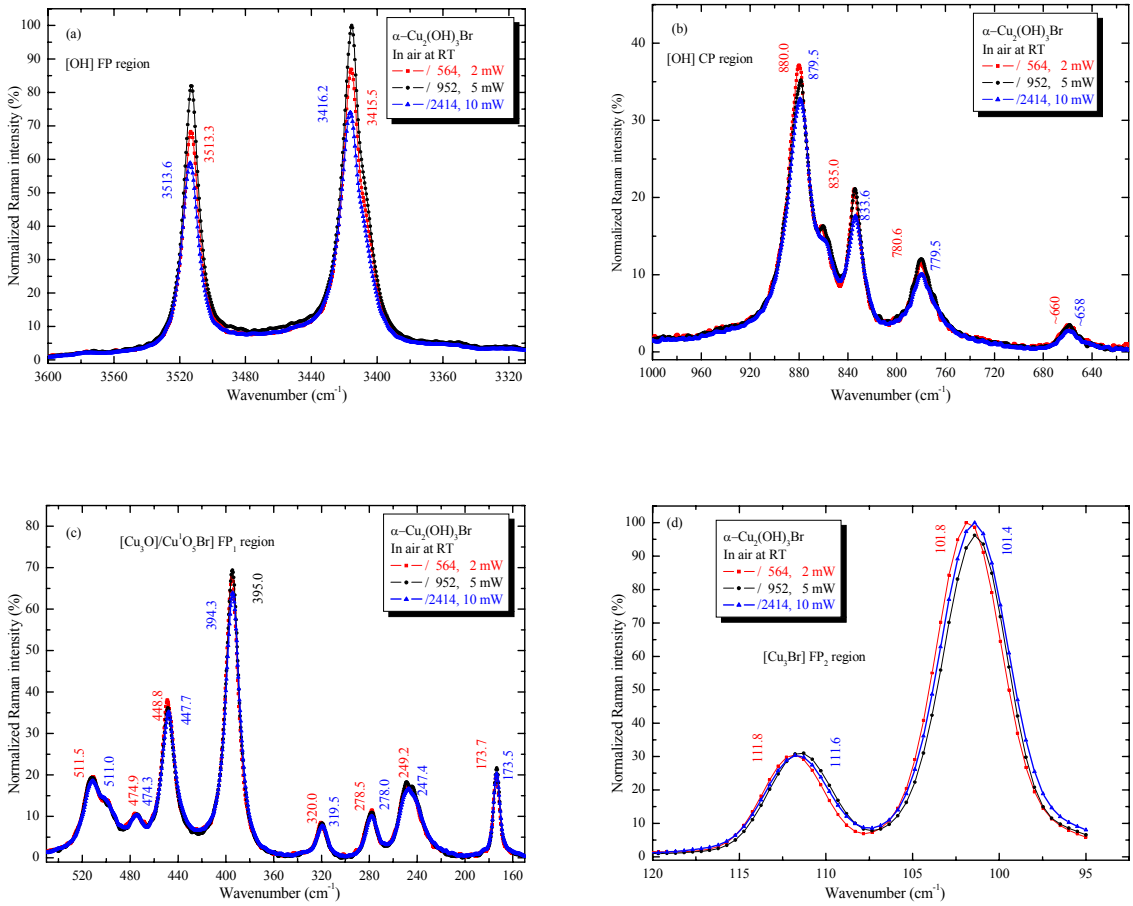

Fig. 3.5.6 Enlarged (a) [OH] FG, (b) [OH] CP, and (c) [Cu_3O]/[Cu^1O_5Br] FP_1 and [Cu_3Br] FP_2 regions of Raman spectra of α-$CU_2(OH)_3Br$ at P_L=2, 5 and 10 mW, respectively.

From Fig. 3.5.6, one can see that the LLH effect on the Raman spectroscopy is not apparent when P_L<10 mW. But from the slightly P_L–dependent LLH effect as shown in Fig. 3.5.6, one can obtain that the temperature coefficients $d\omega/dT$ of the [OH] modes are abnormally positive (blueshifting when T or P_L increases) for most of the Raman normal modes at least around RT, which is in contrast with the lattice thermal expansion rule for the normal materials, but accords with the common phenomena occurred in the materials with relative strong H-bonds.

3.5.3 Spectral analysis of α-$Ni_2(OH/D)_3Br$

The IR and Raman spectra of α-$Ni_2(OH/D)_3Br$ are shown in Figs. 3.5.7 and 3.5.8.

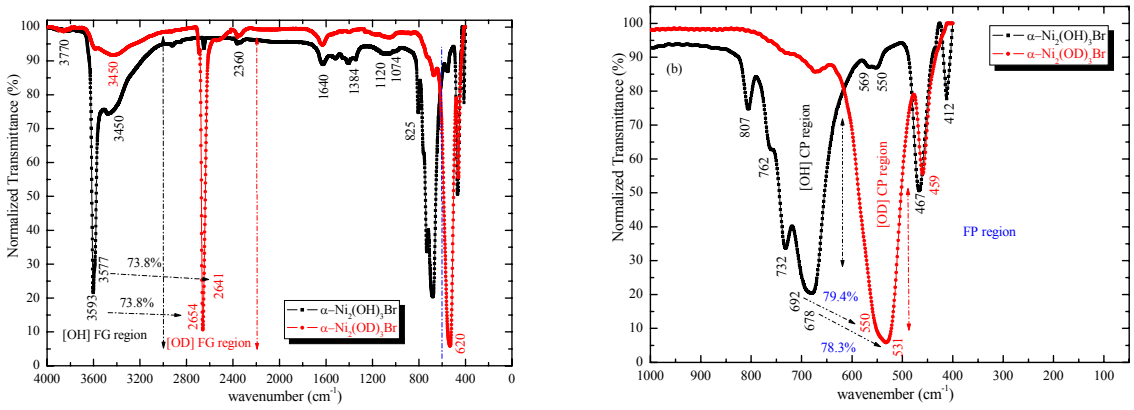

Fig. 3.5.7. The whole IR spectra (a) and the enlarged [OH/D] CP and FP (b) regions of α-$Ni_2(OH/D)_3Br$.

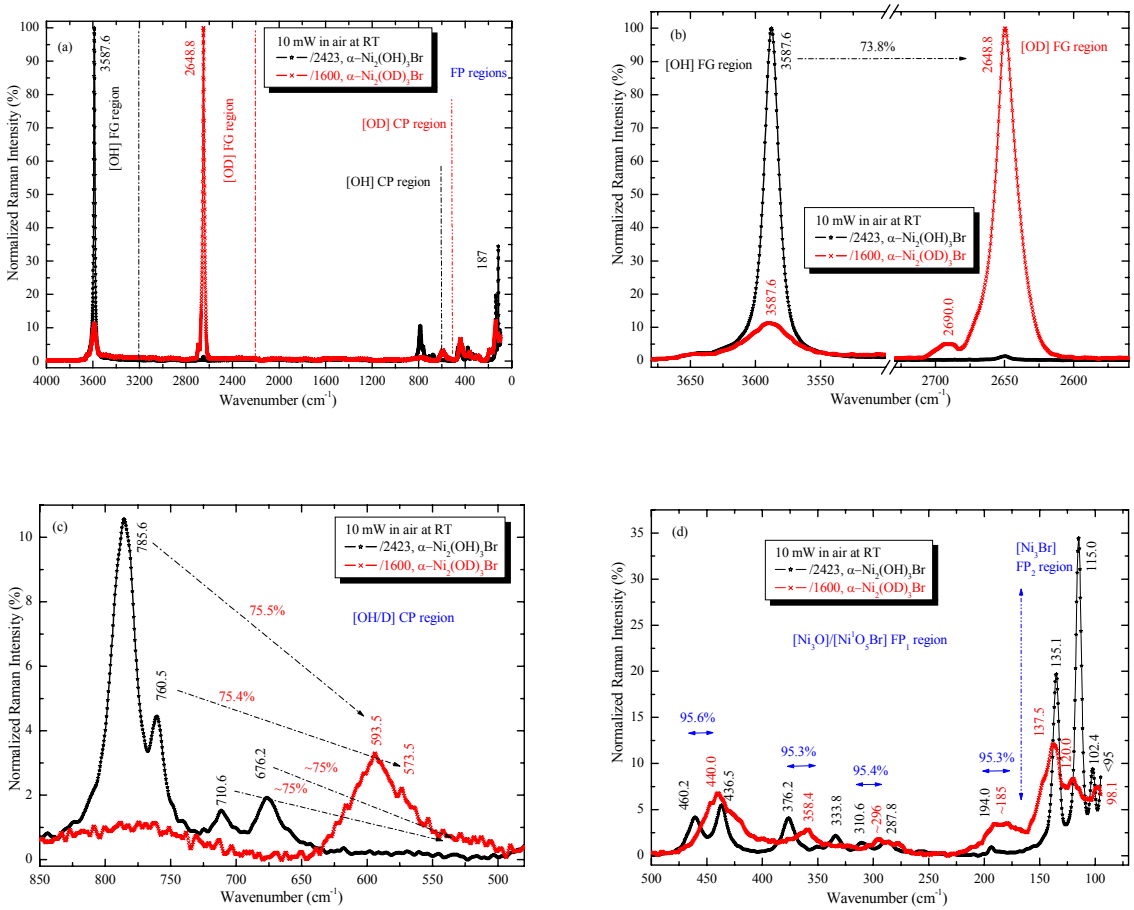

Fig. 3.5.8. The whole Raman spectra (a) and the enlarged [OH/D] FG (b), [OH/D] CP (c) and FP (d) regions of α-$Ni_2(OH/D)_3Br$.

From Fig. 3.5.7 (a), one can see that several small IR bands (i.e., 2360/1640/569/550 cm^{-1} and others) are situated between the [OH/D] FG and CP regions, which may be considered as bands caused by overtones, residual water in the KBr disk, water and CO_2 in air, or the intrinsic shortage of the background deduction technology, while in Fig. 3.5.8 the appearance of small Raman bands (3587.6, 2690.0 and ~780 cm^{-1}) demonstrates that in the α-$Ni_2(OD)_3Br$ sample there are small amount (10%) of α-$Ni_2(OH)_3Br$, which was accidentally generated by the washing process of α-$Ni_2(OD)_3Br$ sediment with the H_2O water and never been detected by the neutron scattering experiments. The IR and Raman spectral lineshapes, especially those in the [OD] CP and FP regions as shown in Figs. 3.5.7 (b) and 3.5.8 (c, d), of the α-$Ni_2(OD)_3Br$ sample indicated that it was badly crystallized.

(1) **[OH/D] stretching modes in the FG region**

In these FG regions, at least two main bands are expected to appear in IR and Raman spectra, respectively, according to the crystal structure experiment that there are two crystallographic non-equivalent [OH/D] FPs ($d(OH/D^1)$= 0.910 Å and $d(OH/D^2)$ = 0.932 Å) like α-$Cu_2(OH)_3Cl$ and α-$Cu_2(OH)_3Br$. From Figs. 3.5.7 (a) and 3.5.8 (b), the fact that all redshift ratios are close to the theoretical prediction 72.8%, two IR (3593/2654 and 3577/2641 cm^{-1}) and one Raman (3587.6/2648.8 cm^{-1}) bands can be safely assigned to the corresponding [O**H/D**] asymmetric and symmetric stretching modes. But from the small IR peak separation (13/12 cm^{-1}) and the Raman one-band structure of this [OH/D] FG region, one can assuredly predict only one crystallographic [OH/D] FP, which **contradicts** the crystal structure simulation in the non-FGA language.

As it has been seen in Sects. 3.2.1 and 3.2.2, even one crystallographic [OH] FP can lead to a double-band structure because of the factor group splitting effect in the $Co_2(OH)_3Cl$ and $Co_2(OH)_3Br$. Therefore the Raman one-band structure of this [OH/D] FG region strongly suggests the refinement of the crystal structure experiment and its data simulation, and the refinement may result in a fact that the α-$Ni_2(OH)_3Br$ belongs to a new space group with a higher symmetry.

This reminds me of comparing its Raman spectrum with that of α-$Cu_2(OH)_3Br$, as shown in Fig. 3.5.9. From Figs. 3.5.9 (a, b), one can also assert categorically that the α-$Ni_2(OH)_3Br$ has a different structure with the α-$Cu_2(OH)_3Br$, and the Raman one-band structure even at very low temperature (see the following Sect. 4.5.3) can deny persistently the accidental degeneracy of two stretching modes of two crystallographic non-equivalent [OH/D] FPs.

From the Raman frequencies 3587.6/2648.8 cm^{-1}, the only force constant can be deduced to be $k(OH/D)$≈7.58 mdyn/Å for α-$Ni_2(OH/D)_3Br$ according to Eqn. (1.4.4).

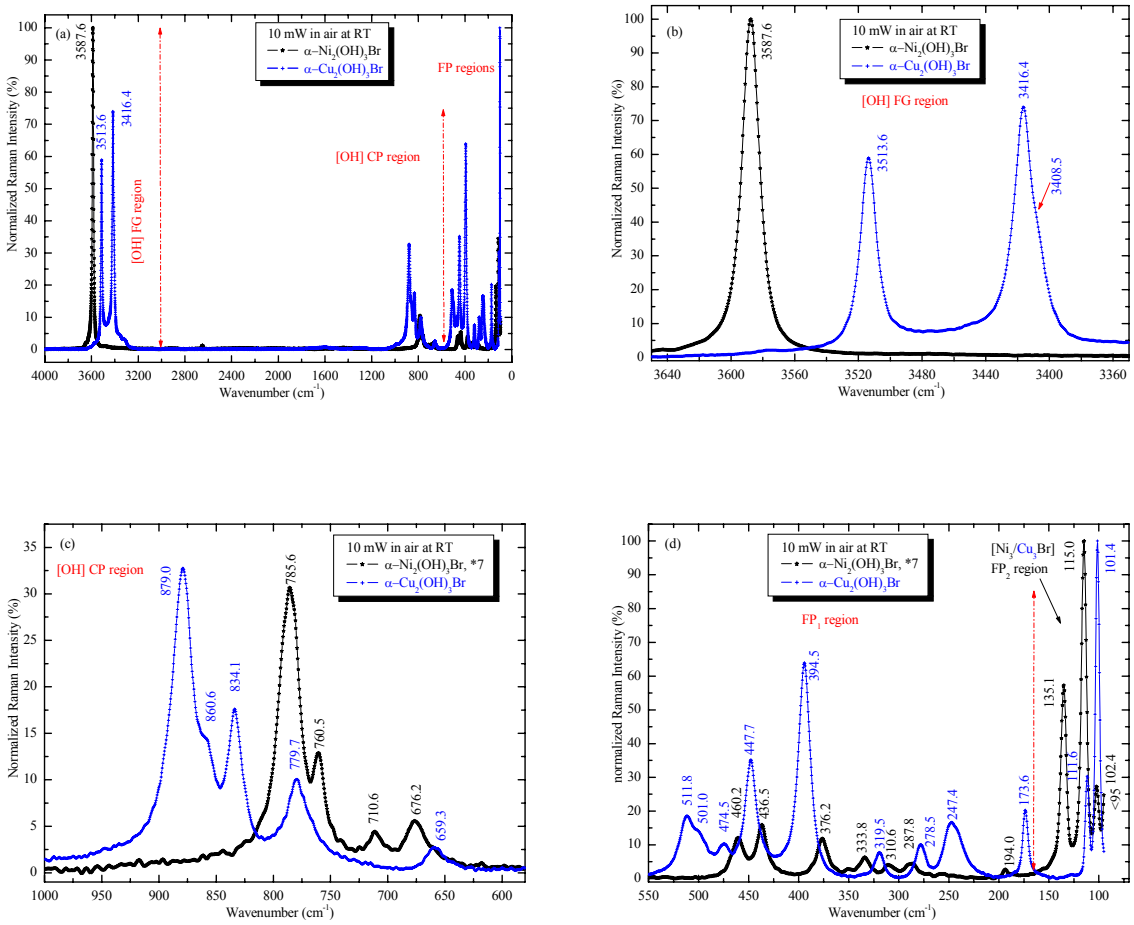

Fig. 3.5.9. The whole Raman spectra (a) and the enlarged [OH] FG (b), [OH] CP (c) and FP (d) regions of α-$Ni_2(OH)_3Br$ and α-$Cu_2(OH)_3Br$.

(2) [OH/D] bending modes in the CP regions

In this region, about three to six main bands (bending vibration modes) may be expected to appear in IR and Raman spectra, respectively, according to the fact that there are five different *d*(NiO), see TABLE A4 in the Appendix A.

From Figs. 3.5.7 (b) and 3.5.8 (c), five IR (807/-, 762/-, 732/-, 692/550 and 678/531 cm^{-1}) and four Raman (785.6/593.5, 760.5/573.5, 710.6/- and 676.2/- cm^{-1}) bands appear in the [OH/D] CP regions, and their redshift ratios are also close to the theoretical prediction 72.8%. Therefore, we can still safely assign them to [O**H**] bending vibration modes. Here the unobserved α-$Ni_2(OD)_3Br$ Raman bands corresponding to the 710.6 and 676.2 cm^{-1} bands of α-$Ni_2(OH)_3Br$ may be immersed in the FP_1 region.

From Figs. 3.5.9 (c), the spectral structure similarity between α-$Ni_2(OH)_3Br$ and α-$Cu_2(OH)_3Br$ is still observed, which suggests strangely their crystal structure similarity.

(3) [Ni_3O]/[Ni^1O_5Br]/[Ni^2O_4Br] vibrational modes in the FP_1 region

In this region, 18 IR ($8A_u+10B_u$) bands caused by [$Ni_3O^{1,2}$]/[Ni^1O_5Br]/[Ni^2O_4Br] and 13 Raman ($7A_g+6B_g$) bands caused by [$Ni_3O^{1,2}$]/[Ni^1O_5Br] are expected to appear according to the FGA in IR and Raman, respectively. Thanks to the Cl/Br halogen anion substitution method, from the Fig. 3.5.2 (d) in the previous section one can determine that the lower bound of this Raman FP_1 region is about 165 cm^{-1}, as shown in Fig. 3.5.8 (d) (or 3.5.9 (d)) . From Fig. 3.5.8 (d), the slight redshift phenomenon of identified bands for α-$Ni_2(OD)_3Br$ just demonstrates that in these vibration modes, as abovementioned, O is in fact moving along with H/D as a whole group [OH/D].

Limited by the IR measurement range (>400 cm^{-1}) and large accidental degeneracy, only two IR (467/459 and 412/- cm^{-1}) main bands and seven Raman (460.2/440.0, 436.5/-, 376.2/358.4, 333.8/-, 310.6/~296, 287.8/- and 194.0/~185 cm^{-1}) main bands are observed, and may be designated to their stretching and deformation modes. In this Raman FP_1 region, the first three (460.2, 436.5 and 376.2 cm^{-1}) main bands can be attributed to the stretching modes of [Ni_3O^2], [Ni_3O^1] and [Ni^1O_5Br], respectively, and one can deduce the effective k[Ni_3O^2] and k[Ni_3O^1] to be about 2.12 and 1.91 mdyn/Å, respectively.

(4) [Ni_3Br] vibrational modes in the FP_2 region

In this **FP_2** region, 3 Raman ($2A_g+B_g$) bands are expected to appear according to the FGA in Raman spectra. In Fig. 3.5.8 (d) (<165 cm^{-1}, or 3.5.9 (d)), the 135.4/137.5, 115.0/120.0 and 102.4/98.1 cm^{-1} bands can be safely assigned to [Ni_3Br] vibrational modes and the highest one is the [Ni_3Br] stretching mode (A_g). Here limited by the Raman experimental range, the fourth band (<95 cm^{-1}) and its origin are therefore not determined. Using the mass m_{Br}=79.9, one can deduced the effective k[Ni_3Br] to be about 0.86 mdyn/Å, which is much larger than that of α-$Cu_2(OH)_3Br$.

IR data of α-$Ni_2(OH)_3Br$ are collected in TABLE B4 in Appendix B, where Raman data are those measured using P_L=10 mW in vacuum at 295 K for the sake of future comparison with the low-T data. It should be also noted that those Raman data must slightly differentiate data presented here, radically because of the LLH effect, as seen from Fig. 3.5.10 showing the Raman spectra at the RT experimental conditions with P_L=2, 10 and 30 mW in air.

From Fig. 3.5.10, one can see that the LLH effect on the Raman spectroscopy is apparent when P_L<30 mW. But from the P_L–dependent LLH effect as shown in Fig. 3.5.10, one can obtain that the temperature coefficients $d\omega/dT$ of the [OH] modes are positive (redshifting when T or P_L increases) for most of the Raman normal modes at least around RT, which is in accordance with the lattice thermal expansion rule for the normal materials with very weak H-bonds.

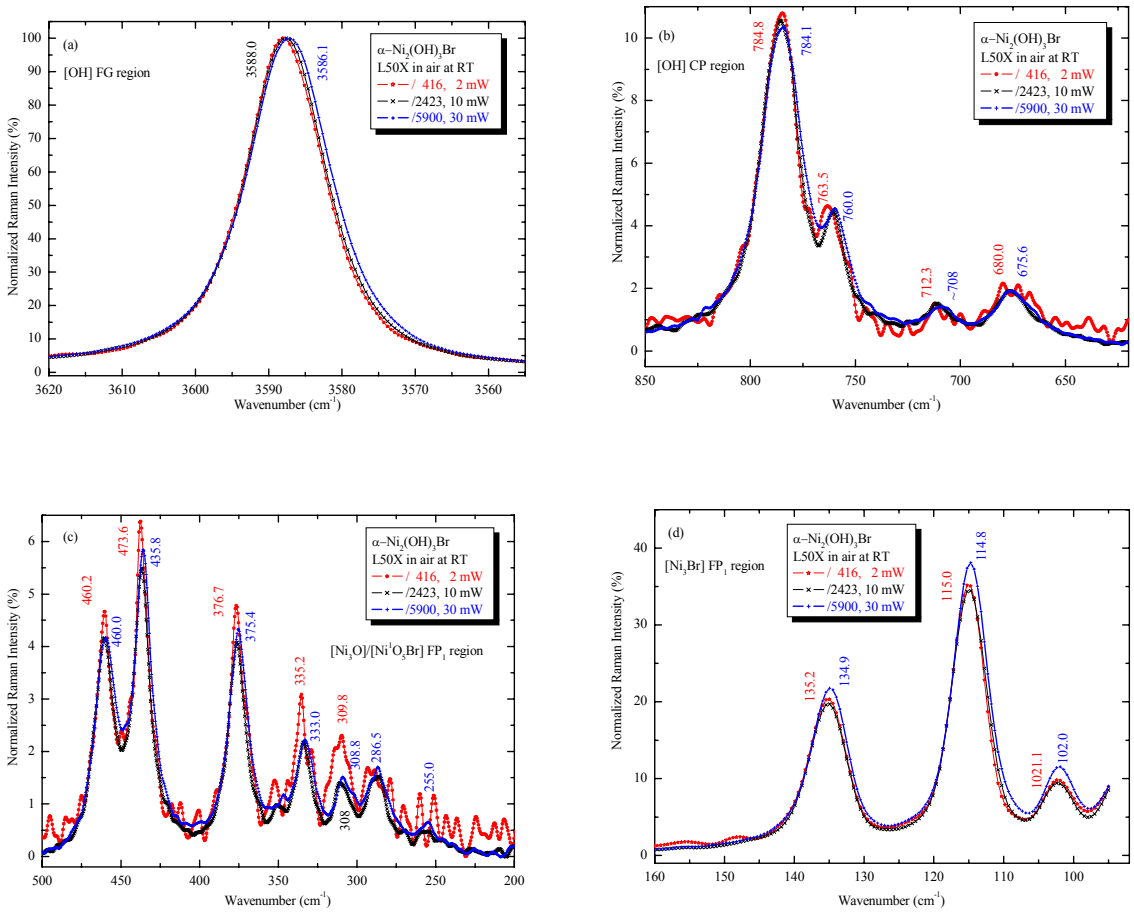

Fig. 3.5.10 Enlarged (a) [OH] FG, (b) [OH] CP, and (c) [Ni_3O]/[Ni^1O_5Br] FP_1 and [Ni_3Br] FP_2 regions of Raman spectra of α-$Ni_2(OH)_3Br$ at P_L=2, 10 and 30 mW, respectively.

3.6 Synthetic RT spectral study on $M_2(OH)_3X$

In this section, the [OH] stretching frequencies of the $M_2(OH)_3X$ in this dissertation will be studied synthetically, associated with discussion on the trimeric H-bond systems called by us. In view of the similarity of reflected physical properties of IR and Raman spectra and those of $M_2(OH)_3X$ and $M_2(OD)_3X$, only Raman spectral data of $M_2(OH)_3X$ are used.

3.6.1 Trimeric hydrogen-bonds

In fact, it is well known in the chemistry, material and spectroscopic communities, most of OH stretching frequencies less than the so-called "free" [OH] stretching frequency ω_v[OH] 3600 cm^{-1} are caused by an H-bond (or say a red-shifted H-bond) which is seldom paid close attention to in the magnetism community (Authors in Refs.[53, 54] simply pointed out that "The Cl is coordinated in a trigonal prismatic arrangement to three H atoms" and it is a "squashed O_3Cl tetrahedron unit"). In general the forming of a typical H-bond like OH···Y (Y is an anion and H-acceptor) should satisfy two conditions: (1) the angle $\theta_{O\text{-}H\text{-}Y}$>90° and (2) the distance $d_{O\cdots Y}$ is near to the sum d^0_{OY} of the common mean O^{2+} radius $R^0_O \approx$ 1.40 Å and Y anion radius R^0_Y. Here for the possible H-acceptors, besides O^{2+}, $R^0_{Cl} \approx$1.81 Å and $R^0_{Br} \approx$1.96 Å. Therefore the second condition becomes $d_{O\cdots O} \approx d^0_{OO}$ = 2.80 Å, $d_{O\cdots Cl} \approx d^0_{OCl}$ = 3.21 Å and $d_{O\cdots Br} \approx d^0_{OBr}$ = 3.36 Å. From the fact that the [OH/D] stretching frequencies vary from the smallest one 3311 cm^{-1} of γ-$Cu_2(OH)_3Cl$ to the largest one 3587 cm^{-1} of α-$Ni_2(OH)_3Br$, we firmly believe that a nonnegligible H-bond exists in each material. To verify this, we have checked the H and X related structural parameters of $M_2(OH)_3X$ and famous $ZnCu_3(OH)_6Cl_2$ as references at different temperatures (mostly at low temperatures because there has no evidence till now that any crystal phase transition occurs down to its corresponding temperature). After we exclude the possible presence of O–H···O (the first condition is not satisfied although the fact that meets the second condition exists), a new kind, to the best of our knowledge, of H-bond [$(OH)_3\cdots M$] (three H donors to one acceptor) and nominate it as the **trimeric** H-bond, which differs completely from the **trifurcated** $(CH_3)\cdots O_3$ H-bond unit (still one H donor to each acceptor), [139] and further confirm the existence of three types of symmetric structures with C_{3v} (in samples of SG No. 166), C_s (in samples of SG Nos. 62 and 11), and C_1 (in the sample of SG No. 14) symmetries, see Figs. 3.6.1 (a~d), respectively.

Further when we check carefully the H^+ positions in the **trimeric** H-bond units, three H^+ ions in samples of Nos. 166, 62 and 14 are found to be located inner the O_3X tetrahedron, while those in samples of No. 11 are all outside. Therefore one can classify each type of **trimeric** H-bond into two subtypes: the so-called H-in subtype (Figs. 3.6.1 a, b and d) and the H-out one (Fig. 3 c).

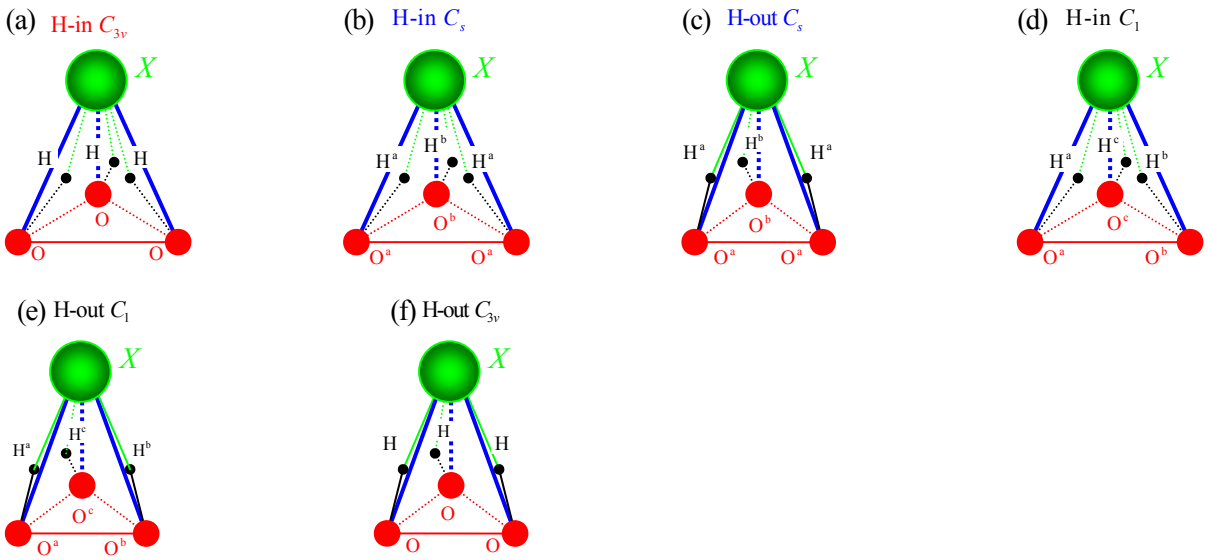

Fig. 3.6.1 Trimeric H-bond schemes of (a) H-in C_{3v}, (b) H-in C_s, (c) H-out C_s, (d) H-in C_{3v} symmetry types found in SG No. 166, 62, 11 and 14 samples, respectively, and predicted (e) H-out C_1, (f) H-out C_{3v} symmetry types.

Consequently, two more subtypes - so-called H-out C_1 and H-out C_{3v} **trimeric** H-bonds are reasonably predicted to exist in some other materials in nature.

3.6.2 On the RT [OH] stretching frequency

The related refined crystal structure parameters, i.e., all the crystallographic distinct distances $d(M_3{\equiv}O)/d(OX)/d(OH)$, and Raman shift data belonging to the $\nu(OH)$ and $\delta(OH)$ are collected in **Table 3.6.1**.

From Table 1 one can see that the distinct $d(OH)$ number is at most three in γ-$Cu_2(OH)_3Cl$ because of the Jahn-Teller effect, and the $d(OH)$ of natural β-$Cu_2(OH)_3Cl$ (Atacamite) is now unavailable because these data should be obtained by its deuterized synthetic sample using the neutron powder diffraction measurement method. Among the $\omega_v(OH)$ values (3546/3528/3575 cm^{-1}) several are assigned to the small Davydov splittings according to the respective available crystal structures, [251-253] and one (3330 cm^{-1} of β-$Cu_2(OH)_3Cl$) may come from the impurity in the natural sample. Except the four values all the $\omega_v(OH)$ values are definitely assigned to respective crystallographic distinct OH group according to the normal concept that the higher $\nu(OH)$ value surely corresponds to the shorter $d(OH)$ regardless of the other part of the hydroxyl system.

From the detail $d(M_3{\equiv}O)$ and $d(OX)$ data one can see most of the MO bonds are strongly covalent for $d(CuO)<2.13$ Å or $d(CoO)<2.145$ Å and at least one typical H-bond appears in each sample for $d(OCl)<3.21$ Å or $d(OBr)<3.36$ Å. Therefore both the M-O bond and the H-bond have exerted influence on the respective OH group and a distance $d(OH)$ ultimately comes into being to correspond to its $\omega_v(OH)$ value. So the reasonably estimated mean distances $D(MO)$ according to $D(MO)=[3(d_1^{-2}+ d_2^{-2}+ d_3^{-2})^{-1}]^{1/2}$ are calculated and listed in

Table 3.6.1 too.

Table 3.6.1 Related crystal parameters and Raman shift data in units of Å and cm^{-1} respectively.

Sample	$d(M_3{\equiv}O)$		$D(MO)$	d(OH)	$d(OX)$	ω_v(OH)	ω_δ(OH)
α-$Cu_2(OH)_3Cl$	$d(Cu_3{\equiv}O^1)$	2.364,1.936,1.936	2.052	0.972	3.315	3507	894,855,
	$d(Cu_3{\equiv}O^{2,3})$	2.013,1.974,2.009	1.999	0.979	3.203	3424	789,673
α-$Cu_2(OH)_3Br$	$d(Cu_3{\equiv}O^1)$	2.345,1.921,1.921	2.039	0.971	3.525	3516	880,834,
	$d(Cu_3{\equiv}O^{2,3})$	2.014,1.986,2.038	2.012	0.980	3.310	3418	781,660.
β-$Co_2(OH)_3Cl$	$d(Co_3{\equiv}O)$	2.079,2.079,2.106	2.088	0.966	3.178	3559 3546[c]	828,652
β-$Co_2(OH)_3Br$	$d(Co_3{\equiv}O)$	2.084,2.084,2.137	2.101	0.969	3.227	3540 3528[c)]	822,652
Natural β-$Cu_2(OH)_3Cl$	$d(Cu_3{\equiv}O^{1,2})$	1.983,2.018,2.032	2.011	(0.987)[b]	3.041	3350 3330[d)]	975,912, 845,820,
	$d(Cu_3{\equiv}O^3)$	1.940,1.940,2.412	2.065	(0.978)[b)]	3.059	3434	592[e)]
β-$Ni_2(OH)_3Cl$	$d(Ni_3{\equiv}O^{1,2})$	2.062,2.038,2.054	2.051	0.952[a)] (0.963)[b)]	3.186	3587	822,795, 758,692,
	$d(Ni_3{\equiv}O^3)$	2.081,2.081,2.090	2.084	0.997 [a)] (0.963)[b)]	3.134	3575 [c)]	673
γ-$Cu_2(OH)_3Cl$	$d(Cu_3{\equiv}O^1)$	2.078,1.947,1.991	2.003	1.032 [a)] (0.991)[b]	3.079	3311	970,927, 892,800,
	$d(Cu_3{\equiv}O^2)$	1.896,2.382,1.960	2.049	1.043 [a)] (0.987)[b)]	3.080	3356	575 [e)]
	$d(Cu_3{\equiv}O^3)$	2.021,1.984,2.047	2.168	0.871 [a)] (0.977)[b)]	2.994	3442	

[a] Value maybe doubtful and incorrect.

[b] Value in parentheses is strongly suggested and need to be confirmed.

[c] Value maybe caused by Davydov splitting effect or by a d(OH) difference of less than 0.002 Å.

[d] Value maybe caused by impurity or by a d(OH) difference of less than 0.002 Å.

[e] Value maybe not the δ(OH) peak although a large d(CuO)=2.412 Å or 2.382 Å exists in its corresponding material.

Fig. 3.6.2 (*a*) and (*b*) show ω_v(OH) *vs* $D(MO)$ and $d(OX)$ at RT, respectively, although it is not strictly reasonable to collect all the data into the same Fig. 3.6.2 (*a*) or Fig. 3.6.2 (*b*) regardless of the difference between Cu^{2+} and Co^{2+} or Cl^- and Br^-. From Fig. 3.6.2 (*a*) and (*b*) one can not find out any simple correlation between the ν(OH) and $D(MO)$ or $d(OX)$ although

it still holds that the shorter $D(MO)$ or $d(OX)$ corresponds to a smaller ω_v(OH) value when the other conditions do not change.

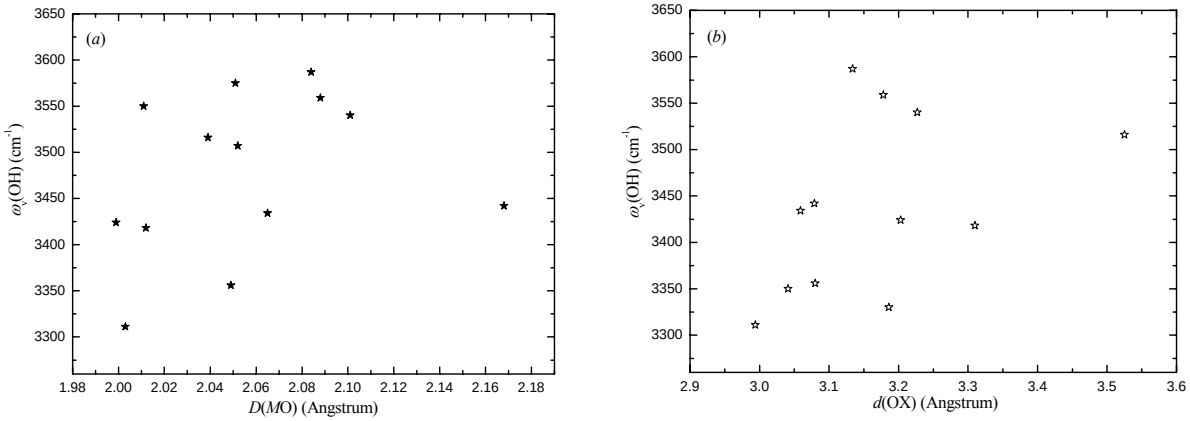

Fig.3.6.2 ω_v(OH) *vs* (a) $D(MO)$ and (b) $d(OX)$.

Like many researchers have done, after ω_v(OH) *vs* d(OH) are plotted into Fig.8, some valuable results can be extracted. Limited to the conditions of the deuterized sample preparation, neutron diffraction measurement and its data analyzing experience, the d(OH) values labeled by triangles are doubtful from the beginning. If one now regards the other experimental data labeled by squares are reasonable, an approximately linear relationship ω_v(OH)=3600-10000(d-0.961) cm^{-1} between ω_v(OH) and d(OH) with the change rate $\rho \equiv \Delta\omega_v(\text{OH})/\Delta d = -10$ cm^{-1}/0.001Å is found in the 270 cm^{-1} difference range of our selected samples to be consistent with the famous relationship $\Delta\omega_v(\text{OH})/\Delta d = -5000\sim12000$ cm^{-1}/Å concluded by Novak. [201]

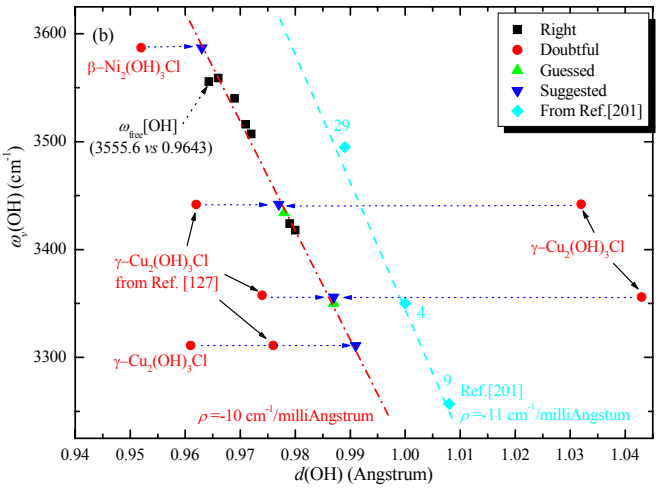

Fig.3.6.3 Selected ω_v(OH) *vs* d(O-H). Among the data symbols, squares ■ are the reasonable experimental data except those of a "free" ν(OH) mode labeled by ν_{free}(OH), balls ● are the d(OH)-doubtful experimental data, reverted triangles ▼ are therefore suggested data to correct the respective star d(OH), and triangles▲ are the guessed data whose wavenumber values are from Raman experiments but d(OH) values are unavailable now.

Till now, one can set up the following questions:

(1) One can guess there are two distinct d(OH) from the crystal parameters and two different ω_v(OH), i.e., and they maybe about 0.978 Å and 0.987 Å respectively, as presented by the black balls in Fig. 3.6.3.

(2) Not like natural β-$Cu_2(OH)_3Cl$ with the same space group of β-$Ni_2(OH)_3Cl$, the latter's ω_v(OH) has only one value 3587 cm^{-1}, and therefore it has at most two approximately equal d(OH) values even the 3575 cm^{-1} peak is thought to be caused by another different d(OH) value. This can be easily understood by the fact that a short D(NiO)= 2.051 Å with a long d(OX) =3.186 Å and a relatively long D(NiO)=2.084 Å with a relatively short d(O*X*) =3.134 Å can reasonably give rise to two approximately equal d(OH) values. Therefore one can correct the two doubtful d(OH)=0.952 Å and 0.997 Å to be 0.963 Å, which needs to be conformed by the future refining experiment, as presented by the triangles top in Fig. 3.6.3.

(3) Similar to (2), one can modifies the other three doubtful d(OH)=1.032/1.043/0.871 Å of γ-$Cu_2(OH)_3Cl$ to be 0.977/0.987/0.991 Å which are consistent with the exact values 0.962/0.974/0.976 Å given by Wills and Henry using the γ-$Cu_2(OD)_3Cl$ at 2K. [77]

(4) When the well-believed true "free" OH stretching fundamental frequency ω_{free}(OH) is selected to be 3555.6 cm^{-1} and bond length d(OH)=0.9643 Å are plotted into Fig. 3.6.3, [213] the data point is almost on the fitting line! This firmly verifies the universality of the monotonous change with an approximate linearity.

From the final data group one can estimate the stretching force constant k(OH) is situated in the range of 6.5~7.6 mdyn/Å for these selected samples.

As to the ω_δ(OH) data in the CP region, they are also of importance to check the more detailed crystal microstructure related to the OH group, because each ω_δ(OH) theoretically corresponds to a special *M*OH···*X* with special d(MO), d(OH), d(H···X) and relative space directions (angles). But from Raman ω_δ(OH) data, one can find that the distinguishable peak number is always less than the number of *M*OH···*X* units because the accidental degeneracy usually occurs to result in the additional complexity and difficulty on the exact assignation to a special unit, just like the situation in the fingerprint region. However the following points manifest the worthiness in studying on the OH related crystal microstructure conformation:

(1) The distinguishable peaks must mean apparently distinct M_3≡OH···*X* units.

(2) Corresponding to the large ω_v(OH) value mode with a small interaction between the OH and the adjacent parts, the respective δ(OH) values are usually small, typically like Fig. 3.2.5 (a). This can help one to evaluate the interaction strength between the OH and the adjacent parts.

(3) One can estimate the ratio of ω_δ(OH) to ω_v(OH) to be about one-fifth to one quarter, therefore easily find out the range of ω_δ(OH) to justify the OH group and its environment, just as the name of correlating peak region implies, and subsequently make the peak assignation of the adjacent FP region more easy.

3.7 Summary

In summary, I have measured IR and Raman spectra of most of hydroxyl halides $M_2(OH)_3X$ (M=Co, Ni, Cu; X=Cl, Br) at RT and performed corresponding spectral analysizing. The following results have been obtained:

(1) Using five spectral analysizing methods, it is found that the whole IR or Raman spectrum of each sample can be divided into four well-separated regions: [OH/D] function group (FG), [OH/D] correlation peak (CP), M-O and M-X fingerprint ($FP_{1,2}$) regions, whose wavenumber ranges are 3600~3200/3000-2000, 1000~600/700~450, 600~200 and 200~0 cm^{-1}, respectively. In addition, wrong assignments of some bands in other authors' published papers are pointed out.

(2) In each spectral region, most experimental spectral bands have been assigned definitely and are considered to correspond well to their normal modes predicted by the standard FGA method. From those sharp band profiles in each spectrum, it is concluded that each sample is well crystallized and suitable for the further spectral study.

(3) From the comparison between the spectra of a hydroxyl halide and its deuteurized counterpart, it is found that each prepared deuteurized counterpart contains really a small amount of the hydroxyl counterpart that can not be found by other experiments.

(4) After checking the [OH] stretching frequency of each sample and its crystal structure, three kinds of $(OH)_3\cdots X$ hydrogen bond (H-bond) are found to exist in these materials according to the structural symmetry, and they have been nominated trimeric H-bond by our research team. The trimeric H-bonds in this series are found to have four subtypes and two more subtypes are predicted to exist in nature. These results may provide a new interesting subject for quantum chemists, material physicists and even quantum magnetic physicists.

(5) Furthermore it is found that the trimeric H-bond concept and the approximate linearity ($\Delta\omega_v$(OH) = –10 cm^{-1}/0.001Å) between the [OH] stretching frequency and [OH] distance can be applied to estimate the OH distance, evaluate the rightness of the OH distance given by other authors, determine the difference between different OH groups, and even compare the interactions with magnetic ions adjacent to it, *etc*.

Chapter 4

T-dependent Raman spectrum and its correlation to magnetism of selected $M_2(OH)_3X$

For a normal material, with decreasing *T*, the anharmonic thermal motion would decrease, which results in a decrease in the lattice constant. Then the phonons should shift to higher frequencies and their line-widths should become narrower. But for a magnetic material, especially for magnetic GF one there is generally spin lattice/phonon coupling closely correlated with exchange interaction of the magnetic cations through their bridging anions. In Sect. 4.1, I will introduce the Raman spectral experiment method at and above liquid helium (LHe) temperature (≥4 K) and the spin lattice/phonon coupling (denoted as SPC) theory. In Sects. 4.2~4.5, T-dependent Raman spectral analysis of the four classes of samples with four space group symmetries is performed, respectively.

4.1 General

4.1.2. General low-T Raman experimental methods

Like the method at RT, low-T Raman spectra were also obtained using HR800 microscopy, and the related experimental conditions are same with RT Raman experiments. The low-T cooling system (see Fig. 4.1.1 (a)) is composed of six parts: (a) Sample chamber (Oxford Microstat^{He}, 4.1.1 (b)), (b) Intelligent temperature controller (ITC503, 4.1.1 (c)), (c) Liquid Nitrogen/Helium Jar, (d) High vacuum pump (VPC-050, ULVAC Kiko Inc.), (e) Gas flow controller, (f) Gas flow pump (behind the jar). The samples are also same with those at RT.

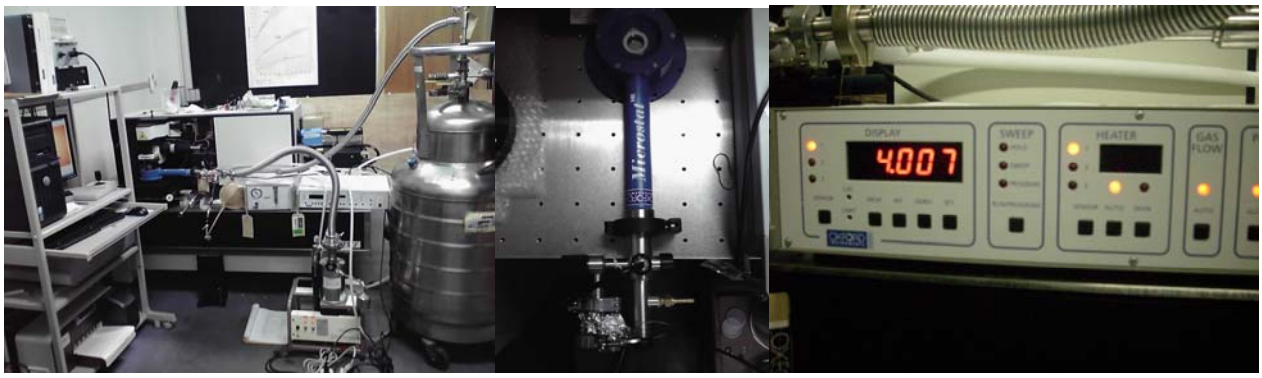

Fig. 4.1.1. (a) Low-T Raman spectroscopy and its (b) sample chamber, and (c) temperature controller.

As mentioned in the previous chapter, after a relatively perfect mode assignment has been done at RT, in order to investigate the MGF effects on the phonons at very low-T, one must use the laser power density weak enough to avoid the local laser heating (LLH) effect as well as possible, although at the expense of the spectral clarity and possible loss of signal-weak modes. So one can study several signal-strong, important and representative Raman modes (1~4 modes in each spectral [OH/D] FG, [OH/D] CP, [*M*O] FP_1 or [*MX*] FP_2 regions). Giving consideration to the low LLH effect, moderate signal-to-noise and comparability among these spectra of all kinds of samples, I use all applied laser powers to be 5 mW for L50X objective using LHe system.

Because the irradiated local environment of each sample surface changed slightly and the systemic difference (about ±1 cm^{-1}, which will be important in LHe experiments) may exist between experiments using LN_2 and LHe. Therefore the data from LN_2 experiments are not used and 290-4 K data are all measured using LHe system.

4.1.2 General T-dependent Raman spectral analysis methods

Complete analysis on the T-dependent change of Raman spectra should include the following aspects:

(1) Band number method: checking if some bands disappear and some more new bands appear with decreasing the T. If this phenomenon occurs, it always means symmetry change (generally lowering) or noticeable structural distort, and the abnormal magnetic or other properties can be well understood. But a small splitting of some main band does not often only mean the degeneracy release or overlapping division, has nothing to do with the anomaly of other physical features.

(2) Lineshape method: checking the T-dependent band lineshape change which maybe caused by the magnetic continuous excitation.

(3) Intensity method: checking the T-dependent relative intensity change which maybe caused by the .

(4) Band shift method: checking the T-dependent band frequency change which maybe caused by the SPC or spin-lattice coupling by using of the usually performed SPC theory.

The SPC theory is generally used for investigation on the relationship between the quantum magnetism caused by geometric frustration and the spectral behaviors around transition temperatures. The change in wave number of a phonon α can be given by: [164]

$$\Delta\omega_\alpha(T) \equiv \omega_\alpha(T) - \omega_\alpha(0) = (\Delta\omega)_{\text{latt}} + (\Delta\omega)_{\text{anh}} + (\Delta\omega)_{\text{ren}} + (\Delta\omega)_{\text{CF-ph}} + (\Delta\omega)_{\text{s-ph}} \qquad (4.1.1)$$

The first term $(\Delta\omega)_{\text{latt}}$ corresponds to the change in the ionic binding energies due to

lattice expansion, or say, a contribution to the phonon frequency due to a change in lattice constant with temperature and is known as quasiharmonic contribution to the frequency change. This lattice contribution $(\Delta\omega)_{\text{latt}}$ to the phonon energy accounts for an expansion or contraction of the lattice leading to a change in the harmonic force constant without changing the phonon population. This change in frequency of a mode α can thus be approximately related to the change in volume using Gruneisen parameter γ_α. The Gruneisen law can approximate this term:

$$\left(\frac{\Delta\omega}{\omega}\right)_{\text{latt}} = -\gamma_\alpha\left(\frac{\Delta V}{V}\right), \tag{4.1.2}$$

Because Eq.4.1.1 is applicable for cubic crystals or for isotropically expanded lattices, however, for the system studied in general case, this is not applicable, and one should also consider the possibility of phonon frequency shift due to lattice anomalies, even in the absence of a lattice unit cell volume.

The second term $(\Delta\omega)_{\text{anh}}$ corresponds to the intrinsic anharmonic contribution, i.e., the anharmonic wave number shift at constant volume. Intrinsic anharmonicity $(\Delta\omega)_{\text{anh}}$ can be estimated from the known temperature dependence of wave numbers if the mode Gruneisen parameters and thermal-expansion (TE) coefficient are known. If these parameters are not known, the temperature dependence of wave numbers (in units of cm^{-1}), resulting from the sum of lattice and phonon-phonon anharmonic terms, can be approximated with the following function:

$$\Delta\omega_\alpha(T) \equiv (\Delta\omega)_{\text{latt}} + (\Delta\omega)_{\text{anh}} = A_\alpha\left(1+\frac{2}{e^{x/2}-1}\right) + B_\alpha\left(1+\frac{3}{e^{x/3}-1}+\frac{3}{(e^{x/3}-1)^2}\right) \tag{4.1.3}$$

with

$$x \equiv \frac{E_{\alpha 0}}{k_{\text{B}}T} = \frac{hc}{k_{\text{B}}}\cdot\frac{\omega_{\alpha 0}}{T} = \frac{6.626\times10^{-34}\times3\times10^{10}}{1.381\times10^{-23}}\cdot\frac{\omega_{\alpha 0}}{T} \quad = \frac{1.44\omega_{\alpha 0}}{T}$$

Above the magnetic ordering T_{c}, there are two cases: positive TE (PTE) and negative TE (NTE). Both cases have no necessary connection with the magnetic ordering developed above the T_{N} or T_{CW}. The former case causes that the phonon frequency ω exhibits a normal increase with decreasing temperature for $T>T_{\text{N}}$ due to the lattice PTE, while the latter behaviors inversely.

The third term $(\Delta\omega)_{\text{ren}}$ accounts for the effect of a renormalization of the electronic states. It can be neglected once it is an isolator.

The fourth term $(\Delta\omega)_{\text{CF-ph}}$ accounts for the crystal field-phonon coupling. The CF-phonon coupling also may lead to both increase as well as decrease in phonon energy. The coupling

between the CF transitions of rare-earth ions and the phonons is usually weak due to the effective shielding of the 4*f* electrons of the rare-earth ions. It can be neglected once it is an isolator, and no coupling to CF excitations is expected.

The last term $(\Delta\omega)_{\text{s-ph}}$ corresponds to the SPC contribution, which becomes important only at those temperatures where some magnetic correlation exists. Therefore, in conventional magnetic systems the wave-number shifts of phonon modes are negligible in the paramagnetic phase. It is well known, however, that in magnetically frustrated systems the spin-correlation function exists above T_N since a highly correlated paramagnetic state is typically formed above T_N. Therefore, in such systems anomalous softening or hardening of modes is often observed well above T_N.

Provided that the crystal potential can be described as

$$U = \sum_{ij} \frac{1}{2} k_0 u_{ij}^2 + \sum_{ij} J(u_{ij}) \left\langle S_i S_j \right\rangle \text{ and } \frac{\partial^2 J(u_{ij})}{\partial u^2} \neq 0 \tag{4.1.4}$$

$$k = k_0 + \sum_{ij} \frac{\partial^2 J_{ij}(u)}{\partial u^2} \left\langle S_i S_j \right\rangle \tag{4.1.5}$$

$$\Delta k = \sum_{ij} \frac{\partial^2 J_{ij}(u)}{\partial u^2} \left\langle S_i S_j \right\rangle \tag{4.1.6}$$

Where u is the atomic displacement from the equilibrium position in the oscillator model, and $\left\langle S_i S_j \right\rangle$ denotes a statistical average over the adjacent spins.

In general, experimentally observed frequency shifts should come from a sum of two terms, namely, due to FM and AFM exchanges respectively, and can be represented as

$$\Delta\omega = \frac{-R_1 \left\langle S_i S_j \right\rangle + R_2 \left\langle S_i S_j \right\rangle}{\left\langle S_0^z \right\rangle^2} \tag{4.1.7}$$

Here, R_1 and R_2 are spin dependent force constants of the lattice vibrations deduced as the squared derivatives of the exchange integrals with respect to the phonon displacements. R_1 describes the nearest-neighbor (NN) FM and R_2 the AFM next-nearest-neighbor (NNN) exchange. Using this formalism, negative and positive frequency shifts depend on the strength of FM or AFM exchange interactions, respectively. Then

$$\omega = \frac{1}{2\pi c} \sqrt{\frac{k_0 + \Delta k}{m_\mu}} \approx \omega_0 + \frac{1}{4\pi c \sqrt{m_\mu}} \Delta k \tag{4.1.8}$$

$$\Delta\omega_\alpha = \lambda_\alpha \left\langle S_i S_j \right\rangle \tag{4.1.9}$$

$$\lambda_\alpha = \frac{1}{4\pi c\sqrt{m_\mu}} \sum_{ij} \frac{\partial^2 J_{ij}(u)}{\partial u^2} \tag{4.1.10}$$

The SPC coefficient λ_α is different for different phonon α, and λ_α can have either a positive or a negative sign, according to the sign of second order derivative of superchange interaction $J(u)$, but having no relationship with the magnetic ordering below T_N, i.e., not the sign of $J(0)$.

For a FM ordering below T_N, $\langle S_i S_j \rangle_\alpha > 0$, if $\lambda_\alpha > 0$, then $\Delta\omega_\alpha > 0$, otherwise $\Delta\omega_\alpha < 0$. Similarly, for an AFM ordering below T_N, $\langle S_i S_j \rangle_\alpha < 0$, if $\lambda_\alpha > 0$, then $\Delta\omega_\alpha < 0$, otherwise $\Delta\omega_\alpha > 0$.

(5) Linewidth method: checking the T-dependent linewidth (FWHM, the full width of the half maxium) change which maybe caused by the spin fluctuation and spin (magnetic) ordering.

In a non-magnetic crystal, the T-dependent linewidth Γ (FWHM, e.g. the phonon damping constant which corresponds to the anharmonic part of the crystal potential U) changes $\Delta\Gamma_\alpha(T) \equiv \Gamma_\alpha(T) - \Gamma_\alpha(T_0)$ and $(\Delta\Gamma_\alpha)_{\text{latt, anh}}$ of phonon α is given by

$$\Delta\Gamma_\alpha(T) \equiv \Delta\Gamma_{\text{latt}} + \Delta\Gamma_{\text{anh}} = C_\alpha \cdot \left(1 + \frac{2}{e^{x/2} - 1}\right) + D_\alpha \cdot \left(1 + \frac{3}{e^{x/3} - 1} + \frac{3}{(e^{x/3} - 1)^2}\right) \tag{4.1.11}$$

with x same as in Eqn. (4.1.3).

At temperatures near T_c where the short-range spin correlation begins to set up, the non-zero $(\Delta\Gamma_\alpha)_{\text{s-ph}}$ can be expressed like Eq. (4.1.9) as:

$$(\Delta\Gamma_\alpha)_{\text{s-ph}} = \gamma_\alpha^{\text{AFM}} \langle S_i S_j \rangle + \gamma_\alpha^{\text{FM}} \langle S_k S_l \rangle \propto \left(\langle M^\alpha \rangle^2 + NkT\chi^{\alpha\alpha} \right) \tag{4.1.12}$$

where $\gamma_\alpha^{\text{AFM}}$ and $\gamma_\alpha^{\text{FM}}$ are spin-phonon coupling parameters of the linewidths, the M^α and $\chi^{\alpha\alpha}$ indicate the α component of magnetization and the $\alpha\alpha$ component of susceptibility tensor, respectively. [169] The magnetization M^α averaged thermally represents the contribution of long range spin ordering and the susceptibility $\chi^{\alpha\alpha}$ does that of the short range spin ordering. The value N indicates the number of magnetic ions in a unit cell. Therefore, Γ_α would generally decrease monotonously, smoothly and slowly with the temperature. But for a magnetic sample, if a sudden change of $\Gamma_\alpha(T)$ occurs, it would indicate the appearance of magnetic ordering or spin fluctuation toward a short range ordering, producing an extremum near the T_c

In a magnetic crystal, the crystal potential U is given by the summation of a non-magnetic part U_0 and a magnetic part U_m.

Also according to the SPC mechanism, the U_m in the FM phase, for example, is given by

an expanded form as [169]

$$U_m = -2\sum_{lm}\langle S_l S_m\rangle\left[(J_{lm})_0 + \sum_i\left(\frac{\partial J_{lm}}{\partial u_i}\right)_0 u_i + \sum_{ij}\left(\frac{\partial^2 J_{lm}}{\partial u_i \partial u_j}\right)_0 u_i u_j + \sum_{ijk}\left(\frac{\partial^3 J_{lm}}{\partial u_i \partial u_j \partial u_k}\right)_0 u_i u_j u_k + \cdots\right]$$
$$+ 2\sum_{ln}\langle S_l S_n\rangle\left[(K_{ln})_0 + \sum_i\left(\frac{\partial K_{ln}}{\partial u_i}\right)_0 u_i + \sum_{ij}\left(\frac{\partial^2 K_{ln}}{\partial u_i \partial u_j}\right)_0 u_i u_j + \sum_{ijk}\left(\frac{\partial^3 K_{ln}}{\partial u_i \partial u_j \partial u_k}\right)_0 u_i u_j u_k + \cdots\right] \quad (4.1.13)$$

where J_{lm} and K_{ln} represent the NN FM and NNN AFM interactions respectively.

The **first** derivative of those with respect to the phonon displacement u, takes any magnitude depending on the SPC strength.

The **second** derivative gives the harmonic force constant. This term is dominant for the frequency shift near and below T_C.

The **third** derivative will be a main term for the phonon damping because the quartic term will be small in the low T region. The T-dependence of Γ near and below T_C, is characterized by the spin correlation ‹S_lS_m› and ‹S_lS_n›. The two-spin correlation function can be given thermodynamically as

$$\langle S_m S_n\rangle \propto \left(\langle M^\alpha\rangle^2 + NkT\chi^{\alpha\alpha}\right) \quad (4.1.14)$$

where the magnetization M^α averaged thermally represents the contribution of the long-range spin ordering and the susceptibility $\chi^{\alpha\alpha}$ does that of the short-range spin-ordering. The value N indicates the number of magnetic ions in a unit cell. The microscopic mechanism of the long-range and short-range spin-orderings on these decay processes can be understood as follows:

The long-range spin-ordering induces the uniform energy shift for the Brillouin zone-boundary-phonon and Brillouin zone-center-phonons. By the shift, the density of state and the transition probability are changed and Γ increases or decreases below T_C.

On the contrary, the coupling of the zone-boundary-phonon with the spin fluctuation caused by the MGF and the short-range spin-ordering gives various energy shifts on the zone-boundary-phonon and also a broadening of its energy level. Then the overlapping of those energy levels may construct the bands. Since the decay time is dominated by the transition probability between the phonon states at zero wave vectors and at the zone boundary, and also by the density of state of both states, the appearance of the band may induce many decay processes and the Γ takes large magnitude. Since the short-range spin-ordering decreases at both sides of T_C, the increasing of Γ will appear only near T_C.

4.2 *T*-dependent Raman spectra and magnetism of γ-$Cu_2(OH)_3Cl$

In light of macroscopic experimental magnetic and thermal properties of γ-$Cu_2(OH/D)_3Cl$, several strong MGF behaviors have been demonstrated: (1) dc and ac susceptibilities evidenced the presence of the strong AFM correlations up to 200 K deducing a $\theta_{CW} \approx -190$ K, [67, 77] a small transition at 18.1 K and successive freezing temperatures 6.4 K and 6.2 K; [67, 68, 77] (2) zero-field/field cooling (ZF/FC) magnetizations showed an anomaly at 6.2 K; [67] (3) ZF/FC specific heat data revealed successive AFM transitions at $T_{c1/2/3}$=18.1/6.4/6.2 K, and about zero-point entropy 0.69*R*ln2. [67, 92] As to microscopic aspects of its magnetic structures and properties, proton NMR spectra and spin-lattice relaxation studies indicated the coexistence of partial spin freezing and large fluctuations due to frustration in the intermediate phase (6.4<*T*<18.1 K); magnetic neutron diffraction data on γ-$Cu_2(OD)_3Cl$ have proposed three kinds of magnetic structure: Lee's, Wills's, and Kim's magnetic-models; [107, 77, 80] inelastic neutron scattering experiments on γ-$Cu_2(OD)_3Cl$ have quantified the characteristic energy scales of the system. On cooling below T_{c1} or increasing the applied magnetic field *H*, the scattering evolves from quasielastic to inelastic, the low energy excitations in the ordered phase have gaps δ of about 1, 2 and 7 meV that arise from exchange interactions;[63, 77] Our μSR experiments identified a long-range AFM order with a surprisingly small entropy release below 18.1 K, the static long-range order transforms abruptly into a metastable state below 6.5 K, and then a coexistence state of a partial long-range order and spin fluctuation down to 20 mK. [69] Till now, the study on the magnetic properties of γ-$Cu_2(OH)_3Cl$ has reached the stage of theoretically modeling its thermodynamics.[99] The first numerical study found that the quasi-2D model suggesting the Cu^T moments in the triangle plane weakly FM coupling ($J' \approx -0.1J_{Clino} = -19$ K) with Cu^K ones in the Kagome planes agrees with the related experimental results.

Contrary to Herbertsmithite $ZnCu_3(OH)_6Cl_2$ which was first revealed in 2007 as a quantum kagome AFM material later than γ-$Cu_2(OH)_3Cl$ but has been intensively researched even by the Raman scattering method theoretically and experimentally,[101-150] obviously there are many issues remaining open on γ-$Cu_2(OH)_3Cl$, especially the nature of the magnetic order state below18 K transition witnessed by μSR, special heat experiments and theoretical modeling. [69, 99, 247] For example, Lee *et al* suggested it as a resonating-valence-bond state originally, [107] but they and other researchers denied the suggestion latterly because of the obtained weak interplane coupling. [77, 80] This section reports, for the first time to the best of our knowledge, the spectroscopic evidences on the existence of successive transitions and coexistence of the magnetic order and spin fluctuations at the intermediate phase in γ-$Cu_2(OH)_3Cl$.

4.2.1 Evidence of the successive magnetic transitions

Figure 4.2.1 shows the four enlarged Raman spectral parts of the γ-$Cu_2(OH)_3Cl$ at T=295, 150 and 4 K in vacuum respectively.

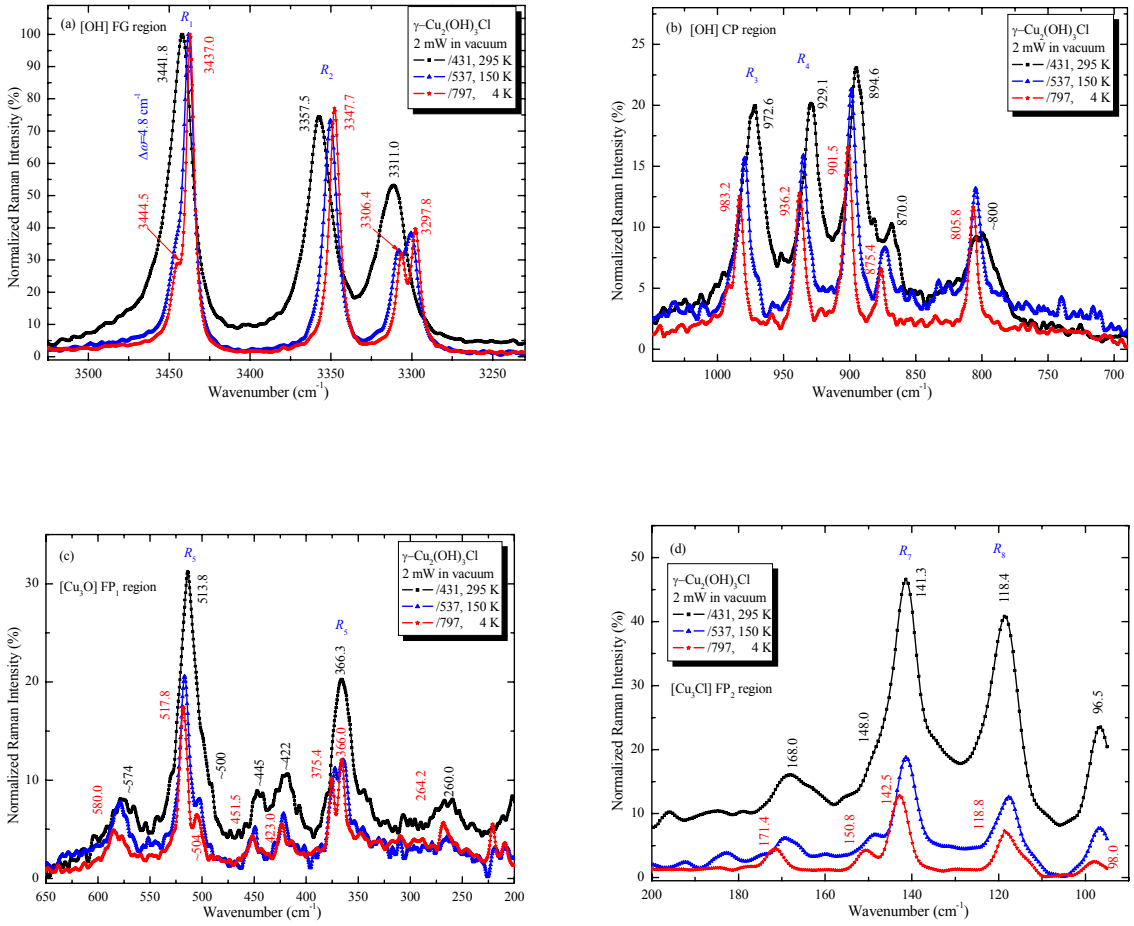

Fig. 4.2.1. Enlarged four Raman spectral parts of the γ-$Cu_2(OH)_3Cl$: (a) [OH] FG, (b) [OH] CP, (c) [Cu_3O] FP_1 and (d) [Cu_3Cl] FP_2 regions at T=295, 150 and 4 K in vacuum.

From Fig. 4.2.1, when the samples are cooled down to 4 K, one can see that:

(1) Most of bands become normally narrower;

(2) No remarkable bands disappear or new intrinsic new bands appear, which indicates no lattice symmetry lowering;

(3) The bands 3441.8, 3311.0 and 366.3 cm^{-1} split into double ones, which are caused by the simple and still partial degeneracy release;

(4) All temperature coefficients $\Delta\omega/\Delta T$ of [OH] FG Raman band frequencies are **positive** and those of CP Raman band frequencies are **negative**, which agrees well the fact of existing non-neglectable H-bonds;

(5) Most of $\Delta\omega/\Delta T$ of [Cu_3O] Raman band frequencies are normally **negative,** most $\Delta\omega/\Delta T$ of [Cu_3Cl] vary not too much, while other $\Delta\omega/\Delta T$ are almost T-independent;

(6) No band is found to possess an apparent Fano line-shape, which demonstrates that no interference occurs between scattering amplitudes of a continuum of states (the background process) and the excitation of discrete states (the Raman phonon transition) above 95 cm^{-1} (12 meV). The band data at 295 and 4 K are collected in TABLE C3 in Appendix C.

I select eight representative Raman normal modes R_{H1} ~R_{H8} (two in each region, labeled in Fig. 4.2.1 respectively) to study their T-dependence of mode frequencies ω_1~ω_8 and FWHMs $\Gamma_{1\sim8}$, as shown in Figs. 4.2.2 and 4.2.3, respectively. Among the modes $R_{1\sim8}$, R_1, R_2, R_5 and R_7 are the "pure" stretching modes, R_3 and R_4 are the "pure" bending modes of two [Cu-O-H] groups, and R_6 and R_8 are the "mixed" deformation ones of the stretching and bending vibrations which may in general mainly show the stretching behavior. Because of the low P_L to avoid the LLH effect as well as possible, the signals above 50 K are not so good, especially for the latter two kinds of modes $R_{3,\,4,\,6,\,8}$, and lead to the relatively large errors in the band frequencies and linewidths in Figs. 4.2.2 and 4.2.3.

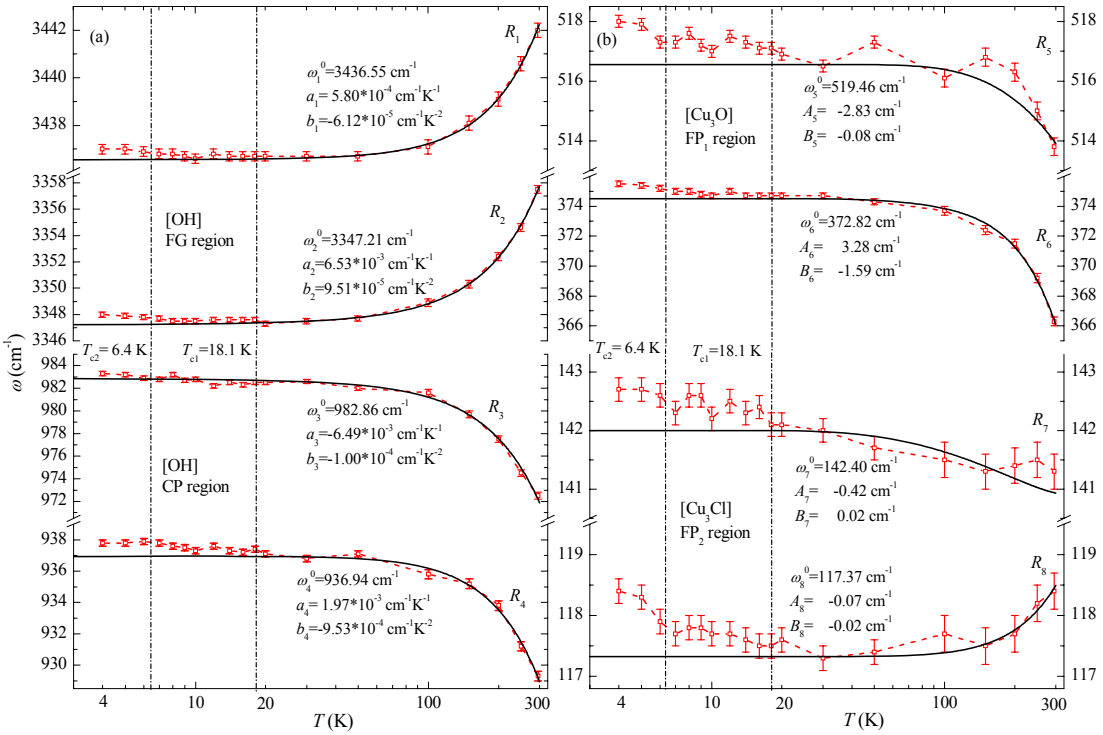

Fig. 4.2.2. T-dependent frequencies $\omega_{1\text{-}8}$ for the Raman normal modes $R_{1\text{-}8}$. The solid lines in (b) represent the common fitting functions $\omega_\alpha(T)$ given by Eqn. (4.1.3), while each of solid lines in (a) is a tentative fitting with a monotonously smoothing quadratic function Eqn. (4.2.2) to present the reasonable trend phenomenologically, all of which reflect only the phonon–phonon interactions. The vertical lines T_{c1} = 18.1 K and T_{c2} = 6.4 K determined by the magnetic experiments before are attached for reference only.

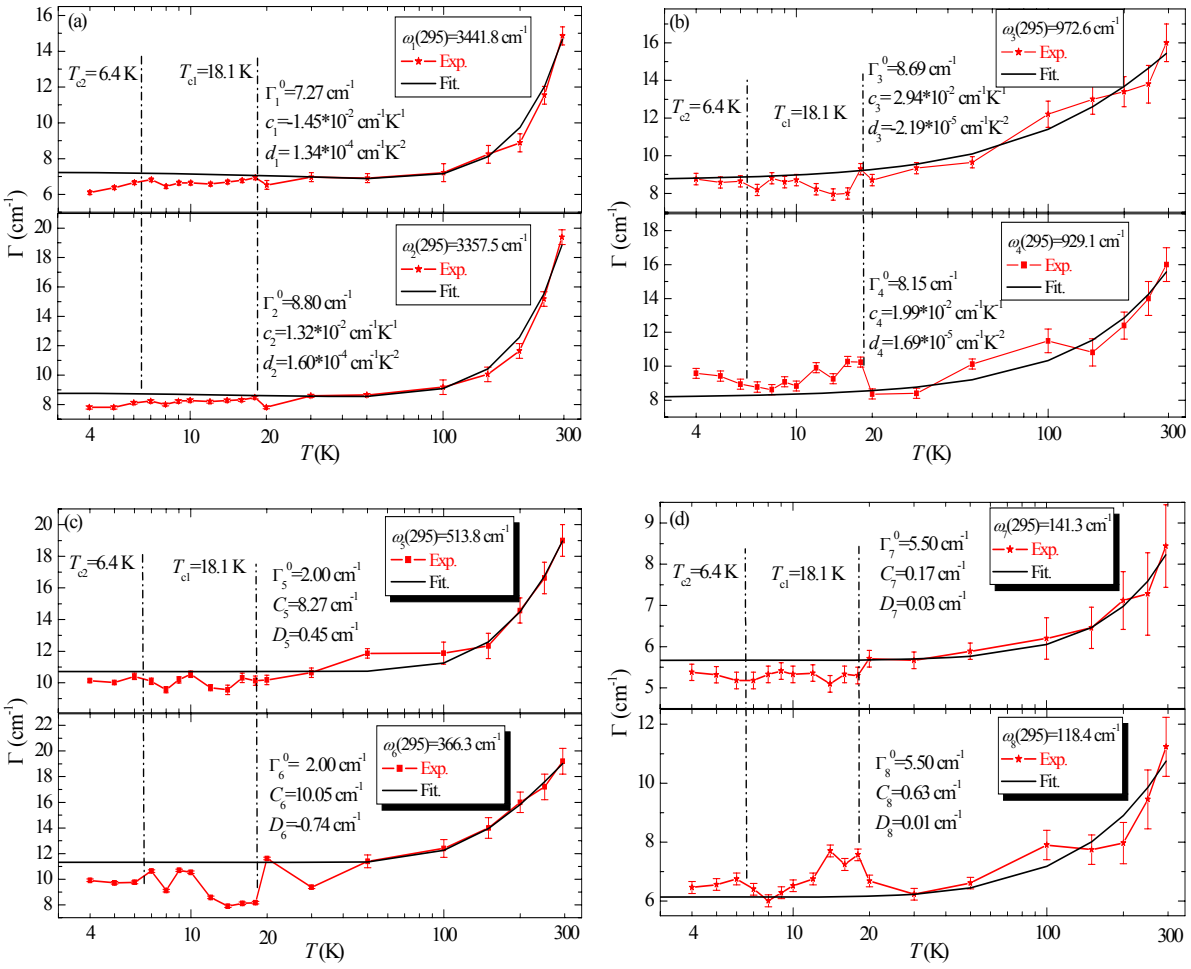

Fig. 4.2.3. T-dependent $\Gamma_{1\text{-}8}$ for the Raman normal modes $R_{1\text{-}8}$. The solid lines in (c, d) represent the common fitting functions $\Gamma_\alpha(T)$ given by Eqn. (5), while each of solid lines in (a, b) is a tentative fitting with a monotonously smoothing quadratic function Eqn. 4.2.2 to present the reasonable trend phenomenologically, all of which reflect only the phonon–phonon interactions. The vertical lines T_{c1} = 18.1 K and T_{c2} = 6.4 K determined by the magnetic experiments before are attached for reference only.

First of all, it can be seen from Figs. 4.2.2 and 3 that the trend as a whole of $\omega_{3\sim7}$ and $\Gamma_{1\sim8}$ variations in the wide-T range presents a normal thermal expansion behavior of a normal non-magnetic and isolating material. Yet the $\omega_{1,2,8}$ shows an abnormal behavior (band redshifting with decreasing the temperature), and we think it can be elucidated by the dominating effect of the trimeric H-bond as shown in Fig. 4.2.4. Considering the influence of Cu_3 left the O^2, for example, and Cl-Cu_3 right the H^2 on the $d(O^2H^2)$, when the sample is cooled both a stronger repulsive interaction of 3 Cu ions against the H^1 and a stronger $(OH)^2\cdots$Cl H-bonding may cause eventually a net $d(O^2H^2)$ elongation against the contraction effect of the "free" $[OH]^2$ group, therefore a softening of the $[OH]^2$ stretching frequency but normal hardenings of related [Cu-O-H] bending frequencies.[201] For the same reason, a

stronger trimeric H-bond leads to a slight hardening of the [Cu_3Cl] stretching frequency and a much small softening of the [Cu_3Cl] deformation frequency. [233]

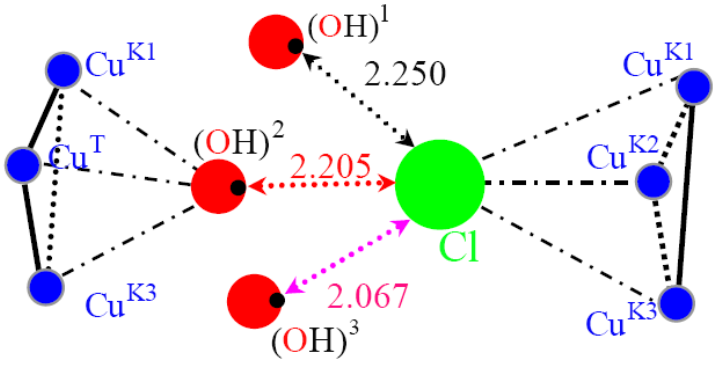

Fig. 4.2.4. Local environment of the trimeric H-bond with three $d(Cl\cdots H^{1\text{-}3})$ in units of Å.

Furthermore, it should be noted that Eqs. (4.1.3) and (4.1.11) were found, for the first time, unsuitable for fitting the high frequency modes $R_{1\sim4}$, when the x value in the equations are large. Here we adopt a monotonously smoothing function for $R_{1\sim4}$ fitting:

$$\omega_\alpha(T) = \omega_\alpha^0(T_0) + a_\alpha \cdot T + b_\alpha \cdot T^2 \qquad (4.2.1)$$

and

$$\Gamma_\alpha(T) = \Gamma_\alpha^0(T_0) + c_\alpha \cdot T + d_\alpha \cdot T^2 \quad . \qquad (4.2.2)$$

Therefore, we use the monotonously smoothing curve only as a reference to check a possible anomaly qualitatively, although a new model with a good physical explanation needs to be established.

For all of the frequencies $\omega_{1\text{-}8}$ and $\Gamma_{1\text{-}8}$, deviations from the fitted smoothing curves occur in the low temperature range (4~30 K). Obvious deviation begins to appear at temperatures close to the magnetic transition at T_{c1}=18.1 K, which has been determined accurately by the magnetic experiments. [67, 69] These anomalies are apparently due to an SPC effect; therefore, the present data provide the Raman evidence of the onset of magnetic ordering at 18.1 K in γ-$Cu_2(OH)_3Cl$.

The anomalous T-dependent trend of the [OH] stretching mode frequencies based on the consideration of the presence of the asymmetric trimeric H-bond has shown the existence of interaction between the high energy [OH] phonon modes and low-energy magnetic excitations through the Cu-O-Cu superexchange and trimeric H-bonds, which is in contradiction to the recent unsealed assertion to support the practice of ignoring the high energy [OH] stretching and deformation modes. [133]

The Raman anomalies of each ω_α and Γ_α due to the SPC effect in γ-$Cu_2(OH)_3Cl$ are

relatively small (less than 1.6 cm^{-1} and 4 cm^{-1}, respectively), which are attributed to the small spin moment of Cu^{2+} although it possesses large frustration index ($f_1 = |\theta_{CW}|/T_{c1} \approx 10$ and $f_2 = |\theta_{CW}|/T_{c2} \approx 30$). [4] Among them, the largest one belongs to the [Cu_3O] stretching mode R_5, which agrees with the expectation that magnetic couplings are dominated by the Cu-O-Cu superexchange interactions. According to specific heat studies [92] and the numerical study [99], γ-$Cu_2(OH)_3Cl$ can be viewed as a weakly coupled kagome AFM system with a weak FM coupling between the triangular layer and the kagome layer. [92] Therefore, we may ignore the weak FM correlation contribution in Eqs. (4.1.10) and (4.1.12), and use the reported value of $\langle S_i S_j \rangle \approx -0.5$ (–0.56 in Ref. [109] and –0.43 in Ref. [121]) for herbertsmithite to get a rough estimation of frequency SPC parameter $|\lambda_5| = 3$ cm^{-1} and linewidth SPC parameter $|\gamma_6| = 6$ cm^{-1} of γ-$Cu_2(OH)_3Cl$. The fact that the linewidth variation $(\Delta\Gamma_6)_{s\text{-}ph}$ has reached 10% of the theoretical linewidth Γ_6 according to Eq. (4.2.11) clearly demonstrates the appearance of some kind of magnetic ordering around 18 K. According to Eqs. (4.1.10) and (4.1.12), because only some Raman resonances ($R_{5\sim8}$) include directly the magnetic ions Cu^{2+}, they can be affected more significantly by the effect of magnetic ordering, while others ($R_{1\sim4}$) including only non-magnetic ions are influenced relatively slightly by the indirectly connected magnetic ions. For all that, all modes are affected by the trimeric H-bonds and their temperature dependences of ω_α and Γ_α behavior not so simple.

Inspecting the details of each ω_α and Γ_α variation from 18 K to 4 K, one can see that the trend is obviously nonlinear and abrupt changes occur near 6 K, which corresponds well with the well-established $T_{c2} = 6.4$ K determined accurately by other experiments. [67, 69] In addition, from the non-zero SPC anomalies of modes $R_{1\text{-}4}$, one can see the existence of interaction between the high energy [OH] phonon modes and low-energy magnetic excitations through the Cu-O-Cu superexchange as well as the trimeric hydrogen bonds, which is in contradiction to the assumptions the high energy [OH] stretching and deformation modes could be ignored in considering the SPC. [148,109]

From the T-dependent ω_α and Γ_α variation of these representative Raman normal modes, one can verify the existence of two successive magnetic transitions at about 18 K and about 6 K, although the nature in the intermediate range $6 < T < 18$ K is still unclear. Fortunately some information can be deduced from the following quantitative analysis on the low frequency quasielastic scattering background at high temperatures and the scattering continuum in the temperature range of $6 < T < 18$ K.

4.2.2 Coexistence of magnetic order and fluctuations

The T-dependent Raman spectral profiles of γ-$Cu_2(OH)_3Cl$ have interesting features, as shown in Fig. 4.2.5 (a): in the FP_2 region, there is a pronounced background at high

temperatures, which is almost completely depressed below 100 K, while below 100 K a wider continuum appears in the whole FP region. Very similar to those of the quasi-two-dimensional quantum spin systems, [241-245, 249] the former background can be explained by the quasielastic scattering (QES) contribution. The latter broad continuum is reminiscent of the so-called Raman magnetic bound state scattering. [242] Fig. 4.2.5 (b) shows an example of the tentative Lorentzian fitting of the QES background using the 295 K data, although optimum fitting should be performed with the low enough wavevector transfer data whose collection is limited by the cut-off frequency (about 90 cm^{-1} for our spectroscope) of the available notch filter, and the large gap between the phonon modes and the fitting curve in the 250-650 cm^{-1} range comes mainly from the overlaps of many phonon modes in the fingerprint region. The fitted values of relative intensity I_Q and the center frequency ω_Q of the QES are plotted in Fig. 4.2.6, from which one can see that the QES background has not only a decreasing intensity I_Q upon cooling, but also a blueshifting maximum ω_Q (e.g, from $\omega_Q(295\ K) \approx 145\ cm^{-1}$ to $\omega_Q(100\ K) \approx 180\ cm^{-1}$). The intensity I_Q and center frequency ω_Q at high temperatures can be approximated by a power-law equation $T^{2.7\pm0.5}$. This fact reflects a very general feature of the QES with a strongly broadened central peak and a Lorentzian lineshape in a spin gapped system at temperatures higher than the singlet-triplet gap, [241-245] resulting from three-magnon scattering. The observed T-dependent scattering intensity I_Q (Fig. 4.2.6) is generally due to scattering on thermally populated and strongly localized triplet states, whose fluctuations of the energy density of the spin system originate from the non-negligible SPC and the underlying spin-spin correlations. [242]

Since the QES intensity is greatly reduced below 100 K and the QES background emerges into wider continuum extending over the whole FP region as shown in Fig. 4.2.5 (a), re-fitting should be done to reflect the feature of the continuum at low temperatures.

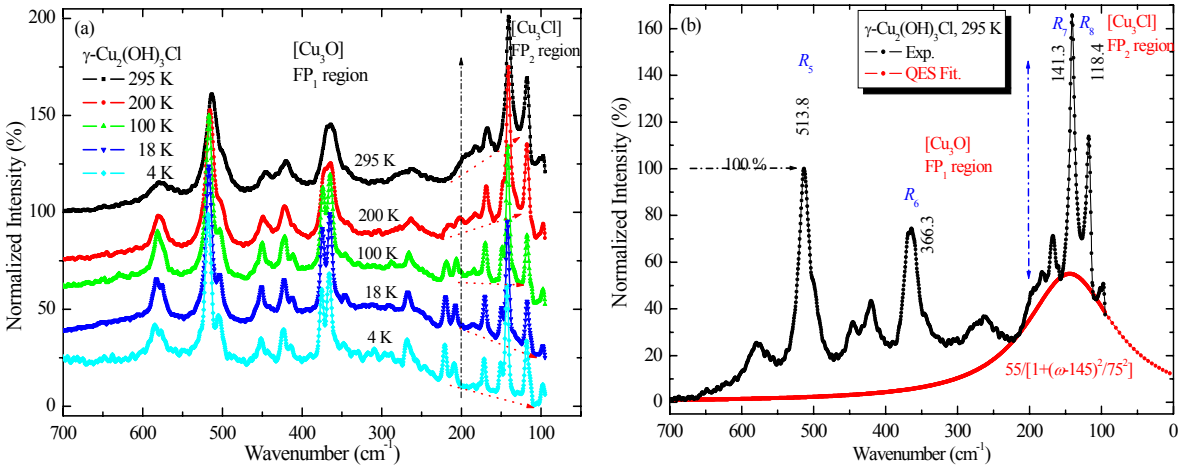

Fig. 4.2.5. (a) T-dependence of the representative Raman spectra in the FP region. Spectra are shifted for clarity. (b) Lorentzian fitting of the QES background of the FP_2 region at 295 K.

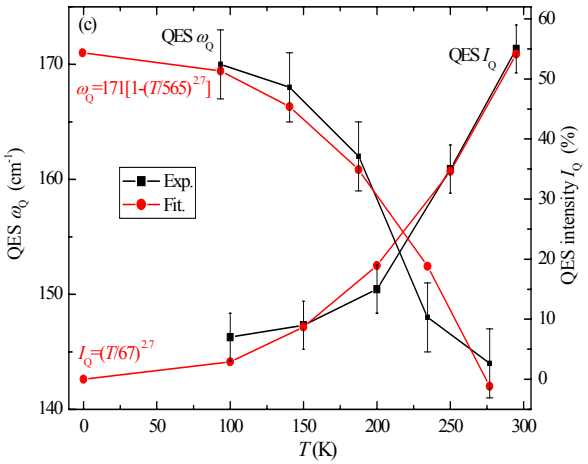

Fig. 4.2.6. T-dependence of the ω_Q and I_Q of the QES background. The solid lines are fitted curves.

In Figs. 4.2.7 (a) and (b), we show an example of parabolic fitting to the broad continuum at 4 K and the fitted continuum intensity I_C for all temperatures, respectively. The continuum intensity I_C data for the temperature range of 25 -100 K can be fitted by a power law relationship ($-T^{2.7\pm0.5}$). It is noted that all continuums are centered at about 450 cm^{-1}. This value matches an energy scale of 3.3 J_{Clino}, suggesting a two-magnon-like scattering process due to spinon scattering. Similar center-constant continuum and relation to J have been observed in other systems, e.g, continuum centered at wave number of $2J$ in isolated tetrahedral quantum spin system $Cu_2Te_2O_5Br_2$ with weak inter-tetrahedron coupling, [244] and that of $2.7J$ in 2D diluted square lattice $K_2V_3O_8$ with an interconnection of magnetic pyramids and non-magnetic tetrahedra. [242] This spinon scattering contribution is suppressed at $T < 20$ K, with abruptly dropped I_C (Fig. 4.2.7(c)). This linear decrease of the continuum intensity in the vicinity of T_C has been extensively observed in spin systems such as in spin-Peierls compound $CuGeO_3$, [249] a spin ladder compound NaV_2O_5 [241] and a spin-gap compound $(VO)_2P_2O_7$ with strong SPC. [243] **It is regarded as a "fingerprint" of magnetic bound states in low dimensional spin systems with a singlet ground state and a gapped excitation spectrum, due to the appearance of the magnetic bound states consisting of strongly interacting triplet excitations**. [242]

These research results may enlighten one on the perfect interpretation of this phenomenon that a magnetic transition possibly occurs at about $6 < T < 18$ K from the present Raman experiment, while the polarization dependence of the continuum peak obtained in further polarized Raman experiment maybe essential to back up the statement.

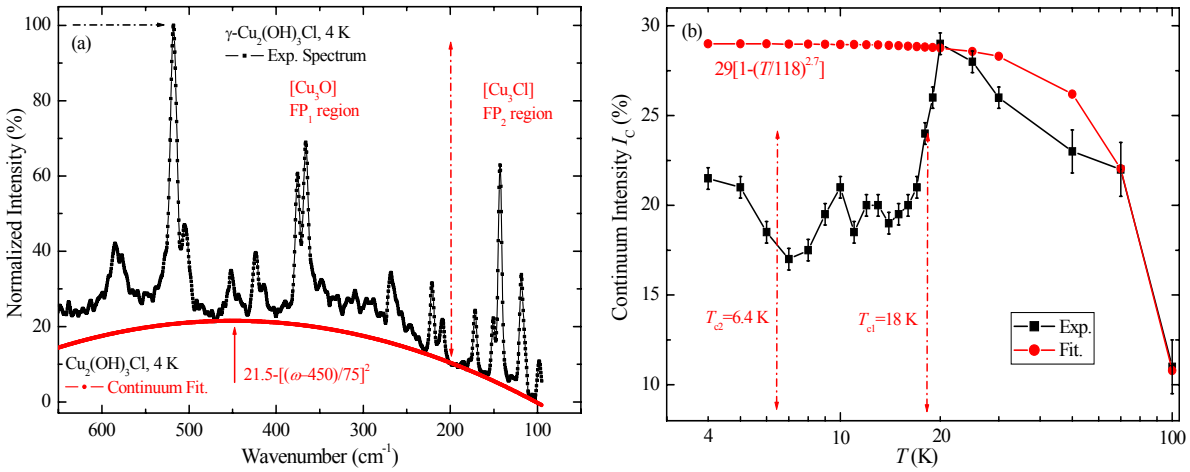

Fig. 4.2.7. (a) Parabolic fitting (thick solid line) to the broad continuum of γ-$Cu_2(OH)_3Cl$ at 4 K. (b) Temperature dependence of the relative intensity I_C of the continuum below 100 K.

In fact, according to the low-symmetric atomic lattice structure of γ-$Cu_2(OH)_3Cl$, the magnetic Cu^{2+} (S=1/2) ionic lattice is quasi-two dimensional and can be described by the Heisenberg model with AFM kagome planes weakly coupled to triangular planes. The magnetic S=1/2 ions on the kagome plane may mainly be dimerized to form a singlet ground state and a gapped triplet excitation spectrum which can be theoretically calculated with the proper Heisenberg model introduced by Khatami, *etc*. [99]

Furthermore, considering the weakly coupled interaction between ions on the kagome and triangular planes, one can obtain more small-gapped exciting states existing in the magnetic bound states. Consequently, in the unavoidable presence of geometric frustration, lattice defects, thermal and magnetic perturbations, although many dimerized ionic groups are in the singlet ground state (S_{total}=0) forming a partial long-range order, other magnetic ions may still transition fast among those small-gapped multiple quantum states, *i.e.*, there are also many ionic spins whose directions fluctuate fast because of the strong magnetic interaction.

In a word, this tentative interpretation means physically that the quantum system in this intermediate phase may possess the property of the coexistence of ordered spins with a lot of fast fluctuating ones (or say the partial magnetic order with strong spin fluctuations) for 6 < T < 18 K.

In consistency with the small entropy release at 18 K despite unambiguous evidence of long-range magnetic order, [67] the intensity I_C remains large in γ-$Cu_2(OH)_3Cl$ (Fig. 4.2.6 (b)). The non-zero and abnormal tendency of I_C for 6 < T < 18 K suggests that the magnetic ordering in this temperature range is really partial, with apparent spin fluctuation produced by strongly interacting multiplet excitations.

The coexistence of partial magnetic order and strong spin fluctuations may be further

assessed through the fact that the fluctuation time approaches the response time τ_R of Raman scattering, as is demonstrated in the case of 2D AFM fluctuations in hexagonal antiferromagnet $YMnO_3$. [250] From the typical linewidth $\Gamma_5 = 10$ cm^{-1}, τ_R is estimated to be $(2\pi c\Gamma_5)^{-1} \approx 5\times10^{-13}$ s = 0.5 ps. This picosecond time scale falls out of the time window of μSR (characteristically 10^{-10} s). Now we can see that the previous μSR experiment has only "seen" the long-range ordered part for the intermediate phase, [69] but overlooked a large part of very fast, almost paramagnetic spin fluctuations in the intermediate phase because they are beyond its time window. Therefore, the present Raman scattering experiment serves quite possibly as a good complement to the μSR study because of the matched time scale to the almost paramagnetic spin fluctuations. In addition, the coexistence of ordered spins with a lot of fast fluctuating ones explains the exceptionally small entropy release at 18.1 K. [67, 92]

It is interesting to compare the present data to those reported for herbertsmithite. The non-zero central peak wave number of the QES background at high temperatures and the irregular change of the continuum intensity are different from the zero QES central peak and the monotonous decrease of the intensity in herbertsmithite with gapless spin excitations. [133] They are likely due to their different magnetic states.

It should be also noted that before the continua in the spectra are analyzed, it is necessary to correct the spectra according to the Bose-Einstein distribution function. But we do not correct them because our Raman spectroscope can not measure the anti-Stokes signals, and luckily the conditions of the low laser power, good thermal transfer, and well crystallized samples have resulted in the small experimental deviation of the Raman peak anomaly temperatures from those obtained in other thermal and magnetic experiments.

4.3 Synthetic T-dependent spectral study on $M_2(OH)_3X$

In this section, qualitative T-dependence of the normal mode frequency is identified to be consistent with its laser-power-density –dependence because of the LLH effect. In addition, [OH] stretching frequencies for the $M_2(OH)_3X$ are found to normally red-shift or abnormally blue-shift for different materials.

4.3.1 Relationship with the local laser heating effect at RT

When the sample temperature is decreased, each normal mode frequency redshifts or blueshifts more or less for every material. This qualitative T-dependence of the normal mode frequency is identified to be consistent with its laser-power-density-dependence because of the LLH effect. As an example, Fig. 4.3.1 shows the [OH] FG and [Co_3Cl] FP regions of $Co_2(OH)_3Cl$ at three temperatures and their corresponding regions at three laser power values (e.g. three laser power density values in the condition of a common objective) at RT.

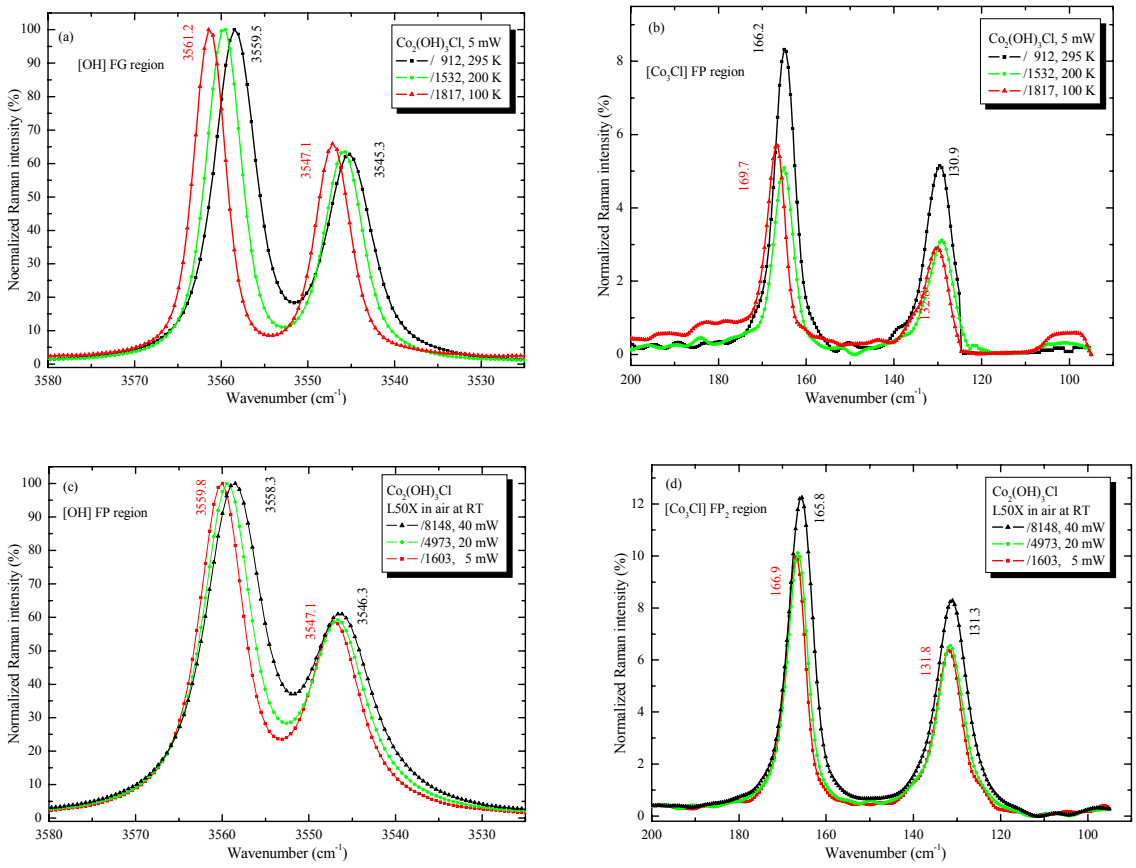

Fig. 4.3.1. (a) and (b) the [OH] FG and [Co_3Cl] FP regions of $Co_2(OH)_3Cl$ at three temperatures (295, 160 and 5 K), respectively, and (c) and (d) their corresponding regions at three laser power values (40, 20 and 5 mW) at RT.

From this Figure, one can see that qualitative T-dependence of the normal mode frequency is consistent with its laser-power-density-dependence because of the LLH effect. This can help one to predict qualitatively the T-dependence of the normal mode frequency by checking the laser-power-density-dependence at RT if the expensive low-T device is not present.

4.3.2 Normal and abnormal band-shifting phenomena

Before the low-T experimental study, I hoped childishly to obtain some large [OH] related $(\Delta\omega)_{s\text{-}ph}$ to "amplify" the possible SPC effect in the GMF material because the frequencies of [OH] stretching modes at RT are 6~10 times larger than those of [M_3O] stretching modes which are more directly affected by this SPC effect. But from the above mentioned low-T experimental data, we have only observed not more than 15 cm^{-1} of frequency change, which corresponds with an [OH] distance change Δd[OH]≈0.001 Å that can not be well resolved by modern technology, for each sample from RT to 4 K, and found two different change trends, e.g., the "regular" T-dependent behavior (the temperature

coefficient $\Omega \equiv \Delta\omega/\Delta T$ is negative, e.g., redshifting with increasing T) for $M_2(OH)_3X$ with M =Ni and Co like an NTE material, and the "abnormal" T-dependent behavior (Ω is positive e.g., blueshifting with increasing T) for every $Cu_2(OH)_3X$ like an NTE material. Here I define:

$$\Delta T \equiv T_{high} - T_{low} > 0, \text{ and } \Delta\omega \equiv \omega(T_{high}) - \omega(T_{low}). \quad (4.3.1)$$

As two examples, Figs. 4.3.2 (a) and (b) show the T-dependences of [OH] stretching frequencies ω[O**H**] of $M_2(OH)_3X$ (M = Co, Ni) and four $Cu_2(OH)_3X$ samples, respectively.

The reasonable explanation should consider the typical microstructural [OH] environment including a trimeric H-bond group, see Fig. 4.6.3. According to the approximate inverse-proportional relationship between ω[OH] and d(OH),[44] the frequency redshift (blueshift) must correspond to the d(OH) elongation (contraction), and vice versa. When the sample is heated from low T to RT, the d(OH) is ultimately determined by the cooperation effect of several factors affecting it. Considering the influence of $[M^{1,2,3}]$ (M_3 on the left of a [OH], for example, $[OH^2]$ in Fig. 4.6.3) and $[XM^{a,b,c}]$ (also M_3 on the right of the [OH]) on the d(OH), when T is decreasing ($\Delta T<0$), $\Delta\omega$ can be written as:

$$\Delta\omega[OH] = \Delta\omega^0[OH] + \Delta\omega[M_3 \equiv O] + \Delta\omega[H\cdots X \equiv M_3] \quad (4.3.2)$$

where $\Delta\omega^0$[OH] (negative) denotes the pure change regardless of the $[M^{1,2,3}]$ (on the left of [OH]) and $[X \equiv M^{a,b,c}]$ effects on the [OH], $\Delta\omega[M_3 \equiv O]$ (positive) is the change by the weaker repulsive interaction of 3 M^{2+} ions against H^+ because of the averaged $[M_3 \equiv O]$ distance elongation, and $\Delta\omega[H\cdots X \equiv M_3]$ (or equally $\Delta\omega[O\cdots X]$) is the change which can be negative induced by the strengthened H-bond because of the $d(H\cdots X)$ or $d(O\cdots X)$ distance contraction, or positive by the weakened H-bond because of the $d(O\cdots X)$ distance elongation.

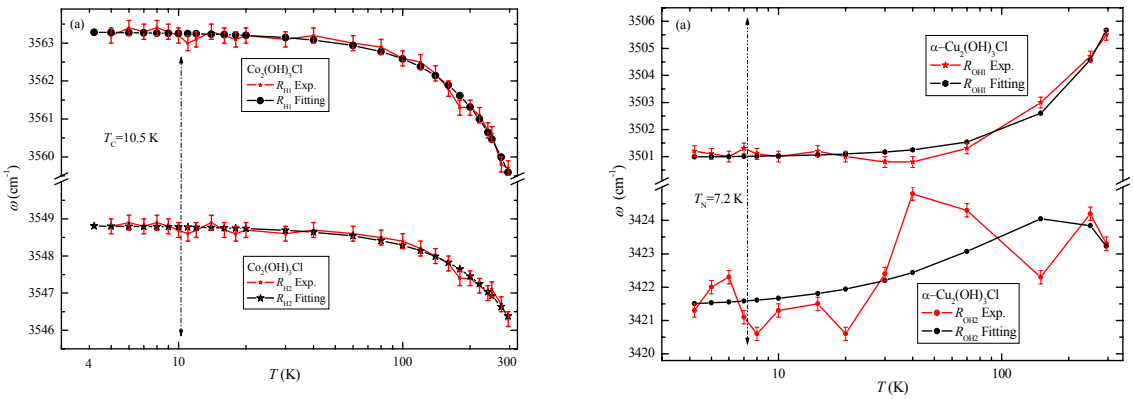

Fig. 4.3.2 T-dependences of two representative [OH] stretching mode frequencies ω[O**H**] for (a) $Co_2(OH)_3Cl$ and (b) α-$Cu_2(OH)_3Cl$.

In order to explain this abnormal band shift (redshift) phenomenon, one should carefully check the microstructure of the hydroxyl environments. Fig. 4.3.3 shows the O_1H_1-site environment as an example (the O^2H^2-site environment is similar with the O^1H^1-site), which includes three Cu ions bounded strongly with O^1 and a Cl-Cu_3 group (the Cl ion is bounded strongly with three Cu ions in the other primitive cell) which connects H^1 with a branch of the newly identified trimeric hydrogen bond.

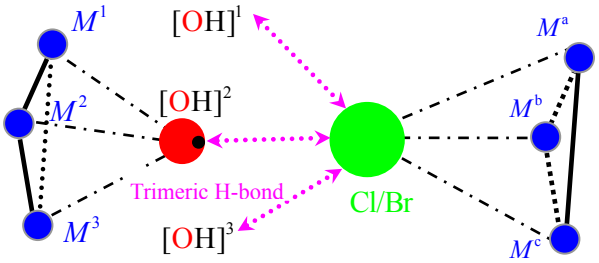

Fig . 4.3.3 Microstructure of the O^1H^1-site environment.

According to the approximate inverse-proportional relationship between the OH stretching mode frequency ω(OH) and the O-H distance d(OH), the redshift of hydroxyl ω(OH) as decreasing T means a corresponding elongation of d(OH). As an example, considering the influence of Cu_3 left the O^1 and Cl-Cu_3 right the H^1 on the d(OH), the change of ω(OH) can be written as:

$$\Delta\omega(\mathrm{OH}) = \Delta\omega^0(\mathrm{OH}) + \Delta\omega(\mathrm{Cu_3O}) + \Delta\omega(\mathrm{H}\cdots\mathrm{ClCu_3}) \qquad (4.3.3)$$

where $\Delta\omega^0$(OH) (positive) denotes the pure change caused by T lowering, $\Delta\omega(Cu_3O)$ (negative) the change by the stronger repulsive interaction of 3 Cu ions against the H^1 because of the Cu_3-O distance contraction, and $\Delta\omega(H\cdots ClCu_3)$ (positive) the change by the weaker H-bond between H^1 and $ClCu_3$ group because of the $ClCu_3$ distance contraction. Here it is the fact that $\Delta\omega(Cu_3O)$ is negative enough that results in the ultimate hydroxyl Raman stretching band redshifting as decreasing T, i.e., $\Delta\omega(\mathrm{OH})\equiv\omega(T_{\mathrm{low}})-\omega(T_{\mathrm{high}})<0$.

4.4 Summary

Through the T-dependent Raman spectroscopic investigation on the MGF material-γ-$Cu_2(OH)_3Cl$, the following results are obtained:

(1) Among eight representative normal modes, the trend as a whole of five frequency variations and all eight width variations in the wide-T range presents a normal thermal expansion behavior of a normal non-magnetic and isolating material. Yet each of the other three frequency variations shows an abnormal behavior (band redshifting with decreasing the temperature), and it has been elucidated by the dominating effect of the trimeric H-bond.

(2) It is found that the commonly used fitting formula of both frequency and width variations resulting from the sum of lattice and phonon-phonon anharmonic terms at the high-T are not suitable for fitting the high frequency modes ([OH] stretching and deforming modes whose wavenumbers are larger than 600 cm^{-1}). A monotonously smoothing binomial function can be selected as a reference.

(3) Obvious evidences of the T_{c1}=18 K magnetic transition are found: the first comes from the apparently anomalous T-dependent Raman band frequencies and linewidths of 8 representative modes below about 18 K because of SPC effect; while the second is based on the quantitative analysis on the pronounced background at high-T and the broad continuum at the intermediate and low-Ts, which verifies the existence of successive transitions and coexistence of partial magnetic order and spin fluctuations of a ps time scale at the intermediate phase in the temperature range of T_{c1}=18 K and T_{c2}=6 K.

(4) It is found that qualitative T-dependence of the normal mode frequency is consistent with its laser-power-density-dependence because of the LLH effect. This can help one to predict qualitatively the T-dependence of the normal mode frequency by checking the laser-power-density-dependence at RT if the expensive low-T device is not present.

(5) For each sample from RT to 4 K, it is found that two different change trends of [OH] stretching frequency exist, e.g., the "regular" T-dependent behavior (redshifting with increasing T) for $M_2(OH)_3X$ with M =Ni and Co like a normal TE material, and the "abnormal" T-dependent behavior (blueshifting with increasing T) for every $Cu_2(OH)_3X$ like an NTE material. These T-dependent behaviors can be qualitatively demonstrated by considering the complex environment of the related trimeric H-bond.

Like other experimental methods, Raman scattering can only provide limited information about the special magnetic order state, and we hope that further experiments, such as the polarization-Raman scattering, NMR, and neutron diffraction experiments on the single crystal in near future can help revealing the exotic nature of the magnetic partly ordered and fast fluctuating state in the range between T_{c1} and T_{c2}.

Chapter 5

Conclusions and outlook

After the four years' work on the IR/Raman spectroscopic experiments, theoretical band assigning investigations and Raman-magnetism relationship studies about the magnetic geometrically frustrated material series - hydroxyl (basic, $[OH/D]^-$) transition metal halides $M_2(OH)_3X$ (M=Cu, Ni, Co; X=Cl, Br), I have obtained some academic results, as given in Sect. 5.1. In Sect. 5.2, I give an outlook.

5.1 Conclusions

First, the author has performed a standard factor group analysis on the space groups of No. 166 (deformed pyrochlore $Co_2(OH)_3Cl$ and $Co_2(OH)_3Br$), No. 62 (Atacamite-type β-$Cu_2(OH)_3Cl$ and β-$Ni_2(OH)_3Cl$) , No. 14 (Clinoatacamite γ-$Cu_2(OH)_3Cl$) and No. 11 (Botallackite-type α-$Cu_2(OH)_3Cl$, α-$Cu_2(OH)_3Br$ and α-$Ni_2(OH)_3Br$), which builds the basic to the complete normal mode assignment.

Second, the author has found that the whole IR or Raman spectrum of each sample can be divided into four well-separated regions: [OH] function group (FG), [OH] correlation peak (CP), metal-O FP_1 and metal-X FP_2 regions, and three kinds of trimeric H-bond exist in these materials according to the structural symmetry. Furthermore the trimeric H-bonds in this series are found to have four subtypes and two more subtypes are predicted to exist in nature. These results may provide a new interesting subject for quantum chemists, material physicists and even quantum magnetic physicists.

Third, in the research of relationship between the [OH] stretching frequency ω and the distance d(OH) of the O and H, the author obtains a practical one: ω=3600-10000(d-0.961) cm^{-1}, and therefore $\Delta\omega/\Delta d$ = 10 cm^{-1}/0.001Å. This relationship can help check the correctness of the distance d(OH/D) obtained in the crystal structure measurements.

Forth, in the low-T Raman scattering experiments on γ-$Cu_2(OH)_3Cl$, by measuring the T-dependent (295 - 4 K) full spectral profiles and main representative modes in spectral regions from 4000 to 95 cm^{-1}, the author has obtained a rough estimation of frequency spin-phonon coupling parameter λ_{max} of about 3 cm^{-1} and linewidth spin-phonon coupling parameter γ_{max} of about 6 cm^{-1}, and the anomalous T-dependent trend of the [OH] stretching mode frequencies based on the consideration of the presence of the asymmetric trimeric H-bond has shown the existence of interaction between the high energy [OH] phonon modes

and low-energy magnetic excitations through the Cu-O-Cu superexchange and trimeric H-bonds, which is in contradiction to the recent unsealed assertion to support the practice of ignoring the high energy [OH] stretching and deformation modes. It is also found that there exists the unsuitability of the related fitting equations of the common spin-phonon coupling theory at high frequency.

Fifth, the author has observed probably signatures of successive magnetic transitions near T_{c1} =18 K and T_{c2} =6.4 K in the Raman band frequencies and peak widths of the representative modes.

Sixth, the author has observed a pronounced Raman spectroscopy background featuring a broad continuum at all temperatures. A quantitative analysis reveals that spin fluctuations may exist on a picosecond time scale in the intermediate phase. This is likely to give a reasonable explanation of the fact that why only a small entropy release occurs at T_{c1}=18 K although a long-range order is formed.

Seventh, T-dependence of each Raman [OH] stretching frequency is also found to behave normally (for *M*= Cu) or abnormally (for *M*= Co and Ni) for different materials. These T-dependent behaviors can be qualitatively demonstrated by considering the complex environment of the related trimeric H-bond.

5.2 Outlook

In the condition that the preliminary evaluation of dynamic coupling of lattice vibration and magnetism in polycrystalline γ-$Cu_2(OH)_3Cl$ sample has been obtained, I think the following research should be continued to do:

Further modeling the correlation of the lattice vibration and magnetism in γ-$Cu_2(OH)_3Cl$ is performed to clarify the underlying physics of the exotic magnetic quantum states.

In order to precisely estimate the correlation, further polarized Raman experimental measurements on prepared γ-$Cu_2(OH)_3Cl$ single crystals are required. In the meanwhile the other existing magnetic and dielectric properties, such as multiferroicity, maybe also clarified.

Appendix A

Crystal structure parameters of the $M_2(OH/D)_3X$

All the distance parameters are in units of Å without giving the error ranges, and the relative distance and degree changes Δ_d(‰) and Δ_θ(‰) are defined to be

$$\Delta_d \equiv \frac{d(RT)-d(LT)}{d(LT)};\ \Delta_\theta \equiv \frac{\theta(RT)-\theta(LT)}{\theta(LT)}.$$

Their crystal structures are shown in the main text. The experiential values of the related ionic radii are also useful for evaluating the interaction intensity among the ions: $R(Co^{2+})$=0.74 Å, $R(Ni^{2+})\approx R(Cu^{2+})$=0.72 Å, $R(O^{2-})$=1.40 Å, $R(Cl^{-})$=1.81 Å, $R(Br^{-})$=1.95 Å.

Table A1. Crystal structure parameters of the D_{3d}^5 (No. 166) $Co_2(OH/D)_3X$ ($Co_2(OH/D)_3Cl$ and $Co_2(OH/D)_3Br$).

	$Co_2(OH/D)_3Cl$			$Co_2(OH/D)_3Br$		
	295 K	20 K	Δ (‰)	295 K	5.2 K	Δ (‰)
$a=b$	6.8370	6.8411	−0.6	6.9717	6.9590	+1.8
c	14.4965	14.4729	+1.6	14.6637	14.6197	+3.0
V(Å^3)	586.8536	586.6045	+0.5	617.24	613.157	+6.6
$d(Co^{K,K})$	3.4185	3.4205	−0.6	3.4858	3.4795	+1.8
$d(Co^{K,T})$	3.1198	3.1174	+0.7	3.1659	3.1579	+2.5
$d(O\text{-}Co^{K})$	2.0785	2.0520	+13	2.0840	2.0704	+6.6
$d(O\text{-}Co^{T})$	2.1060	2.1150	−4.2	2.1366	2.0952	+19.8
$d(X\text{-}Co^{K})$	2.5986	2.5853	+5.1	2.6998	2.6081	+35.2
d(O-H/D)	0.966	0.967	−1.0	0.969	0.9747	−5.8
$d(X\cdots O)$	3.1771	3.234	−18	3.2273	3.3364	−32.7
$d(X\cdots H/D)$	2.312	~	~	2.341	2.4341	−38.2
$\theta(Co^{K}\text{-}O\text{-}Co^{K})$	110.64°	112.93°	−20	113.51°	114.34°	−7.3
$\theta(Co^{K}\text{-}O\text{-}Co^{T})$	96.41°	96.86°	−4.6	97.19°	98.59°	−14.2
$\theta(Co^{K}\text{-}X\text{-}Co^{K})$	82.26°	82.83°	−6.9	80.42°	83.68°	−39.0

Table A2. Crystal structure parameters of the D_{2h}^{16} (No. 62) $M_2(OH/D)_3Cl$ (Natural β-$Cu_2(OH)_3Cl$ and β-$Ni_2(OH)_3Cl$)

Atacamite β-$Cu_2(OH)_3Cl$				β-$Ni_2(OH)_3Cl$			
	295 K	1.4 K	Δ(‰)		295 K	1.4 K	Δ(‰)
a	6.0279	---	---	a	6.2005	6.160	+6.6
b	6.8638	---	---	b	6.7467	6.702	+6.7
c	9.1156	---	---	c	9.1008	9.043	+6.4
V(Å^3)	377.158	---	---	V(Å^3)	380.716	373.408	+19.6
$d(Cu^{1a}\text{-}Cu^{1b})$	3.4319	---	---	$d(Ni^{1a}\text{-}Ni^{1b})$	3.373	3.351	+6.6
$d(Cu^{1a,b}\text{-}Cu^{2a})$	3.1208	---	---	$d(Ni^{1a,b}\text{-}Ni^{2a})$	3.103	3.094	+2.9
$d(Cu^{1a,b}\text{-}Cu^{2b})$	3.3652	---	---	$d(Ni^{1a,b}\text{-}Ni^{2b})$	3.373	3.343	+9.0
$d(Cu^{2a}\text{-}Cu^{2b})$	3.0160	---	---	$d(Ni^{2a}\text{-}Ni^{2b})$	3.100	3.080	+6.5
$d(O^{1}\text{-}Cu^{2a})$	2.4106	---	---	$d(O^{1}\text{-}Ni^{2a})$	2.123	2.151	–13.0
$d(O^{1}\text{-}Cu^{1a,b})$	1.9400	---	---	$d(O^{1}\text{-}Ni^{1a,b})$	2.205	2.006	+99.2
$d(O^{2a/b}\text{-}Cu^{2a})$	2.0306	---	---	$d(O^{2}\text{-}Ni^{2a})$	2.039	2.014	+12.4
$d(O^{2a/b}\text{-}Cu^{2b})$	1.9831	---	---	$d(O^{2}\text{-}Ni^{2b})$	2.070	2.065	+2.4
$d(O^{2a/b}\text{-}Cu^{1a/b})$	2.0189	---	---	$d(O^{2}\text{-}Ni^{1a})$	2.030	2.017	+6.4
$d(Cl\text{-}Cu^{2b})$	2.7517	---	---	$d(Cl\text{-}Ni^{2b})$	2.562	2.514	+19.1
$d(Cl\text{-}Cu^{1a,b})$	2.7742	---	---	$d(Cl\text{-}Ni^{1a,b})$	2.520	2.493	+10.8
$d(O^{1}\text{-}H/D^{1})$	---	---	---	$d(O^{1}\text{-}H/D^{1})$	0.952	0.960	–8.3
$d(O^{2}\text{-}H/D^{2})$	---	---	---	$d(O^{2}\text{-}H/D^{2})$	0.997	0.994	+3.0
$d(Cl\cdots O^{1})$	3.0410	---	---	$d(Cl\cdots O^{1})$	3.271	3.264	+2.1
$d(Cl\cdots O^{2})$	3.0588	---	---	$d(Cl\cdots O^{2})$	3.230	3.228	+0.6
$d(Cl\cdots H/D^{1})$	---	---	---	$d(Cl\cdots H/D^{1})$	2.346	2.322	+10.3
$d(Cl\cdots H/D^{2})$	---	---	---	$d(Cl\cdots H/D^{2})$	2.283	2.281	+0.9
$\theta(Cu^{1a}\text{-}O^{1}\text{-}Cu^{1b})$	124.37°	---	---	$\theta(Ni^{1a}\text{-}O^{1}\text{-}Ni^{1b})$	112.8	---	---
$\theta(Cu^{2a}\text{-}O^{1}\text{-}Cu^{1a,b})$	91.00°	---	---	$\theta(Ni^{2a}\text{-}O^{1}\text{-}Ni^{1a,b})$	96.8	---	---
$\theta(Cu^{1a/b}\text{-}O^{2}\text{-}Cu^{2a})$	97.41°	---	---	$\theta(Ni^{1a/b}\text{-}O^{2}\text{-}Ni^{2a})$	99.4	---	---
$\theta(Cu^{1a/b}\text{-}O^{2}\text{-}Cu^{2b})$	100.82°	---	---	$\theta(Ni^{1a/b}\text{-}O^{2}\text{-}Ni^{2b})$	110.7	---	---
$\theta(Cu^{2a}\text{-}O^{2}\text{-}Cu^{2b})$	114.45°	---	---	$\theta(Ni^{2a}\text{-}O^{2}\text{-}Ni^{2b})$	97.9	---	---

Table A3. Crystal structure parameters of the C_{2h}^5 (No. 14) γ-$Cu_2(OH/D)_3Cl$

γ-$Cu_2(OH/D)_3Cl$							
	RT[a)]	25 K [b)]	Δ(‰)		RT[a)]	25 K [b)]	Δ(‰)
a	6.1636	6.1517	+1.9	V(Å^3)	377.50	377.31	+0.5
b	6.8165	6.8261	–1.4	$d(O^1\text{-}H/D^1)$	---	0.8707	---
c	9.1140	9.1169	–0.3	$d(O^2\text{-}H/D^2)$	---	1.0351	---
β	99.65°	99.75°	–1.0	$d(O^3\text{-}H/D^3)$	---	1.0472	---
$d(Cu^{K1}\text{-}Cu^{K2})$	3.419	3.4262	–2.1	$d(O^1\text{-}Cu^{K2})$	1.960	1.9067	+28.0
$d(Cu^{K1}\text{-}Cu^{K3})$	3.411	3.4143	–1.0	$d(O^1\text{-}Cu^{K3})$	1.896	1.9733	–39.2
$d(Cu^{K1}\text{-}Cu^{T})$	2.994	3.0987	+33.8	$d(O^1\text{-}Cu^{T})$	2.382	2.3303	+22.2
$d(Cu^{K2}\text{-}Cu^{K1})$	3.419	3.4262	–2.1	$d(O^2\text{-}Cu^{K1})$	1.947	1.9521	–2.6
$d(Cu^{K2}\text{-}Cu^{K3})$	3.410	3.4041	+1.7	$d(O^2\text{-}Cu^{K3})$	2.078	2.0152	+31.2
$d(Cu^{K2}\text{-}Cu^{T})$	3.081	3.0758	+1.7	$d(O^2\text{-}Cu^{T})$	1.991	1.9771	+7.0
$d(Cu^{K3}\text{-}Cu^{K1})$	3.411	3.4143	1.0	$d(O^3\text{-}Cu^{K1})$	2.021	1.9805	+20.4
$d(Cu^{K3}\text{-}Cu^{K2})$	3.410	3.4041	+1.7	$d(O^3\text{-}Cu^{K2})$	2.047	1.9833	+32.1
$d(Cu^{K3}\text{-}Cu^{T})$	3.106	2.9955	+36.9	$d(O^3\text{-}Cu^{T})$	1.984	1.9770	+3.5
$d(Cl\text{-}Cu^{K1})$	2.758	2.7447	+4.8	$\theta(Cu^{K2}\text{-}O^1\text{-}Cu^{K3})$	124.3°	124.0°	+2.4
$d(Cl\text{-}Cu^{K2})$	2.776	2.7756	+0.1	$\theta(Cu^{K2}\text{-}O^1\text{-}Cu^{T})$	89.9°	93.4°	–37.5
$d(Cl\text{-}Cu^{K3})$	2.831	2.7980	+11.8	$\theta(Cu^{K3}\text{-}O^1\text{-}Cu^{T})$	92.4°	90.8°	+17.6
$d(Cl\cdots O^1)$	3.080	3.0839	–2.0	$\theta(Cu^{K1}\text{-}O^2\text{-}Cu^{K3})$	115.8°	118.7°	–24.4
$d(Cl\cdots O^2)$	3.079	3.1668	–27.7	$\theta(Cu^{K1}\text{-}O^2\text{-}Cu^{T})$	99.0°	104.1°	–49.0
$d(Cl\cdots O^3)$	2.994	3.0954	–32.8	$\theta(Cu^{K3}\text{-}O^2\text{-}Cu^{T})$	99.5°	97.2°	+23.7
$d(Cl\cdots H/D^1)$	---	2.2504	---	$\theta(Cu^{K1}\text{-}O^3\text{-}Cu^{K2})$	114.3°	118.3°	+33.8
$d(Cl\cdots H/D^2)$	---	2.2055	---	$\theta(Cu^{K1}\text{-}O^3\text{-}Cu^{T})$	96.8°	102.0°	–51.0
$d(Cl\cdots H/D^3)$	---	2.0674	---	$\theta(Cu^{K2}\text{-}O^3\text{-}Cu^{T})$	99.7°	98.2°	+15.3

[a)] Refined in 2008, unpublished.

[b)] O^1 and O^3 in the common 25 K Vesta file may be adverse to those in RT and $d(O^1\text{-}H/D^1)$ may be very small according to the spectral data.

Table A4. Crystal structure parameters of the C_{2h}^2 (No. 11) $M_2(OH/D)_3X$ (α-$Cu_2(OH/D)_3Cl$, α-$Cu_2(OH/D)_3Br$ and α-$Ni_2(OH/D)_3Br$).

	α-$Cu_2(OH)_3Cl$			α-$Cu_2(OH/D)_3Br$			α-$Ni_2(OH/D)_3Br$		
	RT[a)]	25 K[a)]	Δ(‰)	RT[a)]	25 K[a)]	Δ(‰)	RT[a)]	19 K[b)]	Δ(‰)
a	5.6295	5.6347	–0.9	5.6446	5.6366	+1.4	5.5269	5.5121	+2.7
b	6.1197	6.1243	–0.8	6.1408	6.1465	–0.9	6.3655	6.3511	+2.3
c	5.7181	5.7221	–0.7	6.0640	6.0297	+5.7	5.8689	5.8215	+8.1
β	93.11°	93.02°	+0.9	93.78°	93.35°	+4.6	90.76°	90.59°	+1.9
V(Å^3)	196.708	197.192	–2.5	209.774	208.546	+5.9	206.464	203.802	+13.1
$d(M^{1a}$-$M^{1b})$	3.0599	3.0621	–0.7	3.0704	3.073	22.8	3.1827	3.175	+2.5
$d(M^{1a}$-$M^{2a})$	3.1865	3.1990	–3.9	3.1911	3.183	+2.5	3.1241	3.128	–1.3
$d(M^{1a}$-$M^{2b})$	3.2219	3.2148	+2.2	3.2348	3.237	–0.6	3.2545	3.234	+6.3
$d(M^{2a}$-$M^{2b})$	3.0624	3.0640	–0.5	3.0716	3.074	–0.8	3.1870	3.178	+2.8
$d(M^{2a}$-$M^{1a,b})$	3.1865	3.1990	–3.9	3.1911	3.183	+2.5	3.1241	3.128	–1.3
$d(M^{2b}$-$M^{1a,b})$	3.2219	3.2148	+2.2	3.2348	3.231	+1.2	3.2545	3.234	+6.3
$d(O^1$-$M^{1a,b})$	1.9360	1.9578	–11.1	1.921	1.915	+3.1	2.0006	2.008	–3.7
$d(O^1$-$M^{2a})$	2.3641	2.3927	–11.9	2.345	2.351	2.6	2.0588	2.047	+5.9
$d(O^2$-$M^{1b})$	2.0133	2.0436	–14.8	2.014	1.996	+9.0	2.0199	2.055	–17.0
$d(O^2$-$M^{2a})$	2.0092	1.9425	+34.3	2.038	1.984	+27.2	2.0718	2.026	+22.7
$d(O^2$-$M^{2b})$	1.9737	1.9584	+7.8	1.986	2.005	–9.5	2.0589	2.010	+24.4
$d(X$-$M^{1a,b})$	2.7840	2.7928	+3.2	2.9364	2.919	–6.0	2.6534	2.565	+34.5
$d(X$- $M^{2b})$	2.7221	2.7708	17.6	2.8715	2.863	+2.7	2.6705	2.604	+25.5
$d(O^1$-$H^1)$	---	0.8448	---	---	0.971	---	---	0.910	---
$d(O^2$-$H^2)$	---	1.0318	---	---	0.980	---	---	0.932	---
$\theta(M^{1a}$-O^1-$M^{1b})$	104.41°	102.89°	+14.8	106.1°	106.7°	–5.6	105.39°	104.5°	+8.5
$\theta(M^{2a}$-O^1-$M^{1a,b})$	95.11°	94.75°	+3.8	96.4°	96.0°	+4.2	100.62°	100.9°	–2.8
$\theta(M^{2a}$-O^2-$M^{2b})$	100.50°	103.52°	–29.2	99.48°	100.9°	–14.0	100.98°	103.9°	–28.1
$\theta(M^{1b}$-O^2-$M^{2a})$	107.82°	106.72°	+10.3	107.90°	108.8°	–8.3	99.54°	100.6°	–10.5
$\theta(M^{1b}$-O^2-$M^{2b})$	104.77°	106.87°	–19.7	103.88°	105.4°	–14.2	105.85°	104.9°	+9.1
$\theta(M^{1a}$-X-$M^{1b})$	66.67°	66.49°	+2.7	63.04°	63.52°	–7.6	73.70°	76.48°	–36.3
$\theta(M^{2b}$-X-$M^{1a,b})$	71.61°	70.19°	+20.2	67.68°	68.08°	–5.9	75.36°	77.50°	–27.6
$d(X\cdots O^1)$	3.3151	3.2349	+24.8	3.525	3.484	+11.8	3.6016	3.640	–10.5
$d(X\cdots O^{2a,b})$	3.2032	3.2495	–14.2	3.310	3.348	–11.4	3.5107	3.635	–34.1
$d(X\cdots H^1)$	---	2.4225	---	---	2.599	---	---	2.828	---
$d(X\cdots H^{2a,b})$	---	3.3184	---	---	2.466	---	---	2.776	---

Appendix B

IR and Raman spectral data of the $M_2(OH/D)_3X$

Each frequency (wavenumber) is in unit of cm^{-1}, and the related data of the deuterized samples are given in the related figures of this main text.

Table B1. IR and Raman spectral data of the D_{3d}^5 (No. 166) $Co_2(OH)_3X$ ($Co_2(OH)_3Cl$ and $Co_2(OH)_3Br$).

	$Co_2(OH/D)_3Cl$			$Co_2(OH/D)_3Br$			
region	IR [a]	Raman (RT)[a]	Raman (4 K) [b]	IR [c]	Raman (RT) [c]	Raman (4 K) [b]	Suggested mode (Exp. No./FGA No.)
FG	3566	3559.7	3563.2	3550	3539.8	3543.7	IR, R: [OH]
	3549	3546.3	3548.8	3530	3528.2	3530.4	(2/2)
CP	843	828.2	822.9	840	820.9	821.1	IR, R: [OH]
	723	694.0	699.0	727	688.5	697.1	(3/3)
	702	652.4	654.2	707	655.0	659.4	
FP_1		455.1	461.3		480.5	486.8	IR:
	426	430.2	438.4		454.8	461.5	$[Co_3O]$, $[Co^KO_4Cl_2]$,
	<400	396.9	405.5	416	424.0	431.4	$[Co^TO_6]$
		334.2	336.7	<400	331.3	337.7	R: $[Co_3O]$
		240.0	251.6		223.8	212.6	
FP_2	<200	166.0	169.7	<200			IR, R: $[Co_3X]$
		131.4	132.8		118.6	121.3	
		<95	<95		<95	<95	

Data sources and corresponding experimental conditions are presented in the following:

[a] Fig. 3.2.2; [b] Unpublished; [c] Fig. 3.2.5.

Table B2. IR and Raman spectral data of the D_{2h}^{16} (No. 62) $M_2(OH)_3Cl$ (Natural β-$Cu_2(OH)_3Cl$ and β-$Ni_2(OH)_3Cl$).

	Natural β-$Cu_2(OH)_3Cl$					β-$Ni_2(OH)_3Cl$			
region	IR [a]	IR [b]	Raman (RT) [c]	Raman (RT)[d]	Raman (4 K) [d]	IR [e]	Raman (RT)[d]	Raman (4 K)[d]	Suggested mode
FG	3442	3436	3433	3434.3	3431.2	3593	3586.9	3592.6	IR, R
	3358		3349	3349.1	3340.9	3577	3576.7	3580.1	[OH]
	3334	3330	3328	3328.6	3316.1				
	3220			3205.0					
CP	985	984	987		982.4	825	830.0	833.0	
	948	945	974	976.0		800	823.4	825.1	
	914	913	912	912.5	922.3	746	798.5	802.0	
	893	890	864	846.8	852.2	729	758.0	758.6	
	864	869	845	823.4	826.4	692	692.8	696.6	
	848	844	827			674	674.6	677.3	
	819	820	819						
FP_1	608	608			-				[Ni_3O^a]
	596	590	586	595.0					[Ni_3O^b]
		566							
	513		511	514.0	516.2				
	480						476.1	479.8	
	459		451	451.2	455.6	456	451.2	455.8	
	416	<400		413.8	402.0	448	442.2	446.0	
	<400					437			
						421			
			393			404	410.2	413.3	
			362	361.8	367.0	365	378.2	385.8	
						351	353.5	357.4	
						<350	340.6	342.5	
							316.0	322.4	
			267	268.6	278.0		288.8	293.0	
			240	-	248.4				
			217	220.8	224.2				
FP_2	<200	<200	160				188.0	191.9	
			149	149.8	152.2		172.0	175.4	[$M^aO_4Cl_2$]
			138	138.4	139.1		141.5	144.0	[M^bO_5Cl]
			120	120.3	120.4				[M_3Cl]
				106.0	107.6		103.0	103.0	
			<100		<95.0		<95.0	<95.0	

Data sources and corresponding experimental conditions are presented in the following:

[a] Fig. 3.3.2; [b] Table of Ref. 58; [c] Table of Ref. 59; [d] Unpublished; [e] Fig. 3.3.4.

Table B3. IR and Raman spectral data of the C_{2h}^5 (No. 14) γ-$Cu_2(OH)_3Cl$.

region	γ-$Cu_2(OH)_3Cl$					
	IR [a]	IR[b]	Raman (RT) [c]	Raman (RT)[d]	Raman (4 K) [d]	Suggested mode
FG			3475	3457.3	3444.0	IR, Raman:
	3446	3440	3443	3441.8	3437.0	[OH] stretching
	3360	3359	3357	3357.5	3347.7	
				3319.2	3306.4	
	3310	3300	3314	3311.0	3297.8	
CP	987	984	969	972.5	983.2	IR, Raman:
	920		927	929.1	936.2	[OH] Bending
	864	890	892	894.6	901.5	
	827		866	870.0	875.4	
		732	799	800.0	805.8	
FP_1	580	577	576	574.0	580.0	IR: (4/15)
	517	---	511	513.8	517.8	[Cu_3O], [CuO_6], [CuO_4Cl_2]
			---	500.0	504.0	
	457		445	445.0	451.5	Raman: (10/18)
	416		420	422.0	423.0	[Cu_3O]
	<400		---	373.8	375.4	
			364	366.3	366.0	
			256	260.0	264.2	
			206	---	209.0	
			193	196.0	---	
FP_2	<200	---	183	185.3	192.6	Raman: (6/6)
	IR:		165	168.0	171.4	[Cu_3Cl]
	6 bands		---	148.0	150.8	
			142	141.3	142.5	
			118	118.4	118.8	
			---	96.5	98.0	

Data sources and corresponding experimental conditions are presented in the following figures:

[a] Fig. 3.4.1; [b] Table in Ref. 59; [c] Table in Ref. 59; [d] Fig. 4.2.1.

Table B4. IR and Raman spectral data of the C_{2h}^2 (No. 11) $M_2(OH)_3X$ (α-$Cu_2(OH)_3Cl$, α-$Cu_2(OH)_3Br$ and α-$Ni_2(OH)_3Br$).

	α-$Cu_2(OH)_3Cl$			α-$Cu_2(OH)_3Br$			α-$Ni_2(OH)_3Br$			
region	IR[a)]	Raman (RT)[b)]	Raman (4 K)[b)]	IR[c)]	Raman (RT)[b)]	Raman (4 K)[b)]	IR[d)]	Raman (RT)[b)]	Raman (4 K)[b)]	Suggested mode
	3510	3505.5	3501.2	3508	3514.0	3509.4	3593	3586.8	3589.2	
	3427	3434.2	3429.7		3417.2	3413.5	3577			IR, Raman:
FG		3423.3	3421.3							[OH] stretching
		3416.2	3406.0	3398	3407.0	3400.9				
		3350.0	3342.0							
	985	975.0	982.5							IR, Raman:
		---	920.8	896	888.0	888.4				[OH] bending
	902	902.0	902.1	850	859.9	863.8				
		895.6	893.5	802	834.0	837.9				
CP	860	857.6	861.6				807	785.1	790.0	
	817		826.0				762	781.6	785.6	
	785	790.0	806.0				732	760.4	763.4	
	704		795.5	779	781.0	787.0	692	706.2	716.8	
	596	678.0	685.0	680	658.0	667.0	678	675.1	697.0	
	516	512.0	516.0	532	513.1	517.0				IR: (4/15)
		---	503.5	511	499.5	499.0				$[M_3O]$, $[MO_6]$,
		475.8	477.8		477.0	478.0	467			$[MO_4X_2]$
	428	448.0	451.6	422	448.5	453.0		457.8	462.5	
	<400	400.0	403.3	<400	395.7	399.8	412	434.8	439.8	Raman: (10/18)
FP_1		---	361.0				<400	374.2	379.6	$[M_3O]$
		323.4	326.0		320	324.0		332.2	336.2	
		275.5	281.0		279.0	285.0		307.1	313.0	
		250.5	254.5		250.0	253.8		282.9	291.8	
								---	270.3	
								253.8	259.2	
	<200	176.1	177.5	<200	174.7	175.9	<200			Raman: (6/6)
		154.5	158.1							$[Cu_3Cl]$,
FP_2		---	143.0					134.2	136.4	$[Ni_3Br]$
		116.2	116.8		112.8	114.0		114.0	116.0	
		98.5	98.7		102.8	104.8		101.6	103.0	

Data sources and corresponding experimental conditions are presented in the following figures:

[a)] Fig. 3.5.1; [b)] Unpublished; [c)] Fig. 3.5.5; [d)] Fig. 3.5.9.

References

[1] C. Kittel. Introduction to Solid State Physics, 8th Edition, John Wiley & Sons, Inc., New York 2005.

[2] J. M. D. Coey. Magnetism and Magnetic Materials. Cambridge University Press, London 2010.

[3] M. C. Sekhar, S. Lee, G. Choi, C. Lee, and J. G. Park. Doping effects of hexagonal manganites $Er_{1-x}Y_xMnO_3$ with triangular spin structure. Phys. Rev. B 72, 014402 (2005).

[4] J. S. Gardner, M. J. P. Gingras, and J. E. Greedan. Magnetic pyrochlore oxides. Rev. Mod. Phys. 82, 53-107 (2010).

[5] K. Tomiyasu, J. Fukunaga, and H. Suzuki. Magnetic short-range order and reentrant-spin-glass-like behavior in $CoCr_2O_4$ and $MnCr_2O_4$ by means of neutron scattering and magnetization measurements. Phys. Rev. B 70, 214434 (2004)

[6] J. E. Greedan. Frustrated rare earth magnetism: Spin glasses, spin liquids and spin ices in pyrochlore oxides. J. All. Com. 408-412, 444-455 (2006).

[7] L. A. Mol, R. L. Silva, R. C. Silva, A. R. Pereira, W. A. Moura-Melo, and B.V. Costa. Magnetic monopole and string excitations in two-dimensional spin ice. J. Appl. Phys. 106, 063913 (2009).

[8] M. P. Shores, B. M. Bartlett, and D. G. Nocera. Spin-Frustrated Organic-Inorganic Hybrids of Lindgrenite. J. Am. Chem. Soc. 127, 17986-17987(2005).

[9] D. Zhou, C. R. Wiebe, J. A. Janik, L. Balicas, Y. J. Yo, Y. Qiu, J. R. D. Copley, and J. S. Gardner. Dynamic Spin Ice: $Pr_2Sn_2O_7$. Phys. Rev. Lett. 101, 227204 (2008).

[10] S. M. Yan, D. A. Huse, and S. R. White. Spin-Liquid Ground State of the S = 1/2 Kagome Heisenberg Antiferromagnet. Science 332, 1173-1176 (2011).

[11] S. T. Bramwell, S. R. Giblin, S. Calder, R. Aldus, D. Prabhakaran, and T. Fennell. Measurement of the charge and current of magnetic monopoles in spin ice. Nature 461, 956-960 (2009).

[12] L. A. Mol, R. L. Silva, R. C. Silva, A. R. Pereira, W. A. Moura-Melo, and B.V. Costa. Magnetic monopole and string excitations in two-dimensional spin ice. J. Appl. Phys. 106, 063913 (2009).

[13] S. Yoshida, K. Nemoto, and K. Wada. Application of the Cluster Variation Method to Spin Ice Systems on the Pyrochlore Lattice. J. Phys. Soc. Jpn. 71, 948-954 (2002).

[14] J. Snyder, J. S. Slusky, R. J. Cava, and P. Schiffer. Dirty spin ice: The effect of dilution on spin freezing in $Dy_2Ti_2O_7$. Phys. Rev. B 66, 064432 (2002).

[15] R. Higashinaka, H. Fukazawa, and Y. Maeno. Anisotropic release of the residual

zero-point entropy in the spin ice compound $Dy_2Ti_2O_7$:Kagome ice behavior. Phys. Rev. B 68, 014415 (2003).

[16] A. L. Cornelius, B. E. Light, R.S. Kumar, M. Eichenfield, T. Dutton, R. Pepin, and J. S. Gardner. Disturbing the spin liquid state in $Tb_2Ti_2O_7$: Heat capacity measurements on rare earth titanates. Physica B 359-361, 1243-1245 (2005).

[17] C. Urano, M. Nohara, S. Kondo, F. Sakai, H. Takagi, T. Shiraki, T. Okubo. LiV_2O_4 Spinel as a Heavy-Mass Fermi Liquid: Anomalous Transport and Role of Geometrical Frustration. Phys. Rev. Lett. 85, 1052-1055 (2000).

[18] B. Crard, Y. Grandati, and H. Mohrbach. Dirac monopole with Feynman brackets. Physics Letters A 254, 133-136(1999).

[19] M. J. P. Gingras. Observing Monopoles in a Magnetic Analog of Ice. Science 326, 375-376 (2009).

[20] S. Sondhi. Wien route to monopoles. Nature 461, 888-889 (2009).

[21] H. Tsunetsugu. Antiferromagnetic Quantum Spins on the Pyrochlore Lattice. J. Phys. Soc. Jpn. 70, 640-643 (2001).

[22] E. MacLaughlin, M. S. Rose, J. E. Anderson, L. Shu, R. H. Heffner, T. Kimura, G. D. Morris, and O. O. Bernale. Critical slowing down in the geometrically frustrated pyrochlore antiferromagnet $Gd_2Ti_2O_7$. Physica B 374-375, 142-144 (2006).

[23] S. R. Giblin, J. D. M. Champion, H. D. Zhou, C. R. Wiebe, J. S. Gardner, I. Terry, S. Calder, T. Fennell, and S. T. Bramwell. Static Magnetic Order in $Tb_2Sn_2O_7$ Revealed by Muon Spin Relaxation with Exterior Muon Implantation. Phys. Rev. Lett. 101, 237201 (2008).

[24] D. Y. Kim, S. K. Kwon, and R. Ahuja. Ab initio study of the pressure effects on $R_2Mo_2O_7$. J. Phys. Chem. Solids 69, 2245-2247 (2008).

[25] G. Ehlers, E. Mamontov, M. Zamponi, K. C. Kam, J. S. Gardner. Direct Observation of a Nuclear Spin Excitation in $Ho_2Ti_2O_7$. Phys. Rev. Lett. 102, 016405 (2009).

[26] P. H. Conlon and J. T. Chalker. Spin Dynamics in Pyrochlore Heisenberg Antiferromagnets. Phys. Rev. Lett. 102, 237206 (2009).

[27] J. P. Clancy, J. P. C. Ruff, S. R. Dunsiger, Y. Zhao, H. A. Dabkowska, J. S. Gardner, Y. Qiu, J. R. D. Copley, T. Jenkins, and B. D. Gaulin. Revisiting static and dynamic spin-ice correlations in $Ho_2Ti_2O_7$ with neutron scattering. Phys. Rev. B 79, 014408 (2009).

[28] S. Onoda and Y. Tanaka. Quantum Melting of Spin Ice: Emergent Cooperative Quadrupole and Chirality. Phys. Rev. Lett. 105, 047201 (2010).

[29] M. L. Dahlberg, M. J. Matthews, P. Jiramongkolchai, R. J. Cava, and P. Schiffer.

Low-temperature dynamic freezing and the fragility of ordering in $Tb_2Sn_2O_7$. Phys. Rev. B 83, 140410 (2011).

[30] L. Savary and L. Balents. Coulombic Quantum Liquids in Spin-1/2 Pyrochlores. Phys. Rev. Lett.108, 037202 (2012).

[31] T. Katsufuji, S. Mori, M. Masaki, Y. Moritomo, N. Yamamoto, and H. Takagi. Dielectric and magnetic anomalies and spin frustration in hexagonal RMnO$_3$ (R=Y, Yb, and Lu). Phys. Rev. B 64, 104419 (2001).

[32] M. Fiebig, C. Degenhardt, and R.V. Pisarev. Interaction of Frustrated Magnetic Sublattices in $ErMnO_3$. Phys. Rev. Lett. 88, 027203 (2002).

[33] A. Laref and S. J. Luo. Magnetic Excitation and Phonon Dispersion in $LaCoO_3$ Compound. J. Phys. Soc. Jpn. 79, 064702 (2010).

[34] M. Mochizuki, N. Furukawa, and N. Nagaosa. Spin Model of Magnetostrictions in Multiferroic Mn Perovskites. Phys. Rev. Lett. 105, 037205 (2010).

[35] N. O. Golosova, D. P. Kozlenko, A. I. Kolesnikov, V. Yu. Kazimirov, M. B. Smirnov, Z. Jirak, and B. N. Savenko. Evolution of the phonon density of states of $LaCoO_3$ over the spin state transition. Phys. Rev. B 83, 214305 (2011).

[36] F.-K. Chiang, M.-W. Chu, F. C. Chou, H. T. Jeng, H. S. Sheu, F. R. Chen, and C. H. Chen. Effect of Jahn-Teller distortion on magnetic ordering in $Dy(Fe,Mn)O_3$ perovskites. Phys. Rev. B 83, 245105 (2011).

[37] M. Ramazanoglu, W. Ratcliff II, Y. J. Choi, S. Lee, S.-W. Cheong, and V. Kiryukhin. Temperature-dependent properties of the magnetic order in single-crystal $BiFeO_3$. Phys. Rev. 83, 174434 (2011).

[38] A. Daga., Smita Sharma, and K. S. Sharma. First Principle Study of Cubic $SrMO_3$ Perovskites (M = Ti, Zr, Mo, Rh, Ru). J. Mod. Phys. 2, 612-816 (2011).

[39] E. E. Rodriguez, F. Poineau, A. Llobet, B. J. Kennedy, M. Avdeev, G. J. Thorogood, M. L. Carter, R. Seshadri, D. J. Singh, and A. K. Cheetham. High Temperature Magnetic Ordering in the 4*d* Perovskite $SrTcO_3$. Phys. Rev. Lett. 106, 067201 (2011).

[40] I. V. Solovyev. Magnetic structure of the noncentrosymmetric perovskites $PbVO_3$ and $BiCoO_3$: Theoretical analysis. 85, 054420 (2012).

[41] Krimmel, M. Mu¨cksch, V. Tsurkan, M. M. Koza, H. Mutka, and A. Loid. Vibronic and Magnetic Excitations in the Spin-Orbital Liquid State of $FeSc_2S_4$. Phys. Rev. Lett. 94, 237402 (2005).

[42] Y. Okamoto, S. Niitaka, M.Uchida, T. Waki, M. Takigawa, Y. Nakatsu, A. Sekiyama, S. Suga, R. Arita, and H. Takagi. Band Jahn-Teller Instability and Formation of Valence Bond Solid in a Mixed-Valent Spinel Oxide $LiRh_2O_4$. Phys. Rev. Lett. 101,

086404 (2008).

[43] K. Tomiyasu, H. Suzuki, M. Toki, S. Itoh, M. Matsuura, N. Aso, and K. Yamada. Molecular Spin Resonance in the Geometrically Frustrated Magnet $MgCr_2O_4$ by Inelastic Neutron Scattering. Phys. Rev. Lett. 101, 177401 (2008).

[44] M. J. Lawler, H. Y. Kee, Y. B. Kim, and A. Vishwanath. Topological Spin Liquid on the Hyperkagome Lattice of $Na_4Ir_3O_8$. Phys. Rev. Lett. 100, 227201 (2008).

[45] S. Bordacs, D. Varjas, I. Kezsmarki, G. Mihaly, L. Baldassarre, A. Abouelsayed, C. A. Kuntscher, K. Ohgushi, and Y. Tokura. Magnetic-Order-Induced Crystal Symmetry Lowering in ACr_2O_4 Ferrimagnetic Spinels. Phys. Rev. Lett. 103, 077205 (2009).

[46] G. Balakrishnan, T. J Hayes, O. A. Petrenko and D. M. Paul. High quality single crystals of the SrR_2O_4 family of frustrated magnets. J. Phys. Condens. Matter 21, 012202 (2009).

[47] S. Nakatsuji, Y. Nambu, and S. Onodai. Novel Geometrical Frustration Effects in the Two-Dimensional Triangular-Lattice Antiferromagnet $NiGa_2S_4$ and Related Compounds. J. Phys. Soc. Jpn. 79, 011003 (2010).

[48] M. W. Kim, J. S. Kim, T. Katsufuji, and R. K. Kremer. Magnetic susceptibility and specific heat of a spinel MnV_2O_4 single crystal. Phys. Rev. 83, 024403 (2011).

[49] K. Tomiyasu, H. Ueda, M. Matsuda, M. Yokoyama, K. Iwasa, and K. Yamada. Molecular spin-liquid state in the spin-3/2 frustrated spinel $HgCr_2O_4$. Phys. Rev. B 84, 035115 (2011); K. Takubo, R. Kubota, T. Suzuki, T. Kanzaki, S. Miyahara, N. Furukawa, and T. Katsufuji. Evolution of phonon Raman spectra with orbital ordering in spinel MnV_2O_4. Phys. Rev. B 84, 094406 (2011).

[50] Q. Zhang, K. Singh, F. Guillou, C. Simon, Y. Breard, V. Caignaert, and V. Hardy. Ordering process and ferroelectricity in a spinel derived from FeV_2O_4. Phys. Rev. B 85, 054405 (2012).

[51] P. M. de Wolff. The crystal structure of $Co_2(OH)_3Cl$. Acta Cryst. 6, 359-360 (1953).

[52] H. R. Oswald and J. R. Guentier. Crystal data on paratacamite, γ-$Cu_2(OH)_3Cl$. J. Appl. Crystallogr. 4, 530-531 (1971).

[53] M. E. Fleet. The crystal structure of paratacamite, $Cu_2(OH)_3Cl$. Acta Cryst., 31, 183-187 (1975).

[54] J. B. Parise and B. G. Hyde. The structure of atacamite and its relationship to spinel. Acta Cryst. C 42, 1277-1280 (1986).

[55] A. M. Polland, R.G. Thomas, and P. A. Williams. Synthesis and stabilities of the basic copper(II) chlorides atacamite, paratacamite and botallackite. Miner. Mag. 53, 557-563 (1989).

[56] G. Maruta, K. Nishiyama, and S. Takeda. μSR studies on the dimensionality of layered compounds $Cu_2(OH)_3X$. Polyhedron 20, 1185-1188 (2001)

[57] L. Burgio and R. J. H. Clark. Library of FT-Raman spectra of pigments, minerals, pigment media and varnishes, and supplement to existing library of Raman spectra of pigments with visible excitation. Spectrochimica Acta A 57, 1491-1521(2001).

[58] R. L. Frost, W. Martens, J. T. Kloprogge, and P. A. Williams. Raman spectroscopy of the basic copper chloride minerals atacamite and paratacamite: implications for the study of copper, brass and bronze objects of archaeological significance. J. Raman Spectrosc. 33: 801-806 (2002).

[59] W. Martens, R.L. Frost, and P.A. Williams. Raman and infrared spectroscopic study of the basic copper chloride minerals. N. Jb. Miner. Abh. 178, 197-215 (2003).

[60] R.L. Frost. Raman spectroscopy of selected copper minerals of significance in corrosion. Spectrochimica Acta A 59, 1195-1204 (2003).

[61] K. Morii, G. Maruta, and S. Takeda. Ferro- and antiferromagnetic interactions of layer-structured basic copper compounds as studied by solid-state high-resolution deuterium NMR. Polyhedron 22, 1995-2001 (2003).

[62] C. L. Zhu, C. N. Chen, L. Y. Hao, Y. Hu, and Z. Y. Chen. Template-free synthesis of $Cu_2Cl(OH)_3$ nanoribbons and use as sacrificial template for CuO nanoribbon. J. Crystal Growth 263, 473-479 (2004).

[63] A.S. Wills, S. Raymond, and J.-Y. Henry. Magnetic ordering in a distorted pyrochlore antiferromagnet. J. Magn. Magn. Mater. 272-276, 850-851 (2004).

[64] X. G. Zheng and E.S. Otabe. Antiferromagnetic transition in atacamite $Cu_2Cl(OH)_3$. Solid State Commun. 130, 107-109 (2004).

[65] X. G. Zheng and C.N. Xu. Antiferromagnetic transition in botallackite $Cu_2Cl(OH)_3$. Solid State Commun. 131, 509-511 (2004).

[66] V. Hayez, Virginia Costa, J. Guillaume, H. Terryn, and A. Hubin. Micro Raman spectroscopy used for the study of corrosion products on copper alloys: study of the chemical composition of artificial patinas used for restoration purposes. Analyst 130, 550-556 (2005).

[67] X. G. Zheng, T. Kawae, Y. Kashitani, C. S. Li, N. Tateiwa, K. Takeda, H. Yamada, C. N. Xu, and Y. Ren. Unconventional magnetic transitions in the mineral clinoatacamite $Cu_2Cl(OH)_3$. Phys. Rev. B 71, 052409 (2005).

[68] X. G. Zheng, T. Mori, K. Nishiyama, W. Higemoto, H. Yamada, K. Nishikubo, and C. N. Xu. Antiferromagnetic transitions in polymorphous minerals of the natural cuprates atacamite and botallackite $Cu_2Cl(OH)_3$. Phys. Rev. B 71, 174404 (2005).

[69] X. G. Zheng, H. Kubozono, K. Nishiyama, W. Higemoto, T. Kawae, A. Koda, and C. N. Xu. Coexistence of Long-Range Order and Spin Fluctuation in Geometrically Frustrated Clinoatacamite $Cu_2Cl(OH)_3$. Phys. Rev. Lett. 95, 057201 (2005).

[70] H. Kubozono, X. G. Zheng, H. Yamada, and C. N. Xu. Structural analysis for novel materials exhibiting exotic properties II -a structural study of new geometrically frustrated spin system $M_2Cl(OH)_3$. Rep. Fac. Sci, Engrg. Saga Univ. 35-1, 13-21 (2006). [in Japanese]

[71] X. G. Zheng and K. Nishiyama. Geometric frustration in a new material system $M_2X(OH)_3$. *Phys. B* 374-375, 156-159 (2006)

[72] X. G. Zheng, T. Kawae, H. Yamada, K. Nishiyama, and C. N. Xu. Coexisting Ferromagnetic Order and Disorder in a Uniform System of Hydroxyhalide $Co_2(OH)_3Cl$. Phys. Rev. Lett. 97, 247204 (2006).

[73] S. C. Lee, S.-H. Park, S. M. Lee, J. B. Lee, and H. J. Kim. Synthesis and H_2 uptake of $Cu_2(OH)_3Cl$, $Cu(OH)_2$ and CuO nanocrystal aggregate. Catal. Today 120, 358-362 (2007).

[74] X. G. Zheng, M. Hagihala, and T. Toriyi. Co-existence of long-range order and spin fluctuation in a new geometric frustration series $M_2(OH)_3Cl$. J. Magn. Magn. Mater. 310, 1288-1290 (2007).

[75] M. Hagihala, X. G. Zheng, T. Toriyi, and T. Kawae. Antiferromagnetism and geometric frustration in tetrahedral lattice hydroxyhalides $M_2(OH)_3X$. J. Phys.: Condens. Matter 19, 145281 (2007).

[76] F. Li, M. T. Wang, M. G. Kong, S. W. Tao, C. N. Zhang, and K. J. Wang. Synthesis and growth features of copper hydroxide iodide nanoneedles. Mater. Lett. 61, 846-849 (2007).

[77] A. S. Wills and J-Y Henry. On the crystal and magnetic ordering structures of clinoatacamite, γ-$Cu_2(OD)_3Cl$, a proposed valence bond solid. J. Phys.: Condens. Matter 20, 472206 (2008).

[78] H. Kubo, K. Zenmyo, M. Tokita, T. Hamasaki, M. Hagihala, and X. G. Zheng. NMR Study of Spin State in Geometrically Frustrated Compound $Co_2Cl(OH)_3$. J. Phys. Soc. Jpn. 77, 013407 (2008).

[79] X. G. Zheng, M. Hagihala, T. Kawae, and C. N. Xu. Defect-induced short-range-order from a spin-ice related state in deformed pyrochlore $Co_2(OH)_3Cl$. Phys. Rev. B 77, 024418 (2008); X. G. Zheng, M. Fujihala, S. Kitajima, M. Maki, K. Kato, M. Takata, and C. N. Xu. Strong magnetic-dielectric-lattice coupling in transition metal hydroxyhalides and ferroelectric response in rhombohedral $Co_2(OD)_3X$ (X = Cl, Br).

ibid 87, 174102 (2013).

[80] J.-H. Kim, S. Ji, S.-H. Lee, B. Lake, T. Yildirim, H. Nojiri, H. Kikuchi, K. Habicht, Y. Qiu, and K. Kiefer. External Magnetic Field Effects on a Distorted Kagome Antiferromagnet. Phys. Rev. Lett. 101, 107201 (2008).

[81] 郑旭光. 新几何阻挫物质 $M_2(OH)_3X$ 的新颖量子磁性——磁有序和涨落在均匀自旋系的共存. 物理学进展 28, 314-326 (2008). (in Chinese)

[82] T. Malcherek and J. Schluter. Structures of the pseudo-trigonal polymorphs of $Cu_2(OH)_3Cl$. Acta Cryst. 65, 334-341 (2009).

[83] K. Zenmyo, M. Tokita. Magnetic structure of geometrically frustrated compound $Co_2Cl(OH)_3$ determined by proton NMR. J. Magn. Magn. Mater. 321, 2192-6 (2009).

[84] S. Maegawa, A. Oyamada, S. Sato, M. Nishiyama, T. Itou, X. G. Zheng. Spin dynamics in 3d electron pyrochlore-like systems. J. Phys.: Conf. Ser. 145, 012018 (2009).

[85] X. G. Zheng, M. Hagihala, M. Fujihala, and T. Kawae. Recent developments in the magnetic study of the deformed pyrochlore lattice $M_2(OH)_3X$ (M = 3d magnetic ions, X = Cl, Br) - exotic magnetic order in $Ni_2(OH)_3Cl$ and controlled spin-spin interactions in $Co_2(OH)_3Cl_{1-x}Br_x$ and $(Co_{1-x}Fe_x)_2(OH)_3Cl$. J. Phys.: Conf. Ser. 145, 012034 (2009).

[86] A. S. Wills, T. G. Perring, S. Raymond, B. Fak, J.-Y. Henry, and M. Telling. Inelastic neutron scattering studies of the quantum frustrated magnet clinoatacamite $Cu_2(OD)_3Cl$. J. Phys.: Conf. Ser. 145, 012056(2009).

[87] M. Tokita and K. Zenmyo. Magnetic spin structure of geometrically frustrated $Co_2Cl(OH)_3$. J. Phys.: Conf. Ser. 150, 042208 (2009)

[88] M. Hagihala, X.G. Zheng, T. Kawae. Drastic anion substitution effect in deformed pyrochlore lattice $Co_2(OH)_3Cl_{1-x}Br_x$. Physica B 404, 671-373 (2009).

[89] M. Fujihala, M. Hagihala, X.G. Zheng, T. Kawae. Spin-glass state in the mixed system $(Co_{1-x}Fe_x)_2(OH)_3Cl$ on deformed pyrochlore lattice. Physica B 404, 674-676 (2009).

[90] X. G. Zheng, M. Hagihala, K.Nishiyama, and T. Kawae. Exotic antiferromagnetic transition in deformed pyrochlore lattice $Ni_2(OH)_3Cl$ of atacamite-structure. Physica B 404, 677-679 (2009).

[91] X. G. Zheng, T. Yamashita, M. Hagihala, M. Fujihala, T. Kawae. Magnetic transitions in botallackite-structure $Cu_2(OH)_3Br$ and $Cu_2(OH)_3I$. Physica B 404, 680-682 (2009).

[92] H. Morodomi, K. Ienaga, Y. Inagaki, and T. Kawae. Specific Heat Study of Geometrically Frustrated Magnet Clinoatacamite $Cu_2Cl(OH)_3$. J. Phys.: Conf. Ser. 200, 032047 (2010).

[93] S. Maegawa, A. Oyamada, and S. Sato. Novel Frustrated Behavior in Quantum Heisenberg Antiferromagnets on the Pyrochlore Lattice: NMR Studies of $R_2(OH)_3Cl$

(R=Cu and Ni). J. Phys. Soc. Jpn. 79, 011002 (2010).

[94] M. Fujihala, M. Hagihala, X.G. Zheng, and T. Kawae. Antiferromagnetic magnetic transition and spin fluctuations in the deformed pyrochlore compound β-$Fe_2(OH)_3Cl$. Phys. Rev. B 82, 024425 (2010).

[95] M. Fujihala, X. G. Zheng, Y. Oohara, H. Morodomi, T. Kawae, A. Matsuo, K. Kindo. Short-range correlations and persistent spin fluctuations in the undistorted kagome lattice Ising antiferromagnet $Co_3Mg(OH)_6Cl_2$. Phys. Rev. B 85, 012402 (2012).

[96] M. Hagihala, X.G. Zheng, T. Kawae, and T. J. Sato. Successive antiferromagnetic transitions $Co_2(OH)_3Br$. Phys. Rev. B 82, 214424 (2010).

[97] S. Y. Chu, P. Muller, D. G. Nocera, and Y. S. Lee. Hydrothermal growth of single crystals of the quantum magnets Clinoatacamite, paratacamite, and herbertsmithite. Appl. Phys. Lett. 98, 092508 (2011).

[98] J. Zhang, J. S. Xu, H. Zhang, X. Y. Yin, J. H. Qian, L. L. Liu, D. J. Yang, X. Y. Liu. Fabrication of octahedral Atacamite microcrystals via a hydrothermal route. Micro & Nano Lett. 6, 119-121 (2011); Y. Liu, W. Ren, and H. Cui. Large-scale synthesis of paratacamite nanoparticles with controlled size and morphology. *ibid* 6, 823-826 (2011).

[99] E. Khatami, J. S. Helton, and M. Rigol. Numerical study of the thermodynamics of clinoatacamite. Phys. Rev. B 85, 064401 (2012).

[100] G. Bertolotti, D. Bersani, P. P. Lottici, M. Alesiani, T. Malcherek, and J. Schluter. Micro-Raman study of copper hydroxychlorides and other corrosion products of bronze samples mimicking archaeological coins. Anal. Bioanal. Chem. 402: 1451-1457 (2012).

[101] R. S. W. Braithwaite, K. Mereiter, W.H. Paar, and A.M. Clark. Herbertsmithite, $Cu_3Zn(OH)_6Cl_2$, a new species, and the he definition on of par paratacamite. Miner. Mag. 68, 527 (2004).

[102] M. P. Shores, E. A. Nytko, B. M. Bartlett, and D. G. Nocera. A Structurally Perfect S=1/2 Kagome Antiferromagnet. J. Am. Chem. Soc. 127, 13462-13463 (2005).

[103] O. Ofer and A. Keren. Ground state and excitation properties of the quantum kagome system $ZnCu_3(OH)_6Cl_2$ investigated by local probes. arXiv preprint: 0610540 (2006).

[104] W. Krause, H. J. Bernhardt, R. S. W. Braithwaite, U. Kolitsch, and R. Pritchard. Kapellasite, $Cu_3Zn(OH)_6Cl_2$, a new mineral from Lavrion, Greece, and its crystal structure. Miner. Mag. 70, 329-340 (2006).

[105] T. Malcherek and J. Schluter. $Cu_3MgCl_2(OH)_6$ and the bond-valence parameters of the OH-Cl bond. Acta Cryst. B 63, 157-160 (2007).

[106] G. Misguich and P. Sindzingre. Magnetic susceptibility and specific heat of the spin-1/2 Heisenberg model on the kagome $ZnCu_3(OH)_6Cl_2$. Eur. Phys. J. B 59, 305-309 (2007)

[107] S.-H. Lee, H. Kikuchi, Y. Qiu, B. Lake, Q. Huang, K. Habicht, and K. Kiefer. Quantum- spin-liquid states in the two-dimensional kagome antiferromagnets $Zn_xCu_{4-x}(OD)_6Cl_2$. Nature Mater. 6, 853-857 (2007).

[108] F. Bert, S. Nakamae, F. Ladieu, D. L' Hote, P. Bonville, F. Duc, J.-C. Trombe, and P. Mendels. Low temperature magnetization of the S= 1/2 kagome antiferromagnet $ZnCu_3(OH)_6Cl_2$. Phys. Rev. B 76, 132411 (2007).

[109] R. R. P. Singh and D. A. Huse. Ground state of the spin-1/2 kagome-lattice Heisenberg antiferromagnet. Phys. Rev. B 76, 180407 (2007); M. Rigol, R. R. P. Singh. Kagome lattice antiferromagnets and Dzyaloshinsky-Moriya interactions. *ibid* 76, 184403 (2007).

[110] P. Mendels, F. Bert, M. A. de Vries, A. Olariu, A. Harrison, F. Duc, J. C. Trombe,J. S. Lord, A. Amato, and C. Baines. Quantum Magnetism in the Paratacamite Family: Towards an Ideal Kagome Lattice. Phys. Rev. Lett. 98, 077204 (2007); J. S. Helton, K. Matan, M. P. Shores, E. A. Nytko, B. M. Bartlett, Y. Yoshida, Y. Takano, A. Suslov, Y. Qiu, J.-H. Chung, D. G. Nocera, and Y. S. Lee. Spin Dynamics of the Spin-1/2 Kagome Lattice Antiferromagnet $ZnCu_3(OH)_6Cl_2$. *ibid* 98, 107204 (2007).

[111] Y. Ran, M. Hermele, P. A. Lee, and X. G. Wen. Projected-Wave-Function Study of the Spin-1/2 Heisenberg Model on the Kagome Lattice. Phys. Rev. Lett. 98, 117205 (2007); M. Rigol and R. R. P. Singh. Magnetic Susceptibility of the Kagome Antiferromagnet $ZnCu_3(OH)_6Cl_2$. *ibid* 98, 207204 (2007).

[112] R. H. Colman, C. Ritter, and A. S. Wills. Toward Perfection: Kapellasite, $Cu_3Zn(OH)_6Cl_2$, a New Model S=1/2 Kagome Antiferromagnet. Chem. Mater. 20(22): 6897-6899 (2008).

[113] E. A. Nytko, J. S. Helton, P. Muller, and D. G. Nocera. A Structurally Perfect S=1/2 Metal-Organic Hybrid Kagome Antiferromagnet. J. Am. Chem. Soc. 130, 2922-2923 (2008).

[114] R. Chitra and M. J. Rozenberg. Impurity effects in the quantum kagome system $ZnCu_3(OH)_6Cl_2$. Phys. Rev. B 77, 052407 (2008); R. R. P. Singh, and D. A. Huse. Triplet and singlet excitations in the valence bond crystal phase of the kagome lattice Heisenberg model. *ibid* 77, 144415 (2008); C.-H. Chern and M. Tsukamoto. Thermodynamics of the quantum Ising model in the two-dimensional kagome lattice. *ibid* 77, 172404 (2008); O. Cepas, J. O. Haerter, and C. Lhuillier. Detection of weak emergent broken- symmetries of the kagome antiferromagnet by Raman spectroscopy.

ibid 77, 172406 (2008).

[115] M. J. Rozenberg and R. Chitra. Disorder effects in the quantum kagome antiferromagnet $ZnCu_3(OH)_6Cl_2$. Phys. Rev. B 78, 132406 (2008); O. Cepas, C. M. Fong, P. W. Leung, and C. Lhuillier. Quantum phase transition induced by Dzyaloshinskii-Moriya interactions in the kagome antiferromagnet. *ibid* 78, 140405 (2008).

[116] T. Imai, E. A. Nytko, B. M. Bartlett, M. P. Shores, and D. G. Nocera. ^{63}Cu, ^{35}Cl, and ^{1}H NMR in the S=1/2 Kagome Lattice $ZnCu_3(OH)6Cl_2$. Phys. Rev. Lett. 100, 077203 (2008).

[117] A. Olariu, P. Mendels, F. Bert, F. Duc, J. C. Trombe, M. A. de Vries, A. Harrison. ^{17}O NMR Study of the Intrinsic Magnetic Susceptibility and Spin Dynamics of the Quantum Kagome Antiferromagnet $ZnCu_3(OH)_6Cl_2$. Phys. Rev. Lett. 100, 087202 (2008).

[118] M. A. de Vries, K.V. Kamenev, W. A. Kockelmann, J. Sanchez-Benitez, and A. Harrison. Magnetic Ground State of an Experimental S=1/2 Kagome Antiferromagnet. Phys. Rev. Lett. 100, 157205 (2008).

[119] M. J. Lawler, L. Fritz, Y. B. Kim, S. Sachdev. Theory of Neel and Valence-Bond Solid Phases on the Kagome Lattice of Zn Paratacamite. Phys. Rev. Lett. 100, 187201 (2008).

[120] A. Zorko, S. Nellutla, J. van Tol, L. C. Brunel, F. Bert, F. Duc, J.-C. Trombe, M. A. de Vries, A. Harrison, and P. Mendels. Dzyaloshinsky-Moriya Anisotropy in the Spin-1/2 Kagome Compound $ZnCu_3(OH)_6Cl_2$. Phys. Rev. Lett. 101, 026405 (2008).

[121] O. Ma and J. B. Marston. Weak Ferromagnetic Exchange and Anomalous Specific Heat in $ZnCu_3(OH)_6Cl_2$. Phys. Rev. Lett. 101, 027204 (2008). Erratum: Phys. Rev. Lett. 102, 099901 (2009)

[122] O. Janson, J. Richter, and H. Rosner. Modified Kagome Physics in the Natural Spin-1/2 Kagome Lattice Systems: Kapellasite $Cu_3Zn(OH)_6Cl_2$ and Haydeeite $Cu_3Mg(OH)_6Cl_2$. Phys. Rev. Lett. 101, 106403 (2008).

[123] A. Lauchli and C. Lhuillier, Dynamical Correlations of the Kagome S=1/2 Heisenberg Quantum Antiferromagnet. arXiv: 0901.1065 (2009). unpublished.

[124] Z. Hiroi, H. Yoshida, Y. Okamoto and M. Takigawa. Spin-1/2 kagome compounds: Volborthite vs Herbertsmithite. J. Phys.: Conf. Ser. 145**,** 012002 (2009); F. Bert, A. Olariu, A. Zorko, P. Mendels, J. C. Trombe, F. Duc, M. A de Vries, A. Harrison, A. D. Hillier, J. Lord, A Amato, and C. Baines. Frustrated magnetism in the quantum Kagome Herbertsmithite $ZnCu_3(OH)_6Cl_2$ antiferromagnet. *ibid* 145, 012004 (2009);
H. Kikuchi, Y. Kubo, Y. Fujii. ^{1}H-NMR study of S=1/2 frustrated antiferromagnet $Zn_xCu_{4-x}(OH)_6Cl_2$ varying from kagome to pyrochlore. *ibid* 145, 012009 (2009);
S. Okubo, M. Tomoo, H. Ohta, and H. Kikuchi. High field ESR measurements of S= 1/2 kagome heisenberg antiferromagnet $ZnCu_3(OH)_6Cl_2$. *ibid* 145, 012011 (2009);

A. Zorko, S. Nellutla, J. van Tol, L. C. Brunel, F. Bert, F. Duc, J-C Trombe, and P. Mendels. Electron spin resonance investigation of the spin-1/2 kagome antiferromagnet $ZnCu_3(OH)_6Cl_2$. *ibid* 145, 012014 (2009); M. Tomoo, S. Okubo, T. Sakurai, T. Tomita, M. Fujisawa, H. Ohta, and H. Kikuchi. Multi-frequency ESR study of S=1/2 frustration systems $Zn_xCu_{4-x}(OH)_6Cl_2$. *ibid* 145, 012035 (2009).

[125] O. Ofer and A. Keren. Symmetry of the spin Hamiltonian for herbertsmithite: A spin-1/2 kagome lattice. Phys. Rev. B 79, 134424 (2009);
E. S. Sorensen, M. J. Lawler, and Y. B. Kim. Néel and valence-bond crystal order on a distorted kagome lattice: Implications for Zn-paratacamite. *ibid* 79, 174403 (2009).

[126] I. Rousochatzakis, S. R. Manmana, A. M. Lauchli, B. Normand, and F. Mila. Dzyaloshinskii-Moriya anisotropy and nonmagnetic impurities in the *s*=1/2 kagome system $ZnCu_3(OH)_6Cl_2$. Phys. Rev. B 79, 214415 (2009)

[127] Y. Ran, W.H. Ko, P. A. Lee, and X. G. Wen. Spontaneous Spin Ordering of a Dirac Spin Liquid in a Magnetic Field. Phys. Rev. Lett. 102, 047205 (2009).

[128] M. A. de Vries, J. R. Stewart, P. P. Deen, J. O. Piatek, G. J. Nilsen, H. M. Ronnow, and A. Harrison. Scale-Free Antiferromagnetic Fluctuations in the s=1/2 Kagome Antiferromagnet Herbertsmithite. Phys. Rev. Lett. 103, 237201 (2009).

[129] R. H. Colman, A. Sinclair, and A.S. Wills. Comparisons between Haydeeite, γ-$Cu_3Mg(OD)_6Cl_2$, and Kapellasite, γ-$Cu_3Zn(OD)_6Cl_2$, Isostructural S=1/2 Kagome Magnets. Chem. Mater. 22, 5774-5779 (2010).

[130] S. Y. Chu, T. M. McQueen, R. Chisnell, D. E. Freedman, P. Mu ller, Y. S. Lee, and D. G. Nocera, A Cu^{2+}(S = 1/2) Kagome Antiferromagnet $Mg_xCu_{4-x}(OH)_6Cl_2$. J. Am. Chem. Soc. 132, 5570-5571 (2010).

[131] P. Mendels and F. Bert. Quantum Kagome Antiferromagnet $ZnCu_3(OH)_6Cl_2$. J. Phys. Soc. Jpn. 79, 011001 (2010).

[132] W. H. Ko, Z. X. Liu, T. K. Ng, and P. A. Lee. Raman signature of the U(1) Dirac spin-liquid state in the spin-1/2 kagome system. Phys. Rev. B 81, 024414 (2010).

[133] D. Wulferding, P. Lemmens, P. Scheib, J. Roder, P. Mendels, S. Y. Chu, T. H. Han, and Y. S. Lee. Interplay of thermal and quantum spin fluctuations in the kagome lattice compound herbertsmithite. Phys. Rev. B 82, 144412 (2010).

[134] J. S. Helton, K. Matan, M. P. Shores, E. A. Nytko, B. M. Bartlett, Y. Qiu, D. G. Nocera, and Y. S. Lee. Dynamic Scaling in the Susceptibility of the Spin-1-2 Kagome Lattice Antiferromagnet Herbertsmithite. Phys. Rev. Lett. 104, 147201 (2010);
R. R. P. Singh. Valence Bond Glass Phase in Dilute Kagome Antiferromagnets. *ibid* 104, 177203 (2010).

[135] R. H. Colman, A. Sinclair, and A. S. Wills. Magnetic and Crystallographic Studies of Mg-Herbertsmithite, γ-$Cu_3Mg(OH)_6Cl_2$ —A New S=1/2 Kagome Magnet and Candidate Spin Liquid. Chem. Mater. 23, 1811-1817 (2011).

[136] S. Y. Chu. Magnetic properties of geometrically frustrated polymorphic crystals of $Cu_{4-x}Mg_x(OH)_6Cl_2$. J. Phys.: Conf. Ser. 273, 012123 (2011).

[137] P. Mendels and F. Bert. Quantum kagome antiferromagnet: $ZnCu_3(OH)_6Cl_2$. J. Phys.: Conf. Ser. 320, 012004 (2011).

[138] T. M. McQueen, T. H. Han, D. E. Freedman, P. W. Stephens, Y.S.Lee, and D. G. Nocera. $CdCu_3(OH)_6Cl_2$: A new layered hydroxide chloride. J. Solid State Chem. 184, 3319-3323 (2011).

[139] M. Isoda, H. Nakano, and T. Sakai. Thermodynamic properties of spin-1/2 ising-like Heisenberg model on triangle-based lattices. Mod. Phys. Lett. B 25, 909-915 (2011).

[140] T. H. Han, J. S. Helton, S. Chu, A. Prodi, D. K. Singh, C. Mazzoli, P. Muller, D. G. Nocera, and Y. S. Lee. Synthesis and characterization of single crystals of the spin-antiferromagnets $Zn_xCu_{4-x}(OH)_6Cl_2$. Phys. Rev. B 83, 100402 (2011).

[141] Y. Iqbal, F. Becca, and D. Poilblanc. Valence-bond crystal in the extended kagome spin-1/2 quantum Heisenberg antiferromagnet: A variational Monte Carlo approach. Phys. Rev. B 83, 100404 (2011).

[142] T. Imai, M. Fu, T. H. Han, and Y. S. Lee. Local spin susceptibility of the S = 1/2 kagome lattice in $ZnCu_3(OD)_6Cl_2$. Phys. Rev. B 84, 020411 (2011).

[143] V. R. Shaginyan, A. Z. Msezane, and K. G. Popov. Thermodynamic properties of the kagome lattice in herbertsmithite. Phys. Rev. B 84, 060401 (2011).

[144] E. Kermarrec, P. Mendels, F. Bert, R. H. Colman, A. S. Wills, P. Strobel, P. Bonville, A. Hillier, and A. Amato. Spin-liquid ground state in the frustrated kagome antiferromagnet $MgCu_3(OH)_6Cl_2$. Phys. Rev. B 84, 100401 (2011).

[145] Y. Zhou and P. A. Lee. Spinon Phonon Interaction and Ultrasonic Attenuation in Quantum Spin Liquids. Phys. Rev. Lett. 106, 056402 (2011).

[146] M. Jeong, F. Bert, P. Mendels, F. Duc, J. C. Trombe, M. A. de Vries, and A. Harrison. Field-Induced Freezing of a Quantum Spin Liquid on the Kagome Lattice. Phys. Rev. Lett. 107, 237201 (2011).

[147] V. R. Shaginyan, A. Z. Msezane, K. G. Popov, G. S. Japaridze, and V. A. Stephanovich. Identification of strongly correlated spin liquid in herbertsmithite. Europhys. Lett. 97, 56001 (2012).

[148] D. Wulferding, P. Lemmens, H. Yoshida, Y. Okamoto, and Z. Hiroi. The spin dynamics in distorted kagome lattices: a comparative Raman study. J. Phys.: Condens.

Matter 24, 185602 (2012).

[149] M. A. de Vries, D. Wulferding, P. Lemmens, J. S. Lord, A. Harrison, P. Bonville, F. Bert, and P. Mendels. Extension of the zinc paratacamite phase diagram: Probing the effect of spin vacancies in an S = 1/2 kagome antiferromagnet. Phys. Rev. B 85, 014422 (2012).

[150] T. H. Han, S. Y. Chu, and Y. S. Lee. Refining the Spin Hamiltonian in the Spin- 1/2 Kagome Lattice Antiferromagnet $ZnCu_3(OH)_6Cl_2$ Using Single Crystals. Phys. Rev. Lett. 108, 157202 (2012). D. P. Kozlenko, A. F. Kusmartseva, E.V. Lukin, D. A. Keen, W. G. Marshall, M. A. de Vries, and K.V. Kamenev. From Quantum Disorder to Magnetic Order in an s=1/2 Kagome Lattice A Structural and Magnetic Study of Herbertsmithite at High Pressure. Phys. Rev. Lett. 108, 187207 (2012).

[151] W. G. Fateley, F. R. Dollish, N. T. McDevitt, and F. F. Bentley. Infrared and Raman Selection Rules for Molecular and Vibrations: The Correlation Method. John Wiley & Sons Inc. New York 1972.

[152] K. Nakamoto, Infrared and Raman Spectra of Inorganic and Coordination Compounds, Part A: Theory and Applications in Inorganic Chemistry. Sixth Edition. A John Wiley & Sons, New York 2009.

[153] E. Granado, P. G. Pagliuso, J. A. Sanjurjo, C. Rettori, M. A. Subramanian, S. W. Cheong, and S. B. Oseroff. Phonon Raman scattering in $A_2Mn_2O_7$ (A=Tl, In, Y). Phys. Rev. B 60, 6513-6516 (1999)

[154] J.S. Lee, T.W. Noh, J.S. Bae, I.S. Yang, T. Takedab, and R. Kanno, Strong spin-phonon coupling in the geometrically frustrated pyrochlore $Y_2Ru_2O_7$. Phys. Rev. B 69, 214428 (2004).

[155] B. Z. Malkin, A.R. Zakirov, M.N. Popova, S.A. Klimin, E.P. Chukalina, E. Antic-Fidancev, Ph. Goldner, P. Aschehoug, and G. Dhalenne, Optical spectroscopy of $Yb_2Ti_2O_7$ and $Y_2Ti_2O_7$: Yb^{3+} and crystal-field parameters in rare-earth and crystal-field parameters in rare-earth titanate pyrochlores. Phys. Rev. B 70, 075112 (2004)

[156] K. Taniguchi, T. Katsufuji, S. Iguchi, Y. Taguchi, H. Takagi, and Y. Tokura. Raman study of the metal-insulator transition in pyrochlore Mo oxides. Phys. Rev. B 70, 100401 (2004)

[157] C. Z. Bi, J.Y. Ma, B. R Zhao, Z. Tang, D. Yin, C. Z. Li, D. Z. Yao, J. Shi, and X. G. Qiu. Far infrared optical properties of the pyrochlore spin ice compound $Dy_2Ti_2O_7$. J. Phys.: Condens. Matter 17, 5225-5233 (2005).

[158] J.S. Lee, T.W. Noh, T. Takedab, R. Kanno, Roles of the strong spin-phonon coupling in the geometrically frustratedpyrochlore $Y_2Ru_2O_7$. Physica B 359-361, 1240-2 (2005).

[159] J. S. Bae, I.-S. Yang, J. S. Lee, T. W. Noh, T. Takeda, and R. Kanno. Phonon dynamics of the geometrically frustrated pyrochlore $Y_2Ru_2O_7$ investigated by Raman spectroscopy. Phys. Rev. B 73, 052301 (2006).

[160] T. Hasegawa, Y. Takasu, N. Ogita, M. Udagawa, J. Yamaura, Y. Nagao, and Z. Hiroi. Raman scattering in KOs_2O_6. Phys. Rev. B 77, 064303 (2008).

[161] M. Maczka, M. L. Sanjuan, A. F. Fuentes, K. Hermanowicz, and J. Hanuza. Temperature-dependent Raman study of the spin-liquid pyrochlore $Tb_2Ti_2O_7$. Phys. Rev. B 78, 134420 (2008).

[162] S. Saha, S. Singh, B. Dkhil, S. Dhar, R. Suryanarayanan, G. Dhalenne, A. Revcolevschi, and A. K. Sood1. Temperature-dependent Raman and *x*-ray studies of the spin-ice pyrochlore $Dy_2Ti_2O_7$ and nonmagnetic pyrochlore $Lu_2Ti_2O_7$. Phys. Rev. B 78, 214102 (2008)

[163] S. Saha, D. V. S Muthu, S. Singh, B. Dkhil, R. Suryanarayanan, G. Dhalenne, H. K. Poswal, S. Karmakar, S. M. Sharma, A. Revcolevschi, and A. K. Sood. Low-temperature and high-pressure Raman and x-ray studies of pyrochlore $Tb_2Ti_2O_7$: Phonon anomalies and possible phase transition. Phys. Rev. B 79, 134112 (2009).

[164] M. Maczka, M.L. Sanjuan, A.F. Fuentes, L. Macalik, J. Hanuza, K. Matsuhira, and Z. Hiroi. Temperature-dependent studies of the geometrically frustrated pyrochlores $Ho_2Ti_2O_7$ and $Dy_2Ti_2O_7$. Phys. Rev. B 79, 214437 (2009).

[165] T. Hasegawa, N. Ogita, K. Matsuhira, S. Takagi, M. Wakeshima, Y. Hinatsu, and M. Udagawa. Raman scattering study in iridium pyrochlore oxides. J. Phys.: Conf. Ser. 200, 012064 (2010).

[166] S. Saha, S. Prusty, S. Singh, R. Suryanarayanan, A. Revcolevschi, and A. K. Sood. Pyrochlore "dynamic spin-ice" $Pr_2Sn_2O_7$ and monoclinic $Pr_2Ti_2O_7$: A comparative temperature- dependent Raman study. J. Solid State Chem. 184, 2204-2208 (2011).

[167] N. Koshizuka, S. Ushioda, and T. Tsushima. Resonance Rarnan scattering in $CdCr_2S_4$: Magnetic-circular-polarization properties. Phys. Rev. B 21, 1316-1322 (1980).

[168] K. Wakamura, T. Arai. Effect of magnetic ordering on phonon parameters for infrared active modes in ferromagnetic spinel $CdCr_2S_4$. J. Appl. Phys. 63, 5824-5829 (1988).

[169] K. Wakamura. Observation of spin fluctuation effect on phonon damping in ferrimagnetic semiconductor $FeCr_2S_4$. Solid State Commun. 71, 1033-1037 (1989).

[170] H. Cynn, S. K. Sharma and T. F. Cooney, and M. Nicol. High-temperature Raman investigation of order-disorder behavior in the $MgAl_2O_4$ spinel. Phys. Rev. B 45, 500-502 (1992).

[171] T. Rudolf, Ch. Kant, F. Mayr, J. Hemberger, V. Tsurkan, and A. Loidl, Polar phonons

and spin-phonon coupling in $HgCr_2S_4$ and $CdCr_2S_4$ studied with far-infrared spectroscopy. Phys. Rev. B 76, 174307 (2007).

[172] A. B. Sushkov, O. Tchernyshyov, W. Ratcliff II, S.W. Cheong, and H. D. Drew. Probing Spin Correlations with Phonons in the Strongly Frustrated Magnet $ZnCr_2O_4$. Phys. Rev. Lett. 94, 137202 (2005).

[173] C. J. Fennie and K. M. Rabe. Magnetically Induced Phonon Anisotropy in $ZnCr_2O_4$ from First Principles. Phys. Rev. Lett. 96, 205505 (2006).

[174] T. Rudolf, Ch. Kant, F. Mayr, J. Hemberger, V. Tsurkan, and A. Loidl. Spin-phonon coupling in $ZnCr_2Se_4$. Phys. Rev. B 75, 052410 (2007).

[175] R. V. Aguilar, A.B. Sushkov, Y. J. Choi, S.-W. Cheong, and H. D. Drew. Spin-phonon coupling in frustrated magnet $CdCr_2O_4$. Phys. Rev. B 77, 092412 (2008).

[176] T. Rudolf, Ch. Kant, F. Mayr, M. Schmidt, V. Tsurkan, J. Deisenhofer, and A. Loidl. Optical properties of $ZnCr_2Se_4$. Eur. Phys. J. B 68, 153-160 (2009).

[177] Ch. Kant, J. Deisenhofer, T. Rudolf, F. Mayr, F. Schrettle, A. Loidl, V. Gnezdilov, D. Wulferding, P. Lemmens, and V. Tsurkan. Optical phonons, spin correlations, and spin-phonon coupling in the frustrated pyrochlore magnets $CdCr_2O_4$ and $ZnCr_2O_4$. Phys. Rev. B 80, 214417 (2009).

[178] S. Bordacs, D. Varjas, I. Kezsmarki, G. Mihaly, L. Baldassarre, A. Abouelsayed, C. A. Kuntscher, K. Ohgushi, and Y. Tokura. Magnetic-Order-Induced Crystal Symmetry Lowering in ACr_2O_4 Ferrimagnetic Spinels. Phys. Rev. Lett. 103, 077205 (2009).

[179] V. G. Ivanov, M. N. Iliev, Y.-H. A. Wang, and A. Gupta. Ferromagnetic spinel $CuCr_2Se_4$ studied by Raman spectroscopy and lattice dynamics calculations. Phys. Rev. B 81, 224302 (2010).

[180] V. G. Ivanov, M. V. Abrashev, M. N. Iliev, M. M. Gospodinov, J. Meen, and M. I. Aroyo. Short-range B-site ordering in the inverse spinel ferrite $NiFe_2O_4$. Phys. Rev. B 82, 024104 (2010).

[181] H. Li, B. Song, W.J. Wang, X.L. Chen. Facile synthesis, thermal, magnetic, Raman characterizations of spinel structure $ZnMn_2O_4$. Mater. Chem. Phys. 130, 39-44 (2011).

[182] V. Gnezdilov, P. Lemmens, Yu. G. Pashkevich, Ch. Payen, K. Y. Choi, J. Hemberger, A. Loidl, and V. Tsurkan. Phonon anomalies and possible local lattice distortions in giant magnetocapacitive $CdCr_2S_4$. Phys. Rev. B 84, 045106 (2011);

[183] M. Udagawa, K. Kohn, N. Koshizuka, T. Tsushima, and K. Tsushima. Influence of magnetic ordering on the phonon Raman spectra in $YCrO_3$ and $GdCrO_3$. Solid State Commun. 16, 779-783 (1975).

[184] N. Koshizuka and S. Ushioda. Inelastic-light-scattering study of magnon softening in

$ErFeO_3$. Phys. Rev. B 22, 5394-5399 (1980).

[185] Ph. Daniel, M. Rousseau, A. Desert, A. Ratuszna, F. Ganot. Raman scattering study and lattice-dynamics investigation of the $NaMnF_3$ perovskite. Phys. Rev. B 51, 12337-12346 (1995).

[186] V. B. Podobedov, A. Weber, D. B. Romero, J. P. Rice, and H. D. Drew. Effect of structural and magnetic transitions in $La_{1-x}M_xMnO_3$ (M=Sr, Ca) single crystals in Raman scattering. Phys. Rev. B 58, 43-46 (1998)

[187] E. Granado, A. Garcia, J. A. Sanjurjo, C. Rettori, I. Torriani, F. Prado, R. D. Sanchez, A. Caneiro, and S. B. Oseroff. Magnetic ordering effects in the Raman spectra of $La_{1-x}Mn_{1-x}O_3$. Phys. Rev. B 60, 11879-11882 (1999).

[188] K. Takehana, T. Takamasu, M. Hase, G. Kido, T. Masuda, and K. Uchinokura. Spin -phonon coupled modes in the incommensurate phases of doped $CuGeO_3$. Phys. Rev. B 63, 245413 (2001).

[189] C. D. Cruz, F. Yen, B. Lorenz, Y. Q. Wang, Y. Y. Sun, M. M. Gospodinov, C. W. Chu. Strong spin-lattice coupling in multiferroic $HoMnO_3$. Phys. Rev. B 71, 060407 (2005);

[190] J. Laverdiere, S. Jandl, A. A. Mukhin, V. Yu. Ivanov, V. G. Ivanov, and M. N. Iliev. Spin-phonon coupling in orthorhombic $RMnO_3$ (R=Pr, Nd, Sm, Eu, Gd, Tb, Dy, Ho, Y): A Raman study. Phys. Rev. B 73, 214301 (2006);

[191] S. Petit, F. Moussa, M. Hennion, S. Pailhes, L. Pinsard-Gaudart, and A. Ivanov. Spin Phonon Coupling in Hexagonal Multiferroic $YMnO_3$. Phys. Rev. Lett. 99, 266604 (2007).

[192] S. Lee, A. Pirogov, M. Kang, K.H. Jang, M. Yonemura, T. Kamiyama, S.W. Cheong, F. Gozzo, N. Shin, H. Kimura, Y. Noda and J.G. Park. Giant magneto-elastic coupling in multiferroic hexagonal manganites. Nature 451, 805-808 (2008).

[193] M. N. Iliev, P. Padhan, and A. Gupta. Temperature-dependent Raman study of multiferroic Bi_2NiMnO_6 thin films. Phys. Rev. B 77, 172303 (2008);

[194] X. Fabreges, S. Petit, I. Mirebeau, S. Pailhes, L. Pinsard, A. Forget, M. T. Fernandez-Diaz, and F. Porcher. Spin-Lattice Coupling, Frustration, and Magnetic Order in Multiferroic $RMnO_3$. Phys. Rev. Lett. 103, 067204 (2009).

[195] M. K. Singh, W. Prellier, H. M. Jang, and R. S. Katiyar. Anomalous magnetic ordering induced spin-phonon coupling in $BiFeO_3$ thin films. Solid State Commun. 149, 1971-1973 (2009).

[196] A. Ghosh, J. R. Sahu, S. V. Bhat, and C. N. R. Rao. A Raman study of multiferroic $LuMnO_3$. Solid State Sciences 11, 1639-1642 (2009).

[197] S. Issing, A. Pimenov, V. Y. Ivanov, A. A. Mukhin, and J. Geurts. Composition-

dependent spin-phonon coupling in mixed crystals of the multiferroic manganite $Eu_{1-x}Y_xMnO_3$ ($0 \le x \le 0.5$) studied by Raman spectroscopy. Phys. Rev. B 81, 024304 (2010).

[198] F. A. Mir, M. Ikram, and R. Kumar. Temperature-dependent Raman study of $PrFeO_3$ thin film. J. Raman Spectr. 42, 201-208 (2011).

[199] A. A. Schafgans, B. C. Pursley, A. D. LaForge, A. S. Sefat, D. Mandrus, and D. N. Basov. Phonon splitting and anomalous enhancement of infrared-active modes in $BaFe_2As_2$. Phys. Rev. B 84, 052501 (2011).

[200] T. Kanzaki, R. Kubota, and T. Katsufuji. Change of phonon Raman spectra with V trimerization in $BaV_{10}O_{15}$. Phys. Rev. B. 85, 144410 (2012).

[201] A. Novak. Hydrogen bonding in solids. Correlation of spectroscopic and crystallographic data. Struct. Bonding 18, 177-216 (1974).

[202] G. W. Brindley and C. C. Kao. Structural and IR Relations Among Brucite-Like Divalent Metal Hydroxides. Phys. Chem. Minerals 10, 187-191 (1984).

[203] W. Mikenda. Stretching frequency versus bond distance correlation of O-D(H)···Y (Y=N, O, S, Se, Cl, Br, I) hydrogen bonds in solid hydrates. J. Mol. Struc. 147, 1-15 (1986).

[204] H. T. Flakus. On the vibrational transition selection rules for the centrosymmetric hydrogen-bonded dimeric systems. J. Mol. Struc. 187, 35-53 (1989).

[205] R. G. McDonald and M. A. Hrrchman. Normal coordinate analyses for the planar $CuCl_4^{2-}$ and $CuCl_2(H_2O)_2$ complexes and their six coordinate analogues, the $CuCl_6^{4-}$ and $CuCl_4(H_2O)_2^{2-}$ anions. Spectrochimica Acta A 46, 1341-1359 (1990).

[206] N. E. Brese and M. O'Keefee. Bond-valence parameters for solids. Acta Cryst. B47, 192-197 (1991).

[207] K. Beckenkamp and H.D. Lutz, Lattice vibration spectra Part LXXII. OH stretching frequencies of solid hydroxides - correlation with structural and bonding data. J. Mol. Struc. 270, 393-405 (1992).

[208] M. Schmidt and H. D. Lutz, Hydrogen Bonding in Basic Copper Salts: a Spectroscopic Study of Malachite, $Cu_2(OH)_2CO_3$, and Brochantite, $Cu_4(OH)_6SO_4$. Phys. Chem. Minerals 20, 27-32 (1993).

[209] S. Subramanian and M. J. Zaworotko. Exploitation of the hydrogen bond: recent developments in the context of crystal engineering. Coord. Chem. Rev. 137, 357-401 (1994).

[210] H. D. Lutz, H. Moller, and M. Schmidt, Lattice vibration spectra. Part LXXXII. Brucite-type hydroxides $M(OH)_2$ (M = Ca, Mn, Co, Fe, Cd) - IR and Raman spectra, neutron diffraction of $Fe(OH)_2$. J. Mol. Struc. 328, 121-132 (1994).

[211] H. D. Lutz, C. Jung, M. Tromel, and J. Losel. Brown's bond valences, a measure of the strength of hydrogen bonds. J. Mol. Struc. 351, 205-209 (1995).

[212] H. D. Lutz, K. Beckenkamp, and St. Peter. Laurionite-type M(OH)X (M = Ba, Pb; X =

CI, Br, I) and Sr(OH)I. An IR and Raman spectroscopic study. Spectrochimica Acta A 51, 755-767 (1995).

[213] H. D. Lutz. Hydroxide Ions in Condensed Materials-Correlation of Spectroscopic and Structural Data. Struc. Bond. 82, 85-103 (1995).

[214] Ch. Mockenhaupt, Th. Zeiske, and H.D. Lutz. Crystal structure of brucite-type cobalt hydroxide β-Co{O(H,D)}$_2$ -neutron diffraction, IR and Raman spectroscopy. J. Mol. Struc. 443, 191-196 (1998).

[215] H. T. Flakus and A. Banczyk. Abnormal distribution of protons and deuterons between the hydrogen bonds bonds in cyclic centrosymmetric dimers in partially deuterated samples. J. Mol. Struc. 476, 57-68 (1999).

[216] E. Libowitzky. Correlation of O-H Stretching Frequencies and O-H···O Hydrogen Bond Lengths in Minerals. Monatshefte fur Chemie 130, 1047-1059 (1999).

[217] E. D. Isaacs, A. Shukla, P. M. Platzman, D. R. Hamann, B. Barbiellini, and C. A. Tulk. Covalency of the Hydrogen Bond in Ice: A Direct X-Ray Measurement. Phys. Rev. Lett. 82, 600-603 (1999).

[218] G. Gilli and P. Gilli. Towards an unified hydrogen-bond theory. J. Mol. Struc. 552, 1-15 (2000).

[219] S. Deabate, F. Fourgeot, and F. Henn. X-ray diffraction and micro-Raman spectroscopy analysis of new nickel hydroxide. J. Power Sources 87, 125-136 (2000).

[220] C. Murlia, S. M. Sharmaa, S. K. Kulshreshthab, and S. K. Sikka. High-pressure behavior of β-Ni(OH)$_2$ -A Raman scattering study. Physica B 307, 111-116 (2001).

[221] T. Steiner. The hydrogen bond in the solid state. Angew. Chem. Int. Ed. 41, 48-86 (2002).

[222] R. L. Frost, W. N. Martens, P. A. Williams. Raman spectroscopy of the phase-related basic copper arsenate minerals olivenite. J. Raman Spectrosc. 33, 475-484 (2002).

[223] H. D. Lutz. Structure and strength of hydrogen bonds in inorganic solids. J. Mol. Struc. 646, 227-236 (2003). R. Mortel and H. D. Lutz. Hydrogen bonds in solid hydroxides, a bond valence approach. *ibid* 648, 171-176 (2003).

[224] W. Martens, R. L. Frost, J. T. Kloprogge, and P. A. Williams. Raman spectroscopic study of the basic copper sulphates–implications for copper corrosion and 'bronze disease'. J. Raman Spectrosc. 34, 145-151 (2003).

[225] F. Pascale, S. Tosoni, C. Zicovich-Wilson, P. Ugliengo, R. Orlando, and R. Dovesi. Vibrational spectrum of brucite, Mg(OH)$_2$: a periodic ab initio quantum mechanical calculation including OH anharmonicity. Chem. Phys. Lett. 396, 308-315 (2004).

[226] M. J. Wojcik. Dynamic interactions in hydrogen-bonded systems. J. Mol. Struc. 735-736, 225-234 (2005).

[227] S. J. Grabowski. Theoretical studies of strong hydrogen bonds. Annu. Rep. Prog. Chem., C 102, 131-165 (2006).

[228] H. T. Flakus, A. Pyzik. Vibronic model for H/D isotopic "self-organization" effects in hydrogen bond cyclic trimeric systems: 4-Bromopyrazole crystal IR spectra. Chem.

Phys. 323, 479-489 (2006).
[229] Y. Hase. Computational Study of the Solid-State Vibrations and Force Field of Magnesium and Calcium Hydroxides. J. Braz. Chem. Soc. 17, 741-745 (2006).
[230] A. M. Pendas, M. A. Blanco, and E. Francisco. The nature of the hydrogen bond: A synthesis from the interacting quantum atoms picture. J. Chem. Phys. 125, 184112 (2006).
[231] R. Diniz, M. S. Dantas, N. G. Fernandes, and M. T. C. Sansiviero. A short hydrogen bond investigation by polarized Raman spectra of Co^{2+} and Zn^{2+} salts of pyromellitic acid. Spectrochimica Acta A 67, 372-377 (2007).
[232] E. Arunan, Hydrogen bonding and other molecular interactions. Current Science 92, 17-18 (2007).
[233] J. Hanko, M. Orendaca, J. Kucharb, Z.Zak, J. Cernakb, A. Orendacova, A. Feher. Hydrogen bonds mediated magnetism in Cu(*bmen*)$_2$Pd(CN)$_4$. Solid State Commun. 142, 128-131 (2007).
[234] A. D. Buckingham, J. E. Del Bene, and S. A. C. McDowell. The hydrogen bond. Chem. Phys. Lett. 463, 1-10 (2008).
[235] H. T. Flakus, A.Tyl, and M. Jablonska. Effects of strong inter-hydrogen bond dynamical couplings in the polarized IR spectra of adipic acid crystals. Chem. Phys. 364, 76-89 (2009).
[236] I. D. Brown. Recent Developments in the Methods and Applications of the Bond Valence Model. Chem. Rev. 109, 6858-6919 (2009).
[237] V. Yu. Kazimirov, M. B. Smirnov, L. Bourgeois, L. Guerlou-Demourgues, L. Servant, A.M. Balagurov, I. Natkaniec, N.R. Khasanova, E.V. Antipov. Atomic structure and lattice dynamics of Ni and Mg hydroxides. Solid State Ionics 181, 1764-1770 (2010).
[238] E. Arunan, G. R. Desiraju, R. A. Klein, *et al*. Defining the hydrogen bond: An account (IUPAC Technical Report). Pure Appl. Chem., 83, 1619-1636 (2011).
E. Arunan, G. R. Desiraju, R. A. Klein, *et al*. Defining the hydrogen bond (IUPAC Recommendations 2011). Pure Appl. Chem., 83, 1637-1641 (2011).
[239] C. S. Neupane, and S. K. Awasthi. Unique trifurcated hydrogen bonding in a pseudopolymorph of tricyclohexane triperoxide (TCTP) and its thermal studies. *Tetrahedron Lett.* 53, 6067-6070 (2012).
[240] S. J. Grabowski. Red- and Blue-Shifted Hydrogen Bonds: the Bent Rule from Quantum Theory of Atoms in Molecules Perspective. J. Phys. Chem. A 115, 12789-12799 (2011).
[241] M. Fischer, P. Lemmens, G. Els, G. Guntherodt, E. Ya. Sherman, E. Morre, C. Geibel, and F. Steglich. Spin-gap behavior and charge ordering in α'-NaV_2O_5 probed by light scattering. Phys. Rev. B 60, 7284-7294 (1999).
[242] P. Lemmens, G. Guntherodt, C. Gros. Magnetic light scattering in low-dimensional quantum spin systems. Phys. Rep. 375, 1-103 (2003).
[243] M. Grove, P. Lemmens, G. Gunth, B. C. Sales, F. Bullesfeld and W. Assmus.

Magnetoelastic coupling and spin excitations in the spin-gap system $(VO)_2P_2O_7$: A Raman scattering study. Phys. Rev. B 61, 6126-6132 (2000).

[244] P. Lemmens, K.-Y. Choi, E. E. Kaul, C. Geibel, K. Becker, W. Brenig, R. Valenti, C. Gros, M. Johnsson, P. Millet, and F. Mila. Evidence for an Unconventional Magnetic Instability in the Spin-Tetrahedra System $Cu_2Te_2O_5Br_2$. Phys. Rev. Lett. 87, 227201 (2001).

[245] P. Lemmens, M. Grove, M. Fischer, G. Guntherodt, Valeri N. Kotov, H. Kageyama, K. Onizuka, and Y. Ueda. Collective Singlet Excitations and Evolution of Raman Spectral Weights in the 2D Spin Dimer Compound $SrCu_2(BO_3)_2$. Phys. Rev. Lett. 85, 2605-2608 (2000).

[246] T. J. Sato, S. -H. Lee, T. Katsufuji, M. Masaki, S. Park, J. R. D. Copley, and H. Takagi. Unconventional spin fluctuations in the hexagonal antiferromagnet $YMnO_3$. Phys. Rev. B 68, 014432 (2003).

[247] J. Jambor, J. Dutrizac, A. Roberts, J. Grice, and J. Szymanski. Clinoatacamite, a new polymorph of $Cu_2(OH)_3Cl$, and its relationship to paratacamite and "Anarakite". Can. Mineral. 34, 61-72 (1996); J. Grice, J. Szymanski, and J. Jambor, The crystal structure of clinoatacamite, a new polymorph of $Cu_2(OH)_3Cl$. *ibid* 34, 73-78 (1996).

[248] H. D. Lutz, J. Henning, H. Jacobs, and B. Mach. Hydrogen bonds and dynamic disorder in solid hydroxides, infrared and Raman studies on polymorphic RbOH and CsOH. J. Mol. Struc. 145, 277-285 (1986).

[249] P. Lemmens, M. Fischer, G. Guntherodt, C. Gros, P. G. J. van Dongen, M. Weiden, W. Richter, C. Geibel, F. Steglich. Effects of in-chain and off-chain substitutions on spin fluctuations in the spin-Peierls compound $CuGeO_3$. Phys. Rev. B 55, 15076-83 (1997).

[250] V. Gnezdilov, P. Lemmens, Yu. G. Pashkevich, D. Wulferding, I. V. Morozov, O. S. Volkova, and A. Vasiliev. Dynamical lattice instability versus spin liquid state in a frustrated spin chain system. Phys. Rev. B 85, 214403 (2012).

[251] A. S. Davydov. The theory of molecular excitons. Sov. Phys. Usp. 7, 145-178 (1964).

[252] H. B. Ergun, K. A**.** Gehring, and G. A**.** Gehring. Jahn-Teller induced Davydov splitting in $TbVO_4$. J. Phys. C: Solid State Phys. 9, 1101-1115 (1976).

[253] J. M. Lagaron. The factor group splitting phenomenon. Macromol. Symp. 184, 19-36 (2002).

Notes: Literature Distribution

[001-050] on Basic MGF, Pyrochlore, Perovskite, Spinel; [051-100] on $M_2(OH)_3X$;

[101-150] on $Cu_{2-x}Zn_x(OH)_3Cl$; [151-152] on textbooks of IR, Raman and Group Theory;

[153-200] on RT and T-dependent Raman Spectroscopy on MGF Materials;

[201-240] on H-bonds; [241-250] on T-dependent analysis; [251-253] on Davydov splitting.

The author's related publications

1. The most related publications supporting the Dissertation:

[1] **X.D. Liu**, X.G. Zheng, D.D. Meng, X.L. Xu, and Q.X. Guo. Raman spectroscopic study of the frustrated spin 1/2 antiferromagnet clinoatacamite. *J. Phys.*: *Condens. Matter* 25: 256003 (9 pages) (2013).

[2] **X.D. Liu,** M. Hagihala, X.G Zheng, and Q.X. Guo. Vibrational Spectroscopic Properties of Botallackite-structure Basic Copper Halides. *Vibrat. Spectros*. 56, 177-183 (2011).

[3] **X.D. Liu,** M. Hagihala, X.G Zheng, and Q.X. Guo. Raman and mid-IR spectral analysis of the atacamite-structure β-$Ni_2(OH)_3Cl$. *Chin. Phys. Lett*. 28, 087805 (4 pages) (2011).

[4] **X.D. Liu,** M. Hagihala, X.G. Zheng, W.J. Tao, D.D. Meng, S.L Zhang, and Q.X. Guo. Trimeric hydrogen bond in geometrically frustrated hydroxyl cobalt halogenides. *Chin. Phys. Lett*. 28, 017803 (4 pages) (2011).

[5] **X.D. Liu,** M. Hagihala, X.G. Zheng, and Q.X. Guo. Microstructured hydroxyl environments and Raman spectroscopy in selected basic transition-metal halides. *Chin. Phys*. B 20, 087801 (8 pages) (2011).

[6] **X.D. Liu,** M. Hagihala, X.G. Zheng, and Q.X. Guo. Raman and mid-IR spectroscopic study of geometrically frustrated hydroxyl cobalt halides at room temperature. *Chin. Phys*. B 20, 077801 (7 pages) (2011).

[7] **X.D. Liu**, W.J. Tao, X.G. Zheng, M. Hagihala, D.D. Meng, and Q.X. Guo: Mid-infrared spectroscopic properties of geometrically frustrated basic cobalt chlorides. *Acta Physica Sina* 60(3), 037803 (7 pages) (2011). [in Chinese]

2. Other related publications:

[8] **X.D. Liu**, D.D. Meng, X.G. Zheng, X.L. Xu, and Q.X. Guo. Low temperature Raman spectroscopic study on γ-$Cu_2(OH)_3Cl$. *Appl. Mech. Mater.* 341-342: 320-323 (2013).

[9] **X.D. Liu**, X.G. Zheng, D.D. Meng, and X.L. Xu. More than four subtypes of trimeric hydrogen bonds in hydroxyl halides. *Appl. Mech. Mater.* 341-342: 242-245 (2013).

[10] **X.D. Liu**, X.L. Xu, D.D. Meng, M. Fujihala, X.G. Zheng, Z.W. Chen, and Q.X. Guo. Raman Band Redshifting of α-$Cu_2(OH)_3Cl$ with Decreasing the Temperature. *Adv. Mater. Res.*, 430-432, 391-394 (2012).

[11] **X.D. Liu**, J. Lu, M. Fujihala, D.D. Meng, X.L. Xu, X.G. Zheng, Z.W. Chen, and Q.X. Guo. Local Laser Heating Effect on Raman Spectroscopy of β-$Co_2(OH)_3Br$. *Adv. Mater. Res.*, 430-432, 566-569 (2012).

[12] **X.D. Liu,** D.D. Meng, X.G. Zheng, and Q.X. Guo. Spectral properties of Botallackite-structure alpha-$Cu_2(OH/D)_3Br$ at room temperature. *Adv. Mater. Res.*, 391-392, 1493-1497 (2012).

[13] **X.D. Liu,** D.D. Meng, X.G. Zheng, M. Hagihala, and Q.X. Guo. Mid-IR and Raman Spectral Properties of Hydroxyl/Deuteroxyl Cobalt Chlorides. *Adv. Mater. Res.*, 146-147, 1194-1197 (2011).

[14] **X.D. Liu,** D.D. Meng, X.G. Zheng, M. Hagihala, and Q.X. Guo. Mid-IR and Raman Spectral Properties of Clinoatacamite- structure Basic Copper Chlorides. *Adv. Mater. Res.*, 146-147, 1202-1205 (2011).

[15] J. Lu, **X.D. Liu**, X.L. Xu, M. Fujihala, D.D. Meng, X.G. Zheng, Z.W. Chen, and Q.X. Guo. Raman Spectral Properties of β-$Co_2(OH)_3Cl$ down to the Liquid Nitrogen Temperature. *Adv. Mater. Res.*, 430-432, 1257-1260 (2012).

[16] W.J. Tao, **X.D Liu,** X.G. Zheng, D.D Meng, and Q.X. Guo. Mid-IR and Raman Spectral Properties of Geometrically Frustrated Atacamite Hydroxyl Copper Chloride. *Adv. Mater. Res.*, 146-147, 972 (2011).

[17] W.J. Tao, **X.D. Liu,** X.G. Zheng, D.D. Meng, and Q.X. Guo. Mid-Infrared and Raman Spectral Properties of Geometrically Frustrated Atacamite. *Spectrosc. Spectral Analysis,* 31 (9): 2431-2436 (2011). [in Chinese]

Acknowledgement

First of all, I would like to express my deepest gratitude to my supervisor, Prof. Xu-Guang Zheng (Japanese (Jpn)-Chinese (Chn): 郑 旭光) for his four-years' kind support, invaluable guidance and limitless patience. Without his successively generous help, this dissertation would be nearly impossible.

A million thanks should be given to Prof. Qi-Xin Guo (Jpn-Chn: 郭 其新) and Assoc. Prof. Katsuhiko Saito (Jpn: 齊藤 勝彦, Chn: 齐藤 胜彦), who have provided and supervised me how to use the Raman spectroscopic system.

Great appreciate must be expressed to other teachers in the condensed matter physics group: Assoc. Profs. Makoto Maki (Jpn-Chn: 真木 一) and Yoichi Ishiwata (Jpn-Chn: 石渡 洋一), who have given me much care during my study and research period.

Deep gratitude is extended to all my classmates: Dr. Masato Hajihala (Jpn-Chn: 萩原 雅人), Dr. Masayoshi Fujihala (Jpn: 藤原 理賀, Chn: 藤原 理贺), Mr. Dong-Dong Meng (Jpn-Chn: 孟 冬冬) and Mr. Xing-Liang Xu (Jpn: 徐 興亮, Chn: 徐 兴亮) who have prepared samples for the IR and Raman measurements, or assisted me in performing the Raman experiments.

Thanks must be given to four thesis reviewers, Profs. Xu-Guang Zheng (Jpn-Chn: 郑 旭光), Qi-Xin Guo (Jpn-Chn: 郭 其新), Akira Sugiyama (Jpn-Chn: 杉山 晃), and Assoc. Prof. Makoto Maki (Jpn-Chn: 真木 一), who have carefully reviewed my dissertation manuscript and given some correcting suggestions.

I am also thankful to all staffs and faculties in the Department of Physics and International Division of Saga University for their acting concerns.

At last, I would like to express my deeply appreciation to my parents Yi-Chun Liu (Jpn: 劉 義春, Chn: 刘 义春) and Xiu-Ying Huang (Jpn-Chn: 黄 秀英), my wife Zhi-Jun Chen (Jpn: 陳 志君, Chn: 陈 志君) and my daughter Bing-Yang Liu (Jpn: 劉 氷陽, Chn: 刘 冰阳) for their endless encouragement, understanding and sacrifice. Without their careful assistance, it would not be possible to complete my doctoral study. Therefore I would like to dedicate this Dissertation to all my family members, including all my brothers and sisters.

This work was supported by a Grant-in-Aid for Scientific Research from the Japan Society for the Promotion of Science (Zheng, Kiban-B 19340100) and Grant-in-Aids for Scientific Research on Priority Areas (Tokutei 20046012 and 22014008) from the Ministry of Education, Culture, Sports, Science and Technology (MEXT), Japan.